Development of Multi-Scale City Building Energy Model for Urban Climate Resilience

Ali Katal

A Thesis

In the Department

of

Building, Civil and Environmental Engineering

Presented in Partial Fulfillment of the Requirements

for the Degree of

Doctor of Philosophy (Building Engineering) at

Concordia University

Montreal, Quebec, Canada

November 2020

CONCORDIA UNIVERSITY

School of Graduate Studies

This is to certify that the thesis prepared

By:	Ali Katal
Entitled:	Development of Multi-Scale City Building Energy Model for Urban Climate Resilience

and submitted in partial fulfillment of the requirements for the degree of

Doctor of Philosophy (Building Engineering)

complies with the regulations of the University and meets the accepted standards with respect to originality and quality.

Signed by the final Examining Committee:

Dr. Youmin Zhang	Chair
Dr. Laxmi Sushama	External Examiner
Dr. Amin Hammad	External to Program
Dr. Radu Grigore Zmeureanu	Examiner
Dr. Andreas K Athienitis	Examiner
Dr. Liangzhu (Leon) Wang	Thesis Co-Supervisor
Dr. Sylvie Leroyer	Thesis Co-Supervisor

Approved by ______________________________

Dr. Michelle Nokken, Graduate Program Director

December 14, 2020 ______________________________

Dr. Mourad Debbabi, Dean,
Gina Cody School of Engineering and Computer Science

Abstract

Development of Multi-Scale City Building Energy Model for Urban Climate Resilience

Ali Katal, Ph.D.

Concordia University, 2020

In the past decades, the world has experienced rapid urbanization that caused increasing climate change challenges, pollution, energy consumption, and greenhouse gas (GHG) emission. More frequent and more prolonged extreme weather events such as heatwave and cold-wave and urban heat island phenomena are some negative impacts of climate change. The building sector is an essential source of urban energy consumption, GHG emission, and Urban Heat Island (UHI) formation. Different energy efficiency measures can be implemented to reduce building energy consumption, such as retrofitting existing building stock and deploying new technologies. These scenarios will also contribute to the mitigation of UHI, heatwaves, and climate change. Urban building energy models are simulation tools developed to study these kinds of problems. There are several challenges with existing Urban Building Energy Modelling (UBEM) tools, including creating a 3D model of buildings, estimating buildings' properties, and using urban microclimate data for simulation.

On the other hand, accurate building energy simulation and fluxes from buildings to the atmosphere can impact forecasting accuracy by numerical weather prediction tools. Therefore, developing a multi-scale integrated urban building energy and climate simulation tool is essential for modeling both buildings' energy performance and atmospheric fields. In this work, a new urban building energy model called City Building Energy Model (CityBEM) is developed to solve UBEMs' current challenges. First, a building-scale energy and airflow simulation model is developed for modeling a single building. It is based on a coupled thermal/airflow multi-zone network model. The multi-zone network model is then modified for calculation of urban scale buildings’ energy performance. A new method is developed to create the 3D model of buildings by integrating buildings’ footprint data obtained from OpenStreetMap and Microsoft and building height information by Google Earth Application Programming Interface (API). An archetype library is developed for the estimation of buildings’ non-geometrical properties. Buildings are classified based on usage type and age obtained from city shapefile datasets. The geometrical and non-geometrical datasets are joined using the QGIS tool and Mapbox platform.

To use local microclimate data for buildings’ energy performance, CityBEM is integrated with different microclimate simulation tools. First, CityBEM is fully integrated with the CityFFD tool to model the two-way interaction between buildings and microclimate. In the second method, a multi-scale urban climate and buildings energy simulation tool is developed by one-way integration of CityBEM with 3D Global Environmental Multiscale Model (GEM) and Surface Prediction System (SPS) developed by Environment and Climate Change Canada (ECCC). The one-way multi-scale model cannot capture the impact of CityBEM on the atmospheric fields; therefore, to model this impact, the CityBEM is added as a new module to the SPS model. SPS includes a Town Energy Balance (TEB) scheme for modeling the urban surface. In this thesis, CityBEM is added to the TEB for modeling the buildings. Using the developed TEB-CityBEM model in GEM simulations, near-surface forecasting accuracy can be improved, and buildings’ energy simulation is added as a new feature to the GEM model. The multi-scale model can be used to study different mitigation strategies such as retrofitting existing buildings, modeling natural

ventilation and its impact on reducing energy consumption, model new technologies to reduce energy consumption, etc. The TEB-CityBEM model can also be added to the air quality model of ECCC called GEM-MACH to study the impact of urban building modeling on air quality in urban areas.

Finally, due to the importance of aerosol transmission of covid-19 in indoor spaces, it is essential to develop a model to study the impact of different mitigation strategies on reducing the risk of infection in the rooms and their corresponding energy consumption effects. In this thesis, a city-scale model (CityRPI) is developed to estimate airborne transmission of COVID-19 in indoor spaces. The CityRPI model is integrated with the CityBEM. The integrated model is applied to Montreal, and the impact of mitigation strategies on the infection risk and energy consumption is studied for different types of buildings.

Acknowledgments

I would like to express my special thanks of gratitude to my supervisor Dr. Liangzhu (Leon) Wang, for the continuous support of my Ph.D. and giving me the golden opportunity to do this wonderful project on the topic (Development of Multi-Scale City Building Energy Model for Urban Climate Resilience). Without his motivation, patient guidance, and persistent assistance, this thesis would not have been possible.

I would like to express the most profound appreciation to my co-supervisor, Dr. Sylvie Leroyer, at Environment and Climate Change Canada. Completing my dissertation would not have been possible without her support, availability, and constructive suggestions.

Some special words of gratitude go to my friend, who has always been a significant support source in this project and has collaborated on developing a robust urban environment model: Dr. Mohammad Mortezazadeh. Also, I thank my colleague: Maher Albettar for his significant help and collaboration on different projects.

I would also like to extend my deepest gratitude to the members of the examining committee, Dr. Laxmi Sushama, Dr. Radu Grigore Zmeureanu, Dr. Amin Hammad, and Dr. Andreas K Athienitis, for their precious comments on my thesis work.

Last but not least, my deepest gratitude goes to my parents for their unconditional love and support.

Table of Contents

List of Figures

List of Tables

Nomenclature

m_i	Mass of zone i	$[kg]$
t	Time	$[s]$
$F_{ji,k}$	Airflow rate from zone j and zone i through opening k	$[kg/s]$
Ms_i	Airflow source of zone i	$[kg/s]$
$C_{pa,i}$	Air specific heat capacity of zone i	$[J/kgK]$
T_i	Air temperature of zone i	$[K]$
$Q_{zs,i}$	Heat source of zone i	$[W]$
$A_{w,k}$	Area of wall k	$[m^2]$
R_k	Thermal resistance of the wall	$[m^2K/W]$
ΔT_k	Temperature difference across a wall or window	$[K]$
R	Gas constant	$[J/kgK]$
V_i	Volume of zone i	$[m^3]$
P_i	Pressure of zone i	$[Pa]$
$C_{w,i}$	Thermal capacitance of the wall	$[J/K]$
$T_{w,i}$	Temperature of the wall layer	$[K]$
$S_{w,i}$	Heat source of the wall layer	$[W]$
Δx_i	Thickness of wall layer	$[m]$
C_{pw}	Specific heat capacity of the wall	$[J/kgK]$
L_w	Total thickness of the wall	$[m]$
N_w	Number of layers inside the wall	-
k_w	Thermal conductivity of the wall	$[W/mK]$
$h_{comb,in}$	Combined heat transfer coefficient of the interior surface	$[W/m^2K]$
$h_{comb,out}$	Combined heat transfer coefficient of the exterior surface	$[W/m^2K]$
q_{LWR}	Long-wave radiation exchange of the exterior surface	$[W]$
$I_{glo,w}$	Global solar radiation on the wall	$[W/m^2]$
q_{grd}	Long-wave radiation between exterior surface and ground	$[W]$
q_{sky}	Long-wave radiation between exterior surface and sky	$[W]$
q_{air}	Long-wave radiation between the exterior surface and ambient air	$[W]$
F_{grd}	Longwave view factor to ground	-
F_{sky}	Longwave view factor to sky	-
T_{grd}	Ground temperature	$[K]$

T_{sky}	Sky temperature	$[K]$
T_{out}	Outdoor air temperature	$[K]$
C_{ij}	Flow coefficient of the flow path ij	$[kg/sPa^n]$
n_{ij}	Flow exponent of the flow path ij	-
ΔP_{ij}	Pressure difference across the path ij	$[Pa]$
$C_{d,ij}$	Discharge coefficient if path ij	-
L_{ij}	Effective leakage area	$[m^2]$
$\Delta P_{r,ij}$	Reference pressure difference	$[Pa]$
f_{turb}	Turbulence coefficient of the shaft airflow model	-
h_i	Height of the opening relative to the zone floor level	$[m]$
$P_{w,ij}$	Wind-induced pressure across the opening ij	$[Pa]$
$P_{s,ij}$	Pressure differential by stack effect across the opening ij	$[Pa]$
U_H	Approaching wind speed at upwind wall height	$[m/s]$
$C_{p,wind}$	Mean local wind pressure coefficient	-
I_{dir}	Direct normal solar irradiance	$[W/m^2]$
I_{dif}	Diffuse irradiance	$[W/m^2]$
$SHGC$	Solar heat gain coefficient of the glazing	-
$\dot{Q}_{sol}$	Solar radiation transmitted through the glazing	$[W]$
T_{in}	Indoor air temperature	$[K]$
$T_{s,k}$	Interior surface temperature of wall/roof/floor/thermal mass	$[K]$
F_{inf}	Infiltration airflow rate	$[m^3/s]$
F_{nv}	Natural ventilation airflow rate	$[m^3/s]$
$\dot{M}_{sys}$	HVAC system mass flow rate	$[kg/s]$
T_{sup}	Supply air temperature of the HVAC system	$[K]$
Q_{int}	Internal heat gain	$[W]$
$R_{w,i+1}$	Thermal resistance of node i inside the wall	$[Km^2/W]$
R_{cond}	Conductive thermal resistance	$[Km^2/W]$
$R_{conv,in}$	Convective thermal resistance of the interior surface	$[Km^2/W]$
R_{air}	Thermal resistances between the exterior node of the wall and outdoor air	$[Km^2/W]$
R_{sky}	Thermal resistances between the exterior node of the wall and sky	$[Km^2/W]$
R_{gnd}	Thermal resistances between the exterior node of the wall and ground	$[Km^2/W]$
$h_{conv,ext}$	Exterior convective heat transfer coefficient	$[W/m^2K]$
$h_{c,glass}$	Convection coefficient for very smooth surfaces	$[W/m^2K]$

h_n	Natural convective heat transfer coefficient	$[W/m^2K]$
V_z	Local wind speed	$[m/s]$
E_{out}	Exterior long-wave radiation incident on the window	$[W/m^2]$
E_{in}	Interior long-wave radiation incident on the window	$[W/m^2]$
$h_{conv,in}$	Interior surface convective coefficient	$[W/m^2K]$
S_i	Short-wave radiation on the i^{th} face	$[W/m^2]$
$h_{r,\mathrm{i}}$	Surface radiative coefficient	$[W/m^2K]$
Q_s	Design sensible cooling and heating loads	$[W]$
$T_{out,des}$	Outdoor air design temperature	$[K]$
$T_{in,set}$	Set-point indoor air temperature	$[K]$
SHG	Solar heat gain	-
X_{mix}	Mixing ratio of HVAC system	-
F_{rec}	Recirculation air flow rate	$[m^3/s]$
F_{oa}	Outdoor air ventilation rate	$[m^3/s]$
T_{mix}	Mixing temperature of the HVAC system	$[K]$
Q_t	Heating/cooling demand of the building	$[W]$
$Q_{hvac,heat}$	Energy consumed by the HVAC system for the heating	$[W]$
$Q_{hvac,cool}$	Energy consumed by the HVAC system for the cooling	$[W]$
COP_{cool}	Cooling system coefficient of performance	-
SFP	Specific fan power	$[kW/(m^3/s)]$
Δp_{tot}	Fan pressure rise	$[Pa]$

Greek and math symbols

λ	Latitude	-
ω	Hour angle	-
δ	Declination	-
ε	Emissivity	-
σ	Stefan–Boltzmann constant	$[W/m^2K^4]$
ρ	Air density	$[kg/m^3]$
ρ_w	Density of wall	$[kg/m^3]$
η_{tot}	Fan system efficiency	-
η_{heat}	Efficiency of the heating system	-
θ_i	Temperature of window layer i	$[K]$
θ_{su}	Angle of incidence of sun	degree
θ_s	Zenith angle of the sun	degree

φ_s	Azimuth of the sun	degree
φ_p	Azimuth of a plane	-
θ_p	Tilt angle of the surface	degree
α_w	Solar absorptance coefficient of the wall	-

Abbreviations

CityBEM	City Building Energy Model
GHG	Greenhouse Gas
GEM	Global Environmental Multiscale Model
UBEM	Urban Building Energy Modeling
UHI	Urban Heat Island
NWP	Numerical Weather Prediction
CFD	Computational Fluid Dynamics
TEB	Town Energy Balance
MSC	Meteorological Service of Canada
HVAC	Heating, Ventilation, and Air Conditioning
SHGC	Solar Heat Gain Coefficient
STL	StereoLithography
CityFFD	City Fast Fluid Dynamic
LAM	Limited-Area Model
RDPS	Regional Deterministic Prediction System
HRDPS	High-Resolution Deterministic Prediction System
EPiCC	Environmental Prediction in Canadian Cities
ISBA	Interactions between Soil, Biosphere, and Atmosphere
PI	Probability of Infection
RPI	Reduced Probability of Infection
UTCI	Universal Thermal Climate Index
API	Application Programming Interface

Chapter 1 Introduction

In the past decades, the world has experienced rapid urbanization due to population growth, an increasing number of cities, and migration from rural to urban areas [1]. The United Nations estimates that more than two-thirds of the world's population will live in urban areas by 2050 [1]. While ongoing rapid urbanization can improve societies' well-being, it also causes increasing challenges of pollution, energy consumption, and greenhouse gas (GHG) emission [2]. For solving these challenges, many cities have developed long-term GHG emission reduction goals such as a 40% reduction from 1990 to 2025 in San Francisco (SF) [3], an 80% reduction from 2005 to 2050 in New York City [4], and reduction goal of 80% below 2005 level by 2050 in City of Boston [5]. To reduce GHG emissions and energy consumption, Canada is implementing the Pan-Canadian Framework on Clean Growth and Climate Change [6]; while strengthening existing and introducing new GHG reducing measures. The goal of the Pan-Canadian Framework is to reach or exceed the target of a 30 percent reduction of greenhouse gas (GHG) emissions below the 2005 level and beginning work so that Canada can achieve net-zero emissions by 2050.

The building sector is an essential source of urban energy consumption and GHG emission. For example, U.S. residential and commercial buildings account for more than 40% of the total energy usage and 72% of total electricity consumption [7]. Different energy efficiency measures can be implemented to reduce building energy consumption, such as retrofitting existing building stock, deployment of renewable energy resources, and district heating and cooling. More than 75 percent of Canada's building stock in 2030 will be composed of buildings already standing today. Therefore, retrofitting existing buildings can significantly contribute to the GHG emission and energy consumption reduction goal. Canada's government is developing a model code for existing buildings and energy efficiency improvements when renovating buildings. Such information and analysis can be provided by using urban-scale building energy simulation tools. Thus, many urban building energy modeling (UBEM) tools have been developed for the simulations of city-scale building energy consumption and energy efficiency measures.

1.1. Problem Statement

Physics-based UBEM models apply heat and mass balance equations to each building in the city with the capability of achieving any spatial and temporal resolutions. Accuracy and computational time are the most critical factors regarding the simulation engine of a UBEM tool. Some existing UBEM tools use complicated simulation engines such as EnergyPlus [8], which is computationally expensive for large-scale cases such as the whole city or province simulation. Some other tools use simple resistance-capacitance network models, which is not accurate enough. Some essential components regarding the calculation of buildings' energy performance are not considered in such models.

Gathering and processing input data at a city scale is an essential step for urban building energy simulations. Three types of data are required: 3D city and building geometrical data, building non-geometrical data, and weather data, preferably dynamic datasets. UBEM tools need buildings' geometrical information, including shape, floor area, height, window-to-wall ratio (WWR), and other information related to building energy simulations. Preparing building geometrical data is an essential part of a UBEM analysis and often takes a large portion of the modeling time. Non-geometrical properties of buildings, for example, building envelope properties, occupancy schedule, and solar heat gain coefficient (SHGC) are the second type of data required for UBEM. It is almost impossible to collect these data for every single building in a city. UBEM tools usually use archetype libraries to estimate such building properties [9]. First, buildings are divided into several groups according to ages, usages, and shapes. Then a set of properties is assigned to each group of buildings. Therefore, some building-specific information, such as year of construction and building usage data, is required to create an archetype library. Different official datasets are used by previous studies to provide the information. Buildings footprint and non-geometrical properties datasets are usually represented in various formats, and the building indexes and logistics are different in these two files. Therefore, an additional step is needed to combine the data.

Weather data are the last input dataset of a UBEM tool. Most of the existing UBEM platforms use weather data from one or several nearby weather stations for the energy analysis of all buildings. Therefore, they have not considered the impacts of localized microclimate environment. Building energy performance is profoundly affected by urban microclimate conditions [10]. Different wind velocity and temperature around buildings directly impact the building’s thermal load regarding local convective heat transfer coefficients and air infiltration through envelopes [11]. Urban Heat Island (UHI) can increase space cooling demand and reduce HVAC systems' efficiency under higher temperatures [10,12]. UHI can also cause discomfort, respiratory difficulties, heat cramps and exhaustion, non-fatal heat stroke, and heat-related mortality inside buildings [13]. For example, the 2018 Canadian heatwave was associated with more than 90 deaths in Quebec Province [14], many of which occurred in the dense urban areas due to UHI. Hong et al. [15] proposed ten questions and answers, highlighting UBEM challenges and future research works. Integrating UBEM with urban microclimate tools such as high-resolution Numerical Weather Prediction (NWP) or Computational Fluid Dynamics (CFD) to capture the urban atmosphere's impact on buildings’ performance is one of the ten challenges.

On the other hand, NWP is moving toward the representation of near-surface and fine-scale phenomena such as the UHI and interactions between the sea-breeze flow and urban processes. Recent studies show that high-resolution numerical simulations and physical expression of urban areas using the Town Energy Balance (TEB) model positively impact near-surface meteorology prediction [16–18]. The TEB model is used in the urbanized version of the Global Environmental Multiscale (GEM) model developed by the Meteorological Service of Canada (MSC). It is a physically-based urban canopy model that considers a two-dimensional approximation of an urban canyon. It calculates the climate conditions, the drag force, and energy fluxes from surfaces of identical urban canyons, where all the orientations are possible and exist with the same probability [18]. Therefore, buildings' real geometry, essential components of buildings' energy performance, and actual impact of buildings on urban climate are not considered in the current version of the TEB model. Replacing the TEB scheme with a more detailed building energy model can improve the GEM model's near-surface meteorology prediction. It can also add the building's energy performance calculation to the GEM model's operational version for short-term weather forecasting. Therefore, it is necessary to develop an integrated multi-scale (kilometer- to sub-kilometer-scale) urban climate and building energy simulation model to capture the two-way interaction between urban building energy performance and microclimate simulation.

1.2. Thesis Objective

The previous section revealed the need for developing a multi-scale urban buildings' energy and climate model that can model the two-way impacts of buildings and microclimate. Due to the lack of a physics-based UBEM model appropriate for simulation of a big city or province, this thesis's first objective is to develop a new UBEM model covering the significant components for accurate calculation of buildings' energy performance. Preparing building geometrical data is an essential part of a UBEM analysis and often takes a large portion of the modeling time. There is no general methodology to create the 3D model of cities. Also, datasets used by current UBEM tools are limited to specific regions and cities. The thesis's second objective is to develop a new automated model for creating the 3D model of cities using publicly available datasets. Creating an archetype library that can estimate all buildings' non-geometrical properties in a city is the next objective of this thesis. For this purpose, an archetype library is developed by combining data gathered from different datasets.

Buildings’ energy performance is affected by weather conditions. Using local microclimate data instead of a nearby weather station can improve the UBEM result. Microclimate data can be obtained from a Numerical Weather Prediction (NWP) system or a Computational Fluid Dynamic (CFD) model. On the other hand, anthropogenic heat fluxes from building surfaces to the atmosphere can impact the near-surface atmospheric fields. Therefore, there is a two-way interaction between buildings and microclimate. An integrated UBEM and urban climate simulation model is needed to capture this two-way interaction. This thesis's next objective is to model this two-way interaction by integrating the newly developed UBEM tool with an urban microclimate simulation model and an NWP system.

Airborne transmission of COVID-19 is a major route of infection, especially in indoor spaces with poor ventilation. Several mitigation strategies can be applied to indoor spaces to reduce infection risk, such as improving the room’s ventilation condition. The effectiveness of different strategies can change by building type and properties. These strategies can also impact the energy consumption of buildings, especially in winter. Therefore, it is necessary to develop an integrated UBEM and airborne infection risk model to study the impact of different mitigation strategies on reducing infection risk in the rooms and their corresponding energy consumption effects. This thesis's last objective is to develop a city airborne infection risk model and integrate it with the developed UBEM platform.

1.3. Summary

This chapter introduces the current research gaps in the study of urban building energy simulation and its objectives. The difficulties of urban building energy modeling and two-way interaction of buildings and urban microclimate with the current numerical tools are discussed. This research focused on developing a multi-scale urban building energy and climate simulation tool by integrating a new UBEM platform called CityBEM and two urban microclimate simulation tools, GEM and CityFFD. For modeling COVID-19 airborne transmission risk in all buildings of a city and studying the impact of mitigation strategies on reducing risk, a city infection risk model called City Reduced Probability of Infection (CityRPI) is developed. CityRPI is integrated with CityBEM to study the impact of different mitigation strategies on buildings' energy consumption and infection risk.

Chapter 2 presents a comprehensive literature review about urban building energy simulation, two-way impacts of buildings and microclimate, GEM numerical weather prediction system, and the airborne transmission of COVID-19 in indoor spaces.

Chapter 3 presents a new building-scale thermal, airflow, and energy model. A coupled thermal/airflow multi-zone network model developed to simulate airflow and energy in urban infrastructures such as buildings and tunnels. Different coupling strategies are studied, and the best approach considering the convergence and speed is selected for the simulation. The multi-zone network model's performance is analyzed by simulating some benchmark test cases and a hybrid ventilation system in a high-rise institutional building.

Chapter 4 describes the development of a city-scale building energy model called CityBEM. CityBEM physical mode, automated generation of 3D buildings model, and development of an archetype library to estimate buildings' non-geometrical parameters are presented in this chapter.

In Chapter 5, CityBEM is integrated with an urban microclimate simulation tool called CityFFD. The integrated model is used to simulate two extreme weather events in Montreal (cold-wave and heatwave). The buildings' energy performance and two-way interaction between buildings and microclimate are studied.

Chapter 6 describes creating a multi-scale urban building energy and climate simulation model by integrating CityBEM with Global Environmental Multiscale (GEM) and Surface Prediction System (SPS) models. Developed multi-scale model is implemented to the Montreal City. Then the 2018 heatwave is simulated, and the performance of the model is investigated by comparing the result with measurement data.

Chapter 7 describes the integration of CityBEM with the City Reduced Probability of Infection (CiyRPI) model. CityRPI calculates the aerosol transmission of COVID-19 in indoor spaces at the city scale. The integrated CityBEM-CityRPI model is used to model the coldest period of winter 2019. The impact of different strategies on the probability of infection and energy consumption of buildings is studied.

Chapter 8 concludes the thesis with the proposed future work.

Chapter 2 Literature Review

2.1. Building Scale Thermal, Airflow, and Energy Simulations

The buildings sector represents a large portion of the worldwide energy usage and associated greenhouse gas (GHG) emissions. Buildings consume more than 76% electricity and 40% energy in the U.S. [19,20], among which heating, ventilation, and air conditioning (HVAC) systems account for 35% of the total energy use [19]. One way to reduce high HVAC energy usages is to incorporate hybrid ventilation (HV) in buildings. HV is an effective ventilation strategy that combines the benefits of natural and mechanical ventilation to improve indoor environment quality and reduce energy consumptions [21–23].

To facilitate natural airflow and benefit from the maximum level of thermal buoyancy effects, HV systems in high-rise buildings often incorporate a vertical open space, i.e., atrium. The atrium allows free airflow across different building stories under the driving forces naturally created by the wind pressures and the stack effects due to the thermal buoyancy. When the natural driving forces are insufficient for air spreading, mechanical supply and/or exhaust fans are added as auxiliary means [24]. An essential application of the HV systems is night cooling, as the outdoor air conditions are suitable for cooling a building at nights in many climates. Night cooling systems are also often combined with thermal storages through natural building thermal mass (e.g., concrete slabs). With proper controls, the combination could significantly reduce peak cooling demand and reduce HVAC energy usages while maintaining acceptable indoor thermal comfort [25,26].

The effectiveness and full energy-saving potential of an HV system depend on its proper design and operation. It includes the determination of the size, location, and the number of the ventilation openings, geometrical parameters of the open spaces (e.g., height and width of the atria) at the design stage, and the control of the ventilation dampers and their cooperation with the cooling system under variable weather conditions during the operation [27]. For example, the inlet dampers' natural airflow rates could vary significantly with the surrounding weather dynamics. The decision to adjust the opening size or complete close/open should be made in real-time or more often in a proactive (or predictive) manner before changing the weather conditions, e.g., so-called model predictive controls. Understanding the interactions between the building, its systems, and the surrounding environment in a forecasting manner requires a reliable and fast model, which can be implemented in a medium-rise or high-rise building to predict the dynamics using forecasted weather while also considering occupancy patterns [28]. The model implementation should also be relatively simple instead of a detailed whole-building energy solution to be readily applied to the building automation system without a hassle.

The simulation model's expected function is to predict the system's performance, including the airflow rates through openings, the corresponding effects on the building's interior thermal conditions, and the cooling energy saving potentials. In a hybrid ventilated building, air movement and thermal conditions' interdependency poses a coupled thermal airflow problem [29]: the variations of indoor temperatures affect the airflow's driving forces, whereas the amount of natural air ventilation from the ambient affects the indoor temperatures. Historically, various models have been developed to address the coupled thermal airflow problem. Computational fluid dynamics (CFD) models have been widely adopted as useful tools for natural and hybrid ventilation simulations [30–33]. However, several limitations of CFD have been well noted. A typical CFD simulation's high computing cost makes it impractical for transient (or annual) simulations of a whole high-rise building, so it is often used for modeling certain portions of a building under steady-state conditions [34].

Moreover, combining the fluid-solid conjugate heat transfer process with building thermal mass storage in CFD tools shows specific stability issues. It results from the different time scales between the solid conduction and the fluid convection phenomena [35]. An alternative model to CFD is the multi-zone airflow network models, such as CONTAM [36] and COMIS [37], developed for a faster prediction of transient airflows throughout a building than CFD. Typically, these multi-zone airflow models do not solve building energy balances, so all the temperatures must be provided as inputs, e.g., from building energy simulation tools such as EnergyPlus [38] and TRNSYS [39]. Some efforts have been conducted to integrate multi-zone airflow models with energy simulation software based on co-simulation [40]. Users need to have both software tools' expertise making it relatively hard to become a general solution. There existed some other efforts to add energy balance solvers to the multi-zone airflow models. Axley et al. [41] were involved in developing CONTAM97R, a coupled thermal/airflow multi-zone network program, to assess a hybrid ventilation system's performance in an office building with promising results. However, the simulation tool has not been further developed for various reasons [41], so the tool cannot be used for operational purposes such as model predictive simulations and controls of natural and hybrid ventilation systems.

In a recent survey conducted by Zhai et al. [21] on the current status of solving building thermal airflow problems, it was found that the present whole building energy and airflow simulation tools are often too complicated and need a high execution time. These tools may be applicable to design and sizing purposes, whereas it is difficult to apply them to HV systems' online predictive controls. Recently, Yuan et al. [42] developed a simple thermal network model to analyze the thermal comfort condition in the corridors of a high-rise building with an HV system. The model was applied to modeling one floor of the building and was calibrated using measured data. However, the measured airflow rates from inlet dampers were used as inputs instead of calculated, so the model is implacable for the cases with the measured data. Hu and Karava [28] developed a recent coupled thermal and airflow network model in MATLAB. The model was used for off-line predictive controls of one atria section in the same building as Yuan et al. [42]. It was focused on numerical simulations, and they did not demonstrate it for online predictive simulations with the calibrations using actual measurement data. Qi et al. [43] developed a simplified model in CONTAM software for the simulation of the HV system in an institutional high-rise building. They conducted a series of full-scale measurements for the calibration and validation of the model. Their study included both whole-building simulations and the calibrations based on field measurement data. The calibrations were conducted statically. All the calibrated parameters were considered average constants, so the surrounding environments' dynamic interactions on the indoor conditions cannot be addressed. The simulations were also focused on historical data instead of predictive means.

Based on this literature review, the following research gaps were identified for dynamic predictive modeling of HV systems in high-rise buildings:

- A fast, accurate, and relatively simple model needs to be developed for solving the coupled thermal airflow process of HV systems. The model should simplify a detailed whole high-rise building into reduced numbers of zones to be implemented in existing building automation systems with reasonable computing costs when it is used as a predictive model potentially for online predictive controls of the system.

- Field measurement data, e.g., airflow velocity through openings, indoor and outdoor air temperature, etc., are needed to calibrate and validate the numerical simulations. Type, number, and position of the sensors which are adequate for calibration purpose must be studied.
- Consider the impacts of the environmental factors (wind speed, wind direction, and air temperature), how important it is to acquire local weather conditions from a local weather station compared to using a nearby weather station or typical historical weather data. In other words, is a local weather station essential for accurate predictive simulations using the proposed HV model of a high-rise building?

In this thesis, a coupled airflow/thermal multi-zone network model was developed for modeling the energy and airflow in buildings. The model can be used for predictive simulations with dynamic calibrations based on field measurements. The methodology of the developed model is described in Chapter 3. The multi-zone network model can capture the HV system's essential features, including the airflow rate through dampers, air exchange rates among zones, zone temperatures, solar irradiation transmission through glazing, and conjugate heat transfer with concrete slabs. The model has been applied to modeling the HV system of a 17-story high-rise building in Montreal, Canada. An extensive full-scale experimental study was also conducted to measure the airflow velocity through dampers, indoor air temperatures, mechanical fan flow rates, and ambient weather conditions. The measurement is performed for the summers of 2017 and 2018 when the HV system was operational.

2.2. Urban Building Energy Model

Rapid urbanization with the increased energy consumption, especially in the building sector and increased GHG emissions, draw a lot of attention to the understanding of building energy usages at an urban scale, i.e., so-called urban building energy modeling (UBEM) [44–46]. Through UBEM, municipal governments, urban planners, and building and environment researchers can investigate the effect of future potential energy savings through new technologies, standards/codes, and energy management policies on existing or new constructions in terms of urban energy usage and their associations with GHG emissions and regional environmental qualities. There exist two main UBEM approaches: the top-down and the bottom-up models. In top-down models, a group of buildings is analyzed as a single unit, and they do not provide the energy consumption of each building [47,48]. These models are incapable of modeling different energy demand-supply scenarios and retrofitting strategies. They cannot also provide a detailed analysis of a specific neighborhood [46,49].

In contrast, the bottom-up models simulate each building individually by statistical and/or physics-based methods in aggregations to the urban, state, or country scale [47,50–52]. The bottom-up models can provide detailed analyses of every single building, evaluate the impact of new technologies, predict the future energy consumptions of a specific existing neighborhood, and even future urban developments. The bottom-up models can be categorized into two different types: statistical and physics-based models. The statistical models use historical energy usage of end-use buildings or some sample buildings to calculate the total energy uses. The historical data of energy consumption and economic indicators are provided by governments' sources, which may not be available and accessible for all urban areas [48]. Another major limitation of such statistics-based models is poor characterizations of energy services and coarse spatial/temporal resolution of the analysis [47].

In contrast, the physics-based models apply heat and mass balance equations to each building with the capability of achieving any spatial and temporal resolutions. Physics-based models require buildings’ geometrical and non-geometrical parameters, including buildings’ shape, glazing, envelope thermal properties, and occupancy rate and schedule to create the model and calculate buildings' energy consumption [53]. Physics-based models do not require the historical energy consumption data needed by the top-down and statistical bottom-up models. Physics-based models only require buildings parameters and weather data to analyze buildings' energy consumption. Therefore, they can analyze future city infrastructures, making them a promising method for future urban-scale energy consumption and GHG emission analysis studies.

Physics-Based UBEMs

In recent years, several physics-based UBEM tools have been developed. CitySim, developed by Ecole Polytechnique Fédérale de Lausanne University [50], uses a simplified resistor-capacitor network model to estimate buildings' energy usage at the scale of an urban district. [54] developed a geographic information system (GIS)-based UBEM platform to calculate every building's energy use in the city. They used Urban-EPC, a modified Energy Performance Calculator engine, for building energy modeling. Urban-EPC is a modified resistor-capacitor network model. Happle et al. [55] proposed a new methodology based on integrating a hybrid model of dynamic demand prognosis in a GIS framework. The hybrid model is the integration of two bottom-up methods of the statistical and analytical ones. The analytical model is a simplified resistor-capacitor model to predict building heating and cooling loads. A building archetype database was defined to assign standard building envelopes, heating, ventilation, air conditioning (HVAC) systems, and specific buildings' annual consumptions. Buildings were classified according to sixteen occupancy types, six construction periods, and six renovation periods, for a total of 172 building archetypes or building classes. The database was based on the statistical data gathered from official sources.

Another UBEM model, Urban Modeling Interface (UMI) [9], is based on the 3D modeler software platform Rhino [56] and uses EnergyPlus [38] to estimate buildings energy use. UMI has been used to calculate the hourly energy demand of Boston city. The required geometrical and non-geometrical data for creating the city model were provided by an official GIS dataset and an archetype library with 52 classes based on the buildings' usages and ages. The generation of the 3D model of the city required lots of data and user efforts. Another model, CityBES, developed by the Lawrence Berkeley National Lab [57], is an open web platform for simulating city building energy efficiency. It provides a GIS-based building performance visualization for urban-scale building energy retrofit modeling, simulation, and analysis. CityBES model only supports office and retail buildings while the city building database includes other commercial (e.g., hotels, restaurants, schools, and hospitals) and residential building types.

As for the existing UBEM models, some previous studies used a simple resistor-capacitor network model, whereas others used a more detailed physics-based thermal simulation engine such as EnergyPlus [38]. A big community or city simulation would need to model thousands of buildings using EnergyPlus, which requires a massive level of details and high computational time. Therefore, a simplified thermal model without many buildings' details is needed to reduce the computational time while keeping essential components for an accurate calculation of building thermal loads.

Input Data

Gathering and processing input data at a city scale is essential for urban building energy simulations. Three types of data are required: 3D city and building geometrical data, buildings’ non-geometrical data, and weather data, preferably dynamic datasets. UBEM tools need buildings’ geometrical information, including shape, floor area, height, window-to-wall ratio (WWR), and other information related to building energy simulations. Preparing building geometrical data is an essential part of a UBEM analysis and often takes a large portion of the modeling time. 3D digital city models are also crucial for many other applications, such as tourism and marketing, city planning, city climate, noise control, urban environmental research, and navigation systems. In recent years, different datasets and methods have been developed to construct 3D city models, e.g., LiDAR (Light Detection and Ranging) point clouds [58], satellite imagery [59,60], airborne imagery [61], UAV-based photogrammetry [62], laser scanning [63], 2D ground maps [64], and combining Digital Surface Models (DSM) with the cadastral footprints [65]. Huang et al. [66] used the data measured by an aircraft equipped with a laser scanner to create the 3D city model of an actual complex urban area in Tokyo, Japan, for their CFD microclimate simulations. A combination of citywide GIS data and building footprint LiDAR data was used in several UBEM projects.

Quan et al. [67] used the GIS data provided by the New York City Department of City Planning [68] to obtain building footprint information of the Manhattan borough. Cerezo Davila et al. [9] developed a UBEM for Boston with 83,541 buildings base on official GIS datasets, which includes polygon type shapefiles for parcels (PRC) and building footprints (BLD). A 2.5D massing (extruded 2-D building’s footprint based on building height) was chosen for the Boston model based on the BLD dataset footprints and extrusion heights. Preparing building footprints was the most time-consuming step in the massing characterization. The polygon simplification techniques were applied to the GIS datasets to extrude the complex initial shapes into the massing models. Cerezo et al. [69] developed a UBEM model to calculate the Energy Use Intensity (EUI) of 336 residential buildings in a district of Kuwait City. To generate geometric representations of the buildings, they obtained building footprint polygons in a GIS shapefile provided by the city and a digital elevation map for building heights.

With the adventure of Web 2.0 technologies, Volunteered Geographic Information (VGI) as a newly emerged geo-information industry has attracted much attention in academics and industry [70–73]. VGI was first proposed by Goodchild [74] to create and edit geographical information by individuals. OpenStreetMap (OSM), as one of the most well-known opensource VGI projects, is a web mapping platform where contributors can gather and publicize geographic data of real-world objects, e.g., roads, streets, rivers, railways, and buildings [75]. More than 5.6 million OSM registered members, and more than 1 million contributors [76] helped the OSM database's rapid expansion for various applications. OSM represents building geometrical information such as footprint data and the number of levels for generating 3D building models.

Recently, Microsoft released two free sets of deep-learning generated building footprints covering the United States of America and Canada [77,78]. These datasets contain 125 million building footprints in all 50 US states and 11 million building footprints in all Canadian provinces and territories. Microsoft metrics show that the quality of data is better than or similar to OSM building metrics in most cases. These datasets are freely available and can be imported to OSM. In recent years, several UBEM projects have used OSM building footprint data for creating building models. It was found that the OSM building footprint data are reasonably accurate [79], whereas the building heights are often in doubt for almost all the cities. Fonseca and Schlueter [80] combined the data from official datasets and OSM to create a city district model in Zug, Switzerland. Schiefelbein et al. [81] presented a method to automatically extract primary city district data from OSM and enriched them based on national building stock statistics. While these methods can automatically extract the building data from OSM, local datasets must also be available to create an accurate city model.

Google Earth (GE) [82] is a universal and free tool of the discrete surface model with real heights of buildings and terrains. In its virtual environment, the Earth is mapped by the superimposition of satellite imageries, aerial photographs, and GIS onto a 3D digital globe. GE provides the application programming interface (API) to allow users to extract information, including but not limited to addresses, GIS, terrain topologies such as elevations on the screen based on latitudes and longitudes. Mei et al. [83] presented a new method for building the digital surface model (DSM) based on the terrain elevation data extracted using the GE API. They created a planar triangular mesh covering the selected study area and made the DSM by obtaining elevation of vertices from GE. This method can be extended for creating the 3D model of cities by extracting 3D building elevation data but scanning an urban area with acceptable resolution needs many grid points, which is time-consuming. However, urban features, including buildings, trees, and other terrains, cannot be differentiated if following their method, and extra works must be conducted to make a 3D model for urban building energy and microclimate simulation. Therefore, there is still a lack of an automated and general method to create the 3D city model with accurate building footprints and heights.

Non-geometrical properties of buildings, for example, building envelope properties, occupancy schedule, and solar heat gain coefficient (SHGC) are the second type of data required for UBEM. It is almost impossible to collect these data for every single building in a city. UBEM tools usually use archetype libraries to estimate such building properties [9]. First, buildings are divided into several groups according to ages, usages, and shapes. Then a set of properties is assigned to each group of buildings. Therefore, some building-specific information, such as year of construction and building usage data, is required to create an archetype library. Different official datasets are used by previous studies to provide the information. Among them, a few well-known studies include but are not limited to Urban Modeling Interface (UMI) [9], created an archetype library of 52 usage/age archetypes for Boston City to assign building properties including envelope, HVAC, internal loads, and operational schedules. The City Energy Analyst (CEA) tool developed by Fonseca et al. [80,84] combines buildings' geometric properties with occupancy-related properties provided by an archetypes database. A set of 172 building archetypes for 16 building occupancy types, six construction periods, and six renovation periods is considered. On the other hand, buildings footprint and non-geometrical properties datasets are usually represented in different formats, and the building indexes and logistics are different in these two files. Therefore, an additional step is needed to combine the data.

Weather data are the last input data of a UBEM tool. Most of these existing UBEM platforms use weather data from one or several nearby weather stations for the energy analysis of all buildings. Therefore, they have not considered the impacts of localized microclimate environment. The airflow velocity and temperature around buildings are affected by building configurations, heights, and neighboring building locations. Different wind velocity and temperature around buildings directly impact buildings’ thermal load regarding local convective heat transfer coefficients and air infiltration through envelopes [11]. Deformed energy balance in densely built urban areas could lead to higher temperatures than surrounding rural areas. This phenomenon, known as Urban Heat Island (UHI), can increase space cooling demand and reduce HVAC systems' efficiency under higher temperatures [10,12]. Buildings also influence the urban climate by releasing heat to the ambient air and contributing to UHI formation. Persistent heat can also cause discomfort, respiratory difficulties, heat cramps and exhaustion, non-fatal heat stroke, and heat-related mortality inside buildings [13]. For example, the 2018 Canadian heatwave was associated with more than 90 deaths in Quebec Province [14], many of which occurred in the dense urban areas due to UHI. Simulation techniques may achieve the understanding of the UHI impacts and the development of mitigation strategies [85–89], such as NWP simulation models [17] and computational fluid dynamics (CFD) simulations of urban microclimate [12,90,91]. Hong et al. [15] proposed ten questions and answers, highlighting UBEM challenges and future research works. Coupling UBEM with urban microclimate tools to capture the impact of urban microclimate on buildings' energy performance is among the ten challenges. It is crucial to properly develop an integrated UBEM and urban microclimate simulation method and associated tools to model urban building energy and environmental performance.

In this thesis, new ideas are proposed to overcome the drawbacks of existing UBEM tools. A new UBEM, so-called CityBEM, is developed by considering the essential components of accurate buildings' energy performance simulation. CityBEM is the extended version of the building scale energy and airflow simulation model presented in chapter 3, modified for urban scale buildings' energy performance simulation. This thesis introduces an automated approach to creating the 3D city model by integrating freely available datasets (OSM and Microsoft footprints) and GE. The building footprints with building-specific 2D information, such as addresses, indexes, and shapes are provided from the OSM and/or Microsoft building footprint data. GE API provides building heights for modifying that information in OSM/Microsoft. The modified OSM city/building model in the OSM format is then converted to the STL ("StereoLithography") file [92] of the 3D city for urban building energy simulations. Then, an archetype library was created according to building ages and types. An official dataset provides building properties in the format of the shapefile for the region of interest. Shapefile and OSM file data are joined using the QGIS tool [93]. For modeling the impact of urban microclimate data on buildings' energy performance, CityBEM is coupled with the Global Environmental Multiscale (GEM) model developed by Meteorological Service of Canada (MSC) and the City Fast Fluid Dynamic (CityFFD) model developed by Mortezazadeh and Wang. The whole process of creating the city's 3D model, combining different datasets, and dynamic simulation using CityBEM is designed to be fully automatic or semi-automatic with minimum manual efforts.

2.3. Multi-scale Urban Microclimate and Building Energy Simulation

2.3.1. High-Resolution Deterministic Prediction System

Over the past decades, computational resources have increased significantly in operational weather centers worldwide, which resulted in increased capacity to run complex NWP systems. It helped more extensive coverage of Limited-Area Model (LAM) domains and developed high-resolution models [95]. Over the past two decades, the Meteorological Service of Canada (MSC), which provides official operational weather prediction from Environment and Climate Change Canada (ECCC), has been moving toward kilometer-scale systems. In 1997, MSC ran an operational system called Regional Deterministic Prediction System (RDPS), which provided short-term (48-h) forecast runs on a global grid with a grid spacing of 24-km over the region covering a large portion of North America [96]. In the last few years, EC has been involved in several projects for real-time kilometer-scale and higher horizontal resolution forecasting using the GEM model. in November 2014, the experimental 2.5-km pan-Canadian High-Resolution Deterministic Prediction System (HRDPS) was introduced, with 48-h integrations run four times per day. From 2016–2018, ECCC has run the HRDPS operationally with domains that cover all the Arctic region. The pilot model of the HRDPS is the RDPS with a 10 km grid spacing (Fig. 2-1).

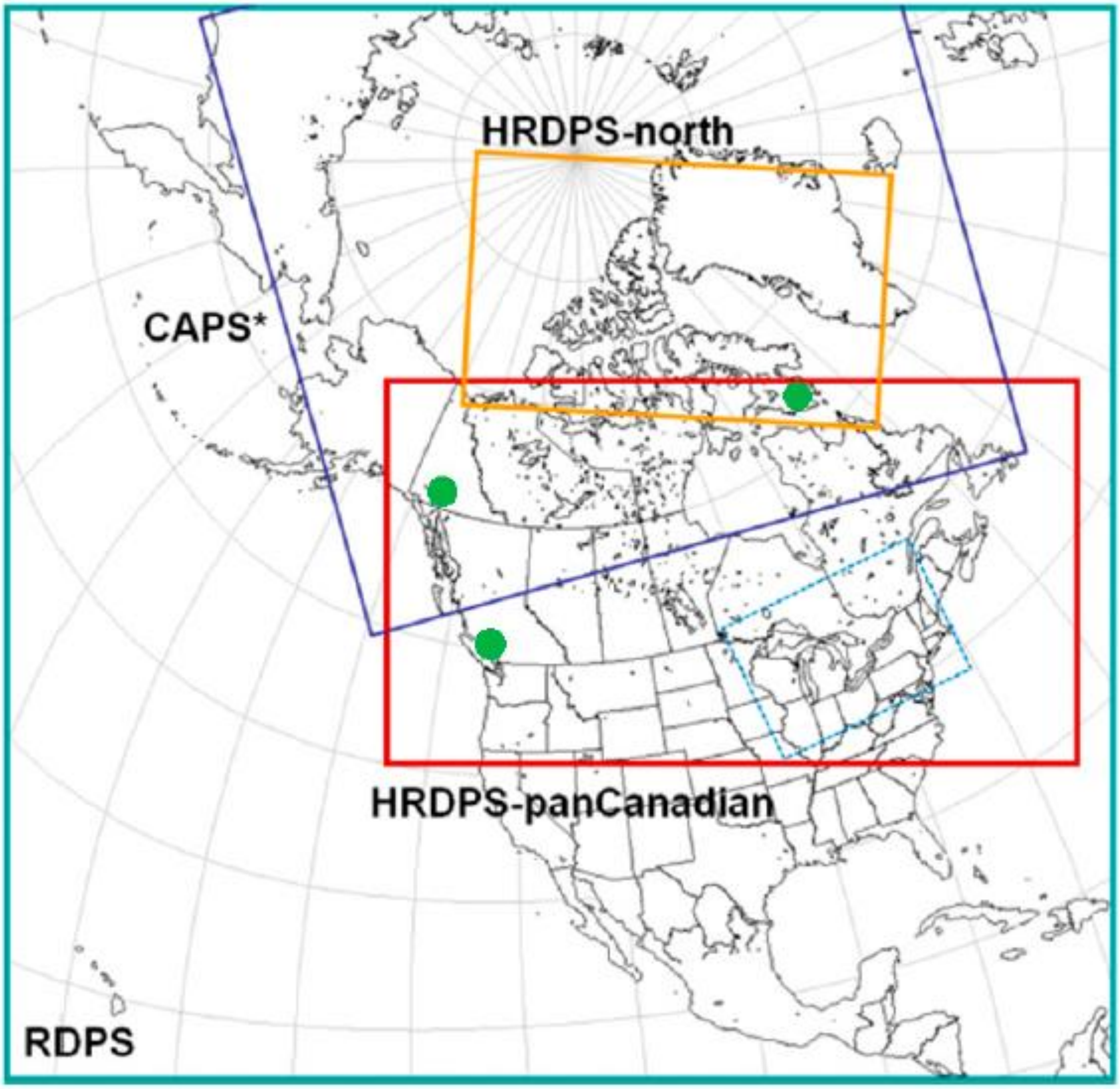

Figure 2-1 Locations of the computational model domains for the 10-km RDPS (cyan); 2.5-km HRDPS (red); 3-km Canadian Arctic prediction system (CAPS) (blue); HRDPS-north (orange) [97]

2.3.2. Urbanized GEM Atmospheric Model

The land coverage changes and increased energy consumption in cities caused by rapid urbanization can significantly impact the urban meteorological conditions such as urban heat island (UHI) effects, precipitation, humidity, street canyon winds, surface energy fluxes, and sea and land breezes in coastal cities [16,98,99]. Also, urban meteorology and climate change can impact the air quality in urban areas through the concentration of gaseous pollutants and aerosols. To improve the representation of surface and boundary-layer processes in the urban environment, the Meteorological Service of Canada has developed an urbanized version of the GEM mesoscale atmospheric model by adding the TEB urban canopy model [100].

Town Energy Balance Model

TEB model represents the physical mechanisms inside the urban canopy and the exchanges between the built-up covers and the atmosphere. The TEB model calculates the turbulent fluxes into the atmosphere at the surface of a mesoscale atmospheric model covered by buildings, roads, or artificial material. It parameterizes both the urban surface and the roughness sublayer so that the atmospheric model only ‘sees’ a constant flux layer as its lower boundary. Each building's shapes are not considered, and TEB geometry is based on the canyon hypothesis. A set of mean geometric parameters, defined at each grid point, describes the urban canopy arrangement: building fraction, building height, canyon aspect ratio (i.e., the ratio between building height and width of the street), and the ratio between walls and horizontal built-up areas. Radiative and thermal properties are associated with each urban facet. Following assumptions are considered in the TEB model:

1. Buildings in the same grid point have the same height and width, and the roof level is at the atmospheric model's surface level.
2. Buildings are along identical roads, and the length of the road is much larger than the width. The space between two adjacent buildings is defined as the canyon.
3. All road and canyon orientation exist with the same probability, and in all calculations that include the canyon orientation, the averaged value over 360° is used.

The urban canyon is represented by three generic surfaces in the TEB model: a wall, a road, and a roof. Each surface is discretized into several layers to calculate the conduction fluxes from the wall, roof, or road surface (Fig. 2-2a). The energy balance is resolved independently for roads, roofs, and walls by considering shadow effects and radiation trapping inside the canyon. The turbulent exchanges inside the canyon and between the canyon and the upper atmosphere are determined using an aerodynamic resistance network with exchange coefficients that depend on wind speed and stability conditions (Fig. 2-2b). A mean urban micro-climate is resolved inside the canyon, and mean air temperature, mean specific humidity and mean wind speed obtained in the middle of the street at the mid-height of the buildings.

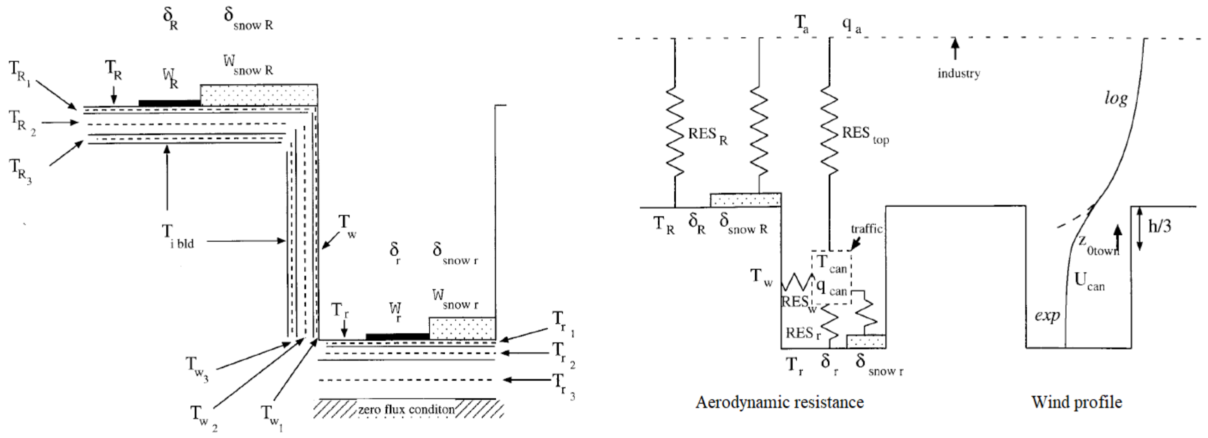

(a) (b)

Figure 2-2 a) Discretization of the surfaces and prognostic variables in the TEB model, b) Scheme options for aerodynamic resistance, and wind profile within and above the canyon. [100]

Coupling GEM with TEB Model

In the GEM model physics, the surface is described as a mosaic composed of four tiles: natural soils and vegetation, water, continental ice, and sea ice. For including the TEB scheme in the GEM model, a new “urban” tile is added in the surface mosaic for considering the built-up covers. The land-use land-cover description is evolving through the time. First, the GEM model was using the land-cover classification developed by Lemonsu et al. [101]. It provides a 60-m resolution of land-use land-cover classifications composed of 12 urban classes. The TEB input parameters associated with each type were defined from aerial photograph analysis and the literature [102]. A more general methodology defining directly input parameters on a model grid is currently used. It was developed in order to characterize all of urban areas in the HRDPS as implemented in 2018 version [103], and for the experimental modeling for the PanAmerican Games in Toronto [104].

To study near-surface meteorological parameters using a high-resolution GEM urbanized model, a numerical set-up was developed based on the one-way grid-nesting system of the limited-area version the GEM model (i.e., GEM-LAM) cascading from 2.5- to 1-km grid sizes, and from 1-km to 250-m grid sizes. Initial and boundary conditions for the 2.5-km GEM-LAM are provided by the 15-km operational GEM regional model [105]. The multi-scale (kilometer- to sub-kilometer-scale) model is used in several of MSC's projects. Lemonsu et al. [17] used it for modeling two intensive observational periods in Oklahoma City, U.S.A, 2003. An extensive evaluation against near-surface and upper-air observations show that the TEB scheme correctly simulates the urban micro-climate, positive nighttime urban heat island, and "cool" island during the morning. Leroyer et al. [16] applied the kilometer- to sub-kilometer-scale numerical simulations to the complex urban coastal area of Vancouver, British Columbia, Canada, during a sea-breeze event. Observations collected from the Environmental Prediction in Canadian Cities (EPiCC) network and satellite imagery were used to evaluate the results. Results show that the use of sub-kilometer grid spacing provides a more detailed representation of the surface-related phenomena. They recommend the joint analyses of kilometers- and sub-kilometer-scale numerical experiments for different environmental applications. Real-time prediction of the urban microclimate down to 250-

m was successful during the Pan-American Games in Toronto in 2015 [106,107]. Alavi et al. [103] performed a scenario study for heat island mitigations in Montreal by modifying urban surface parameters. A sub-kilometer high-resolution NWP system has been employed to evaluate the sensitivity of near-surface air temperature, wind speed, and boundary layer evolution to Montreal's urban surfaces. The modeling system was run with 250-m grid spacing for two intensive heatwave periods during summer 2010, which had an enormous impact on dwellers. Results show that increasing the albedo of the different urban surfaces (wall, roofs, roads) and increasing the vegetation fraction in the metropolitan area results in reduced surface air temperature (2-m) for all the hours during the heat waves.

Recent studies show that high-resolution numerical simulations and physical representation of urban areas using the TEB model positively impact near-surface meteorology prediction accuracy. The current version of the TEB model used in the urbanized version of the GEM is simplified. Some essential factors regarding the buildings' properties are not considered in the model, such as buildings' façade orientation, type and year of construction that affect buildings' thermal properties, buildings' energy performance, window and solar radiation transmitted into the building, etc. Bueno et al. [18] added a simple resistance-capacitance network model of buildings to the TEB scheme of the SURFEX numerical weather prediction system in France. They used it to analyze the interactions between the energy performance of buildings and the urban climate. They later replaced it with a building energy model and studied occupant behavior's impact on the anthropogenic heat fluxes from building to the atmosphere. The model can perform a better representation of buildings' impact on the atmosphere and can be used for coupled urban climate and building analysis, relevant for both the urban climate and the climate change mitigation and adaptation communities [108,109].

Therefore, it is crucial to add a UBEM model to the TEB scheme in the GEM model's urbanized version and perform kilometers- to sub-kilometer- and building-scale simulation. It can add many new features to the GEM model, such as improve the accuracy of the near-surface simulation, perform buildings’ energy analysis at the city level, accurately calculate the anthropogenic heat flux from buildings o atmosphere, study the impact of building-related strategies on the energy consumption and microclimate, and study the effects of buildings on the urban air quality. In this thesis, CityBEM is integrated with the GEM-LAM model. A multi-scale (kilometer- to sub-kilometer- and building-scale) numerical set-up is used based on a one-way grid-nesting system of the GEM-LAM model cascading from 10- to 2.5-, 1- km, and 250-m grid sizes.

2.3.3. Surface Prediction System

The surface Prediction system (SPS) is the Canadian external surface modeling system [110,111]. SPS consists of the same ISBA (Interactions between Soil, Biosphere, and Atmosphere) and TEB (Town Energy Budget) surface models used in the GEM-LAM model. The SPS has been developed to provide surface and near-surface meteorological variables to improve numerical weather prediction and become a tool for environmental applications. The SPS's surface model uses separate schemes for land, water, sea ice, continental ice (glaciers and ice sheets), and urban. It calculates the surface-induced fluxes of heat, moisture, and momentum over each of these five types of surfaces by solving classical aerodynamic equations. Grid cells in SPS are independent of each other, and there is no communication between adjacent grid cells. The external surface system is driven by meteorological fields obtained from a coarser-resolution forecast system, and there is no feedback from SPS on the atmosphere fields. SPS is a 2D model; therefore, it is computationally inexpensive and suitable for high-resolution modeling of surface and near-surface fields. Several studies investigate the SPS model's accuracy and its impact on the GEM-LAM model's near-surface atmospheric fields. Separovic et al. [112] performed offline surface modeling using SPS over Canada. Then, the outputs of SPS integrations were used as the reference land surface conditions for the relaxation of GEM-LAM simulations' surface variables. Results show that the SPS model's outputs can improve the near-surface atmospheric fields in GEM-LAM simulations. Leroyer et al. [113] used the SPS model to simulate the Montreal metropolitan area from 1 May to 30 September 2008. They used the output of the RDPS 15-km model as the forcing data of the SPS model.

A comparison of SPS results with the regional deterministic 15-km model and measurement data show that significant improvements have been achieved with this system over EPiCC urban and suburban sites. A recent study by Rochoux et al. [114] highlights the potential of an SPS–GEM two-way coupling strategy for refining predictions near the surface through the upscaling of high-resolution surface heat fluxes to the coarser atmospheric grid spacing. Solving the surface at high resolution in a surface–atmosphere fully coupled system becomes an essential aspect for improving numerical weather and environmental forecast performance. In this work, a new SPS model is developed and used to simulate the Montreal metropolitan area during the 2018 summer heatwave. The horizontal grid spacing of the SPS model is 250-m. The SPS model's output is then interpolated on each building in CityBEM to calculate buildings' energy performance. The one-way integration method cannot model the impact of buildings on the SPS model's near-surface parameters. Therefore, the CityBEM is a new module added to the TEB model and is used for the SPS simulation.

2.4. Airborne Transmission of Infectious Aerosols in Indoor Environments

A novel coronavirus disease was first reported in Wuhan, China, in late December 2019, later named COVID-19 [115,116]. It was declared a pandemic by the World Health Organization

(WHO) on the 11th March 2020 [117]. As of October 8, 2020, the total number of COVID-19 cases exceeded 35.6 million worldwide, with confirmed 1,044,269 total deaths [118]. The main routes of transmission of SARS-CoV-2 are direct and indirect contact transmission with the infected people, respiratory transmission by large droplets within 1 m distance from an infected person, and transmission by aerosol (airborne) [119–121]. Human expiratory activities such as coughing, sneezing, speaking, singing, and even breathing release particles in a wide range of sizes, with most of them between 2 and 100 μm [122]. The small respirable particles $< 5 - 10\ \mu m$ can remain airborne and are capable of spreading at large distances. The largest droplets, fall next to the source, within a distance of 1–2 m, as a result of gravitational force [123]. The latest research findings show that airborne transmission of aerosols produced by asymptomatic individuals is a large portion of the spread of COVID-19 disease, especially in indoor spaces with poor ventilation conditions, large gathering, and long-duration exposure to high concentrations of aerosols [123–127]. A study on 318 outbreaks with three or more cases in China shows that they all occurred in indoor environments with a possibly low ventilation rate [128]. Another study on 110 cases among eleven clusters in Japan shows that all of them happened in indoor environments, including fitness gyms, a restaurant boat on a river, hospitals, and a snow festival where there were eating spaces in tents with minimal ventilation rate [129]. Several studies on aerosol transmission in indoor spaces show that improving the ventilation condition, wearing a face mask, avoiding overcrowding, and shortening the event time (exposure time) can significantly reduce infection risk through airborne transmission [130–132]. Buonanno et al. [133] evaluated the number of people infected by an asymptomatic SARS-CoV-2 subject in Italian indoor microenvironments. The results show the great importance of proper ventilation in the containment of the virus in indoor environments. Curtius et al. [134] tested the efficiency of operating four air purifiers equipped with HEPA filters and the total air exchange rate of 5.5 h-1 in a high school classroom. The concentration of aerosol particles was reduced by more than 90 % within less than 30 minutes after running the purifiers. Based on their estimations, while staying for two hours in a closed room with a super infective person, the maximum concentration levels of the virus-containing aerosol are reduced by a factor of six by using air purifiers with a total air exchange rate of 5.7 h-1. Dai and Zhao [135] calculated the required ventilation rate to ensure a low airborne Probability of Infection (PI) for different exposure times. The required ventilation rate was higher than the normal ventilation mode of buildings. The required ventilation rate can be reduced to a quarter achieved by normal ventilation mode by wearing the mask. A study on infection risk in indoor environments, such as office, classroom, choir practice room, and reception/party environments show that active room ventilation and the wearing of face masks by all subjects may reduce the individual infection risk by a factor of five to ten, similar to high volume HEPA air purifier [136]. Miller et al. [127] studied an outbreak that occurred at a weekly rehearsal. Results highlight four essential factors that increase the risk of aerosol transmission indoors: dense occupancy, long duration, loud vocalization, and poor ventilation. Increasing the aerosol loss rate by higher ventilation rate and deposition onto surfaces and reducing the event duration can reduce the infection risk by a factor of two. Current studies evaluated the mitigation measures in reducing aerosol transmission risk in limited buildings or specific cases. The effectiveness of mitigation measures can change by building type because of different ventilation conditions, occupants density, event time, dominant age of occupants, etc. Therefore it is essential to cover more building types and investigate the impact of different strategies in reducing aerosol transmission risk based on the building usage type. Also, increasing the outdoor ventilation rate during the winter will increase the building's energy consumption, and it may not be a cost-effective strategy. It can also increase the peak energy demand, and the possibility of power outage will be increased. Therefore, it is crucial to analyze the Reduced Probability of Infection (RPI) obtained with each strategy and the corresponding possible increased energy consumption.

In this thesis, the City Reduced Probability of Infection (CityRPI) model is developed to calculate the RPI obtained by different mitigation measures and their impact on all buildings' energy consumption in the City of Montreal. An archetype library is developed based on various standard codes, and required parameters are assigned to each building. Simulation is done for the coldest period of winter 2019, and all mitigation measures are evaluated during this period. The CityBEM is integrated with CityRPI to investigate the impact of mitigation measures on reduced risk and buildings' energy consumption.

Chapter 3 Building-Scale Thermal, Airflow, and Energy Model

In this chapter, a building-scale energy and airflow simulation model is developed to calculate the building's energy consumption, model the natural and hybrid ventilation in buildings, and simulate the airflow through the openings. It is based on a coupled thermal airflow multi-zone network model. Different problems are solved using the developed model to study the model's performance.

3.1. Governing Equations

A coupled thermal airflow multi-zone network model treats a building as a collection of nodes representing zones, i.e., rooms, plenums, etc., with inter-nodal connections representing the flow paths associated with cracks, doors. The air is assumed to be well-mixed in the multi-zone network model, so air temperature and density are assumed uniform within each zone, and air momentum effects are neglected [29]. Air pressure and temperature and wall temperature are three unknown parameters of the problem. Three types of conservation equations are solved to calculate the unknown parameters. Transient mass and energy balance equations are solved for each zone to calculate air pressures and temperatures. A transient energy balance equation is solved for each wall/floor to calculate the temperature distribution. An airflow path equation is also used to calculate the air flow rate through each opening. The 3D model of a building with two rooms and five openings (doors and windows) and plan view of the corresponding multi-zone network model are shown in Fig. 3-1.

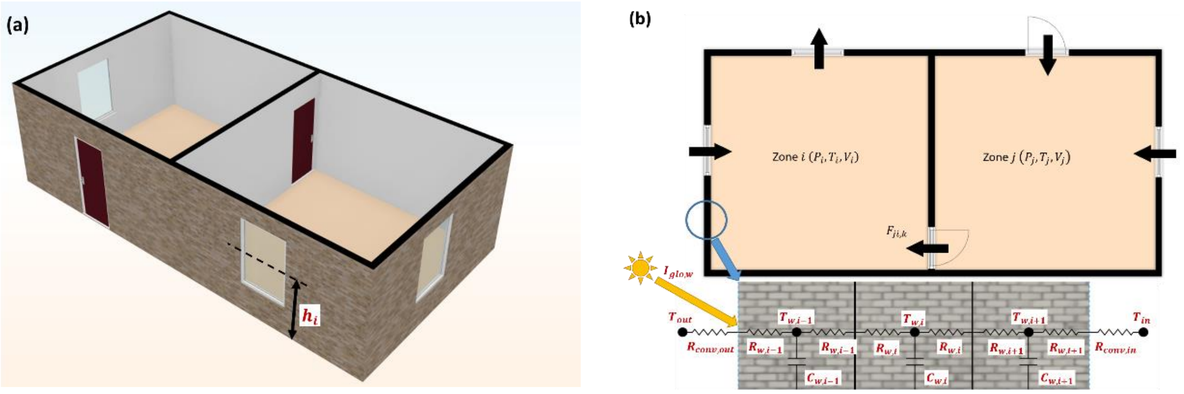

Figure 3-1 a) 3D model of a building with two zones and five openings, b) plan view of the simple multi-zone network model.

3.1.1. Mass and Energy Balance Equations of Air in Zone i

The transient mass and energy balance equations of each zone are

$$\frac{dm_i}{dt} = \sum_{j=1}^{N} \sum_{k=1}^{n_{ij}} F_{ji,k} + Ms_i \qquad \text{Eq. 3-1}$$

$$\frac{d\left(C_{pa,i} T_i m_i\right)}{dt} = \underbrace{\sum_{j=1}^{N} \sum_{k=1}^{n_{ij}} C_{pa,j} T_j F_{ji,k}}_{if\ F_{ji,k}>0} + \underbrace{\sum_{j=1}^{N} \sum_{k=1}^{n_{ij}} C_{pa,i} T_i F_{ji,k}}_{if\ F_{ji,k}<0} + Q_{zs,i} + \sum_{k} \frac{A_{w,k} \Delta T_k}{R_k} \qquad \text{Eq. 3-2}$$

$F_{ji,k}$, the airflow rate from zone j and zone i through opening k, is positive if the airflow is from zone j to zone i, and negative if the airflow is from zone i to zone j. ΔT_k is the temperature difference across a wall or window. For a wall, it is the difference between internal air temperature T_i and the temperature of the first node inside the wall $T_{w,1}$. For glazing, ΔT_k is the indoor and outdoor air temperature difference. R_k is the thermal resistance of the wall or window.

The ideal gas law is used to calculate air mass as a function of air pressure and temperature (Eq. 3-3).

$$m_i = \frac{P_i V_i}{R T_i} \qquad \text{Eq. 3-3}$$

3.1.2. Energy Balance Equations of Thermal Mass

The transient heat balance equation is also solved to calculate the temperature distribution inside the wall and other thermal mass. Fig. 3-1b shows the thermal network model of a wall. The equation's right-hand side is discretized implicitly, and the tridiagonal matrix equation is solved using the Thomas algorithm [137].

$$C_{w,i}\frac{dT_{w,i}}{dt} = \frac{T_{w,i-1} - T_{w,i}}{R_{w,i-1} + R_{w,i}} + \frac{T_{w,i+1} - T_{w,i}}{R_{w,i+1} + R_{w,i}} + S_{w,i} \qquad \text{Eq. 3-4}$$

$$C_{w,i} = \rho_w A_w \Delta x_i C_{pw} \qquad \text{Eq. 3-5}$$

A wall is divided into several layers of equal thickness $\left(\Delta x_i = \frac{L_w}{N_w}\right)$. L_w is the thickness of the wall, and N_w is the number of nodes. For walls with multiple materials, layers of the same material have an equal thickness. Still, the thickness can change by material depending on the thickness and number of nodes.

For non-boundary nodes $(i \neq 1, i \neq N_w)$:

$$R_{w,i} = R_{w,i-1} = R_{w,i+1} = \frac{R_{w,t}}{2N_w} \qquad \text{Eq. 3-6}$$

Where $\left(R_{w,t} = \frac{L_w}{k_w A_w}\right)$ is the total thermal resistance of the wall.

If i is the first node inside the wall ($i = 1$):

$$R_{w,i} = R_{w,i+1} = \frac{R_{w,t}}{2N_w} \quad \text{Eq. 3-7}$$

$$R_{w,i-1} = \frac{1}{h_{comb,in}A_w} \quad \text{Eq. 3-8}$$

If i is the last node inside the wall ($i = N_w$):

$$R_{w,i} = R_{w,i-1} = \frac{R_{w,t}}{2N_w} \quad \text{Eq. 3-9}$$

$$R_{w,i+1} = \frac{1}{h_{comb,out}A_w} \quad \text{Eq. 3-10}$$

$$S_{w,i} = \begin{cases} 0 & \text{interior wall} \\ 0 & \text{exterior wall}, i \neq N_w \\ \alpha_w I_{glo,w} + q_{LWR} & \text{exterior wall}, i = N_w \end{cases} \quad \text{Eq. 3-11}$$

$$q_{LWR} = q_{grd} + q_{sky} + q_{air} \quad \text{Eq. 3-12}$$

$$\begin{cases} q_{grd} = \varepsilon\sigma F_{grd}A_w\left(T_{grd}^4 - T_{surf}^4\right) \\ q_{sky} = \varepsilon\sigma F_{sky}\beta A_w\left(T_{sky}^4 - T_{surf}^4\right) \\ q_{air} = \varepsilon\sigma F_{sky}(1-\beta)A_w\left(T_{out}^4 - T_{surf}^4\right) \end{cases} \quad \text{Eq. 3-13}$$

Where $F_{grd} = 0.5\left(1 - \cos\theta_p\right)$, $F_{sky} = 0.5\left(1 + \cos\theta_p\right)$, $\beta = \sqrt{0.5\left(1 + \cos\theta_p\right)}$.

3.1.3. Airflow Resistance Equations

As explained earlier, airflow paths represent openings between zones or to ambient. Different types of models were used to model all openings of the building. Table 3-1 shows airflow models and corresponding equations [138]. Appendix A provides a detailed description of airflow models.

Table 3-1 airflow models and corresponding equations.

Airflow model	Equation
power-law equation	$F_{ij} = C_{ij}\left(\Delta P_{ij}\right)^{n_{ij}}$
Orifice airflow equation	$F_{ij} = C_{d,ij}A_{ij}\sqrt{2\rho\Delta P_{ij}}$
leakage area model	$F_{ij} = C_{ij}\left(\Delta P_{ij}\right)^{n_{ij}}$ $C_{ij} = L_{ij}C_{d,ij}\sqrt{2\rho}\left(\Delta P_{r,ij}\right)^{0.5-n_{ij}}$
Shaft airflow model	$F_{ij} = f_{turb}\sqrt{\rho}\left(\Delta P_{ij}\right)^{n_{ij}}$

ΔP_{ij} is the pressure difference across the path ij. In airflow equations of table 1, if $\Delta P_{ij} > 0$, $\rho = \rho_i$, and if $\Delta P_{ij} < 0$, $\rho = \rho_j$. The Bernoulli's equation is used for the calculation of pressure drop across path ij which is

$$\Delta P_{ij} = \left(P_i - \rho_i g h_i + \frac{\rho_i v_i^2}{2} + g z_i\right) - \left(P_j - \rho_j g h_j + \frac{\rho_j v_j^2}{2} + g z_j\right) + P_w \qquad \text{Eq. 3-14}$$

Kinetic pressure terms can be neglected here.

$$\Delta P_{ij} = (P_i - \rho_i g h_i) - \left(P_j - \rho_j g h_j\right) + P_{w,ij} \qquad \text{Eq. 3-15}$$

Eq. 3-15 can be rearranged as

$$\Delta P_{ij} = P_i - P_j + P_{s,ij} + P_{w,ij} \qquad \text{Eq. 3-16}$$

$$P_{s,ij} = \rho_j g h_j - \rho_i g h_i \qquad \text{Eq. 3-17}$$

$P_{w,ij}$ is the wind-induced pressure at path ij, which is explained in the next section.

3.1.4. Wind-Induced Pressure

Wind-induced pressure load on the buildings' exterior surface is the difference between the pressure on the building surface and the local outdoor atmospheric pressure at the same level in an undisturbed wind approaching the building [139].

$$P_w = \frac{\rho_a U_H^2}{2} C_{p,wind} \qquad \text{Eq. 3-18}$$

U_H is the approaching wind speed at upwind wall height H (m/s), which can be the wind speed measured by a weather station at the top of the building. Values of the mean local wind pressure coefficient $C_{p,wind}$ depends on different parameters, including building shape, wind direction, effects of nearby buildings, and terrain features. Accurate determination of $C_{p,wind}$ can be obtained only from wind tunnel model tests of the specific site and building or full-scale tests. Surface-averaged pressure coefficients may be used to determine ventilation and/or infiltration rates. The surface pressure coefficient averaged over the complete wall and roof of a tall building provided by the ASHRAE Fundamentals Handbook [139] are used in this work.

3.1.5. Solar Irradiance Calculation

Solar irradiance on a tilted surface contains three components: direct, diffuse sky, and ground reflected irradiance. The global irradiance on an unshaded flat surface tilted at an angle θ_p (Fig. 3-2a) is

$$I_{glo,p} = I_{dir} \cos \theta_i + I_{dif} F_{sky} + I_{glo,hor} \rho_g F_{grd} \qquad \text{Eq. 3-19}$$

$$I_{glo,hor} = I_{dir} \cos \theta_s + I_{dif} \qquad \text{Eq. 3-20}$$

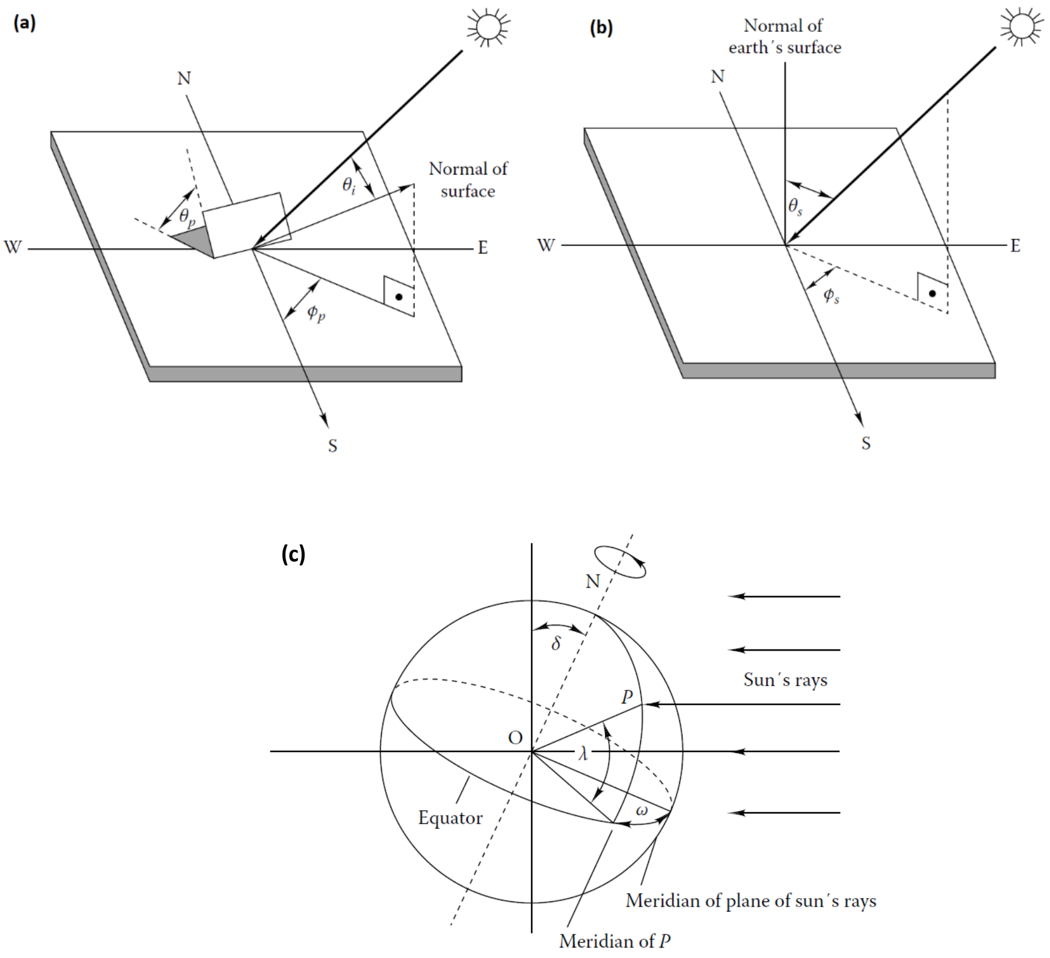

Figure 3-2 (a) Zenith angle θ_p and azimuth φ_p of a plane and angle of incidence θ_i of sun on this plane. (b) Zenith angle θ_s and azimuth φ_s of sun. (c) Latitude λ, hour angle ω, and declination δ. O = center of earth, N = north pole, P = point in earth's surface [140].

If only global horizontal irradiance $I_{glo,hor}$ is given by the weather station data, the diffuse irradiance I_{dif} can be estimated by

$$\frac{I_{dif}}{I_{glo,hor}} = \begin{cases} 1.0 - 0.09k_T & 0 \leq k_T \leq 0.22 \\ 0.9511 - 0.1604k_T + 4.388k_T^2 - 16.638k_T^3 + 12.336k_T^4 & 0.22 \leq k_T \leq 0.8 \\ 0.165 & 0.80 \leq k_T \end{cases}$$ Eq. 3-21

where

$$k_T = \frac{I_{glo,hor}}{I_0 \cos\theta_s}$$ Eq. 3-22

$$I_0 = \left(1 + 0.033\cos\frac{360 \times n}{365.25}\right) \times 1373\ W/m^2$$ Eq. 3-23

$$\cos\theta_s = \cos\lambda\cos\delta\cos\omega + \sin\lambda\sin\delta$$ Eq. 3-24

$$\omega = \frac{(t_{sol} - 12h) \times 360°}{24h}$$ Eq. 3-25

$$t_{sol} = t_{std} + \frac{L_{std} - L_{loc}}{15°/h} + \frac{E_t}{60\ min/h}$$ Eq. 3-26

$$E_t = 9.87\sin 2B - 7.67\sin(B + 78.7)$$ Eq. 3-27

$$B = 360° \times \frac{n_d - 81}{364}$$ Eq. 3-28

$$\sin\delta = -\sin 23.45° \cos\frac{360° \times (n + 10)}{365.25}$$ Eq. 3-29

The definition of all terms used in Eqs. 3-21 to 3-29 is presented in nomenclature and Figs. 3-2b and 3-2c. The solar radiation transmitted through the glazing absorbed by the floor is:

$$\dot{Q}_{sol} = A_w \times SHGC \times I_{glo,p} \qquad \text{Eq. 3-30}$$

3.2. Numerical Solvers

3.2.1. Zone Mass and Energy Balance Equations Solver

Eqs 3-1 and 3-2 are discretized by applying the backward Euler method:

$$f_i = \frac{V_i}{R\Delta t}\left(\frac{P_i}{T_i}\right)_{t+1} - \frac{(m_i)_t}{\Delta t} - \sum_{j=1}^{N}\sum_{k=1}^{n_{ij}} F_{ji,k} - Ms_i = 0 \qquad \text{Eq. 3-31}$$

$$g_i = \frac{C_{pa,i}V_i}{R\Delta t}(P_iT_i)_{t+1} - \frac{\left(C_{pa,i}T_im_i\right)_t}{\Delta t} - \underbrace{\sum_{j=1}^{N}\sum_{k=1}^{n_{ij}} C_{pa,j}T_jF_{ji,k}}_{if\ F_{ji,k}>0} - \underbrace{\sum_{j=1}^{N}\sum_{k=1}^{n_{ij}} C_{pa,i}T_iF_{ji,k}}_{if\ F_{ji,k}<0} \qquad \text{Eq. 3-32}$$

$$- Q_{s,i} - \sum_{k} \frac{A_k\Delta T_k}{R_k} = 0$$

For a building with N zones, the air mass and energy balance equations of all zones are

$$\begin{cases} f_1(P_1, P_2, \dots, P_N) = 0 \\ f_2(P_1, P_2, \dots, P_N) = 0 \\ \vdots \\ f_N(P_1, P_2, \dots, P_N) = 0 \end{cases} \qquad \text{Eq. 3-33}$$

$$\begin{cases} g_1(T_1, T_2, \dots, T_N) = 0 \\ g_2(T_1, T_2, \dots, T_N) = 0 \\ \vdots \\ g_N(T_1, T_2, \dots, T_N) = 0 \end{cases} \qquad \text{Eq. 3-34}$$

The non-temporal terms of equations 34 and 35 are obtained at the time $t + 1$. Therefore they are non-linear equations of $(P_1, P_2, \dots, P_N)$ and $(T_1, T_2, \dots, T_N)$ because of the power-law equation (Table 3-1) used for the calculation of $F_{ji,k}$.

Three different strategies can be implemented for coupling the airflow and thermal modules in a multizone based simulation program. The first one is the “fully-simultaneous” coupling strategy. In this strategy, the mass and energy balance equations for all zones are solved simultaneously. The second strategy is the “semi-simultaneous” coupling strategy. The mass and energy balance equations for one zone are solved simultaneously in an internal loop, and this procedure is repeated for all zones in sequence. This sequence of steps will be repeated in an external loop until the overall convergence is achieved. The third is the “segregated” coupling strategy. In the segregated, the airflow and thermal modules are run in a sequence. In other words, the segregate approach solves the mass balance equations for all zones. The airflows are provided to the energy balance equations, and temperatures are calculated for all zones. Finally, all zones' updated temperatures are substituted back into the mass balance equation, and this procedure is repeated until the overall convergence of the problem is attained. The matrix formulations of these three solvers are provided in the following sections.

Fully-Simultaneous Method

As mentioned earlier, in this method, the continuity and energy equations for all zones are solved simultaneously

$$\begin{cases} f_1(P_1, P_2, \dots, P_N) = 0 \\ g_1(T_1, T_2, \dots, T_N) = 0 \\ f_2(P_1, P_2, \dots, P_N) = 0 \\ g_2(T_1, T_2, \dots, T_N) = 0 \\ \qquad\quad \vdots \\ f_N(P_1, P_2, \dots, P_N) = 0 \\ g_N(T_1, T_2, \dots, T_N) = 0 \end{cases} \qquad \text{Eq. 3-35}$$

The system of Equation 3-35 can be combined into a matrix formation

$$\mathbf{F}(\mathbf{X}) = \mathbf{0} \qquad \text{Eq. 3-36}$$

$$\mathbf{F} = (f_1, g_1, f_2, g_2, \dots, f_N, g_N)^T \qquad \text{Eq. 3-37}$$

$$\mathbf{X} = (P_1, T_1, P_2, T_2, \dots, P_N, T_N)^T \qquad \text{Eq. 3-38}$$

Semi-Simultaneous Method

In the semi-simultaneous method, the continuity and energy equations of each zone are solved separately. The corresponding system of equations of zone i is as follows

$$\begin{cases} f_i(P_i, T_i) = 0 \\ g_i(P_i, T_i) = 0 \end{cases} \qquad \text{Eq. 3-39}$$

Segregated Method

The system of equations for solving mass balance and energy equations using the segregated method is as follows

$$\begin{cases} f_1(P_1, P_2, \dots, P_N) = 0 \\ f_2(P_1, P_2, \dots, P_N) = 0 \\ \qquad \vdots \\ f_N(P_1, P_2, \dots, P_N) = 0 \end{cases} \qquad \text{Eq. 3-40}$$

$$\begin{cases} g_1(T_1, T_2, \dots, T_N) = 0 \\ g_2(T_1, T_2, \dots, T_N) = 0 \\ \qquad \vdots \\ g_N(T_1, T_2, \dots, T_N) = 0 \end{cases} \qquad \text{Eq. 3-41}$$

Applying the Newton-Raphson method to non-linear systems of Equations 3-35, 3-39, 3-40, and 3-41 yields linear systems of Jacobian-based equations, which will be solved by a linear solver. This process is considered as the internal loop.

$$\boldsymbol{J}\left(\boldsymbol{X}^{(\boldsymbol{n})}\right)\left(\Delta\boldsymbol{X}^{(\boldsymbol{n})}\right)=\boldsymbol{f}\left(\boldsymbol{X}^{(\boldsymbol{n})}\right) \qquad \text{Eq. 3-42}$$

After equation 3-42 is solved, the zones state variables can be corrected by Eq. 3-43.

$$\boldsymbol{X}_i^{n+1}=\boldsymbol{X}_i^n-\Delta\boldsymbol{X}_i^n \qquad \text{Eq. 3-43}$$

L_∞ norm of error is used to measure the convergence of a non-linear system of equations, which is defined as follows

$$Error=\max_i\left|f_i^{n+1}\right| \qquad \text{Eq. 3-44}$$

Matrix Condition Number

Condition number of square non-singular matrix $\boldsymbol{A}$ defined by

$$\boldsymbol{cond}(\boldsymbol{A})=\|\boldsymbol{A}^{-1}\|\times\|\boldsymbol{A}\| \qquad \text{Eq. 3-45}$$

For matrices with a large condition number, solving an associated linear system might pose numerical difficulties. For a matrix $\boldsymbol{A}$ with a large condition number, the problem $\boldsymbol{Ax}=\boldsymbol{b}$ is referred to as ill-conditioned. A large condition number indicates a nearly singular matrix. In contrast, a matrix with a condition number close to 1 is far from being singular and indicative of a well-posed and solvable equation system.

Comparison of Coupling Strategies

An investigation of many steady-state problems shows that the segregated solver will converge for all the studied cases. Still, the semi-simultaneous and fully-simultaneous solvers show convergence problems in most cases. The convergence problem is due to the large condition number of the A matrix, which means that the non-linear and linearized equations in these two solvers are ill-conditioned. A case with an analytical solution is first solved using all methods to verify developed programs. Two other cases, including a 3-zone horizontal case and a light well, are simulated using all solvers.

Analytical Test Case

A three-zone steady case with an analytical solution [40] was developed and implemented to verify the coupling strategies. The case illustrated in Fig. 3-3 is a three-zone model having one zone cooled to a constant temperature below that of the outdoor temperature. There is an analytical solution for this problem by solving the heat balance equations for the three zones, A, B, and C, which can be solved for the three unknowns T_A, T_B, and $\dot{Q}_C$. Analytical solution of the equations yields values for T_A, T_B and $\dot{Q}_C$ of 30.31 ℃, 23.95 ℃, and 1600 W, respectively.

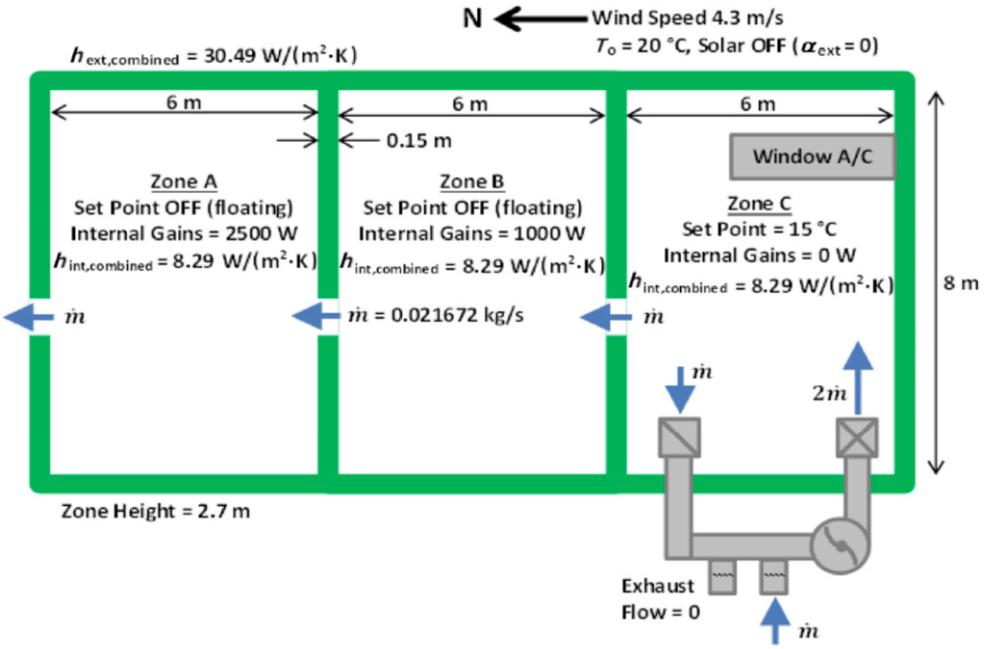

Figure 3-3 Plan view of the analytical case [40]

The resultant simulation values of different strategies and simulation values of Dols et al. [40] are precisely the same as those of the analytical values (Table 3-2).

Table 3-2 Simulation results for the analytical test case.

Solver	Zone air temperature			Cooling load
	T_A	T_B	T_C	Q_C
All strategies	30.31	23.95	15.0	1600

3-zone Horizontal Test Case

The second test case consists of 3-zones arranged horizontally (Fig. 3-4). Zone 3 is at a constant temperature of 30 ℃ higher than the outdoor temperature. Zones are connected to neighboring zones and/or ambient by airflow paths located at various elevations. Implementation of the semi-simultaneous method shows fluctuations in solving the system of equations of zone 1, which occurs after 28 iterations of the external loop. Fig. 3-5 shows fluctuations of the semi-simultaneous internal loop and the coefficient matrix's condition number. The coefficient matrix has a very large condition number, which means that the linearized and the corresponding non-linear equations are ill-conditioned, causing convergence problems. The reason for the large condition number in the semi-simultaneous method will be discussed in the next section.

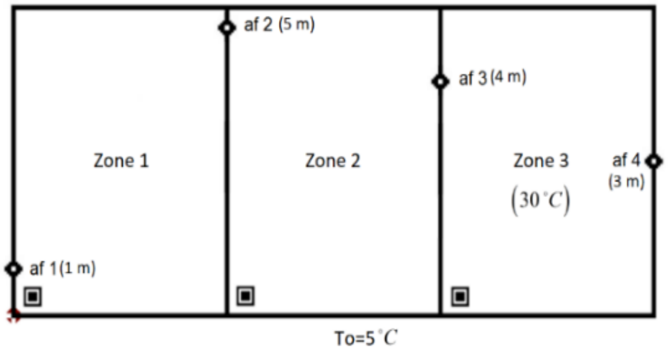

Figure 3-4 The plan view of the 3-zone test case

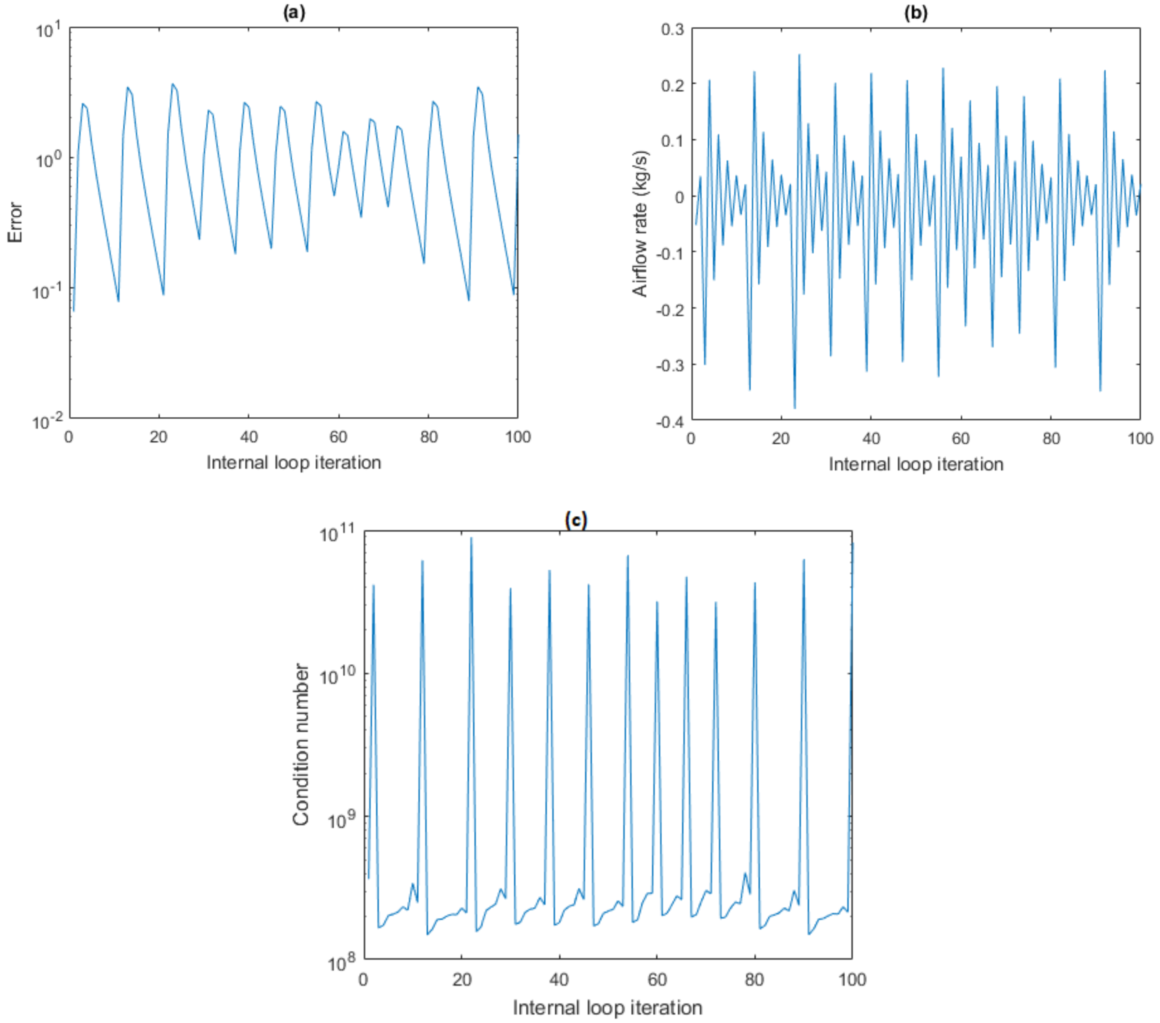

Figure 3-5 Semi-simultaneous method, (a) Error history, (b) airflow rate of af 2, c) Condition number of the matrix equation

The fully-simultaneous method shows a similar fluctuation problem (Fig. 3-6a,b). The linearized equation's coefficient matrix has a very large condition number for all iterations (Fig. 3-6c). Therefore, the non-linear system of equation is ill-conditioned, so the fully-simultaneous method performs poorly and cannot reach convergence.

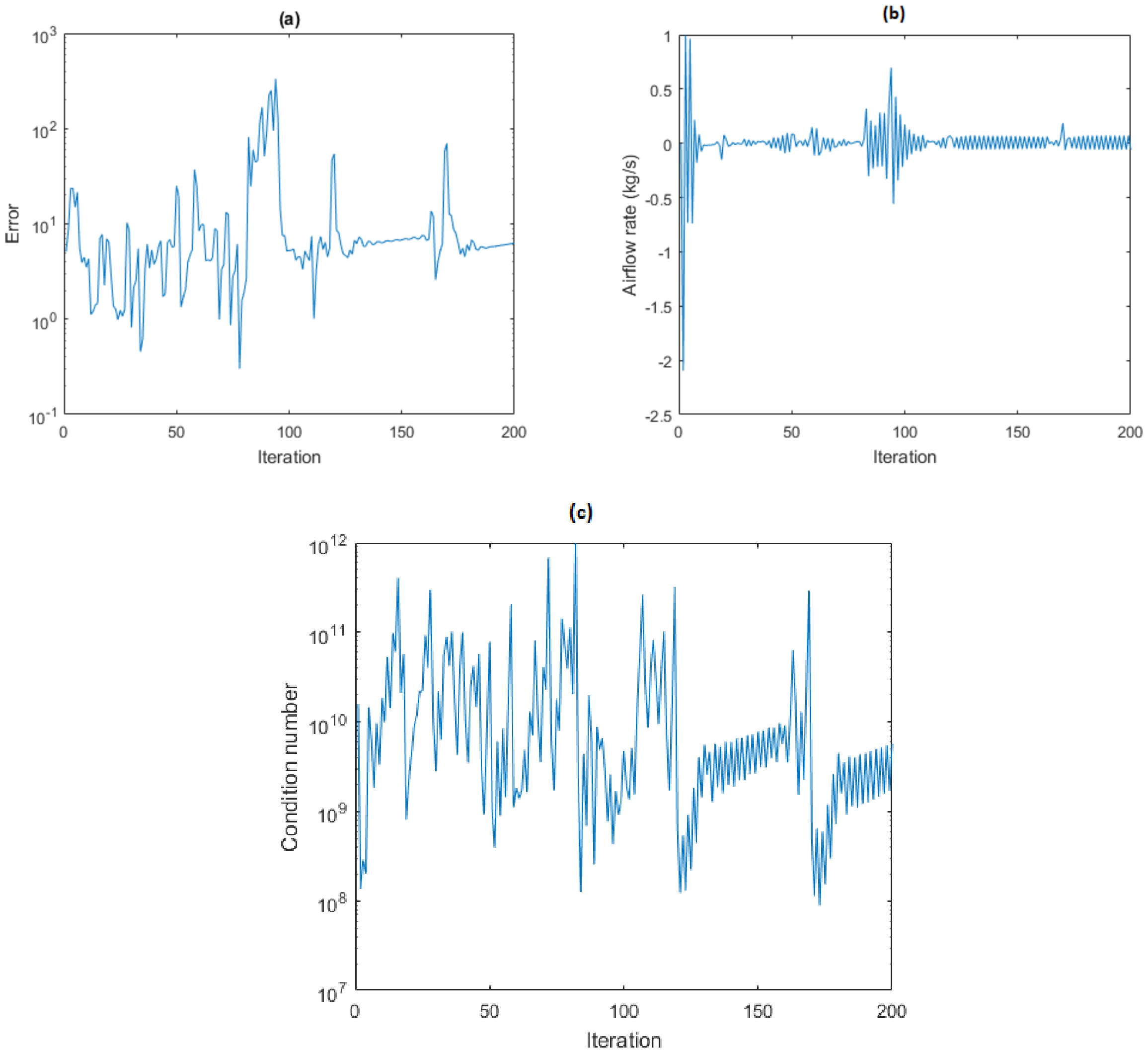

Figure 3-6 Fully-simultaneous method, a) Error history, b) airflow rate of af 2, c) Condition number of the matrix equation

Unlike the two other methods, the segregated solver shows a convergent solution for this problem, as shown in Fig. 3-7. The condition number for this case using this solver is always smaller than ten, which means that the equation system is well-conditioned and solvable.

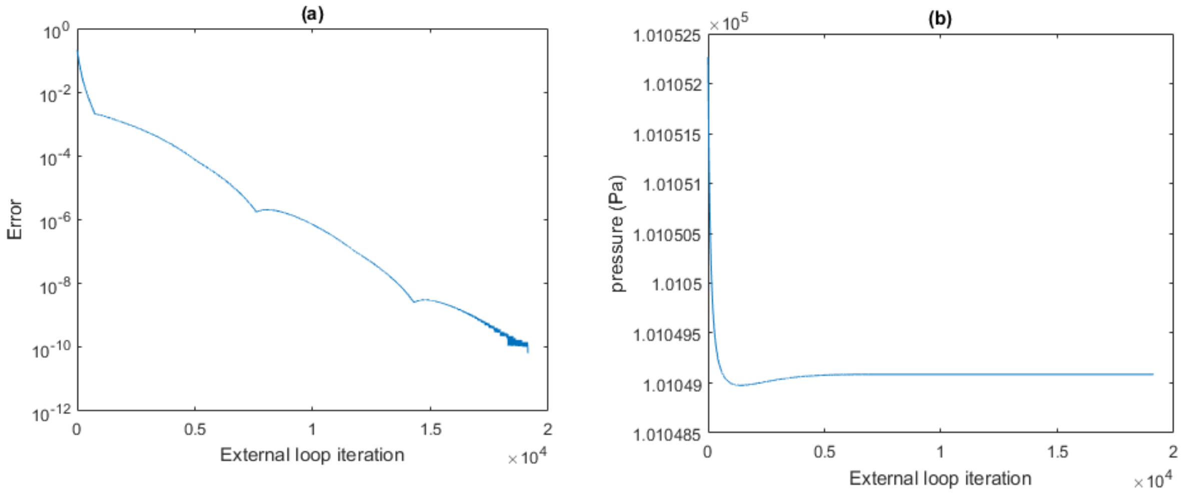

Figure 3-7 Convergence history of segregated solver, a) Error history, b) airflow rate of af 2.

Lightwell Natural Ventilation Case

The third case is a light well with airflows driven by both wind force and thermal buoyancy. Wind tunnel data are available to validate the simulation results [141]. The light well's schematic corresponds to a 1:250 scaled model of a 41-story high-rise apartment building, and simulation parameters are shown in Table 3-3. An orifice airflow equation is used for all the openings. Walls are considered to be adiabatic because heat transfer through them is neglected in the experiment. Simulation of the light well problem using the semi-simultaneous and fully-simultaneous methods show the same fluctuations in the solution, which is due to the large condition number of the coefficient matrices. Unlike the semi-simultaneous and fully-simultaneous solvers, the segregated solver provides a convergent result for this case. The condition number of the segregated system for this case is always smaller than 10, indicating a well-conditioned problem.

Table 3-3 Schematic of the light well [141] and simulation parameters

<table>
<tr><td rowspan="9">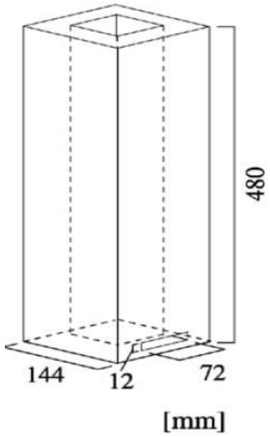
</td><td colspan="2">Heat generation rate (W)</td><td>40</td></tr>
<tr><td colspan="2">Wind velocity (m/s)</td><td>0</td></tr>
<tr><td colspan="2">Outside Temperature (C)</td><td>12</td></tr>
<tr><td colspan="2">Number of the zones</td><td>8</td></tr>
<tr><td colspan="2">Height of the zones (m)</td><td>0.0585</td></tr>
<tr><td rowspan="3">Discharge coefficient</td><td>Top opening</td><td>2.187*</td></tr>
<tr><td>Bottom opening</td><td>0.855*</td></tr>
<tr><td>Inter-zonal openings</td><td>1*</td></tr>
<tr><td colspan="3">* adopted from the original study (source)</td></tr>
</table>

The simulated airflow rate through the light well obtained by the segregated solver is compared to Kotani et al.'s measured data [141] and simulation studies and shown in Fig. 3-8a. Temperature distribution in the light well is compared to measured data in Fig. 3-8b. The overall trend of the simulation results agrees reasonably well with the measured values.

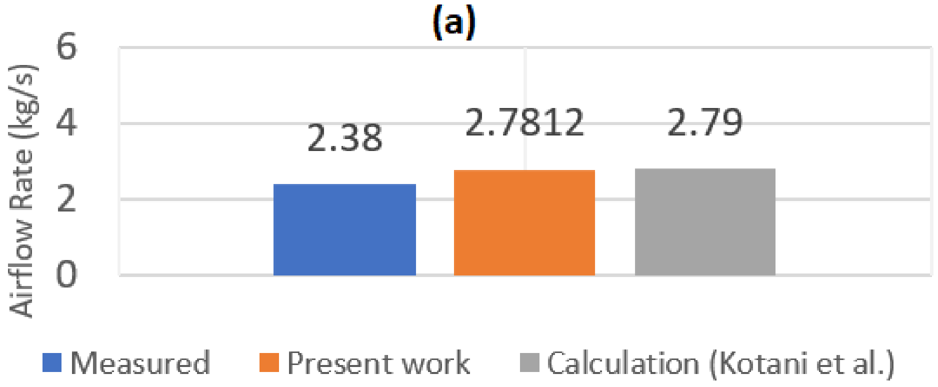

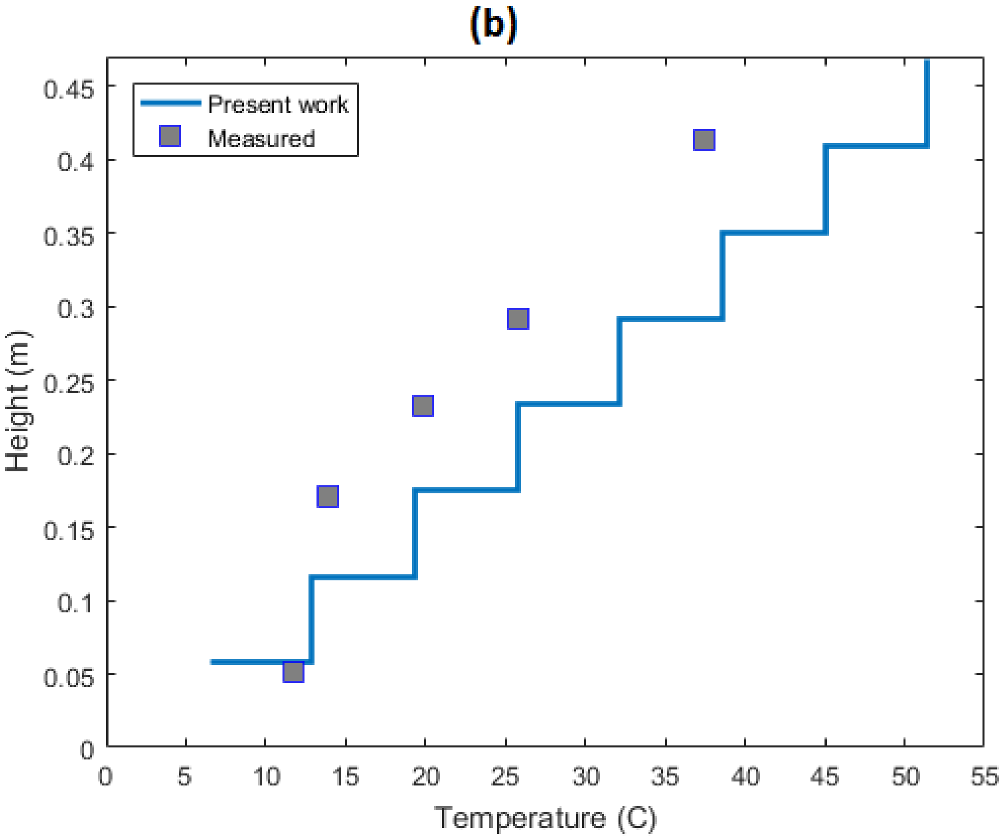

Figure 3-8 a) Airflow rate through the light well, b) Temperature variation inside the light well.

Condition Number Investigation

In this case, the condition numbers of the semi-simultaneous and fully-simultaneous methods are very large, which means that the equations system is ill-conditioned. In most of the problems, we observe fluctuations in the solution. The condition number of matrix equations in the segregated solver is very small (smaller than 10). Therefore, the segregated solver's matrix equations are well-conditioned, and this solver shows convergent results in all simulated cases. This section explains the reason for ill-conditioned and well-conditioned equations by drawing the equations' corresponding curves. Fig. 3-9 shows a general case for the investigation of condition numbers for the semi-simultaneous method. It is a single zone surrounded by four zones and is meant to be a typical zone in any problem, for example, the three-zone test case or light well problem. The system of equations in the fully-simultaneous method is an extended form of the semi-simultaneous method. In the one-zone problem, the system of equations of the fully- and semi-simultaneous solvers are the same.

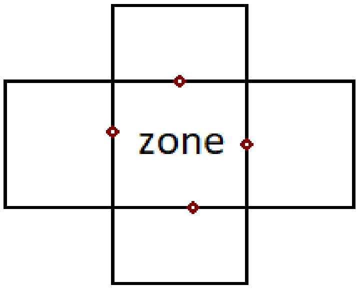

Figure 3-9 The general case for investigating the condition number of semi-simultaneous and fully-simultaneous methods

Mass and energy balance equations of this single zone as a function of $(P_i = x, T_i = y)$ are as follows:

$$f(x,y) = \sum_j sign(\Delta P_{ij}) C |\Delta P_{ij}|^n + Ms_i = 0 \qquad \text{Eq. 3-46}$$

$$g(x,y) = \sum_{j:F_{ji}>0} C(\Delta P_{ji})^n C_{pa} T_j - \sum_{j:F_{ij}>0} C(\Delta P_{ij})^n C_{pa} y + S_i + Dy + E = 0 \qquad \text{Eq. 3-47}$$

$$\Delta P_{ij} = x\left(1 + \frac{a_j}{y}\right) + b_j \qquad \text{Eq. 3-48}$$

$$\begin{cases} a_j = -\dfrac{gH_i}{R} + \dfrac{g}{2R}\left(z_i + H_i - z_j - H_j\right) = f(H, z) \\ b_j = -\left(P_j - \rho_j g H_j\right) + \dfrac{\rho_j g}{2}\left(z_i + H_i - z_j - H_j\right) + P_{ij,w} = f(P, T, H, z, P_w) \\ D = -\sum_k h_k A_k \\ E = \sum_k h_k A_k T_{mk} \end{cases} \qquad \text{Eq. 3-49}$$

The system of equations is exponential functions of pressure and temperature. According to Equations 3-46 to 3-49, when different cases are simulated using semi-simultaneous and fully-simultaneous methods, changes in the parameters, i.e., $P, T, H, z,\ and\ P_w$ will lead to changes in the coefficients $\left(a_j, b_j, D,\ \text{and}\ E\right)$, but these coefficients do not change the general shape of the functions. Therefore, we can conclude that Equations 3-46 and 3-47 have similar curves in all cases. Fig. 3-12 shows the shape of the functions for the 3-zone and light well test cases. As seen in both cases, corresponding curves of mass and energy balance equations are two nearly parallel curves. Parallel curves similar to Fig. 3-10 correspond to an ill-conditioned equation system [142]. Therefore, linearized systems of equations in the semi-simultaneous and fully-simultaneous methods are ill-conditioned, and the coefficient matrix A is almost singular.

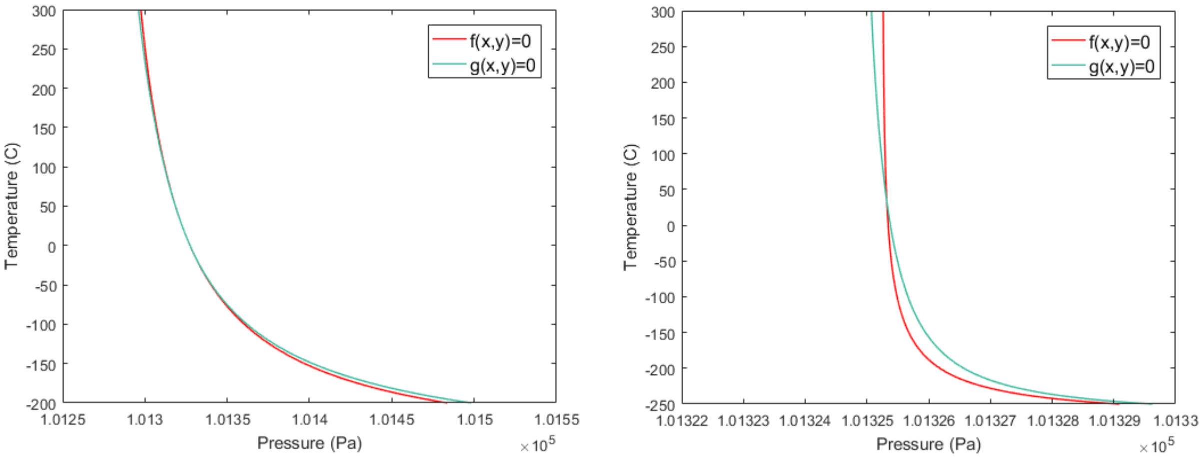

Figure 3-10 Corresponding curves of mass and energy balance equations (a) 3-zone test case, (b) light well test case

In conclusion, solving different problems using all three solvers is shown that for most of the cases, the fully-simultaneous and semi-simultaneous solvers show fluctuations in the solution. In contrast, the segregated solver shows good convergent results for all cases. Studying the condition number of the matrix equations shows that fully and semi-simultaneous solvers have very large condition numbers, which means that these two solvers' equations are ill-conditioned. In contrast, the matrix equations corresponding to the mass and energy balance equations of segregated solver have smaller condition numbers. Therefore, the matrix equations of the segregated solver are well-conditioned for the cases tested. To show that the matrix equation of fully and semi-simultaneous methods is always ill-conditioned, the parametric mass and energy balance equations of a typical one-zone case are extended. Results show that corresponding curves of mass and energy balance equations are nearly parallel, which results in an ill-conditioned system of equations.

Segregated Thermal Airflow Solver

According to the previous section results, the segregated (Ping-Pong) [143] strategy is selected and used to couple the air mass and energy balance equations. In this section, the details of the segregated approach are presented. In the segregated strategy, the air mass and energy balance equations will be solved in a sequence with internal iterations until the solution's convergence at each time step. The segregated strategy consists of the following steps for solving the problem. The iterative algorithm of segregated (ping-pong) strategy is schematically described through the flowchart in Fig. 3-11. An initial value is provided for zone pressures, zone temperatures, and thermal mass temperatures. At steps 2 and 3, all zones' mass and energy balance equations are solved (system of equations 3-40 and 3-41) to update the pressure and temperature of zones. At step 4, wall temperatures are updated by solving the energy balance equation of walls. Finally, convergence is checked at step 5 by calculating the absolute value of the difference between the zone pressures and temperatures in two consecutive iterations. If the solution is converged, it goes to the next step; otherwise, the iteration counter is updated, and the solution is continued at step 2.

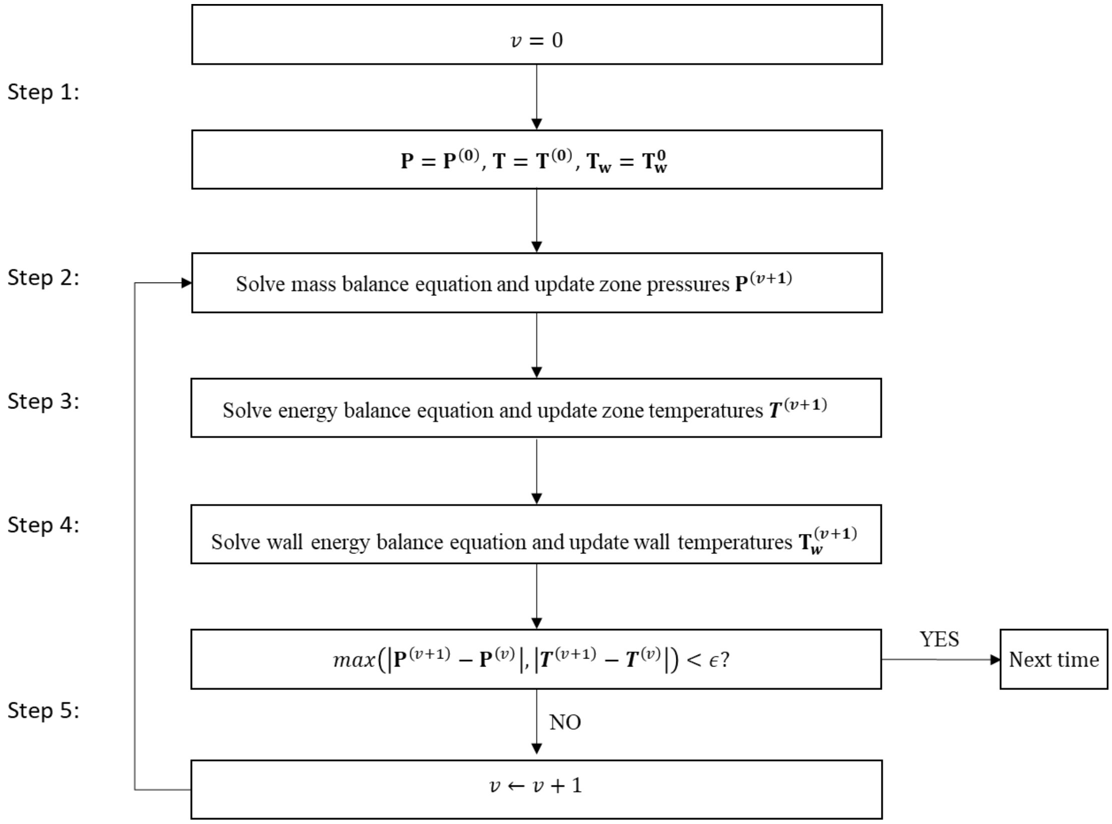

Figure 3-11 Algorithm flowchart for the segregated (ping-pong) solver

For solving the mass and energy balance equations (steps 3 and 4), the system of equations 3-40 and 3-41 can be rewritten as

$$\mathbf{f}(\mathbf{P}) = \mathbf{0} \qquad \text{Eq. 3-50}$$

$$\mathbf{g}(\mathbf{T}) = \mathbf{0} \qquad \text{Eq. 3-51}$$

The Newton-Raphson method is used for solving the system of nonlinear equations 3-50 and 3-51. Newton-Raphson method is an iterative method that uses initial values for the unknowns and, then, at each iteration, updates these values until no change occurs in two consecutive iterations. The Newton-Raphson algorithm consists of the following steps for solving nonlinear equations 3-50 (the same algorithm is used for solving equation 3-51).

Step 0: initialize the iteration counter $(v = 0)$ and provide an initial value for vector **P**, i.e., $\mathbf{P} = \mathbf{P}^{(v)} = \mathbf{P}^{(\mathbf{0})}$.

Step 1: computing the Jacobian matrix **J**:

$$\mathbf{J} = \left[\begin{bmatrix} \frac{\partial f_1(\mathbf{P})}{\partial P_1} & \frac{\partial f_1(\mathbf{P})}{\partial P_2} & \cdots & \frac{\partial f_1(\mathbf{P})}{\partial P_n} \\ \frac{\partial f_2(\mathbf{P})}{\partial P_1} & \frac{\partial f_2(\mathbf{P})}{\partial P_2} & & \frac{\partial f_2(\mathbf{P})}{\partial P_n} \\ \vdots & & \ddots & \vdots \\ \frac{\partial f_n(\mathbf{P})}{\partial P_1} & \frac{\partial f_n(\mathbf{P})}{\partial P_2} & \cdots & \frac{\partial f_n(\mathbf{P})}{\partial P_n} \end{bmatrix}\right] \qquad \text{Eq. 3-52}$$

Step 2: solve $\mathbf{J}^{(v)}\Delta\mathbf{P}^{(v)} = \mathbf{f}\left(\mathbf{P}^{(v)}\right)$ by the Gauss-Seidel method.

Step 3: compute $\mathbf{P}^{(v+1)}$ as

$$\mathbf{P}^{(v+1)} = \mathbf{P}^{(v)} - \Delta\mathbf{P}^{(v)} \qquad \text{Eq. 3-53}$$

Step 3: check every element of the absolute value of the difference between the values of vector **P** in two consecutive iterations is lower than a prespecified tolerance $\boldsymbol{\epsilon}$, i.e., $\left|\mathbf{P}^{(v+1)} - \mathbf{P}^{(v)}\right| < \boldsymbol{\epsilon}$. If so, the algorithm has converged, and the solution is $\mathbf{P}^{(v+1)}$. If not, continue at Step 4.

Step 4: update the iteration counter $v \leftarrow v + 1$ and continue at Step 1.

3.2.2. Wall Energy Balance Solver

The Crank-Nicolson method [144] discretizes the thermal mass energy balance equation (Eq. 3-4). Crank-Nicolson scheme is the average of the explicit scheme at (i, t) and implicit scheme at $(i, t + 1)$. This method is second-order, implicit in time and unconditionally stable.

$$\begin{aligned} C_i\left(\frac{T_{w,i}^{t+1}-T_{w,i}^{t}}{\Delta t}\right) \\ &= \frac{1}{2}\left(\frac{T_{w,i-1}^{t}-T_{w,i}^{t}}{R_{i-1}+R_i}+\frac{T_{w,i+1}^{t}-T_{w,i}^{t}}{R_{i+1}+R_i}+Q_{w,i}^{t}\right) \\ &+ \frac{1}{2}\left(\frac{T_{w,i-1}^{t+1}-T_{w,i}^{t+1}}{R_{i-1}+R_i}+\frac{T_{w,i+1}^{t+1}-T_{w,i}^{t+1}}{R_{i+1}+R_i}+Q_{w,i}^{t+1}\right) \end{aligned} \tag{Eq. 3-54}$$

Or, letting $r=\frac{\Delta t}{2C_i}$ gives

$$\begin{aligned} -\frac{r}{R_{i+1}+R_i}T_{w,i+1}^{t+1}+\left(1+\frac{r}{R_{i-1}+R_i}+\frac{r}{R_{i+1}+R_i}\right)T_{w,i}^{t+1}-\frac{r}{R_{i-1}+R_i}T_{w,i-1}^{t+1} \\ &= \frac{r}{R_{i+1}+R_i}T_{w,i+1}^{t}+\left(1-\frac{r}{R_{i-1}+R_i}-\frac{r}{R_{i+1}+R_i}\right)T_{w,i}^{t} \\ &+ \frac{r}{R_{i-1}+R_i}T_{w,i-1}^{t}+r\left(Q_{w,i}^{t+1}+Q_{w,i}^{t}\right) \end{aligned} \tag{Eq. 3-55}$$

Rewriting (3-55) gives the new form

$$\left\{\begin{array}{c} a_i^{t+1}T_{w,i-1}^{t+1}+b_i^{t+1}T_{w,i}^{t+1}+c_i^{t+1}T_{w,i+1}^{t+1}=d_i^{t+1} \\ \text{where} \\ a_i^{t+1}=-\frac{r}{R_{i-1}+R_i} \\ b_i^{t+1}=1+\frac{r}{R_{i-1}+R_i}+\frac{r}{R_{i+1}+R_i} \\ c_i^{t+1}=-\frac{r}{R_{i+1}+R_i} \\ d_i^{t+1}=\frac{rT_{w,i+1}^{t}}{R_{i+1}+R_i}+\left(1-\frac{r}{R_{i-1}+R_i}-\frac{r}{R_{i+1}+R_i}\right)T_{w,i}^{t}+\frac{rT_{w,i-1}^{t}}{R_{i-1}+R_i}+r\left(Q_{w,i}^{t+1}+Q_{w,i}^{t}\right) \end{array}\right. \tag{Eq. 3-56}$$

Equation (3-56) can be written as a tridiagonal system of equations

$$\begin{bmatrix} b_1 & c_1 & & & \\ a_2 & b_2 & c_2 & & \\ & a_3 & b_3 & \ddots & \\ & & \ddots & \ddots & c_{n-1} \\ & & & a_n & b_n \end{bmatrix} \begin{bmatrix} T_{w,1}^{t+1} \\ T_{w,2}^{t+1} \\ T_{w,3}^{t+1} \\ \vdots \\ T_{w,n}^{t+1} \end{bmatrix} = \begin{bmatrix} d_1^{t+1} \\ d_2^{t+1} \\ d_3^{t+1} \\ \vdots \\ d_n^{t+1} \end{bmatrix} \quad \text{Eq. 3-57}$$

The Tridiagonal Matrix Algorithm (TDMA), also known as the Thomas Algorithm [137], which is a particular form of Gauss elimination, is used to solve the tridiagonal system of equations 3-57. The solution is obtained in $O(n)$ operations, instead of $O(n^3/3)$ required by Gaussian elimination. Appendix B provides a detailed description of TDMA for solving a tridiagonal system of equations.

3.3. Case Study: Hybrid Ventilation System in an Institutional High-Rise Building

In this section, the coupled airflow/thermal multi-zone network model is applied to modeling the HV system of a 17-story high-rise building in Montreal, Canada [25,34,42,43]. An extensive full-scale experimental study is conducted to measure airflow velocity through dampers, indoor air temperatures, mechanical fan flow rates, and ambient weather conditions. The data are collected for the summers of 2017 and 2018 when the HV system was operational. To study the impacts of the local weather conditions on the simulation result, three different ways of acquiring the weather conditions are compared together: from the local weather station, using the nearby weather station data, and using the forecasted weather data provided by the High-Resolution Deterministic Prediction System (HRDPS) [145] with a 2.5 km horizontal grid spacing over one main Pan-Canadian region. The HRDPS fields are made four times a day for the Pan-Canadian domain for a 48-hour forecast period.

3.3.1. Field Measurements

A 17-story high-rise building with a fan-assisted HV system was selected for the current study (Fig. 3-12). The total floor area of the building is about $53{,}000\ m^2$ with the average window-to-wall ratio (WWR) of 50%, providing natural daylighting and, in the meantime, high solar heat gain and thus the cooling load. Each floor of the building consists of offices, laboratories, and an atrium located at the building's southwest façade. The atrium is extended from the second to the sixteenth floor and is subdivided into five stacked atria sections with three floors per section. A concrete floor slab separates these five atrium sections with motorized floor grilles. The $0.4\,m$ thick concrete floor slabs provide an excellent thermal mass that can absorb and dissipate heat for passive cooling and reduce diurnal air temperature fluctuations and peak cooling load. Two motorized inlet dampers are located at the end of the corridors in the southeast and northwest façade of each floor. The full opening area of the inlet dampers is about $1.4\,m^2$ which can be adjusted in percentage. A variable-speed fan with a maximum airflow rate of $40{,}000\ L/s$ is installed on the roof to assist naturally-driven airflow throughout the building (Fig. 3-12). The motorized inlet dampers and those at the atrium floor grilles are controlled by the building automation system (BAS). The HV system typically operates when the outdoor temperature is between $15\ ℃$ and $25\ ℃$, and the relative humidity is less than 70% [42]. When the system is operating, cold outside air enters the building through inlet dampers, moves upward through the atria-connecting floor grilles, and exits from the roof exhaust assisted by the roof fan. The concrete floor slabs absorb a portion of the heat gains from the sun, lighting, equipment, and occupants during the day. At night, they absorb the cooling energy from the outside air introduced by the HV system. In other words, the absorbed daytime heat is removed from the thermal mass, allowing a cold start temperature for the following day.

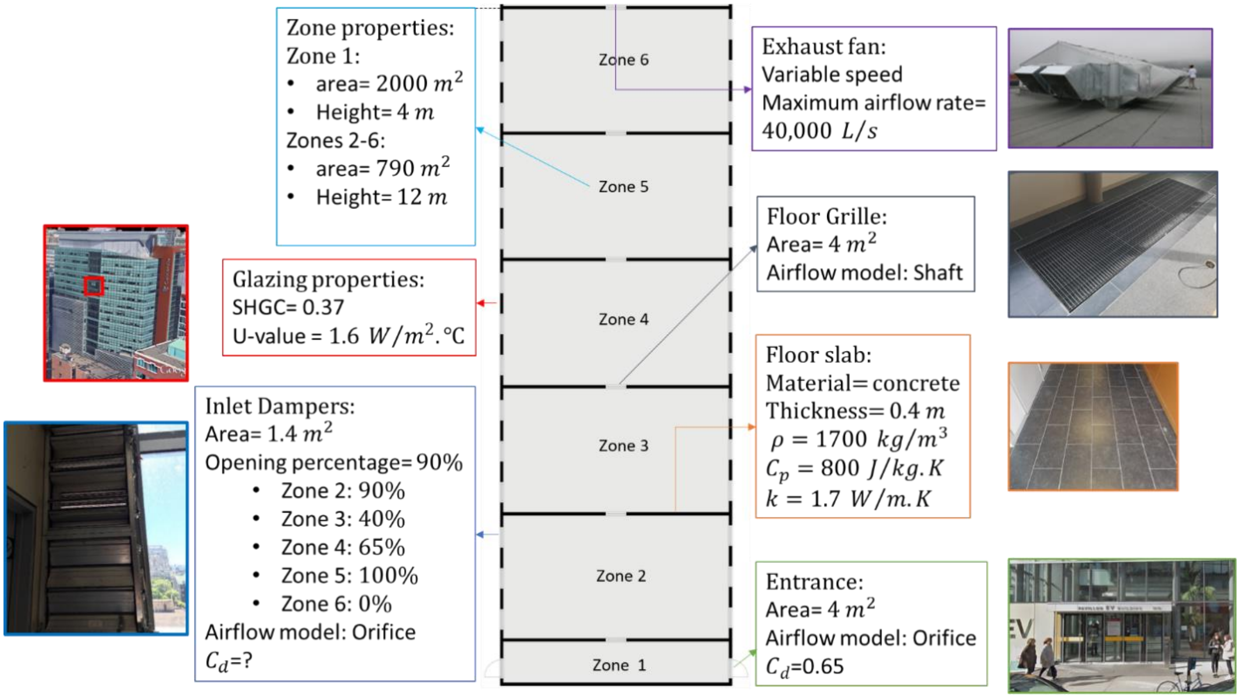

Figure 3-12 Schematic of the HV system of EV building, and simplified 6-zone model for simulating by the multi-zone network model.

Full-scale measured data are needed for the validation and dynamic calibration of the simplified multi-zone network model. The measurements were conducted during the operation of the HV system in the summers of 2017 and 2018. A weather station installed on the EV building's roof provides weather data, including outdoor air temperature, wind velocity, wind direction, and solar radiation. The building automation system can access measured weather data, the fan flow rate, and the HV system's operation times. Measured velocities through inlet dampers are needed for the dynamic calibration and validation of the model. One-directional hot-wire anemometers are used for this purpose. The airspeed measurement range is 0.2 ~ 25 m/s, and the accuracy is ± (5%+0.1 m/s). Nine anemometers were installed on the southeast façade of the 4th, 5th, 8th, 10th floors, and the northwest façade of the 5th, 8th, 10th, 11th, and 13th floors for covering all atrium sections. The time-step of recording the data is 2 minutes. Multiple thermostats that are part of the building automation system provide each building floor's indoor air temperature.

3.3.2. Numerical Simulations

A simplified multi-zone network model was created and previously compared against a more detailed model [43]. The simplified model is a 6-zone network model with one zone for each atria section and one zone on the first floor (Fig. 3-12). Each zone includes two glazings at SE and NW façade. The glazing is double-glazed, with a low e-coating and Argon-filled with the following properties: solar heat gain coefficient (SHGC) equal to 0.37; and center-of-glass U-value equal to $1.6\ W/m^2.℃$. Solar radiation transmitted through the glazing is considered a heat source absorbed by the concrete floor slab's surface. Offices and laboratories surround corridors and atrium. The HVAC system controls the temperature of offices and labs. Therefore, it is supposed that they are at a constant set-point temperature of $24\ ℃$. The conductive heat transfer through walls is calculated to model offices and labs' effect on the atrium. Concrete floor slabs are also modeled as a thermal mass with multiple layers between two zones. Each zone includes several openings as inlet dampers and floor grilles. As explained in the previous section, atrium sections are separated by floor slab with a $4\ m^2$ floor grilles with motorized dampers. Floor grilles are fully opened during the HV system operation and are modeled by the shaft airflow model. The exhaust fan at the top of the building is modeled by an airflow source in the last zone (zone 6). Inlet dampers are modeled by orifice airflow equation. During the operation of the HV system, inlet dampers are not fully opened. A constant pre-defined opening percentage is used for inlet dampers. A different opening percentage is used for different sections of the atrium (Fig. 3-12). The orifice airflow equation's discharge coefficient depends on the opening geometry and the direction of approaching flow. A flat plate orifice in which the air stream is directed at right angles to the opening typically has a value of approximately 0.61 – 0.65. Such a range is widely used in preliminary design calculations. However, for practical components, the actual value is dependent on the element itself and airflow direction.

We use measured velocities through inlet dampers to dynamically calibrate the discharge coefficients (Eq. 3-58).

$$F_{ij} = \rho A_{ij} v_{ij} = C_{d,ij} A_{ij} \sqrt{2\rho \Delta P_{ij}} \rightarrow C_{d,ij} = \frac{v_{ij,measured}}{\sqrt{2\Delta P_{ij}/\rho}} \qquad \text{Eq. 3-58}$$

Fig. 3-13 shows the flowchart of the dynamic calibration process. The time interval of dynamic calibration and prediction is one hour. One hour measured velocity with weather station and fan flow rate data is used for the estimation of C_d. The time step of the simulation is 5 minutes, and it is supposed that the C_d is constant at each time step. The forecasting weather data and final calibrated C_d is used for the prediction of the performance of the HV system in the next one hour. All dampers are calibrated in a repeated sequence in an internal loop in the calibration step until the convergence. Calibration is converged if the absolute value of the difference between calculated C_d in two consecutive iterations is lower than a prespecified tolerance $\epsilon = 10^{-4}$, i.e., check if $max\left(\left|C_{d,ij}^{(v+1)} - C_{d,ij}^{(v)}\right|\right) < \epsilon$.

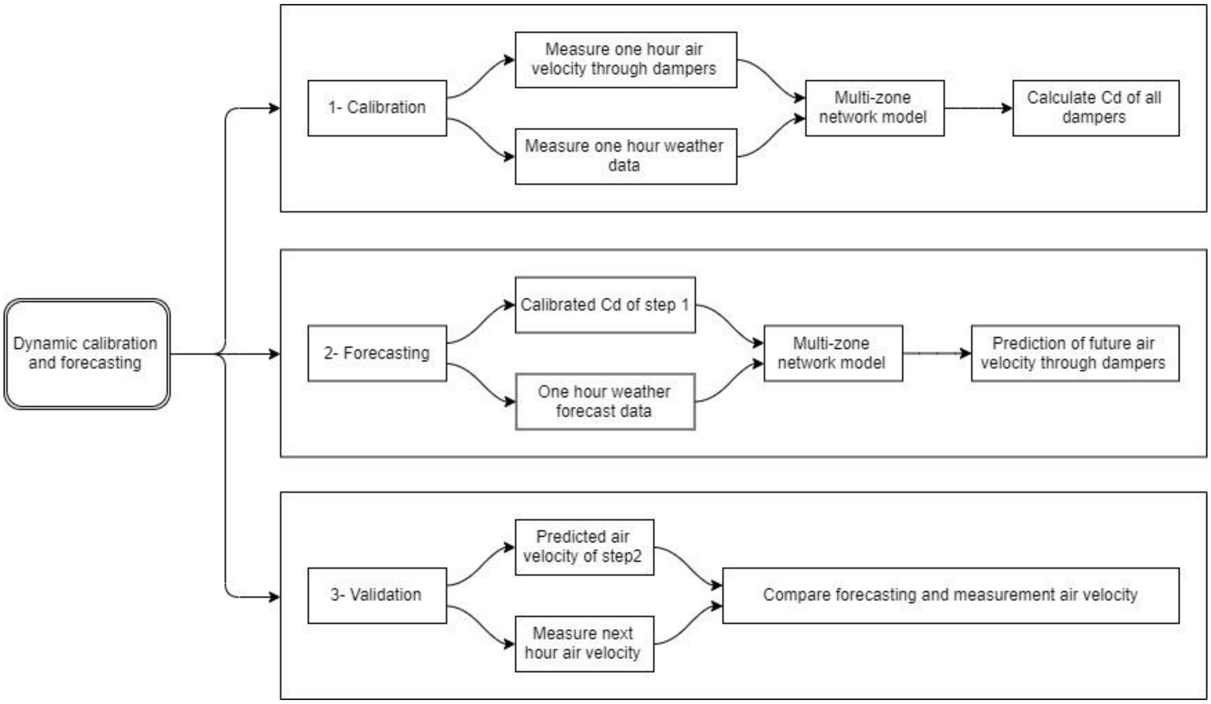

Figure 3-13 Flowchart of dynamic calibration of the simplified multi-zone network model and prediction of HV system performance.

3.3.3. Results and Discussions

Validation of Result

In this section, the HV system is simulated from 00:00 of 08/30/2017 to 07:00 of 08/31/2017. The result is compared with measurement data for validation of the developed model. Measured weather data is shown in Fig. 3-14. Outdoor air temperature is between $14 - 22$ ℃, which meets the condition of using the HV system. Studied days are sunny, and large solar radiation can be a significant source of the building’s cooling load. Two sets of measured data, indoor air temperature and airflow velocity through inlet dampers, are used to validate the model.

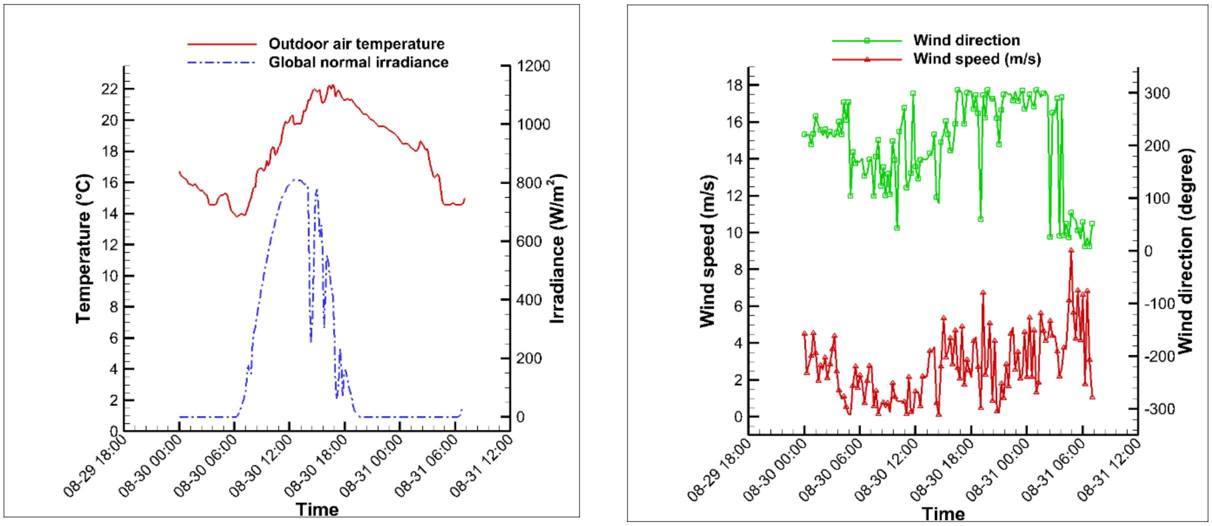

Figure 3-14 Weather station data: a) outdoor air temperature and Global normal irradiance, b) Wind speed and direction (08/30/2017).

<u>Indoor air temperature</u>

The simulated indoor air temperature of different atria sections is compared with the measured air temperature in Fig. 3-15. Although the model is simplified and three floors are modeled with only one zone, each zone's simulated temperature is close to the measured temperature by thermostats located on different floors.

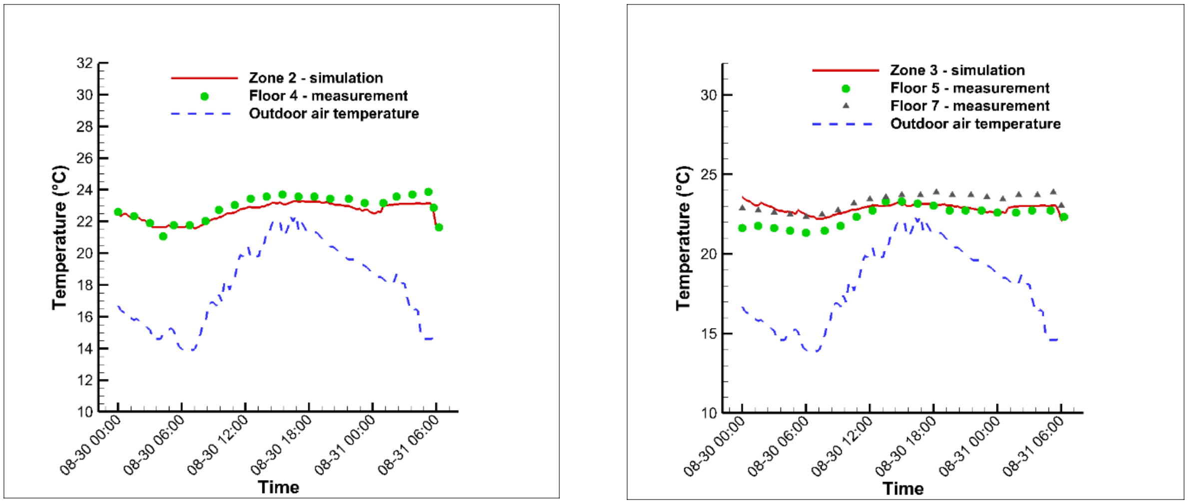

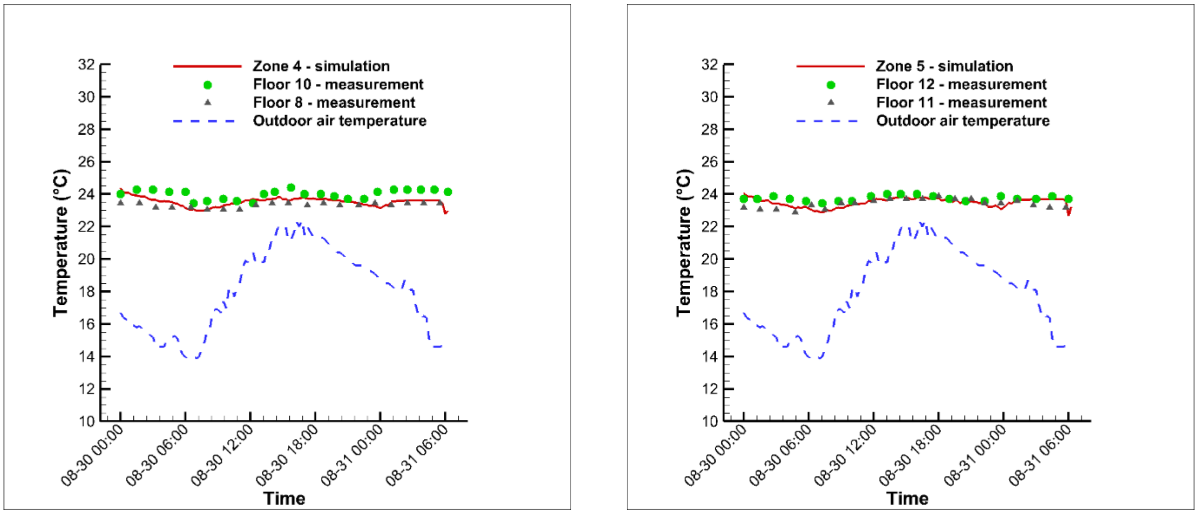

Figure 3-15 Comparison of simulated and measured indoor air temperature of different atria sections (00:00 of 08/30/2017 to 07:00 of 08/31/2017).

Airflow velocity through inlet dampers

The predicted airflow velocity through inlet dampers simulated by the dynamic calibration method is compared with the corresponding non-calibrated model and measurement data by hot-wire anemometers (Fig. 3-16). There is a large difference between the predicted result by the non-calibrated model and experiment data. Using dynamic calibration shows a considerable improvement in the predicted airflow velocity. The normalized root mean square error (NRMSE) of results obtained by dynamic calibration and non-calibrated model with a constant C_d for all nine inlet dampers are compared in Fig. 3-17. The NRMSE of the calibrated model is reduced in all nine inlet dampers. In summary, Figs. 3-16 and 3-17 show that dynamic calibration strategy can improve the accuracy of prediction compared to the non-calibrated model with a constant value of C_d and results are well compared with measurement data. Therefore, it is essential to continuously measure the velocity through inlet dampers and use it for the dynamic calibration of the model to predict the HV system's performance accurately. The weather data used for the current simulation is the weather station's measured data because of the lack of local weather forecast data for this simulation's date and time. In the next section, real forecasting of the system’s performance is done for the summer of 2018 using dynamic calibration strategy and the local weather forecast data provided by the HRDPS model.

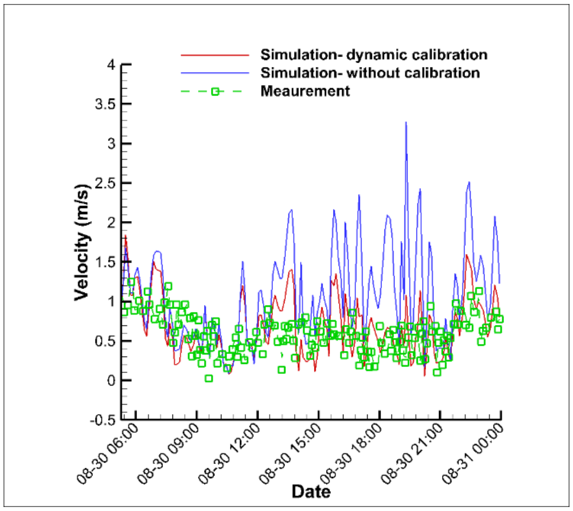

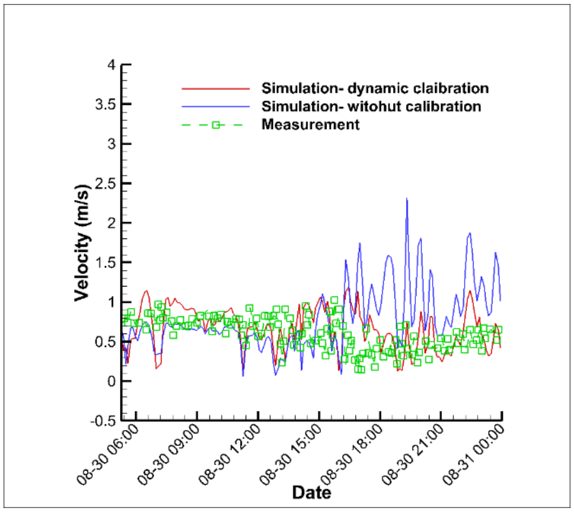

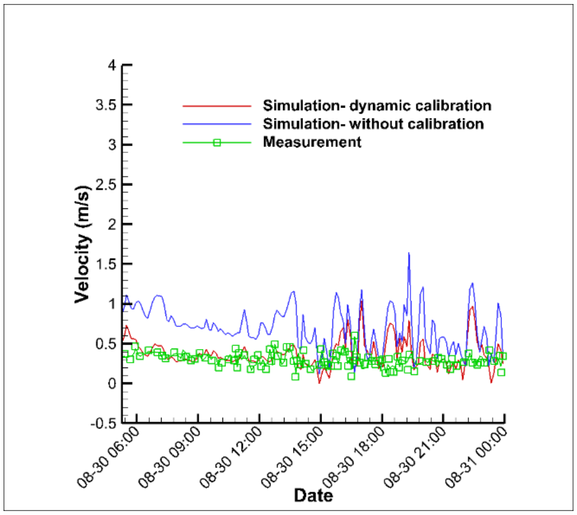

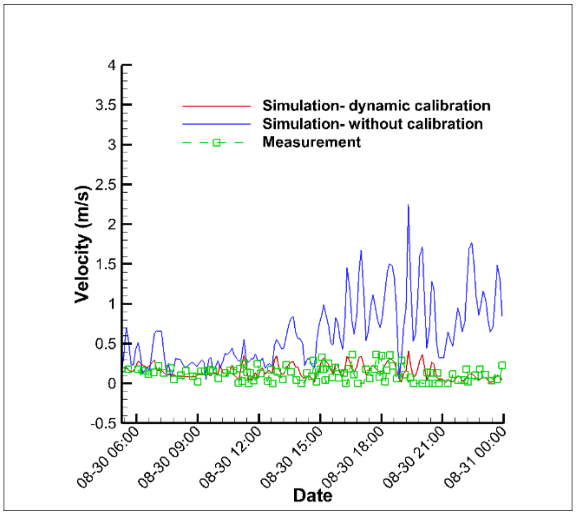

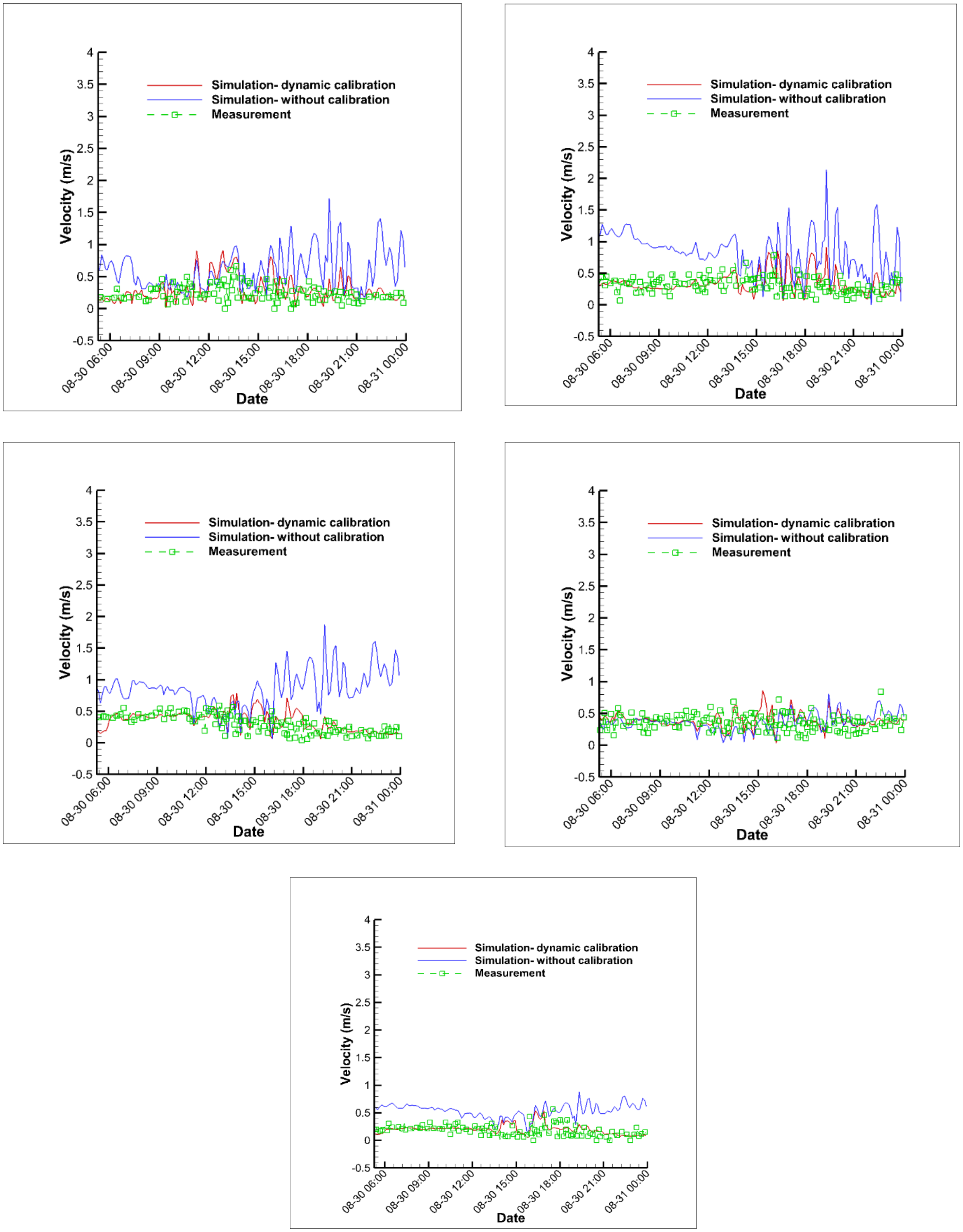

Figure 3-16 Comparison of simulated and measured indoor air temperature of different atria sections (00:00 of 08/30/2017 to 07:00 of 08/31/2017).

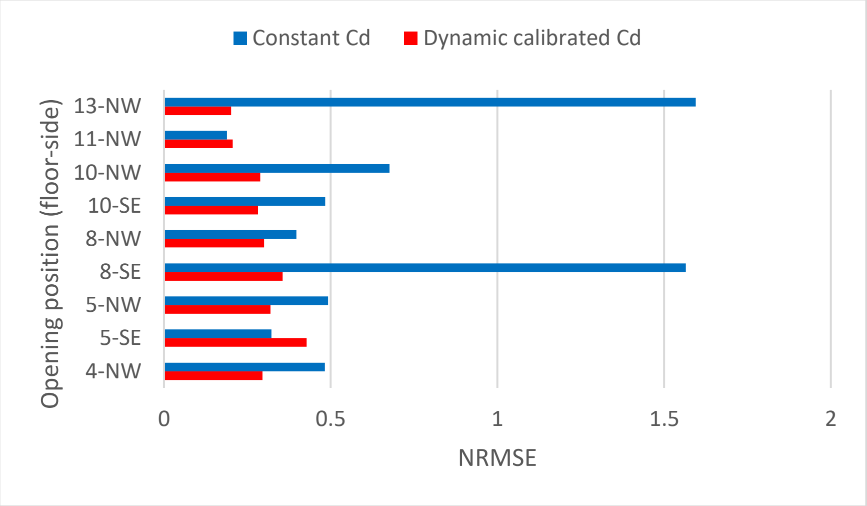

Figure 3-17 Normalized root mean square error of predicted air velocity through different dampers: dynamic calibrated and constant C_d.

Local Weather Data

The HV system's operation is a function of local air temperature and humidity. Therefore, the HV system's prediction needs the local weather data instead of a nearby weather station. Fig. 3-18 compares the local weather data measured by the weather station of EV building and weather data of the nearby weather station at Trudeau airport. Due to the differences between air temperature and humidity, Trudeau weather station's operation hours are different from real operation conditions, which affect the accuracy of the simulation. It is especially crucial for short-time prediction and optimization of the HV system by using weather forecast data. Results presented by non-accurate weather forecast data might be far from the real performance of the HV system.

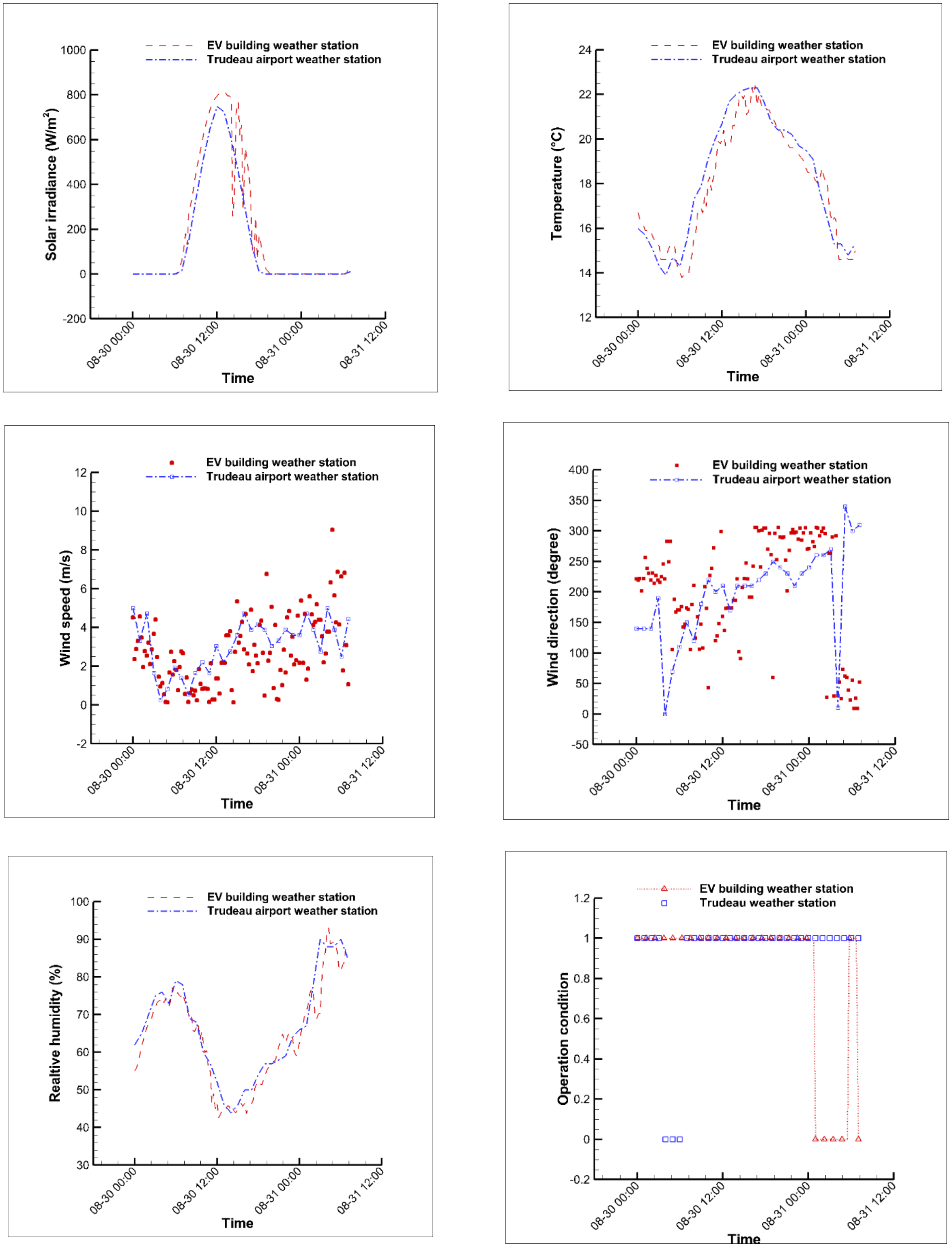

Figure 3-18 Comparison of local weather data by weather station of EV building and nearby weather station data and Trudeau airport (08/30/2017 - 08/31/2017).

Predictive Simulations

Before using the system's predictive control model, it is crucial to investigate the model's accuracy by doing real forecasting using weather forecasting data. As shown in the previous section, it is essential to use local weather forecasting data instead of nearby weather station data. Therefore, in this section, the HRDPS GRIB2 data provides the local weather forecast data for simulation. HRDPS model is a version of the Global Environmental Multiscale (GEM) model with a 2.5 km horizontal grid spacing over one main Pan-Canadian region. The HRDPS high-resolution dataset fields are made four times a day for the Pan-Canadian domain for a 48-hour forecast period. Two days of summer 2018 (September 7th- September 9th) are chosen for the simulation. All 48 hours of weather forecast data are exported simultaneously and are not updated during the simulation. Weather forecast data, including temperature, wind velocity, wind direction, the HV system's operation time, and global horizontal radiation, are compared with real measured data provided by EV building's weather station in Fig. 3-19. The forecasted temperature is close to the actual temperature, especially in the first 6 hours. Wind speed and direction, and global horizontal radiation forecasted by the HRDPS model are in good agreement with the real measured data. Fig. 3-19d shows the HV system's operation hours based on the temperature and humidity of outdoor air. Forecasted weather data well predicts the operation hour. Altogether, the weather forecasting data is in good agreement with the weather station's measured data, especially in the first 6 hours. Therefore, it is essential to update weather forecast data every 6 hours using the new HRDPS result.

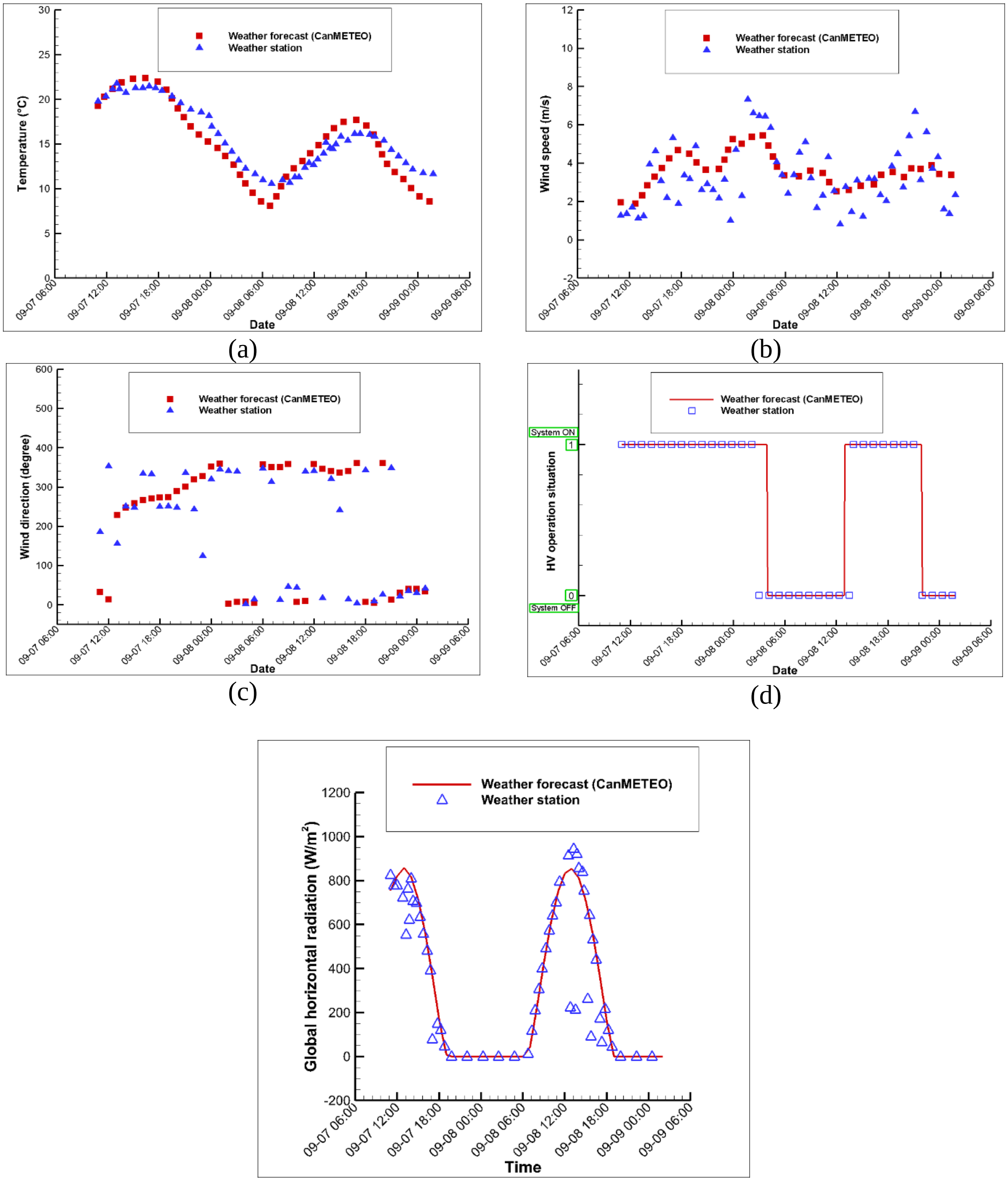

(a) (b)

(c) (d)

Figure 3-19 Comparison of weather forecasting data by HRDPS and real measured weather data by weather station of EV building.

One hour of measured weather and air velocity is used by the dynamic calibration method to calculate the average calibrated C_d. Then, calibrated C_d and one-hour weather forecast data is used to predict the HV system for the next one hour. This procedure is repeated every hour by updating the measured weather and air velocity and using the following one-hour weather forecast data. To investigate the accuracy of the model in predicting the performance of the HV system using weather forecast data, predicted air velocity through inlet dampers and indoor air temperature are compared with the measured data (Figs. 3-20 and 3-21). Results are compared for the first 6 hours of forecasting because weather forecast data are relatively more accurate. Predicted results are in good agreement with the measured data. Results show that combining the dynamic calibration strategy and automatic updating of weather forecasting data can accurately predict the HV system's performance, which can later be used for the system's online predictive control.

Fig. 3-22 shows the total cooling load, free cooling by inlet dampers, and the building's average indoor air temperature predicted by dynamic calibration and weather forecast data. A positive value means that heat is added to the building and a negative value means that heat is removed from the building. Some part of the cooling load is removed by conductive heat transfer from the walls, which is negligible. Free cooling provided by inlet dampers removes the main part of the cooling load. The total predicted cooling load of studied time is 2797.37 kWh, and total free cooling by inlet dampers is 2656.50 kWh, which means that 95% of cooling load is removed by operation of the HV system.

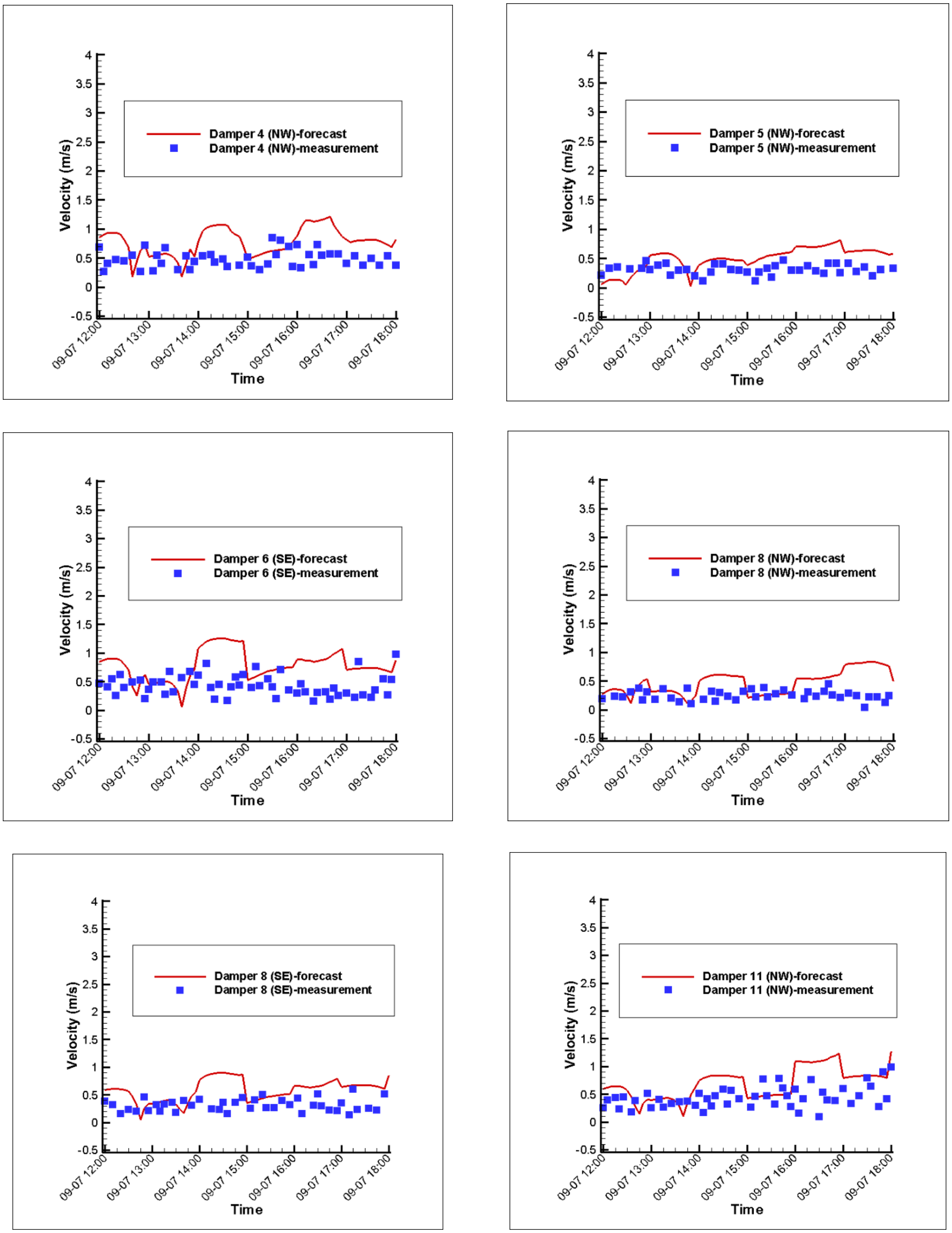

Figure 3-20 Comparison of forecasting and measured air velocity through different dampers (12:00-18:00 September 7th, 2018).

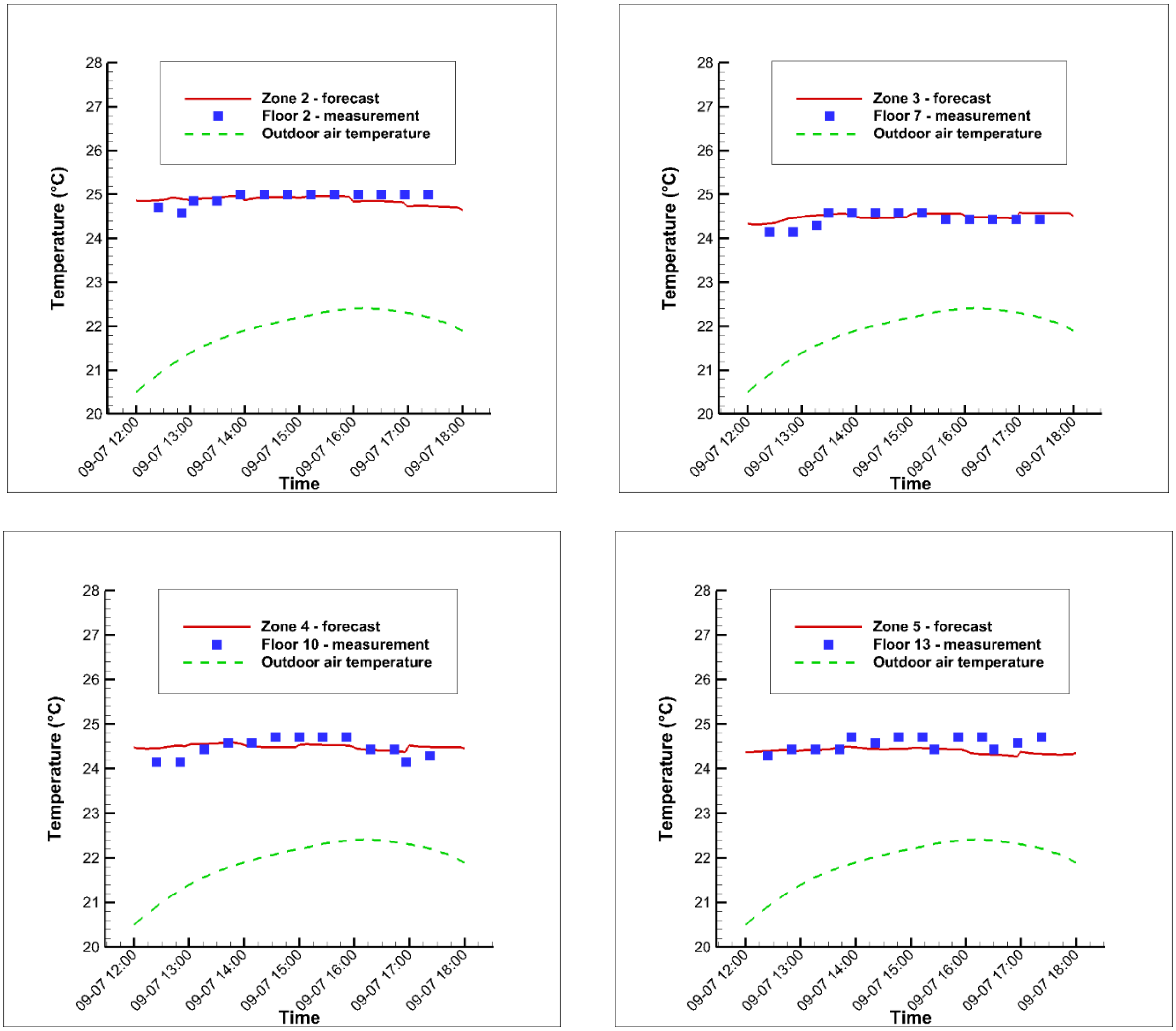

Figure 3-21 Comparison of forecasting and measured indoor air temperature (12:00-18:00 September 7th, 2018).

Note that the calculated cooling load is only for the atrium and corridors. The offices and laboratories are not considered in calculating the cooling load because a mechanical ventilation system is operating in these rooms. The HV system provides thermal comfort and fresh air for the atrium and corridors of the building. Using short-time weather forecast data, the model can predict how much energy saving can be obtained by the HV system and optimize its operation hours, especially in heatwave periods. Night-time cooling can freely remove a large portion of the cooling load and reduce the building's energy consumption.

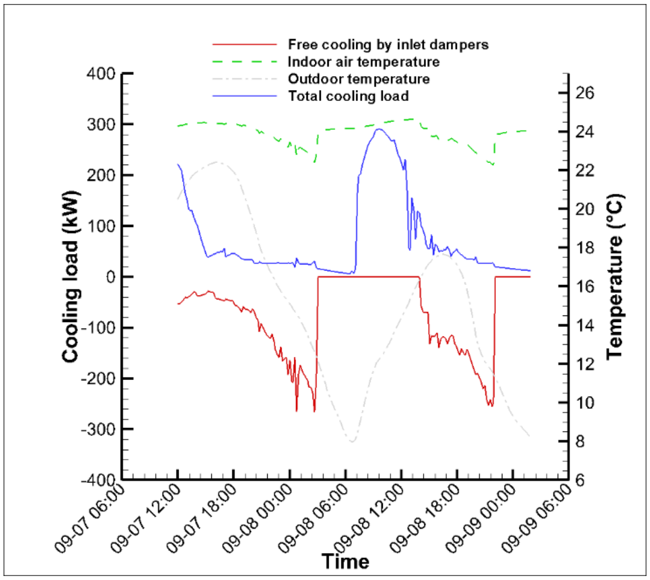

Figure 3-22 Predicted cooling load, free cooling, and indoor air temperature using the dynamic calibration method and weather forecast data (September 7th – September 9th, 2018)

3.4. Summary

This chapter presents a model for the simulation of energy and airflow in buildings. It is based on a coupled thermal/airflow multi-zone network model and can simulate a natural or hybrid ventilation system in a building. The building is divided into several zones with multiple openings, walls, and windows. The model can estimate the internal air temperature, pressure, airflow rate through openings, and temperature distribution inside the walls. Three strategies can be used for coupling airflow and energy balance equations: fully-simultaneous, semi-simultaneous, and segregated schemes. Several test cases are simulated by three coupling strategies. The results and convergence rate of the three approaches are compared. Segregated solver shows the best convergence rate because of its well-conditioned equation systems.

The multi-zone network model is used to predict a fan-assisted hybrid ventilation system's performance in a 17-story institutional building. The hybrid ventilation system is composed of an atrium extended from the 2nd to 16th floor and is divided into five 3-story atria sections. Atria sections are separated by concrete floor slabs and are interconnected by motorized floor grills. There are two motorized inlet dampers at two sides of each floor. A variable-speed fan installed on the roof of the building is used to increase the pressure difference of inlet dampers. When the HV system is operating, cold outside air enters the building through inlet dampers, moves upward through the atria-connecting floor grilles, and exits from the roof exhaust. The thick concrete floor slab absorbs a portion of solar, lighting, and occupants' heat gain during the day. With the HV system, the absorbed heat is removed from thermal mass and starts the following day at a cold temperature. The orifice airflow equation's discharge coefficient for modeling the inlet dampers should be calibrated dynamically using measured data to predict system performance accurately. Therefore, a full-scale measurement is done to provide the required data for the model's calibration and validation. Measured airflow velocity from inlet dampers is used for the dynamic calibration of the model. The results obtained by the calibrated model are compared with the non-calibrated model, which shows a significant improvement in predicted airflow velocity from inlet dampers. Comparing simulated indoor air temperature at different atria sections with measurement data shows that the model is accurate enough for predicting the HV system. At the next step, the calibrated model is integrated with short-time local weather forecast data provided by the HRDPS to perform the short-time forecasting of HV system performance. Results show that the model can achieve reliable forecasting of system performance at the first 6 hours of forecasting because local weather forecast data are close to the real measured data at these times. Detailed analysis on the HV system shows that the system can remove 95% of the atrium and corridors' total cooling load in a typical summer, increasing by optimizing the operation hours, especially at night, because thermal comfort is not very important. The coupled thermal/airflow multizone network model is successfully applied to one building. Study the impact of NV and HV systems at the city scale needs an urban building energy model. In the next chapter, the multi-zone network model is extended to city-scale simulation.

Chapter 4 City-Scale Building Energy Model - CityBEM

In this chapter, the methodology of developing a new UBEM platform, the so-called City Building Energy Model (CityBEM), is described. The automated CityBEM platform is shown in Fig. 4-1. The simulation engine is the modified version of the multi-zone network model introduced in the previous chapter. Three sets of input data are required for the CityBEM simulation: a 3D model of a city, building properties, and weather data. The integration of OSM and GE generates the 3D city model. Building footprint data are provided by the OSM website [75] and/or Microsoft building footprint data [77,78]. The OSM file is then corrected by the building height information obtained from the GE API [82]. The whole process of creating the 3D model is presented with details in section 4.2. Building properties, including age and usage data, are provided by official datasets [146] and joined with the OSM file using the "Join attributes by location" processing algorithm of the QGIS tool [93]. The building age and usage data are then used to create the archetype library to estimate buildings' non-geometrical properties. The methodology of creating the archetype library for the region of study is presented in detail in section 4.3. Weather data, including air temperature, solar radiation, wind speed, and wind direction, are provided by local weather stations or urban microclimate simulation tools.

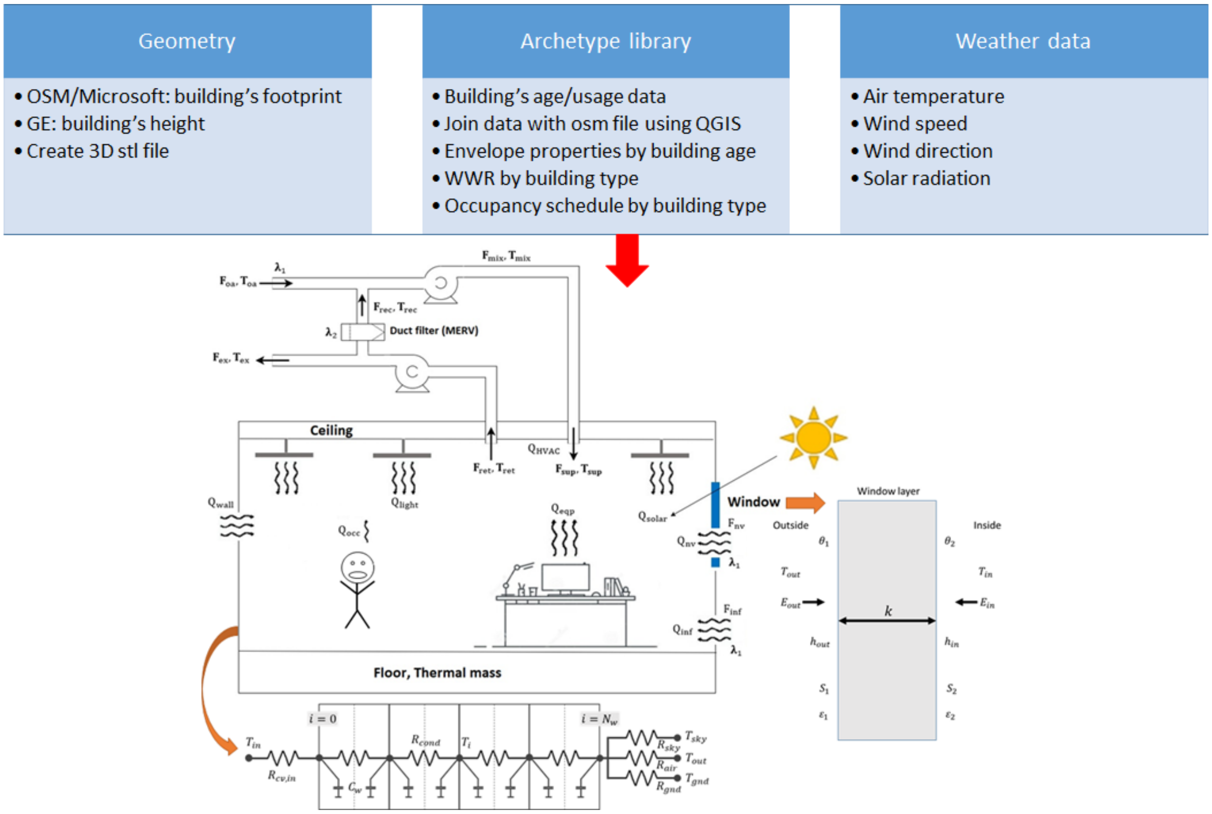

Figure 4-1 Schematic of the CityBEM model.

4.1. CityBEM Methodology

CityBEM is an urban building energy model covering all essential heat and mass transfer mechanisms for the calculations of building heating/cooling loads, energy consumption, and indoor air and building surface temperature. The coupled thermal/airflow multi-zone network model described in the previous chapter is modified, and some simplifications are performed to use it for urban scale simulation. The current version of the CityBEM only includes the energy solver, i.e., the airflow solver is disabled in the current version. The openings' location and size are unknown, and the focus is on the buildings' energy consumption. CityBEM also includes an HVAC model for calculating HVAC energy consumption for cooling and heating of the building.

The model is considerably faster than other simulation engines with acceptable accuracy for urban scale energy analysis. The schematic of the models is shown in Fig. 4-1.

4.1.1. Indoor Air Temperature Calculation

Building's indoor air temperature is calculated by applying the transient heat balance equation to the indoor space modeled as a control volume (Eq. 4-1).

$$\rho V C_p \frac{\Delta T_{in}}{\Delta t} = \sum_{k=1}^{n} A_{w,k} h_{conv,in} (T_{s,k} - T_{in}) + \left(F_{inf} + F_{nv}\right) \cdot \rho \cdot C_{pa} (T_{out} - T_{in}) + Q_{int} + \dot{M}_{sys} \cdot C_{pa} \left(T_{sup} - T_{in}\right) \qquad \text{Eq. 4-1}$$

where the left-hand side of the equation is the rate of change of energy in the building. The first term at the right-hand side is heat transmission through the building's fabric (walls, windows, roof, floor) and thermal mass; the second term is the heat transfer due to air infiltration and Natural Ventilation (NV); the third term is the sensible internal heat gains from occupants, lighting, and equipment; and the last term is the HVAC system heat delivery.

4.1.2. In-wall Temperature

A thermal resistance network model is used and solved to calculate the interior and exterior surface temperature of walls, roof, floor, and thermal mass. Fig. 4-1 shows the thermal resistance network of external walls and roof. A similar model is used for the floor and thermal mass. The only difference is the exterior surface of the floor and thermal mass ($i = N_w$) which is located near the ground and indoor area, respectively. Only convective heat transfer is considered between the exterior surface and the surrounding area. The transient heat balance equation (Eq. 4-2) is solved to calculate the wall's temperature distribution.

$$C_{w,i}\frac{\Delta T_{w,i}}{\Delta t} = A_w\frac{T_{w,i-1} - T_{w,i}}{R_{w,i-1}} + A_w\frac{T_{w,i+1} - T_{w,i}}{R_{w,i+1}} + S_{w,i} \quad \text{(Eq. 4-2)}$$

$$C_{w,i} = \rho_w A_w \Delta x_i C_{pw} \quad \text{(Eq. 4-3)}$$

where ρ_w, A_w, C_{pw} are density (kg/m^3), area (m^2), and specific heat (J/kgK) of the wall; Δx_i is the thickness of layer i; $T_{w,i}$ is the temperature of node i inside the wall (K); $R_{w,i-1}$ is the thermal resistance of node i (Km^2/W); and $S_{w,i}$ is other heat sources inside layer i (W). The Crank-Nicolson method [144] is used to discretize Eq. 4-2. The Crank-Nicolson scheme is the average of the explicit scheme at (i, t) and implicit scheme at (i, t+1). It is second-order, implicit in time, and unconditionally stable.

$$\begin{aligned} C_{w,i}\frac{T_{w,i}^{t+1} - T_{w,i}^{t}}{\Delta t} \\ &= \frac{1}{2}\left(A_w\frac{T_{w,i-1}^{t+1} - T_{w,i}^{t+1}}{R_{w,i-1}} + A_w\frac{T_{w,i+1}^{t+1} - T_{w,i}^{t+1}}{R_{w,i+1}}\right) \quad \text{(Eq. 4-4)} \\ &+ \frac{1}{2}\left(A_w\frac{T_{w,i-1}^{t} - T_{w,i}^{t}}{R_{w,i-1}} + A_w\frac{T_{w,i+1}^{t} - T_{w,i}^{t}}{R_{w,i+1}}\right) + S_{w,i} \end{aligned}$$

Rewriting Eq. 4-4 gives a tridiagonal system of equations

$$\begin{bmatrix} b_1 & c_1 & & & \\ a_2 & b_2 & c_2 & & \\ & a_3 & b_3 & \ddots & \\ & & \ddots & \ddots & c_{N-1} \\ & & & a_N & b_N \end{bmatrix} \begin{bmatrix} T_{w,1}^{t+1} \\ T_{w,2}^{t+1} \\ T_{w,3}^{t+1} \\ \vdots \\ T_{w,N}^{t+1} \end{bmatrix} = \begin{bmatrix} d_1^{t+1} \\ d_2^{t+1} \\ d_3^{t+1} \\ \vdots \\ d_N^{t+1} \end{bmatrix} \quad \text{(Eq. 4-5)}$$

Coefficients a_i, b_i, c_i, d_i are calculated using Eq. 4-6 for all nodes inside the wall.

$$2 \le i \le N-1\colon \begin{cases} a_i = \dfrac{-r_i A_w}{2R_{cond}} \\ b_i = 1 + \dfrac{r_i A_w}{2R_{comd}} + \dfrac{r_i A_w}{2R_{cond}} \\ c_i = \dfrac{-r_i A_w}{2R_{cond}} \\ d_i = \left(1 - \dfrac{r_i A_w}{2R_{cond}} - \dfrac{r_i A_w}{2R_{cond}}\right) T_i^t + \left(\dfrac{r_i A_w}{2R_{cond}}\right) T_{i-1}^t \\ \qquad + \left(\dfrac{r_i A_w}{2R_{cond}}\right) T_{i+1}^t \end{cases}$$

$$i = 1\colon \begin{cases} a_i = 0 \\ b_i = 1 + \dfrac{r_i A_w}{2R_{conv,in}} + \dfrac{r_i A_w}{2R_{cond}} \\ c_i = \dfrac{-r_i A_w}{2R_{cond}} \\ d_i = \left(1 - \dfrac{r_i A_w}{2R_{conv,in}} - \dfrac{r_i A_w}{2R_{cond}}\right) T_i^t + \dfrac{r_i A_w}{2R_{conv,in}} \left(T_{in}^{t+1} + T_{in}^t\right) \\ \qquad + \left(\dfrac{r_i A_w}{2R_{cond}}\right) T_{i+1}^t \end{cases} \tag{Eq. 4-6}$$

$$i = N\colon \begin{cases} a_i = \dfrac{-r_i A_w}{2R_{cond}} \\ b_i = 1 + \dfrac{r_i A_w}{2R_{cond}} + \dfrac{r_i A_w}{2R_{air}} + \dfrac{r_i A_w}{2R_{sky}} + \dfrac{r_i A_w}{2R_{gnd}} \\ c_i = 0 \\ d_i = \left(1 - \dfrac{r_i A_w}{2R_{cond}} - \dfrac{r_i A_w}{2R_{air}} - \dfrac{r_i A_w}{2R_{sky}} - \dfrac{r_i A_w}{2R_{gnd}}\right) T_i^t + \left(\dfrac{r_i A_w}{2R_{cond}}\right) T_{i-1}^t \\ \qquad + \dfrac{r_i A_w}{2R_{air}} \left(T_{air}^{t+1} + T_{air}^t\right) + \dfrac{r_i A_w}{2R_{sky}} \left(T_{sky}^{t+1} + T_{sky}^t\right) \\ \qquad + \dfrac{r_i A_w}{2R_{gnd}} \left(T_{gnd}^{t+1} + T_{gnd}^t\right) + r_i \alpha_w I_{glo,w} \end{cases}$$

Where $R_{cond} = R_t/(N+1)$ is the thermal resistance between nodes; R_t is the total thermal resistance of the wall; and $r_i = \Delta t / C_{w,i}$. R_{air}, R_{sky}, and R_{gnd} are thermal resistances between the exterior node of the wall and outdoor air, sky, and ground, respectively, calculated by Eqs. 4-7 to 4-9.

$$R_{air} = 1/\left(h_{conv,ext} + h_{r,air}\right), \qquad h_{r,air} = \frac{\varepsilon\sigma F_{sky}(1-\beta)(T_{air}^4 - T_s^4)}{T_{air} - T_s} \tag{Eq. 4-7}$$

$$R_{sky} = 1/h_{r,sky}, \qquad h_{r,sky} = \frac{\varepsilon\sigma F_{sky}\beta\left(T_{sky}^4 - T_s^4\right)}{T_{sky} - T_s} \tag{Eq. 4-8}$$

$$R_{gnd} = 1/h_{r,gnd}, \qquad h_{r,gnd} = \frac{\varepsilon\sigma F_{gnd}\left(T_{gnd}^4 - T_s^4\right)}{T_{gnd} - T_s} \tag{Eq. 4-9}$$

where $F_{sky} = 0.5\left(1 + \cos\theta_p\right)$; $F_{grd} = 0.5\left(1 - \cos\theta_p\right)$; $\beta = \sqrt{0.5\left(1 + \cos\theta_p\right)}$; θ_p is the zenith angle of the wall; $h_{conv,ext}$ is the exterior convective heat transfer coefficient (W/m^2K); T_{air}, T_s, T_{sky}, and T_{gnd} are outdoor air, exterior wall surface, sky, and ground temperature, respectively (K). The Tridiagonal Matrix Algorithm (TDMA), also known as the Thomas Algorithm [137], which is a form of Gauss elimination, is used for solving the tridiagonal system of Eq. 4-5. The solution is obtained in $O(n)$ operations, instead of $O(n^3/3)$ required by the Gaussian elimination.

4.1.3. Exterior Convective Heat Transfer Coefficient

The exterior convective heat transfer coefficient between outdoor air and the external surface of walls and roof is calculated using the EnergyPlus DOE-2 model [38].

$$h_{conv,ext} = h_n + R_f\left(h_{c,glass} - h_n\right) \tag{Eq. 4-10}$$

where $h_{c,glass}$ is the convection coefficient for very smooth surfaces (e.g., glass) and is calculated as $h_{c,glass} = \sqrt{h_n^2 + [aV_z^b]^2}$. V_z is the local wind speed; h_n is the natural convective heat transfer coefficient, and a and b are constants in Table 4-1. The detailed natural convection model presented by Walton [147] is used for the calculation of h_n. This model correlates the convective heat transfer coefficient to the surface orientation and the difference between the surface and zone air temperatures. The same model is used for the calculation of the interior convective heat transfer coefficient.

$$\begin{cases} h_n = \dfrac{9.482|\Delta T|^{\frac{1}{3}}}{7.283 - |cos\Phi|}, & \text{heat flow up} \\ h_n = \dfrac{1.810|\Delta T|^{\frac{1}{3}}}{1.382 + |cos\Phi|}, & \text{heat flow down} \end{cases} \quad \text{(Eq. 4-11)}$$

where ΔT = Tair - Tsurface, and Φ is the surface tilt angle.

Table 4-1 Constants of the DOE-2 model

Wind direction	$a\ [W/m^2K(m/s)^b]$	b
Windward	3.26	0.89
Leeward	3.55	0.617

4.1.4. Window Heat Balance Equation

Window properties, including solar absorptance, reflectance, and transmittance, are needed to calculate window surface temperature. Only two window properties, U-value and SHGC, are known from the archetype library. A simple window model that converts a window into an equivalent single-layer window is used in this work for the estimation of unknown window properties [148]. This method is appropriate for urban scale simulation because window properties are unknown, and single-layer calculation is faster than multi-layer calculations. For solar optical calculations, at the first step, the model calculates the solar transmittance at normal incidence based on some correlations that are functions of SHGC and U-value. Then, properties at non-normal incidence angles are calculated using new correlations selected based on SHGC and U-value values. More details on the simple window model may be found from the reference [148]. After calculating window properties, window face temperature is calculated by solving each face's heat balance equations and every time step. Heat storage in the window is neglected because the glass layer is thin enough. Therefore, the heat capacity term is removed from the equation. Fig. 4-1 shows the simple window model and variables used for solving the heat balance equation.

$$E_{out}\varepsilon_1 - h_{r,1}\theta_1 + k(\theta_2 - \theta_1) + h_{conv,\mathrm{ext}}(T_{out} - \theta_1) + S_1 = 0 \qquad \text{(Eq. 4-12)}$$

$$E_{in}\varepsilon_2 - h_{r,2}\theta_2 + k(\theta_1 - \theta_2) + h_{conv,in}(T_{in} - \theta_2) + S_2 = 0 \qquad \text{(Eq. 4-13)}$$

where S_i is the short-wave radiation on the i^{th} face. It is assumed that short-wave radiation is split equally between the two faces of a layer, i.e. $S_1 = S_2 = \frac{1}{2}\alpha_{win}I_{glo,win}$. E_{out} and E_{in} are exterior and interior long-wave radiation incident on the window, and $h_{r,i} = \varepsilon_i\sigma\theta_i^3$

Eqs. 4-12 and 4-13 are two by two linear systems of equations and are solved using the LU decomposition method [149]. Surface convective and radiative coefficients $(h_{r,i}, h_{conv,in})$ are functions of surface temperature, therefore Eqs. 4-12 and 4-13 are solved in an iteration manner, and at each iteration, coefficients are updated based on new calculated surface temperatures. Iteration continues until the convergence of the solution.

4.1.5. HVAC System Design

The HVAC system modeled by CityBEM is a Constant Air Volume (CAV) system designed for both heating and cooling. The schematic of the system is shown in Fig.4-1. The mass flow rate of the system $\dot{M}_{sys}$ required for the whole building is determined based on the designed sensible cooling and heating loads. Existing air-conditioned buildings show that fan power consumption accounts for up to half of the total energy consumption by HVAC systems [150]. Therefore, systems are typically designed at the lowest flow rates to reduce energy consumption. For calculation of $\dot{M}_{sys}$, the design sensible cooling and heating loads are calculated using Eq. 4-14.

$$Q_s = \sum_{k=1}^{n} \frac{(T_{out,des} - T_{in,set})}{R_w} + \rho C_{pa}(F_{inf} + F_{nv})(T_{out,des} - T_{in,set}) + Q_{int} + SHG \quad \text{Eq. 4-14}$$

where $T_{in,set}$ is the set-point indoor air temperature, and $T_{out,des}$ is the outdoor air design temperature. Table 4-2 shows the heating and cooling set-point temperatures used for winter and summer days. Different set-point temperatures are used for occupied and unoccupied hours. Outdoor air conditions used for air conditioning systems' design are selected based on the frequency of outdoor air conditions. To determine the outdoor design condition, a target of a total accumulated percentile of annual hours is set, and individual frequencies of the dry bulb temperature are summed from the extreme situation until the target is reached. In this work, 0.4% and 99.6% percentiles are used for cooling and heating outdoor design temperatures, respectively. Summer and winter outdoor design temperatures for an air conditioning system for a building in Montreal are $30\ ℃$ and $-23.1\ ℃$, respectively [139]. These values are calculated based on the hourly weather data of MONTREAL TRUDEAU INTL weather station [151].

Table 4-2 Heating and cooling set-point temperatures used for winter and summer days

Season	Indoor air set-point temperature (℃)	
	Occupied hours	Unoccupied hours
Winter (heating)	21	19
Summer (cooling)	24	26

After calculating the design sensible cooling and heating loads $Q_{s,c}$ and $Q_{s,h}$, the required airflow rate of the HVAC system to offset the $Q_{s,c}$ is calculated using Eq. 4-15.

$$\dot{M}_{sys} = \frac{Q_{s,c}}{C_{pa}(T_{sup} - T_{in,set})} \qquad \text{Eq. 4-15}$$

where T_{sup} is the design supply air temperature and is equal to 12.8 ℃. For winter heating, the AC system becomes an air heating system, and the maximum supply air temperature is calculated using $\dot{M}_{sys}$ and $Q_{s,h}$ (Eq. 4-16).

$$T_{sup,max} = \frac{Q_{s,h}}{C_{pa}\dot{M}_{sys}} + T_{in,set} \qquad \text{Eq. 4-16}$$

If the maximum calculated supply air temperature is too high for satisfactory room air diffusion (> 50 ℃), the $\dot{M}_{sys}$ is calculated based on the $Q_{s,h}$ and supply air temperature of 50 ℃ (Eq. 4-17).

$$\dot{M}_{sys} = \frac{Q_{s,h}}{C_{pa}(50 - T_{in,set})} \qquad \text{Eq. 4-17}$$

Outdoor air for ventilation purposes is supplied to the occupied space via the ductwork system. If the required ventilation rate F_{oa}, is less than the air mass flow rate of the HVAC system $\dot{M}_{sys}$, then the difference between them is recirculated within the system and is mixed with outdoor air. But if F_{oa} is larger than $\dot{M}_{sys}$, then all the air supplied to the occupied space is drawn from the outdoor space, and there is no recirculation of returned indoor air. All returned indoor air is exhausted to the outdoor space.

4.1.6. Supply Air Condition and HVAC Energy Consumption

Mixing ratio X_{mix}, recirculated air flow rate F_{rec}, and mixing air temperature are calculated using Eqs. 4-18 to 4-20. The building's heating/cooling load is estimated, considering the actual indoor air temperature (Eq. 4-21). Finally, the supply air temperature is calculated based on the heating/cooling load and mixing and indoor air temperatures (Eq. 4-22).

$$X_{mix} = \frac{\rho_{oa} F_{oa}}{\dot{M}_{sys}} \quad \text{Eq. 4-18}$$

$$F_{rec} = \frac{(1 - X_{mix})\dot{M}_{sys}}{\rho_{in}} \quad \text{Eq. 4-19}$$

$$T_{mix} = X_{mix} T_{oa} + (1 - X_{mix}) T_{in} \quad \text{Eq. 4-20}$$

$$Q_t = \sum_{k=1}^{n} A_{w,k} h_{conv,in} (T_{s,k} - T_{in}) + \left(F_{inf} + F_{nv} + F_{oa}\right) \cdot \rho \cdot C_{pa} (T_{out} - T_{in}) + Q_{int} \quad \text{Eq. 4-21}$$

$$T_{sup} = T_{mix} - \frac{Q_t}{\dot{M}_{sys} C_p} \quad \text{Eq. 4-22}$$

Energy consumed by the HVAC system for the heating/cooling of the space is calculated from the heating/cooling demand of the building Q_t divided by the efficiency of the heating/cooling system (Eq. 4-23).

$$\begin{cases} Q_{hvac,heat} = \dfrac{Q_t}{\eta_{heat}} \\ Q_{hvac,cool} = \dfrac{Q_t}{COP_{cool}} \end{cases} \quad \text{Eq. 4-23}$$

where η_{heat} is the heating system efficiency and COP_{cool} is the system coefficient of performance.

4.1.7. Fan Energy Consumption

Fans electricity consumption is the dominant source of the HVAC electrical energy end-use [152]. Fan electricity use depends on flow rate, operating hours, flow resistance, and fan system efficiency. Specific fan power (SFP) is a useful measure of these factors. SFP is defined as the ratio between the electrical input power and the air circulated through the fan. SFP can also be expressed as a function of the fan pressure rise (total pressure loss in the system including ductwork, AHU, and air transport inside the building) and the fan's efficiency (Eq. 4-24). Fan power consumption is calculated using Eq. 4-25.

$$SFP = \frac{\Delta p_{tot}}{\eta_{tot}} \quad \text{Eq. 4-24}$$

$$Q_{fan} = \frac{SFP.\dot{M}_{sys}}{\rho_a} \quad \text{Eq. 4-25}$$

A typical SFP for single-family houses that is around 2.7 $kW/(m^3/s)$ at normal conditions [153] is used in this work for all buildings.

4.2. 3D City Model Generation

A 3D city model includes building topology, footprint information, façade area, height, and floor numbers. The building topology and footprint data are provided from OSM and/or Microsoft open data sets, and building height information is from GE. Building footprint data from other datasets and formats such as GEOJSON [154] can be converted to the OSM format. Microsoft [77,78] provides USA and Canada building footprint data with more buildings data than the OSM website. The OSM represents buildings at various levels of details (LOD) (Fig. 4-2). LOD1 models buildings with a flat roof and an average height, and LOD2 and LOD3 cover roof details. In this work, for generalization, all buildings are modeled in LOD1 for each building's average height.

The proposed method, however, can be applied to LOD2 and LOD3, if more data points are specified for each roof so the roof details can be obtained from GE.

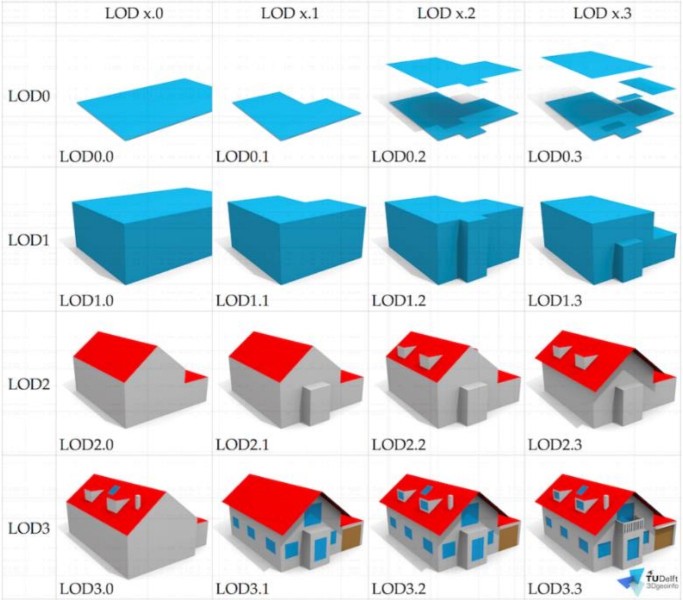

Figure 4-2 Level of building details in OSM [155].

Fig. 4-3 illustrates the steps to create the 3D city model. First, the OSM model of a selected city region is defined and extracted from the OSM website or Microsoft dataset. Then, the coordinates of several points on the building footprint are calculated, and the heights of these points are identified by using the GE API. The average height is calculated for each building and is then modified in the OSM file. Finally, the OSM file is converted to the 3D model in the STL format [92] for the CityFFD-CityBEM simulation (Fig. 4-3a). An STL file is a triangular representation of 3-D surface geometries. Each surface is broken down into a series of small triangles (facets). Each facet is identified by a unit normal and three vertices (corners). An STL file only contains a 3D object's surface geometries without model attributes, and the generated file is significantly smaller than other file formats. To illustrate the above procedure, we applied these steps to create the 3D model of an urban area with 12 buildings in Montreal, Canada (Figs. 4-3b to 4-3d).

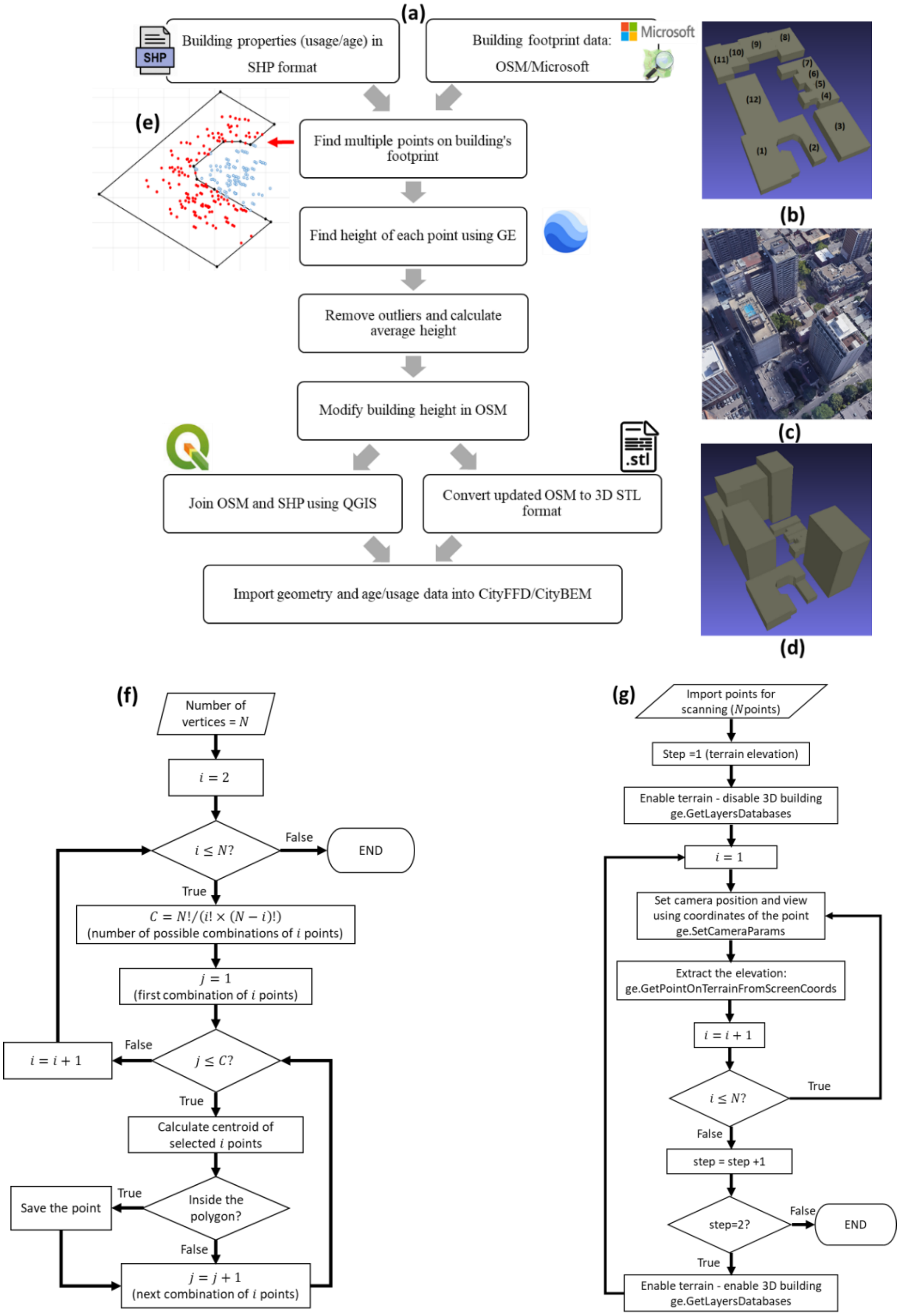

Figure 4-3 a) Flowchart of creating a 3D building model, b) initial OSM model of an urban area in Montreal, c) Urban image in GE, d) modified OSM model, e) points inside and outside of a building's footprint, f) flowchart of finding points inside the building's polygon, g) flowchart of scanning the points using GE API.

Step 1 – Define and extract the OSM file of the desired area from the OSM website or convert Microsoft GeoJSON to OSM (Fig. 4-3b).

Step 2 – Extract coordinates (latitudes and longitudes) of the points on each building footprint.

First, to calculate the average height of a building using the GE API, it is required to find several scattering points inside the building footprint. In most cases, the coordinates of buildings' polygons in GE and OSM/Microsoft are slightly different because they use different methods for finding buildings' footprints. An internal point near the edge of the polygon in OSM/Microsoft may be located outside GE's building footprint. Therefore, the GE API may find the elevation of the ground instead of the actual building. By finding enough points inside the polygon, the possible exterior points are detected as outliers and are removed from the group of points using the method explained later in step 4. The GE API extracts a point's elevation using the latitude and longitude of the point. The OSM building footprint is represented as a polygon with its vertices identified only by coordinates (latitudes and longitudes). Therefore, to find several points scattered on the building footprint, a new method is developed and implemented in this work. The flowchart of the process is shown in Fig. 4-3f.

- First, we find a group of possible points that may be located inside the polygon.
- We then try all combinations of the building's vertices to calculate the centroid of selected points to identify the point possibly inside the building. We start with combinations of two points out of N building's vertices and continue it for all combinations of 3, 4 ⋯ N points.
- After finding a possible point, the Winding Number (WN) method [156] (See Appendix C) is used to determine if the point is inside the closed polygon. It does this by computing how many times the polygon winds around the point. A point is outside only when the polygon does not

wind around the point and when the winding number is zero. Details of the WN method are explained in Appendix C. If the examined point is inside the polygon, the coordinates of this point are saved for scanning using GE API.

- If all combinations of the building's vertices are examined, or it reaches the maximum required number of points inside the building, e.g., 150 points in this study, the loop is stopped. Otherwise, it goes to the next combination of points.
- Fig. 4-3e shows the points inside and outside the polygon of building 1 in Fig. 4-3b. The black points are the building vertices, blue points are identified outside of the building polygon, and the red points are calculated inside the polygon. The points are scattered around the building's footprint, resulting in an accurate estimation of the building's average height. Many of the points are far from the polygon's edges and are randomly distributed around the footprint.

Step 3 – Find the point's height by GE API (Fig. 4-3g)

The coordinates (latitudes and longitudes) of all points extracted from the previous step are imported into the GE API to calculate all points' heights. The GE API consists of some useful classes to scan a point on the screen according to its position (latitude and longitude) and extract its elevation. The steps for calculating the height of the points are as follows, which is also shown in Fig. 4-3g:

- Read the coordinate of the points generated from Step 2
- The camera's position and view on the GE screen are changed using the coordinate of each point by the GE API function "ge.SetCameraParams." This step is necessary to reposition the camera, so the viewport is right above the point to be scanned to avoid the tilted view and, thus,

inaccurate height. In other words, to get the actual height of a point, one must measure (view) directly on the top of that point.

- After the camera is positioned correctly, the current point's elevation is extracted using the "ge.GetPointOnTerrainFromScreenCoords" function. This function provides the elevation of the point on the GE screen relative to the sea level, which is different from the actual height of the point above the local ground. The exact height is the difference between the local terrain's elevations and the roof point obtained by the next two steps.
- To get the local terrain height, GE consists of different layers such as roads, 3D buildings, oceans, and terrains, which can be enabled or disabled separately. The 3D buildings are disabled, and the terrain layers are only enabled. By extracting the elevation by "ge.GetPointOnTerrainFromScreenCoords", we can get the terrain height.
- To get the 3D building layer elevation, we turn on both the terrain and 3D building layers and extract the elevation by the "ge.GetPointOnTerrainFromScreenCoords" function.
- Finally, the height of each point is calculated by subtracting the terrain elevation from the building elevation.
- The camera setting and elevation extractions' procedure is repeated for each point by a whole GE screen scanning process.

Step 4 – Find and remove each building's outliers and calculate the building's average height based on all the points inside the building footprint.

As previously mentioned, some points generated on a building's footprint may be relatively close to building edges. The calculated height may be on the terrain because of the small difference in the latitude and longitude between OSM and GE. These outliers must be removed. Here, the InterQuartile Range (IQR) rule [157] is used to determine and remove outliers. IQR is the difference between the first and third quartiles. The first quartile denoted Q_1, is the value in the data set that holds 25% if the values below it. The third quartile denoted Q_3, is the value in the data set that holds 25% of the values above it. The IQR is defined as $IQR = Q_3 - Q_1$. The outliers are defined as those below $Q_1 - 1.5 \times IQR$ or above $Q_3 + 1.5 \times IQR$. By removing the outliers from data set, the procedure is repeated for all points until there is no outliers.

For the demonstration, the above method was applied to the selected urban area in Fig. 4-3c, and the average heights of all buildings are calculated. For validation, the building elevation and the number of floors were compared to other available datasets in Table 4-3. Building elevation data is obtained from the Montreal Numerical Surface Model (NSM), which reproduces the shape of the Earth's surface by including all the permanent and visible elements of the landscape provided by the City of Montreal [158]. The number of floors of buildings is calculated by counting the floors in Google Street View (GSV) [159]. Assuming that one-floor height is 3 m (a typical value for ceiling height), the average building height calculated by the proposed method is converted to the number of floors and is compared with the GSV data. The results from the proposed method are in good agreement with the NSM and GSV data. The average percentage of elevation difference between the current method and NSM data is 3.1%. The difference is because the building elevation data from the present method is the average value, whereas the NSM data is manually extracted for one point on each building. The number of floors calculated by the current approach is close to the GSV data, and the maximum floor number difference is one.

Table 4-3 Validation of calculated buildings' elevation and the number of floors

Building number	Building elevation (m)		Elevation difference (%)	Number of floors	
	Current	Numerical Surface Model (NSM)		Current	Google Street View (GSV)
1	65.09	67.14	3.1	5	6
2	58.21	60.48	3.9	3	4
3	106.9	108.19	1.2	22	22
4	60.38	63.169	4.6	3	4
5	56.47	58.97	4.4	2	3
6	56.72	58.99	4.0	2	3
7	58.91	61.85	4.5	3	4
8	106.6	109.68	2.9	22	21
9	99.73	101.15	1.4	19	19
10	101.87	101.03	0.8	20	19
11	85.22	83.21	2.3	13	13
12	99.15	103.24	4.1	18	18

Step 5 – Modify the OSM file and generate the 3D city model in STL format

In the final step, the OSM file is modified by adding the buildings' calculated average height (Fig. 4-3d). The modified OSM file is converted to the 3D STL format for the urban microclimate and building energy modeling. The STL file contains each façade of the building defined by multiple triangles, and CityBEM and CityFFD calculate one average value of air/building properties for each triangle during the coupling process. More information about the triangles and data exchange is presented in Chapter 5. CityGML [160] is another format to store the digital 3D model of cities and has been used as one of the standard input data formats. The current 3D city format can be converted later to CityGML for other simulation models when necessary.

4.3. Archetype Library of Buildings Properties

Calculation of building thermal and energy performance by CityBEM needs buildings’ thermal properties, occupancy schedules for internal load calculations, and Window-Wall-Ratio (WWR) for solar heat gains. An archetype library was developed and implemented here based on the building year of construction and usage type. Then, the required parameters are assigned to each group of buildings. Nineteen reference building types, including single-family houses, Multi-Unit Residential Building (MURB), and seventeen commercial buildings, are used to estimate WWR. An average WWR is assigned to each building type following the recommendations of the U.S. Department of Energy [161], ASHRAE Standard 90.1 [162], and Quebec and Ontario building construction codes [163,164]. For the estimation of building envelope properties, buildings were classified based on the year of construction. There was no common typology existing for the Quebec building stock. Therefore, the most useful data from different sources were collected and combined [162–164]. Ten construction periods were considered for this purpose, and data were averaged for each period (Table 4-4). The building stock was divided into ten building types to estimate the internal load of buildings. The operation hours, average loads by occupants, appliances, lighting, and the average usage rate are the parameters defined for each group and used to estimate the transient internal load of buildings [165] (Table 4-5).

Table 4-4 Archetype segmentation by year of construction for the estimation of building envelope characteristics.

U-value (W/m^2K)	1958	1964	1974	1981	1990	1995	2002	2006	2010	2013
Roof	1.42	1.42	0.6	0.35	0.25	0.25	0.25	0.25	0.25	0.18
Wall	1.7	1.7	1.0	0.6	0.45	0.45	0.35	0.35	0.35	0.26
Floor	0.45	0.45	0.45	0.45	0.45	0.45	0.25	0.25	0.25	0.25
Window	5.7	5.7	5.7	5.7	5.7	3.3	2.7	2.2	2.2	1.6
SHGC	0.8	0.8	0.76	0.76	0.76	0.68	0.56	0.36	0.33	0.31

Building age and usage data for classification can be obtained from the official datasets. For example, the Montreal City data were provided by the property assessment units (PAU) [146].

PAU is the vector geospatial data of the subdivision of the Montreal agglomeration properties containing the general information on the units of property assessments, particularly the codification of use (CUBF), year of construction, and the approximate dimensions. The indexes of buildings in PAU shapefile and OSM file are different. The QGIS software [93], a free GIS tool, is then used to join the PAU and OSM files for assigning age and usage data to the OSM buildings. This step is done by a function named "join attribute by location," which finds the same building in two different files using the location information and joins them.

Table 4-5 Archetype segmentation for the estimation of operation hours and average loads.

Building type	Operation hours		Occupancy		Appliances		Lighting	
	Time	Day	Usage rate	Load W/m^2	Usage rate	Load W/m^2	Usage rate	Load W/m^2
Detached house	00:00-0:00	7	0.60	2.8	0.60	2.4	0.10	8.0
Apartment building	00:00-0:00	7	0.60	4.2	0.60	3.0	0.10	8.0
Office building	07:00-18:00	5	0.55	4.0	0.55	7.0	0.55	7.0
Department store	08:00-21:00	7	0.60	9.3	1.00	1.0	0.58	20.0
Hotel	00:00-00:00	7	0.58	5.6	0.37	1.0	0.41	8.0
Restaurant	06:00-00:00	7	0.46	19.7	0.20	4.0	0.64	20.0
Sport, terminal, theatre	08:00-22:00	7	0.60	9.3	0.00	0.0	1.00	14.0
School	08:00-17:00	5	0.50	21.3	0.50	8.0	0.50	15.0
Daycare center	07:00-19:00	5	0.40	15.5	0.40	4.0	0.40	15.0
Hospital	00:00-00:00	7	0.54	10.8	0.62	4.0	0.62	9.0

4.4. Summary

In this chapter, the methodology of the CityBEM is presented. CityBEM is a physics-based UBEM platform designed to calculate energy consumption, indoor air temperature, and all buildings' surface temperature in large urban areas. Generating the 3D model of buildings and creating an archetype library are two main challenges with current urban simulation tools. In this study, an automated platform is developed to cover all these three challenges. For creating the 3D model of buildings, a new method is developed by the integration of freely available data sets (OpenStreetMap and Microsoft footprints) and a commercial tool (GoogleEarth). OSM and Microsoft provide building footprints, whereas GE provides the height of the building. The integration of these datasets results in creating an accurate 3D model of buildings. The accuracy of the developed method is studied by modeling an urban area in Montreal. An archetype library that provides buildings' non-geometrical parameters is an essential step for improving the city-scale building energy simulation accuracy. In this study, a comprehensive archetype library is developed by gathering data from different sources and assigning them to buildings based on their usage type and age. Usage type and age of buildings are provided by official datasets and are joined with the 3D model using the QGIS tool.

Chapter 5 Integration of CityBEM and Urban Microclimate Models

In this chapter, CityBEM is integrated with City Fast Fluid Dynamic (CityFFD) model to capture the two-way interaction between buildings and microclimate. The integrated platform is then used to simulate two historical extreme weather events: cold-wave and heatwave. The developed platform of automated 3D buildings' model, estimation of the buildings' non-geometrical properties, dynamic simulation of buildings' energy performance, and the two-way interaction of buildings and microclimate, is applied for modeling two urban areas in Montreal.

5.1. Integration of CityBEM and CityFFD

Most of these existing UBEM platforms use weather data from one or several nearby weather stations for the energy analysis of all buildings. Therefore, they have not considered the impacts of localized microclimate environment. The airflow velocity and temperature around buildings are affected by building configurations, heights, and neighboring building locations. Different wind velocity and temperature around buildings directly impact buildings' thermal load regarding local convective heat transfer coefficients and rates and air infiltration through envelopes [11]. To better predict an individual building's energy use, it is essential to consider the impact of local microclimate and aerodynamics conditions and neighborhood on the building's energy consumptions [54,57]. In this section, for capturing the two-way interaction between buildings and microclimate, CityBEM is integrated with the CityFFD microclimate simulation tool. The CityFFD model is based on a 3D fast fluid dynamics (FFD) solver [94] to predict local microclimate and neighborhoods. Compared to the conventional CFD model, the FFD solver is a high-order semi-Lagrangian-based model. It is unconditionally stable, fast, and accurate to simulate urban aerodynamics [94]. The high-order forward-backward sweeping interpolation of the solver can provide accurate results even on the coarse computational domain, so it is suitable for large-scale modeling problems such as a city [166]. The model is written in the NVIDIA CUDA [167] for GPU computing to achieve superior performance on a personal computer. The CityFFD model provides local aerodynamics conditions around each building, including average temperatures, average wind velocities, and local exterior surface convective heat transfer coefficient around each building's external surfaces. The average value is calculated using all mesh cells on each building's surface (See Fig. 5-1).

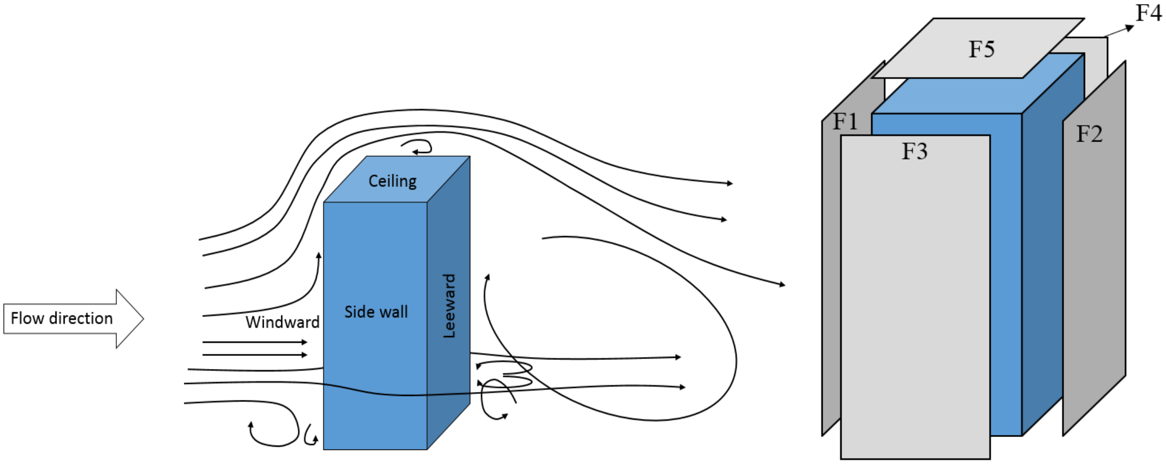

Figure 5-1 CityFFD data provided for the CityBEM model.

The local outdoor temperature is used in Eqs. 4-1 to 4-14 for the calculation of the building's thermal load. Local wind velocity is used to analyze the exterior convective heat transfer coefficient in Eq. 4-10. The building surface temperatures calculated by CityBEM are used as boundary conditions by CityFFD for the next time step simulation. Using the ping-pong method in transferring data between CityBEM and CityFFD, it is crucial to start the simulation with an accurate initial condition. For this purpose, at the first time-step, the data is transferred between CityFFD and CityBEM in an inner loop until the convergence and converged buildings surface temperature is used as the initial data for CityFFD simulation. Fig. 5-2 shows the flow diagram of parameter initialization and transient simulation.

5.2. Case Study 1: Summer Heatwave

In this section, the presented method is demonstrated for the dynamic simulation of an urban area in downtown Montreal, Canada (Fig. 5-3). The size of the urban area is $550\ m \times 600\ m$ with 255 buildings. This area is chosen because of the diversity in building types, year of construction, and heights. The dynamic CityBEM-CityFFD simulation was conducted for 15 days of the summer of 2019 (06/24/2019-07/08/2019). The 3D model is generated using the integrated OSM-GE model. Fig. 5-3 shows the initial OSM model, modified OSM model, the aerial view map provided by GoogleEarth as a comparison, and weather station data installed on the roof of EV building used for the validation of the result. The initial OSM heights of the buildings are inaccurate (Fig. 5-3c). The accuracy of the OSM-GE method is already studied in Chapter 4 and is not repeated here for brevity. Building usage and age data are obtained from the PAU shapefile and joined with the OSM file using the QGIS tool. The time is only 15 minutes for creating the 3D city model for this region and 15 minutes to join the PAU data with the OSM file.

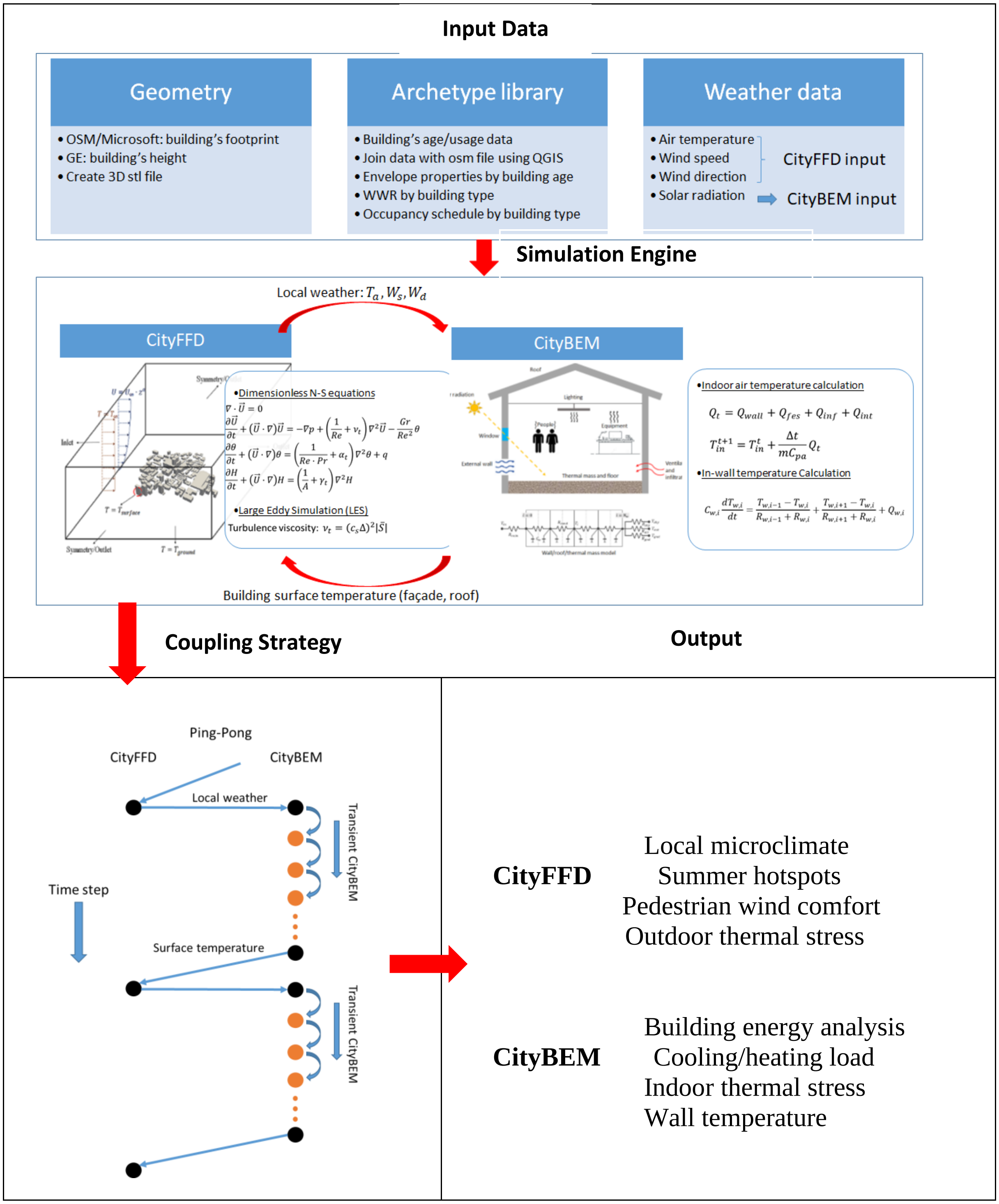

Figure 5-2 The workflow of dynamic urban building and microclimate simulation.

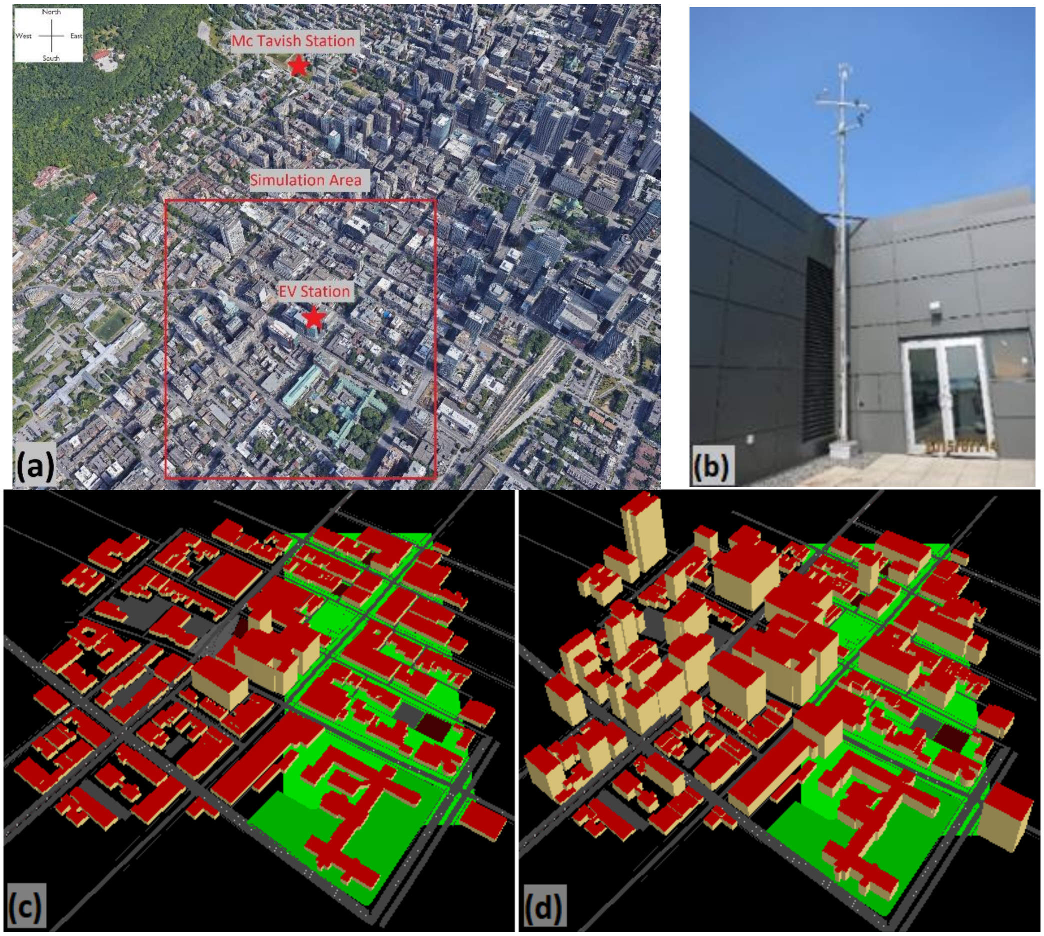

Figure 5-3 Aerial view map of the region of study, b) Weather station on the roof of EV building, c) Initial osm model, d) Modified osm model.

Weather data are the last inputs to start the simulation. As shown in Fig. 5-3a, measured weather data from the closest weather station, the Montreal McTavish weather station [168], were applied as the boundary conditions for CityFFD each time step. For the study period (06/24/2019-07/08/2019), the temperature varied between 15 ℃ and 32 ℃, with most of the days were sunny and high daily temperature (Fig. 5-4). The wind speed was less than 5 m/s, and the dominant wind direction was from the southwest.

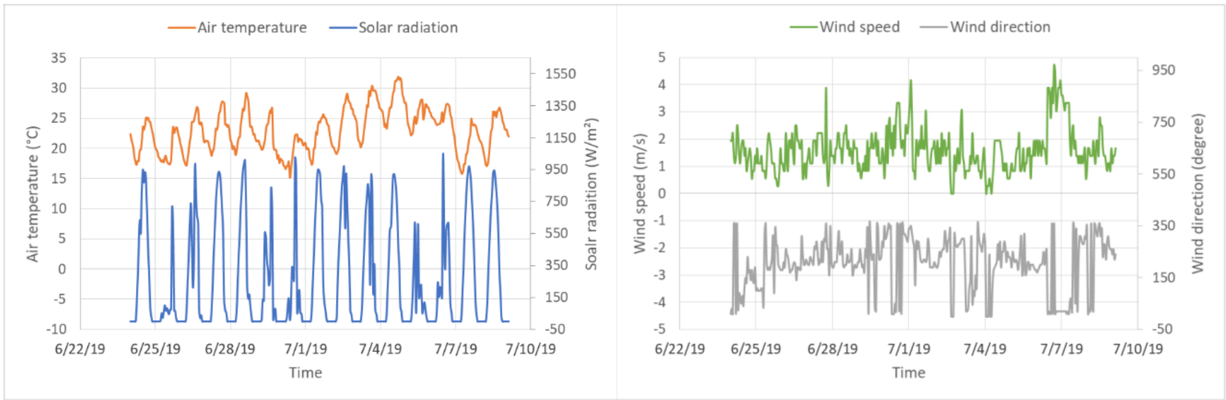

(a) (b)

Figure 5-4 Input weather data for CityFFD/CityBEM simulation: a) air temperature, solar radiation, b) wind speed and direction.

The computational domain and grid of the CityFFD model are shown in Fig. 5-5. If H is the height of the tallest building, according to the AIJ guidelines [169], the size of the computational domain in horizontal and vertical directions is 10H and 5H, respectively. In this case, the height of the tallest building in the area is 112.5 meters. Therefore, the domain size is $2250\ m \times 2250\ m \times 562.5\ m$. The total grid number is 4.2 million and the grid resolution near the buildings is around 4 meters. A finer mesh is used near the buildings to capture near-surface flow phenomena. Vertical boundary conditions vary based on the weather data and at each time step two of boundaries are considered as inlet and the others are outlets. The top of the domain is modeled as symmetry. Wall boundary condition is applied to the building surfaces and also the floor of the domain. The time step of transferring data between CityFFD and CityBEM models is one hour. At each time step, CityFFD simulates the urban microclimate with the time step of two seconds. CityFFD simulations are completely independent for each hour, when a new simulation starts with the new B.C. inputs from the weather data and CityBEM. This method has been consistent with the previous microclimate simulations by CFD [86,170]. For example, Antoniou et al. [170] used an hourly time step to model the heatwave using CFD for an actual urban area. CityBEM simulates 1-hour transient urban building energy performance with the internal time step of 5 minutes. The initial wall temperature for CityBEM transient simulation is obtained from the previous time step result. In CityBEM, each building is modeled as a single block. An indoor setpoint temperature of 24 °C for summer is used for all buildings.

Each façade of the building is divided into multiple triangles (Fig. 5-5). CityFFD calculated an average air temperature and wind components near each triangle, which is transferred to the CityBEM model for calculating wall surface temperature and building cooling load. CityBEM also calculates the surface temperature of each triangle and is used by CityFFD as the wall B.C. The computational time of CityFFD simulation is 20 minutes (about 4.8 minutes per 1 million grid) on a PC with 16 GB RAM and the Intel(R) Core(TM) i7-6700 CPU@4.0GHz and the NVIDIA GeForce GTX 970 graphic card. The computational time of 1-hour transient simulation of CityBEM is 2 minutes on the same PC. The total time to prepare the input data and run the integrated model for 15 days with a time step of 1-hour is 132.5 hours (5 days and 12 hours).

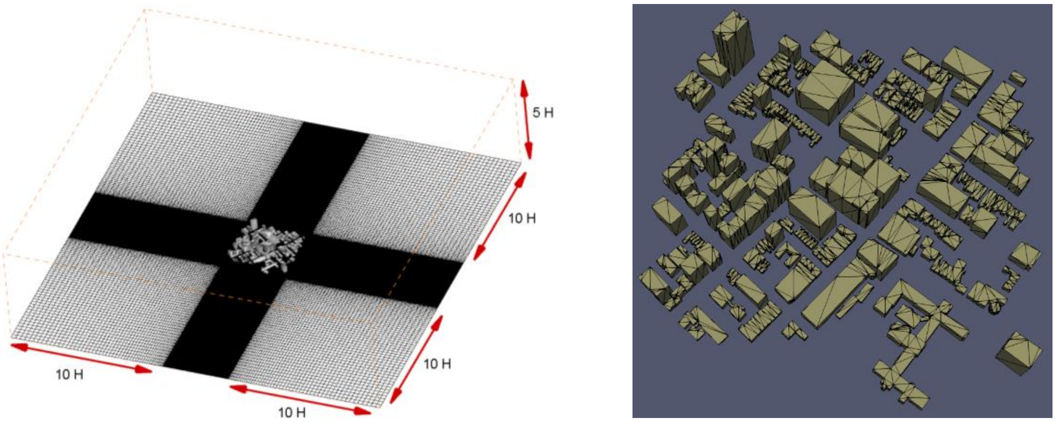

Figure 5-5 Left: Computational domain and grid of the CityFFD/CityBEM model; Right: 3D model of the buildings and triangles on each façade.

5. 2.1. Validations

The simulation results were compared with corresponding measurement data to investigate the accuracy of the automated CityFFD-CityBEM model. For the validation of the CityBEM model, cooling energy consumption of EV buildings of Concordia University in this region was obtained in the form of a 5-min resolution of electricity consumption provided by the Building Automation System (BAS). The cooling system is all-electric, with an average COP of 4.5 provided by the building's facility manager. Fig. 5-6a compares the cooling electricity consumption between the simulation results and measurement data. Cooling electricity consumption is higher during the daytime because the building is occupied, and internal heat gains from occupants and equipment are higher than the nighttime. Solar heat gain and higher outdoor air temperature during daytime are two other reasons for the high daytime cooling energy consumption. The maximum measured cooling electricity consumption is around 1 MW, which occurred at 5 PM on June 27. The weather data show that the outdoor air temperature and solar radiation of June 27 (12 PM - 5 PM) is around 28.5 °C and 900 kW, respectively, higher than other days. The Normalized Root Mean Square Error (NRMSE) between simulated and measured electricity consumption is 22%. A study by Quan et al. [67] for Manhattan using the urban EPC engine shows that the average error of annual energy consumption compared to the measurement data is around 69 %. They compared the result with the error for simulating monthly energy consumption of a single building presented by the ASHRAE standard, which is 15%. They mentioned that the model's accuracy is sufficient, considering the problem's scale and many uncertainties in the modeling parameters and input data. Therefore, the present work's accuracy in calculating the hourly energy consumption seems acceptable compared to the ASHRAE standard and urban EPC simulation.

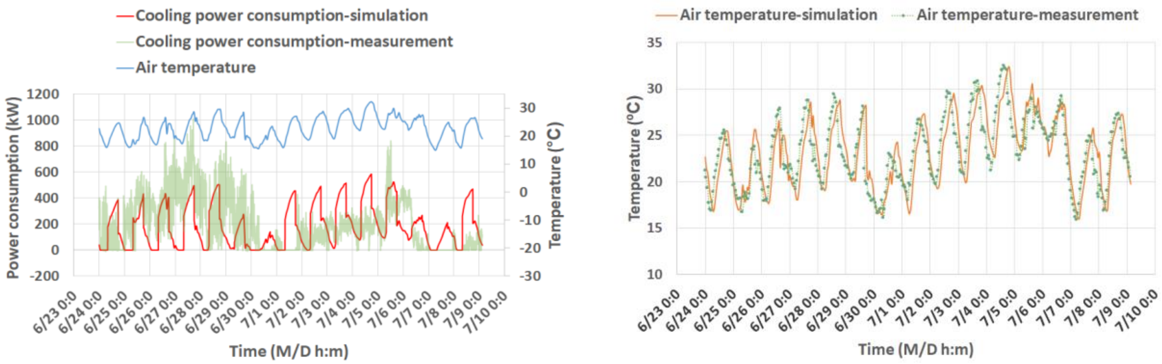

Figure 5-6 a) comparison of calculated and measured electricity consumption of three buildings of Concordia University, b) comparing simulated and measured air temperature on the roof of EV building.

For CityFFD, some previous studies have conducted various validations for a group of buildings in wind tunnels and actual urban areas based on the literature data [171]. In the current study for the dynamic simulations, the predicted urban local weather data on the roof of one building, i.e., the EV building, by CityFFD, were compared with the corresponding weather station data in Fig. 5-6b. The location of the weather station is shown in Fig. 5-3b. As can be seen, the simulated air temperature is close to the measurement data, and the NRMSE between simulated and measured air temperature is around 12.3% (MRSE=2.05 °C). The small difference indicates the validity of the model. The buildings' impact on the local urban microclimate around the EV building is relatively small when comparing the local EV building weather to the McTavish weather. The NRMSE of McTavish weather data compared to the EV weather data is around 8.7% (MRSE=1.45 °C). These two weather stations are with a distance of about 800 m, which is relatively close.

Moreover, the EV building weather station is located at the height of 70 meters. The EV building is the tallest in this area. The simulation results also show at this height, the air temperatures during these selected summer days for the validation are relatively uniform and are close to the inlet B.C.

A better comparison would be to use the weather station data near the urban street level, which is unavailable at the moment. We are working on more validation work by installing multiple weather stations near low-rise buildings in this area.

5.2.2. Building Cooling Load

Building cooling load consists of three components: transmission load, ventilation/infiltration load, and internal load. Building envelope thermal properties, local weather, solar radiation, and occupancy schedules contribute to the cooling load. In this section, the transient cooling loads were compared among buildings with different usages and ages.

5.2.3. Nighttime and Daytime Cooling Loads

Fig. 5-7 shows the year of construction and the contour map of the cooling load of buildings at three selected hours of the day 07/04/2019, the hottest (at 6 PM) sunny day with a diurnal temperature range of 10 °C and the light breeze. It shows that during the nighttime, the cooling loads of all buildings are less than 15 W/m^2. To investigate the accuracy of the calculated cooling loads of buildings, the nighttime cooling load of EV building is calculated using the building's measured electricity consumption and footage area. The cooling load of the building is around 9.5 W/m^2 during the night. The building was constructed in 1996, and considering the range of years of construction of all buildings in Fig. 5-7a (1870-2015), the range of simulated cooling load is acceptable. When comparing different buildings, new commercial buildings such as the building shown by the black box in Fig. 5-7b that are unoccupied during the night and are better insulated represent a lower cooling load ($< 5\ W/m^2$). On the other hand, old residential buildings such as the building shown by the red box in Fig. 5-7b show a higher cooling load ($> 10\ W/m^2$) because they are occupied during the nighttime and are not well-insulated.

The daytime cooling load of buildings gradually rises because of the increasing solar radiation and outdoor air temperature. The maximum cooling load ($34\ W/m^2$) occurs at 6 PM for a commercial building constructed in 1880, the building shown by the black box in Fig. 5-7d. The measured cooling electricity consumption of the EV building shows that the maximum cooling load of this building is around $19\ W/m^2$. Therefore, the calculated range of cooling load seems reasonable compared to the EV building measured data. Old commercial buildings show a higher cooling load during the working hours because of the low insulation of these buildings and higher indoor heat gains (according to the prEN16798-1 standard [165] presented in Table 4-5).

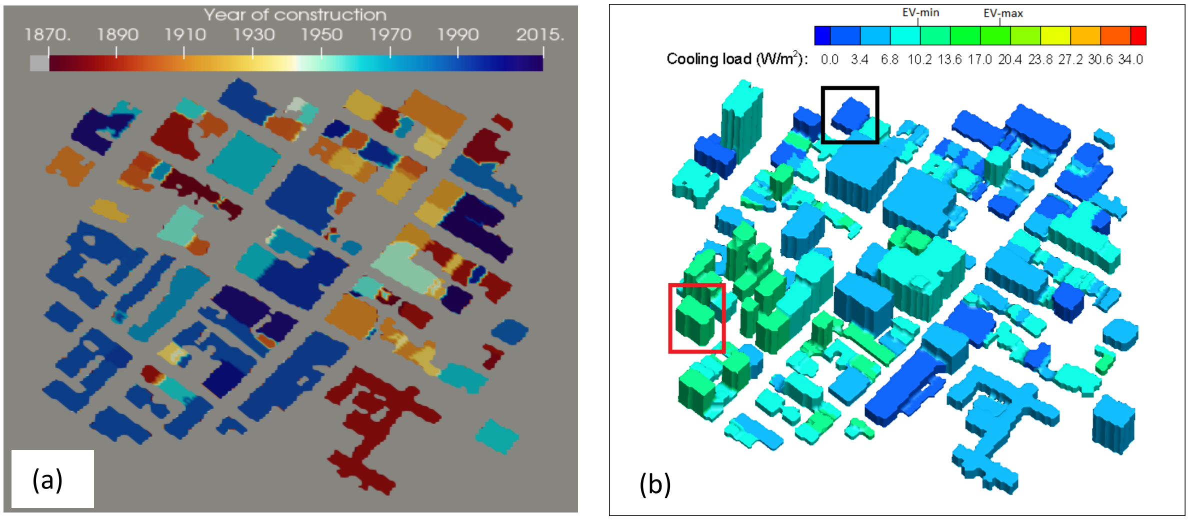

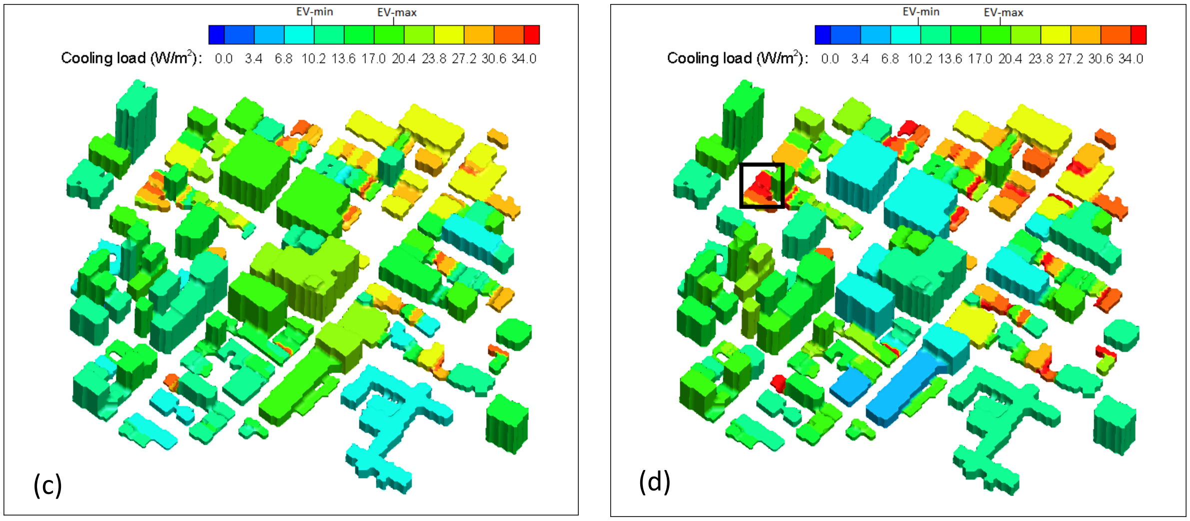

Figure 5-7 a) buildings year of construction, and contour map of the cooling load of buildings at 07/04/2019: b) 6 AM, c) noon, d) 6 PM

5.2.4. Transient Cooling Load of Two Representative Buildings

In this section, two representative buildings with the highest and lowest aggregated cooling loads are selected, and transient cooling load components are compared. The presented results can provide useful information on selecting mitigation strategies to reduce the buildings' energy consumption. Fig. 5-8a shows the cooling energy consumption per floor area of buildings, which is the aggregated cooling energy consumption for the whole period. As studied in the previous section, buildings' usage type and age are the most dominant factors affecting the buildings' cooling energy consumption. In the study area, commercial buildings such as stores and restaurants are mainly low-rise buildings and relatively older than other building types, especially high-rise residential and office buildings. The cooling energy consumption results show that buildings with higher cooling energy values ($> 5\ kwh/m^2$) are old commercial buildings mostly located at the top right corner of the region. These buildings have higher IHG, transmission, and infiltration loads. On the other hand, new residential and office buildings, mostly located at the left bottom corner, show lower energy consumption for cooling ($< 3\ kwh/m^2$) due to better insulation and lower internal heat load.

The transient cooling load of one old commercial building (built-in 1932) (hereafter as CB) and one newer office building (built-in 2003) (subsequently as OB) in Fig. 5-8a are compared in Fig. 5-8b. The CB cooling load is significantly higher (more than two times) during the daytime and a little lower during the nighttime than the OB. The cooling load components, including IHG, infiltration, and transmission loads, are compared in Figs. 5-8c-e. It should be noted that solar radiation transmitted through the glazing is not considered directly in cooling load calculation. Solar radiation is first absorbed by internal thermal mass, and its temperature increases slowly with time. The heat stored inside the thermal mass is transferred to the indoor air with the time delay, and the effect of solar radiation on the indoor environment remains after the sunset. Therefore, the instantaneous building heat gain and cooling load are different because of thermal mass.

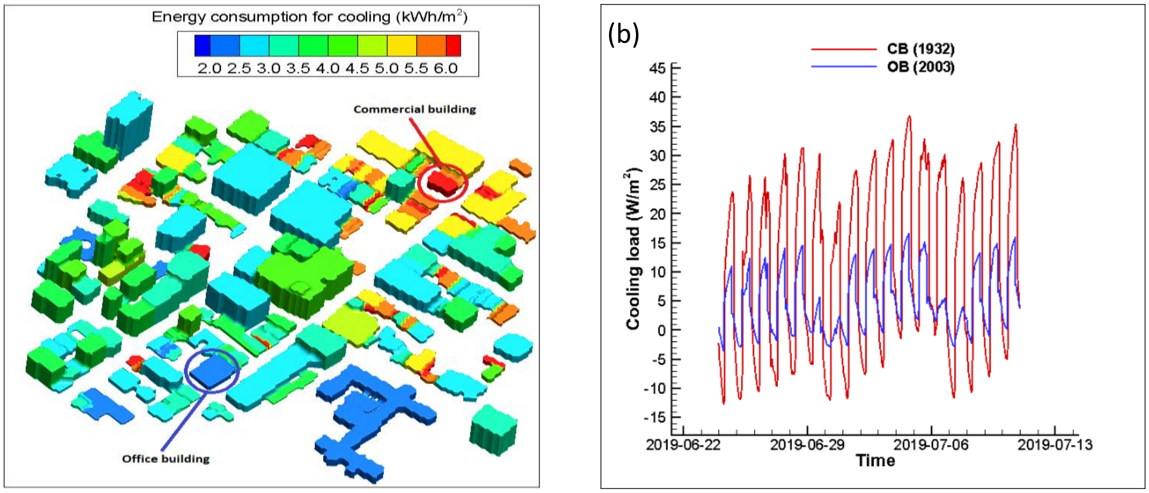

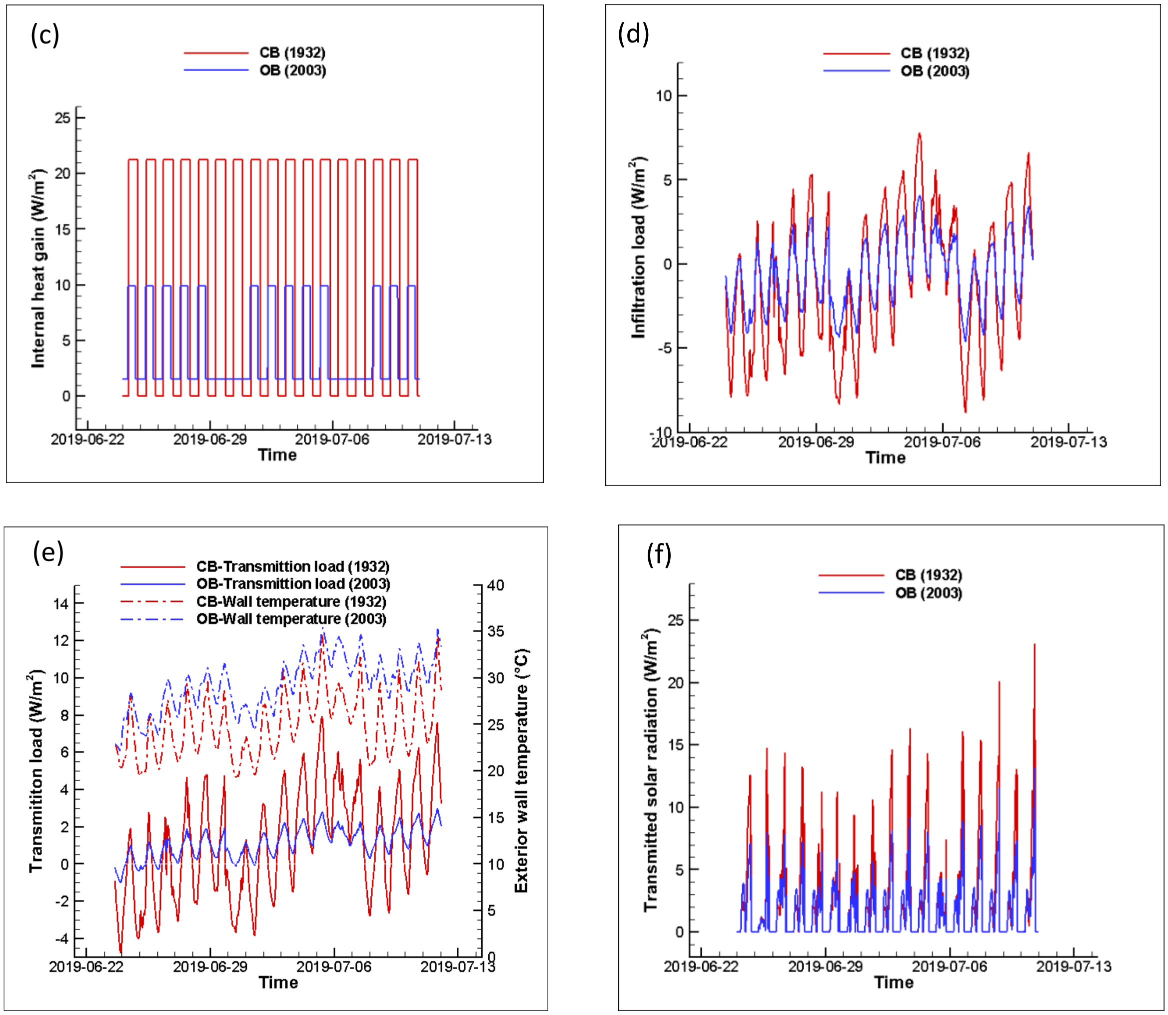

Figure 5-8 a) Contour map of total energy consumption for cooling of the buildings, and comparing cooling load components of two commercial and office buildings: b) total cooling load, c) internal heat gain, d) infiltration load, e) transmission load, f) transmitted solar radiation through the glazing.

The internal heat load is the dominant cooling load component during the day (Fig. 5-8c), which is almost two times larger for the CB, according to the building archetype library (Table 4-3). The infiltration heat load of two buildings is compared in Fig. 5-8e. The magnitude of the infiltration load of the CB is always higher than the OB, 7.8 W/m^2 and 4.1 W/m^2 at the 6 PM of 07/04/2019, because of its poor insulation and higher leakage area. The transmission heat load of the CB is almost three times larger than the OB during the day (Fig. 5-8d). Transmission load is the summation of heat transfer through walls, roof, window, floor, and interior thermal mass.

Exterior walls' surface temperature in Fig. 5-8e shows that the newer (office) building's surface temperature is always higher than the older (commercial) building. The average surface temperature difference is 4 ℃ because the OB is better insulated, and the surface temperature is closer to the outdoor air temperature. Even though the surface temperature of the CB is lower than OB, its higher U-value (Table 4-2) causes a higher heat load through walls, windows, and the roof in CB compared to the OB. SHGC of new buildings usually is smaller than the old buildings because of energy-efficient glazing, such as double or triple glazing used in new buildings. Therefore, solar radiation absorbed by the CB's thermal mass is 1.5 to 2 times larger than the OB (Fig. 5-8f). The higher absorbed solar radiation and the U-value of the CB cause more extensive heat transfer from the thermal mass in the CB compared to the OB.

Based on the above analysis, we can reach some general conclusion: comparison of two CB (old) and OB (new), which are two representative building types in the studied area, shows that during hot and sunny summer days, the cooling load of CB is higher than OB because of low insulation (Higher U-value), higher SHGC, and higher IHG of CB compared to OB.

Canada is committed to implementing the Pan-Canadian Framework on Clean Growth and Climate Change [6] to reduce GHG emissions and energy consumption. Strengthening existing and introducing new GHG reduction measures can exceed Canada's 2030 target of a 30 percent reduction below 2005 levels of greenhouse gas (GHG) emissions, and beginning work so that Canada can achieve net-zero emissions by 2050. The building sector is a significant source of energy consumption and GHG emission in Canada. More than 75 percent of the building stock in

2030 will be composed of buildings already standing today. Therefore, retrofitting existing buildings can significantly contribute to the GHG emission and energy consumption reduction goal. The government is trying to develop a model code for existing buildings and energy efficiency improvements that can be made when renovating buildings. Extending the presented model to the whole city and its results can provide useful information on finding buildings with top priority for retrofitting (old commercial buildings in this region). It can also provide information on choosing the most effective measures for reducing energy consumption based on the buildings' usage type and age. For example, in old commercial buildings, the contribution of transmission load, infiltration load, and transmitted solar heat gain in the building's total cooling load is significant. All these three components must be reduced using retrofit measures. Adding an insulation layer to the walls' exterior surface can reduce the transmission and infiltration cooling/heating loads. Retrofitting double glazing and exterior and interior shading devices can also reduce the solar heat gain.

5.2.5. Dynamic Interactions of Urban Microclimate and Building Thermal Performance

The building's surface temperature depends on several parameters, including wall construction, orientation, local weather condition, and indoor air condition. In this case, a setpoint temperature is assumed for all buildings. Therefore, buildings' surface temperature differences are caused by building envelope properties (U-value) and local weather conditions (air temperature and wind speed). For the newer buildings with lower U-value, the heat transfer rate is lower, and the exterior surface of the wall is less affected by the indoor condition. Therefore, the surface temperature of newly constructed buildings is higher than old buildings. Local weather data affects the building's surface temperature through convective heat-transfer and long-wave radiation. Both higher ambient temperature and wind speed result in the higher surface temperature of buildings. Higher wind speed could result in a higher convective heat transfer coefficient between ambient air and the building's surface. A higher building surface temperature results in more transmission load and increases the building's cooling load and energy consumption. Meanwhile, the buildings' surface temperature directly affects the local surrounding air temperature through the heat flux from the building surface to ambient air. This effect is modeled in CityFFD by using the surface temperature of buildings as B.C. in solving the energy conservation equation.

To study the two-way interaction of buildings and the surrounding urban microclimate, we presented the building surface temperatures, local air temperatures, and local wind around buildings at the hottest day and time (07/04/2019 – 6 PM) of the selected period in Fig. 5-9. The spatial variation of building surface temperature (the difference between highest and lowest surface temperatures) is higher than 10 ℃. Due to the increased solar radiation absorbed by the wall, its temperature gradually rises during the day and reaches the maximum temperature around 6 PM because of the heat storage. As already mentioned, because of the different orientation and properties of buildings and local weather data, building surface temperatures are different.

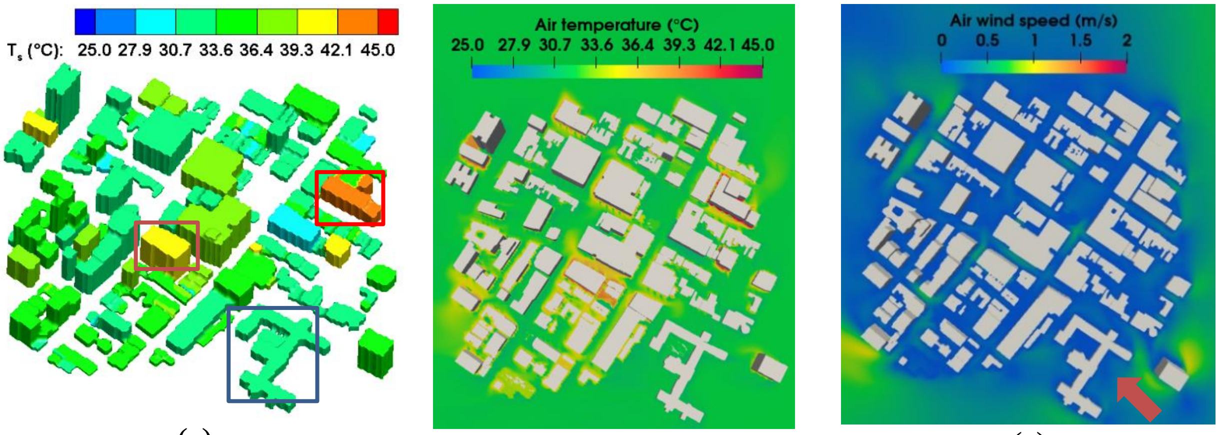

(a) (b) (c)

Figure 5-9 a) buildings' surface temperature, b) Air temperature, c) Wind speed at 07/04/2019 - 6 PM.

Three buildings with different construction years are marked in Fig. 5-9a, as the red, orange, and blue buildings, constructed in 2014, 2009, and 1884, respectively. The surface temperature of the buildings is 43 ℃, 40 ℃, and 31 ℃, respectively: a maximum difference of 12 ℃. For the distribution of local air temperature, the spatial variation is more than 15 ℃. Fig. 5-9c also shows the buildings' local wind distribution. Depending on the buildings' free-stream wind and configuration, lower wind speed leads to lower convective and higher diffusion effects. So, in the area with lower wind speed, local air temperature tends to be high and results in higher building surface temperature.

To better investigate the impact of local weather data on building energy performance, we modeled the same case only by CityBEM and using McTavish weather station data (Fig. 5-4) for all buildings (i.e., without the urban microclimate modeled by CityFFD). Results are compared with the integrated CityFFD+CityBEM model. Exterior surface temperature change and percentage difference in transmission, infiltration, and total cooling loads of all buildings on 07/04/2019 - 6 PM are shown in Fig. 5-10. Surface temperature changes are between 0.9 ℃ and 3.5 ℃. Buildings with higher local air temperature in Fig. 5-9b show more significant changes in wall temperatures. Outdoor air and wall temperature directly affect the building's transmission and infiltration load. As a result of higher outdoor air and wall surface temperature, the transmission, infiltration, and total cooling loads of buildings are increased by up to 25%, 40%, and 23%, respectively. These results indicate that local urban microclimate can significantly affect buildings' energy consumption, especially in extreme weather conditions such as heatwaves. Therefore, it is essential to use an integrated building energy and microclimate simulation tool to improve the accuracy of the urban scale simulations.

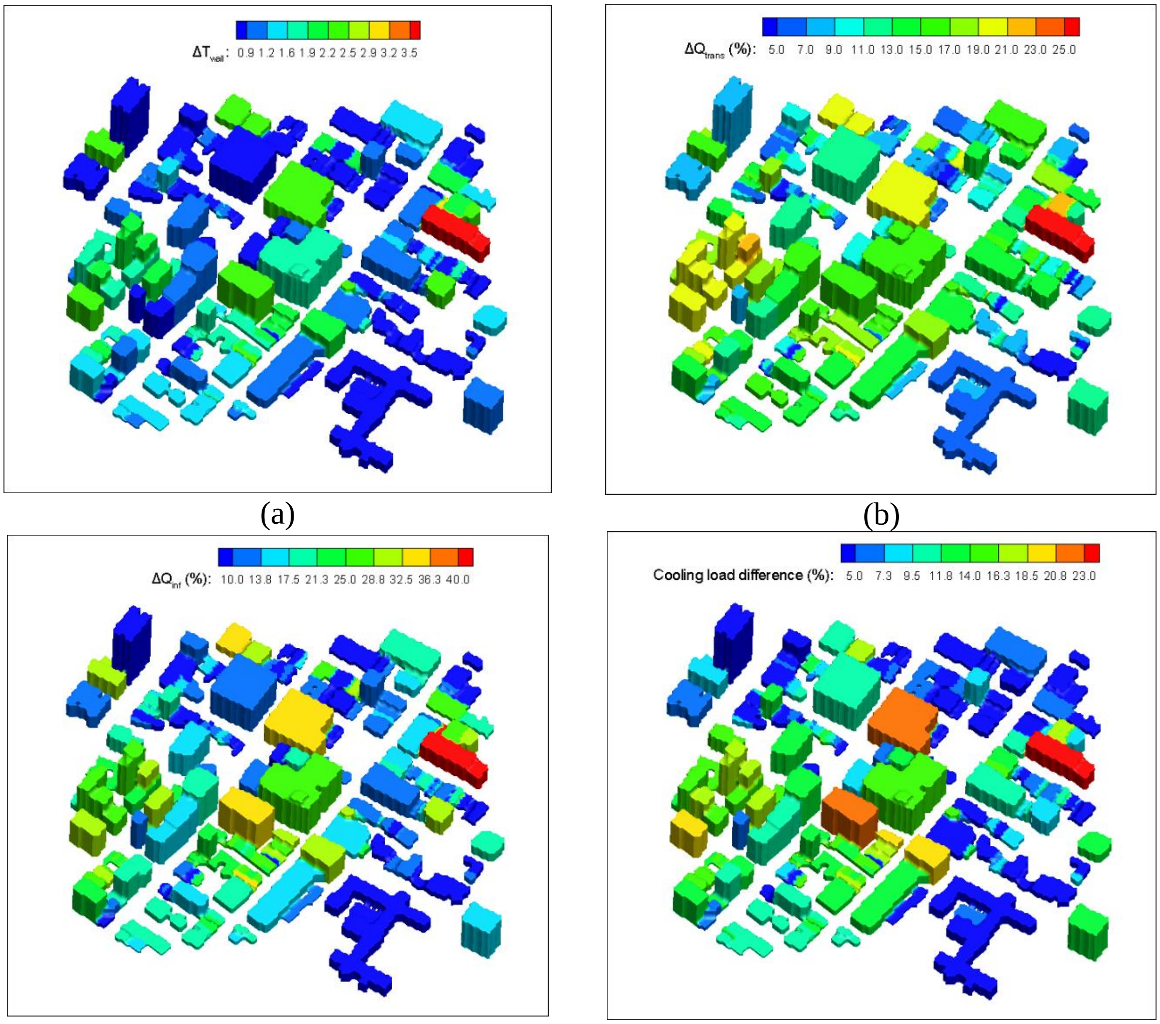

(a) (b)

(c) (d)

Figure 5-10 a) Exterior surface temperature difference, b) Transmission load difference, c) Infiltration load difference, d) Total cooling load difference at 6 PM, 07/04/2019 when comparing urban energy simulation results with and without using local microclimate data.

5.3. Case Study 2: Snow-Storm of Century

As a second case study, the Ile-des Soeurs community in Montreal, Canada, was selected. A hypothetical power outage in the region based on the real event of the Montreal “snowstorm of the century” (SOC) in March 1971 was simulated to study the thermal resilience of the region. The effect of building envelope retrofitting on the buildings' thermal performance is then analyzed to demonstrate using the proposed urban models for a real scenario.

5.3.1. Urban District

As a part of the city of Montreal, Quebec, Ile-des Soeurs is an island with a total area of 3.74 km^2, around 1,500 buildings, and 19,000 populations [172]. The island is primarily composed of multi-unit residential apartments, condos and townhouses. The various types of buildings with different years of constructions and the available database of buildings geometry make the island a good test case for the current study. Fig. 5-11 shows the Ile-des Soeurs' aerial map view with years of constructions [173].

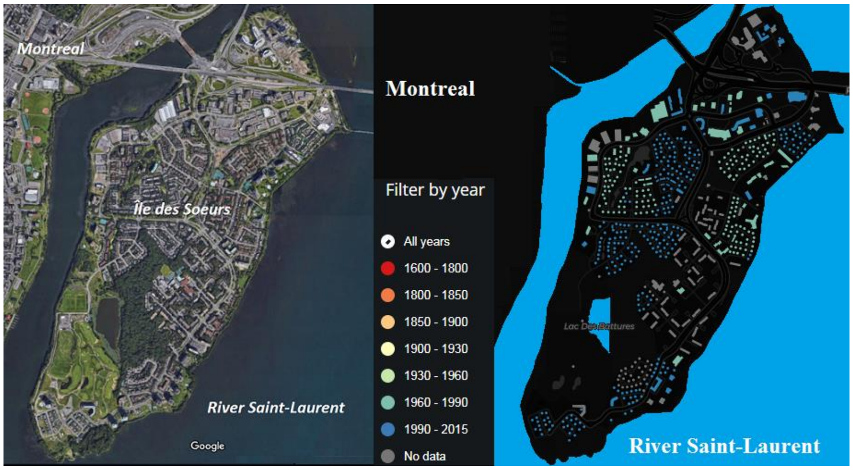

Figure 5-11 The Ile-des Soeurs aerial view map (left) [174] and Ile-des Soeurs building year of construction map (right) [173]

5.3.2. Model Verification

Uncertainties in input data are one of the main limitations of UBEM models [175]. Occupant behavior is an essential factor in physics-based models' uncertainty [176]. The archetype library used in UBEM tools is another source of uncertainty that can affect the simulations' accuracy [177]. Therefore, validation and calibration processes are essential in UBEM tools for better simulation. Most UBEMs have been calibrated using monthly or yearly measured data, and only a few of them have been validated against hourly measured data.

In this case study, the annual space heating and cooling energy consumption in the buildings were calculated and compared with the corresponding metered data provided by Hydro-Quebec [178] (see Fig. 5-13). Hydro-Quebec provides the annual detailed electricity consumption of buildings. In Canada, about 63 percent of residential building energy use is for space heating and cooling [179]. To compare with Hydro-Quebec electricity consumption data, it is necessary to find the buildings that use electricity for heating and cooling. In Montreal, most residential buildings built before 1990 use electricity for space heating [179]. Therefore, about 170 single-family residential buildings, most of which were built before 1990, was selected for the comparison. To calculate the building's annual heating and cooling energy consumption, monthly average weather data were used in the CityFFD model, as shown in Fig. 5-12. The outdoor airflow and temperature were simulated for 12 months of the year by CityFFD at quasi-state simulations to obtain average local temperature around buildings surfaces for CityBEM to calculate the buildings' annual thermal load. The hourly thermal load was then multiplied by the number of hours per month to calculate the total monthly and then annual load of a building.

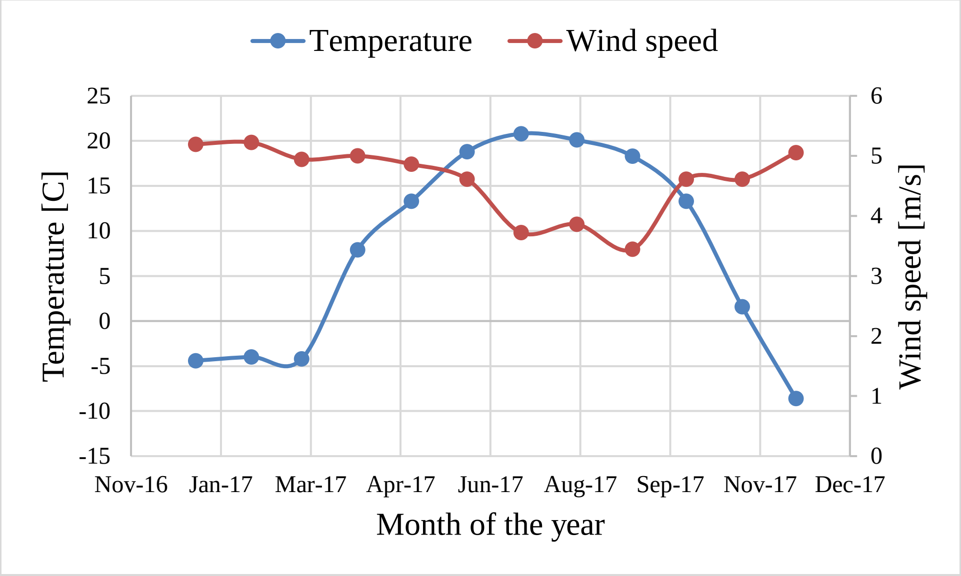

Figure 5-12 Monthly average weather data.

Fig. 5-13 shows the histogram of error percentage distribution in predicting the annual space heating and cooling energy consumption. The average error of the predicted energy consumption is 47%. According to the ASHRAE standard, the average error for a single building's monthly energy consumption is around 15% [54]. However, for the urban building energy simulation, previous works' average error is about 69% [54], which has been considered acceptable for UBEM because of more uncertainties in assumed data and modeling parameters. In this study, some buildings show the error larger than 100%, probably because some buildings may use natural gas heating instead of electrical heaters. Therefore, the lack of data regarding space heating type details could be a significant source of uncertainty, which may be reduced with more data from other official sources.

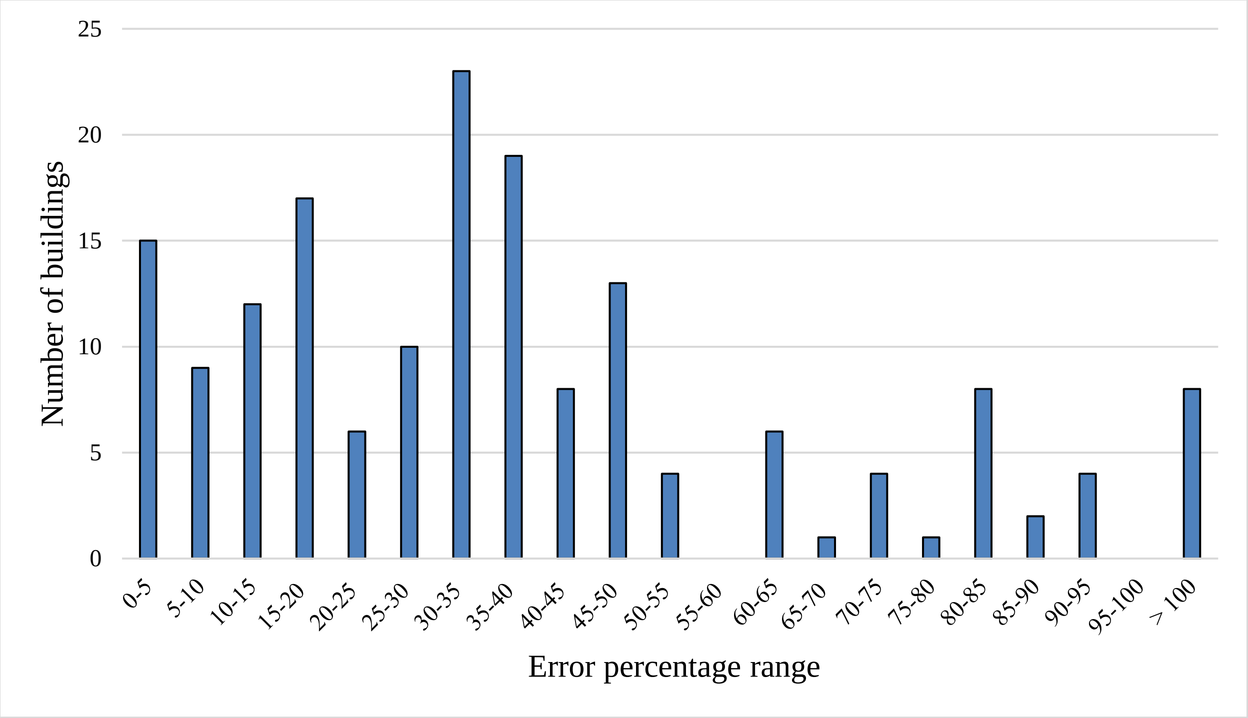

Figure 5-13 Histogram of error in calculating the annual energy consumption of buildings.

5.3.3. Modeling Building Resilience During the Snowstorm of the Century

One of the significant applications of urban energy modeling is investigating the city/community thermal (or energy) resilience against extreme weather events. In this study, we modeled one historical snowstorm on March 4th, 1971, the so-called Snowstorm of the Century (SOC) of Montreal. 47-cm snow was dumped on Montreal with a maximum 110-km/h wind, resulting in broken power lines and cables and a significant power outage lasting for full ten days on the island. Because most of Montreal's households relied on electric heating, the power outage caused a severe drop in these households' indoor air temperature. In this section, three consecutive days after the storm were simulated by the proposed integrated urban models to study the snowstorm impact on the Ile-des Soeurs community's buildings indoor air temperatures focusing on thermal resilience. Fig. 5-14 shows the input weather data of these three days provided by Environment Canada [180].

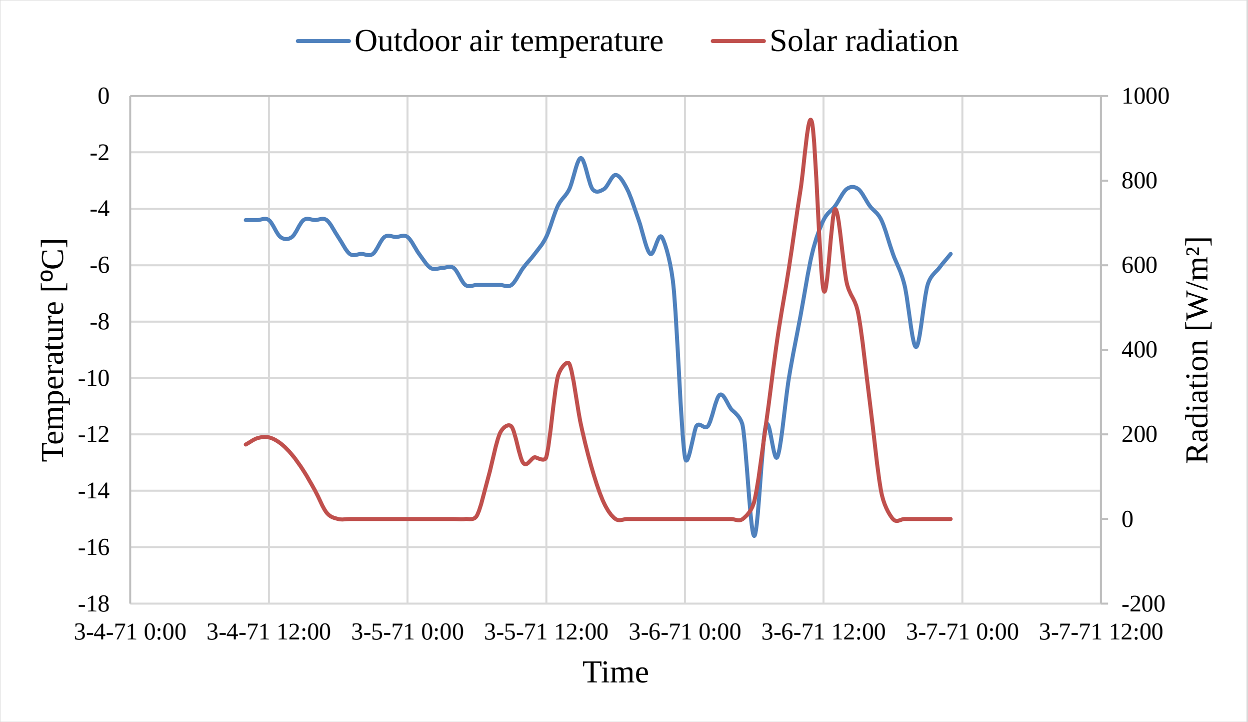

Figure 5-14 Input weather data during the March 4-6 snowstorm in 1971.

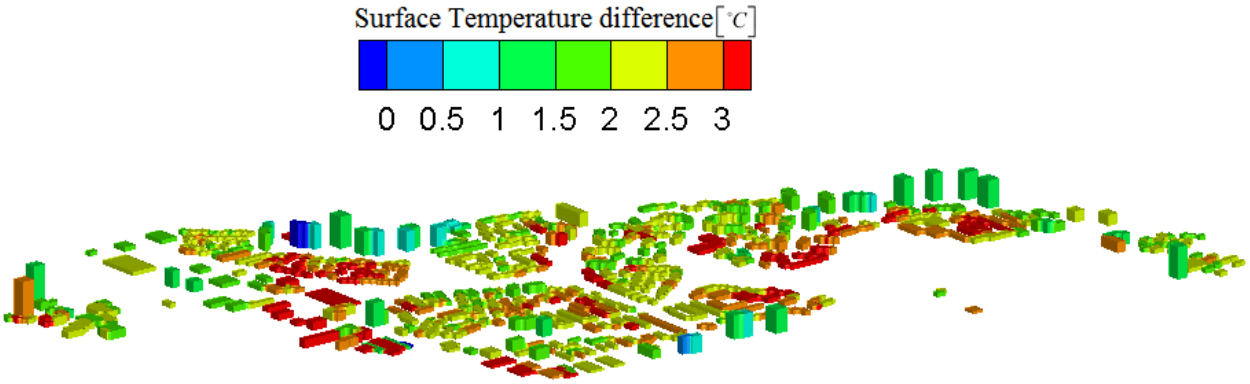

Figure 5-15 Buildings surface temperature difference with and without using the local microclimate data calculated by CityFFD.

To show the necessity of using local microclimate data from CityFFD for CityBEM simulation, we did the CityBEM simulation with constant weather data for all the buildings. Then we repeated the simulation using integrated CityFFD and CityBEM model considering the local microclimate effect on CityBEM simulation. The difference of calculated buildings surface temperature at a selected time step is shown in Fig. 5-15. The average building surface temperatures calculated by the integrated model are about 2.5 °C higher than that of all buildings' constant weather data. There are two main reasons for this difference related to the different local wind velocity and air temperature calculated by CityFFD compared to those provided by the weather station. First of all, in CityFFD simulation, the ground surface temperature, which is the simulation's boundary condition, is averagely 1.5 °C higher than the air temperature. Therefore, the simulated local air temperature around the buildings is higher than the weather station's air temperature, used for all the first simulation buildings. Secondly, the average wind velocity around the buildings' surfaces is lower than those at the weather station outside the city. This decrease is attributed to the city's increased surface roughness parameter compared to the values in nearby non-urban regions [181]. A lower wind velocity leads to a lower exterior convective heat transfer coefficient, a linear wind velocity function. By decreasing the exterior surface convective heat transfer coefficient, the heat transfer between the wall's exterior surface and outdoor air also reduces. Therefore, exterior surfaces are more affected by indoor air temperatures higher than the outdoor air, resulting in higher exterior surfaces' temperature. The variation of this difference is from 0 to 3 °C, depending on different buildings' materials and convective heat transfer coefficients as a function of local aerodynamics around buildings. The temperature difference of 3 °C could become critical in building survivability and resilience in the power outage condition during storms, as discussed in the later section.

Change of local wind around a group of buildings with changing wind direction and speed is shown in Fig. 5-16. The left and right figures show the microclimate on March 6th at 2:00 pm and March 6th at 11:00 pm, respectively. The wind speed of the left figure is 1.39 m/s from south to north, while the wind speed and direction of the right figure are 2.22 m/s and from east to north. With the wind boundary condition change, the local airflow pattern and velocity around the buildings varied significantly. A closer look near a high-rise building highlighted by the arrow reveals that the average wind velocity around the specified surface of the building is 0.1 m/s and 6 m/s, respectively. In the left figure, the airflow is perpendicular to the studied surface, and the wind velocity near the wall is very low, which is similar to the stagnation point. While in the right figure, airflow is parallel to the surface. Therefore air is moving freely over the surface without any considerable resistance, and the local wind velocity is higher than the left figure. The local exterior convective heat transfer coefficient is a linear function of local wind velocity, which means that a higher wind velocity leads to a higher thermal advection rate near the surface. Therefore different wind velocity of left and right figures leading to different convective heat transfer coefficients of 3.95 $(W/m^2 \cdot ℃)$ and 41.18 $(W/m^2 \cdot ℃)$, respectively.

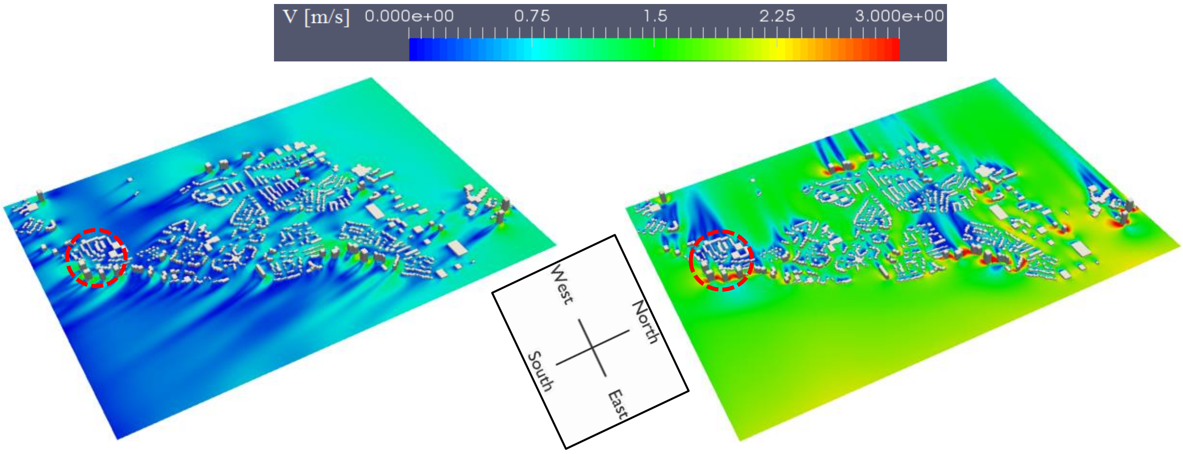

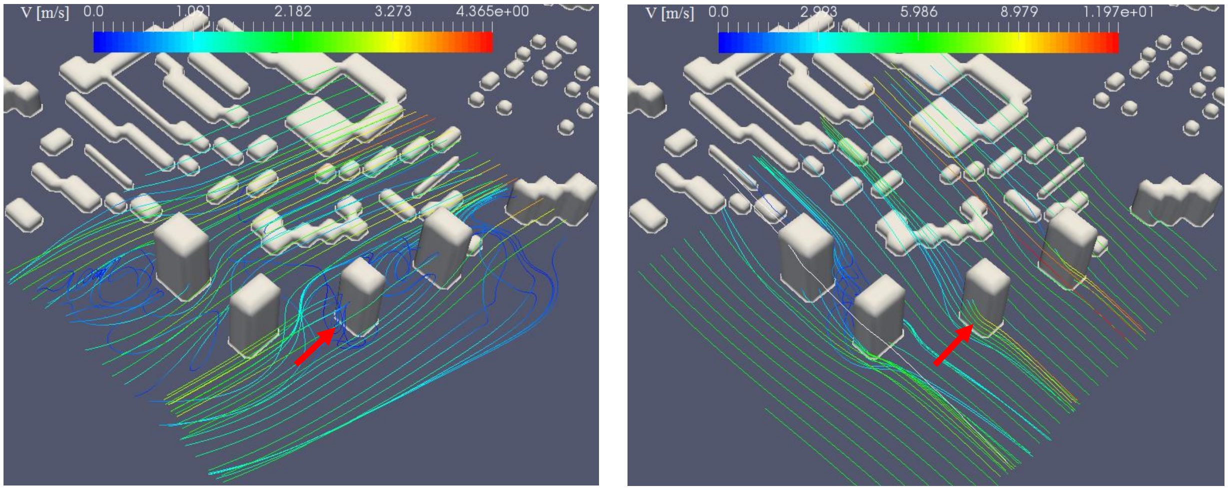

Figure 5-16 Local microclimate variations with changing wind direction and speed modeled by CityFFD.

Fig. 5-17 shows the building indoor air temperatures at different times after the power outage. The initial temperatures for all buildings were set to be around 21 °C at about 13:00, March 4th, 1971. After about 12 hours to 1:00, March 5th (Fig. 5-17b), most of the building temperatures dropped below zero. However, the ambient temperature did not decrease significantly during the same period, i.e., < 1 °C, as shown in Fig. 5-14. Later around 13:00, March 5th (Fig. 5-17c), with the increases of both the ambient temperature to about -4 °C and the solar radiation, the temperatures returned to above zero degree for most of the buildings. Due to the sudden decrease of the ambient temperature to around -12 °C, all buildings reached the lowest temperatures at about 1:00 March 6th (Fig. 5-17d): the lowest temperature could be close to the ambient level, less than -11 °C, for many buildings. On the following day of March 7th (Fig. 5-17e), the solar radiation peaked around noon, so all buildings were heated, returning to the above-zero-degree level: some buildings could be as high as around 8 °C under the "sunshine". The temperatures then later again dropped back to below zero at night after 12 hours (Fig. 5-17f).

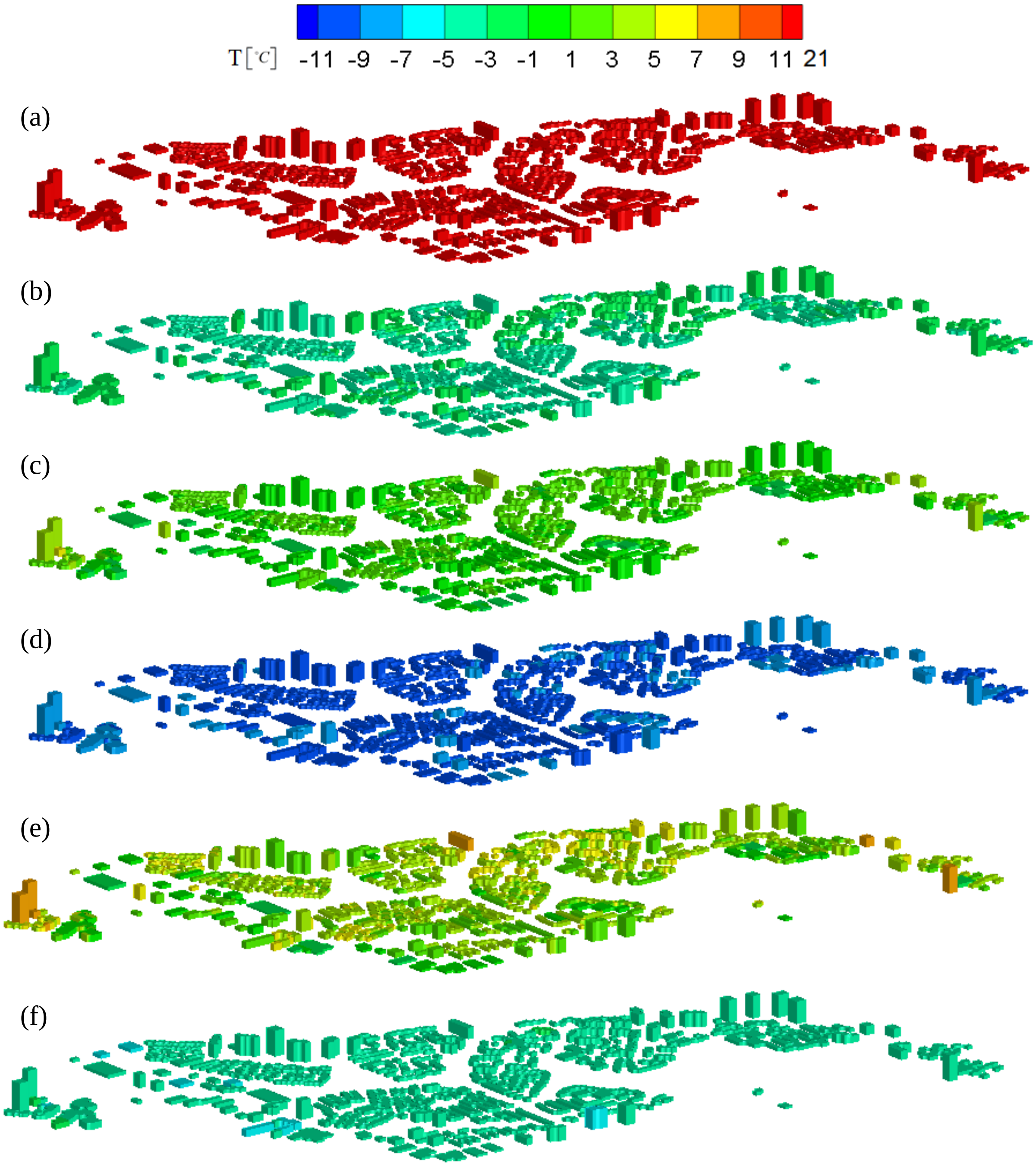

Figure 5-17 Buildings temperature map during power outage caused by snowstorm, from top to bottom: (a). March 04, 13:00, (b). March 05, 01:00, (c). March 05, 13:00, (d). March 06, 01:00, (e). March 06, 13:00, and (f). March 07, 01:00.

Therefore, the time history of the calculated indoor temperatures illustrates the significant impacts of indoor ambient conditions, especially solar radiation. It also highlights that without heating, the temperatures dropped so quickly to below zero just within a few hours for all buildings, although there existed a certain level of delays for some buildings.

One way to identify the group of buildings most vulnerable to the SOC is to compare the resultant temperatures at one of the worst scenarios during the storm. Fig. 5-18 shows the indoor temperatures when the outdoor temperature was the lowest during the storm. The highest temperatures were observed for quite a few high-rise multi-unit residential buildings (MURBs) at the left (the North), lower (the West), and the right sides (the South) of the island. These are the newer constructions, and the left-side and the right-side communities are the newest ones. In comparison, some MURBs were with the lowest temperature, e.g., a few buildings in the lower part of the island, because these buildings were older than other ones. Therefore, the year of construction is one of the most significant parameters in terms of storm vulnerability.

On the other hand, for buildings with similar years of constructions, e.g., for the right-side (the southern) community, some low-rise residences showed lower temperatures than the high-rises nearby. These high-rises were insulated as well as the low-rises and had more surface areas for benefiting from passive solar heating. It indicates that the building type also plays an essential role in terms of vulnerability.

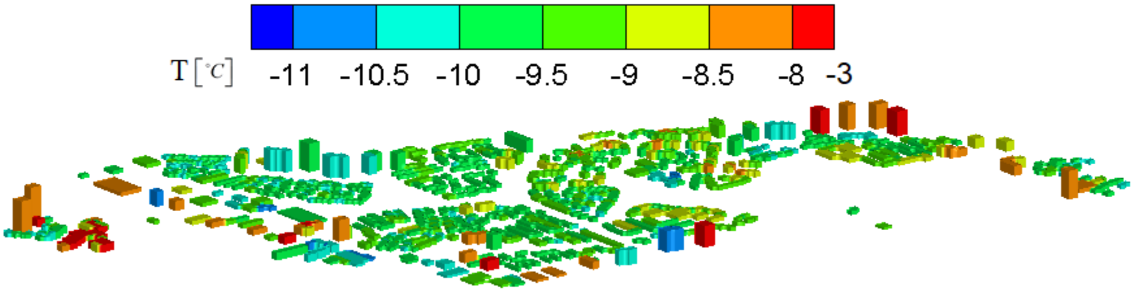

Figure 5-18 Buildings' indoor air temperature at the lowest outdoor temperature during the storm.

A more vulnerable building shows lower resiliency against an extreme weather event. Here, one way to define “building resilience” is that a building remains safe to occupy during a power outage. For example, suppose a building is well-insulated or designed to stay functional probably from passive solar heating in the winter. In that case, it is considered being resilient enough to sustain the power outage condition. The Passive Survivability-Winter (PSW) [182] is thus defined and applied here to evaluate buildings' resilience. PSW is the time (in hours) from when heating is shut off to when the indoor operative temperature reaches 15 °C (59 °F) from an original heating set-point of 21°C (70°F). Fig. 5-19 shows the calculated PSW values for all buildings. The PSW varies from 1 to more than 3 hours, depending on building types and year of constructions. Specifically, the temperature decrease rate varied among buildings due to various building envelope materials, occupancy schedules, WWR, and local microclimate data.

It should be noted that within the immediate few hours of the power outage, the sky was cloudy, and the calculated solar heat gain was found to be negligible, so the building temperatures dropped relatively fast. Higher buildings seem to have lower PSW values when compared to low-rise residences on the island. Without the added benefits from solar heating, these buildings have larger footage and surface areas and are subject to higher heat losses. Therefore, building resilience against extreme cold events is closely related to building type, year of construction, and ambient conditions, especially solar radiation, for the current study. Although the ambient conditions may be predicted, they are not controllable. In comparison, the first two factors are directly related to the thermal insulation levels, which can be managed to improve survivability and energy performance. This study, therefore, demonstrates the possibility of retrofitting techniques to enhance building resilience.

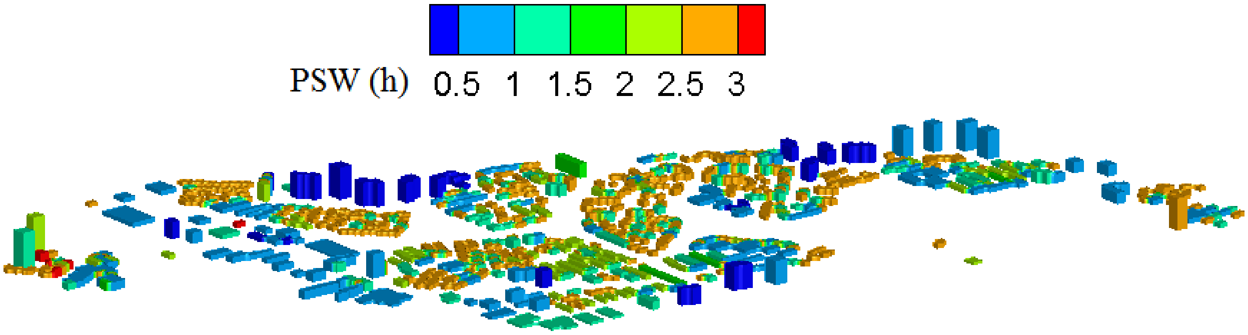

Figure 5-19 Calculated building resilience in terms of "Passive Survivability-Winter" (PSW) after the power outage.

5.3.4. Building Retrofit to Improve Resilience

Another major application of the proposed model is to evaluate building retrofitting strategies to improve their resilience against the winter power outage. For example, adding more thermal insulations is one of the common choices. Here, an 80-mm thick expanded polystyrene (EPS) layer was added to all buildings' external walls' outer surface. The R-value of the EPS layer is around 2.1 m^2K/W, which doubles the insulations for old high-rise residential buildings, which are among the vulnerable buildings, as shown in Figs. 5-18 and 5-19. Fig. 5-20 compares the temperature profile of one selected old high-rise building (one of the four buildings in the top right part in Fig. 5-18) before and after adding the extra insulation layer. The PSW value increases about two more hours with the added insulation. Interestingly, it was also found that the extra insulation also prevents the building from reaching 0 °C and thus avoid the freezing of water pipes and other problems for the whole duration of the three-day power outage. Therefore, in terms of the resilience against property damages, a single layer of extra insulation seems to be quite effective against the power outage for the building under consideration. For other buildings, a single retrofit measure may not be enough for keeping them from freezing, so it is also possible to evaluate other retrofitting options, preferably based on building specifics, e.g., using thermal storage and emergency heating devices, etc. This case study is mostly for demonstration purposes, and more detailed analysis can be explored further in future studies.

On the other hand, as noted previously from Fig. 5-15, the calculated indoor temperatures with the local microclimate information from CityFFD are by average 2.5 °C higher than without it. For the selected building in Fig. 5-20, this may be translated into that the building could remain above the freezing temperature most of the time, even without adding the insulation layer since the lowest temperature is around -3 °C. Accordingly, the current insulation level for retrofitting may be overestimated and could be reconsidered for economic concerns. Moreover, when the extra insulation layer was added for the same building, this temperature difference also means a few more hours of survivability time (i.e., PSW), which are critical for occupants and buildings themselves during extreme weathers. This analysis again shows the importance of including local urban microclimate into urban building energy model when evaluating building thermal response and resilience against weather extremes.

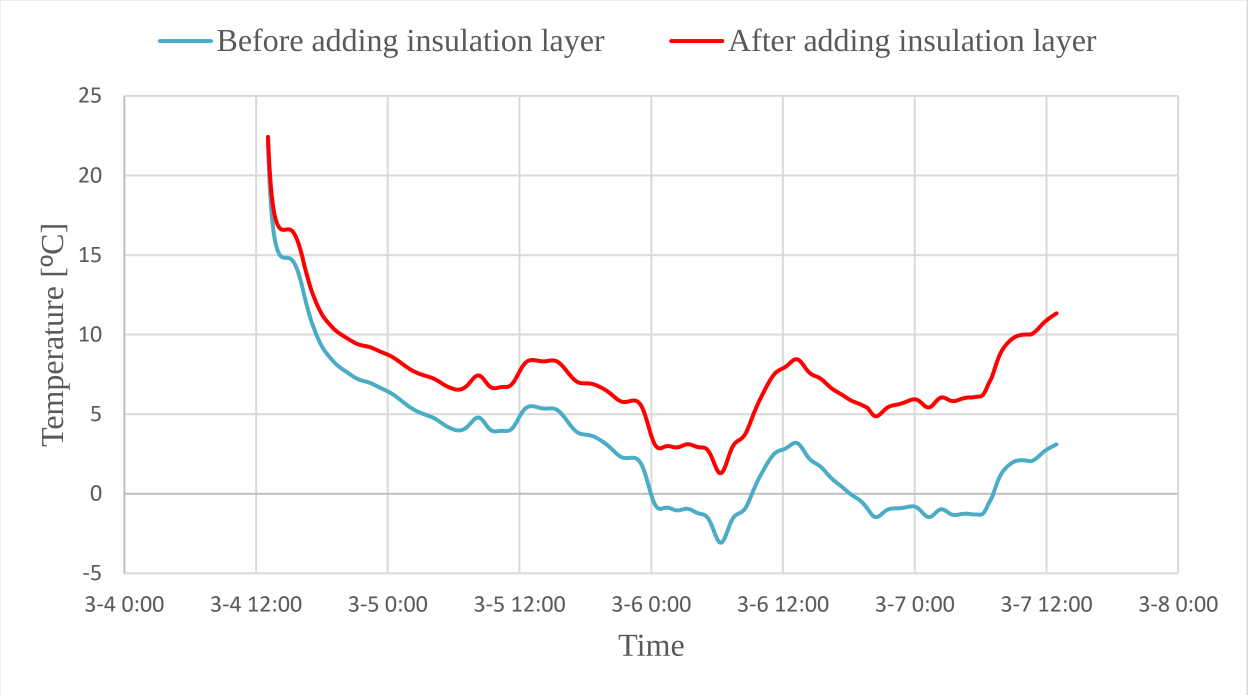

Figure 5-20 Effect of installing an insulation layer to the exterior surface of an old high-rise residential building on enhancing building resilience.

5.4. Summary

In this chapter, two extreme weather events, heatwave and snow-storm, in Montreal, are modeled by the integrated CityBEM-CityFFD platform. 3D model of buildings is generated by the integrated OSM/Microsoft + GE model. Buildings' non-geometrical parameters are estimated using the developed archetype library, and dynamic urban buildings energy and microclimate simulation is performed by integration of CityBEM and CityFFD. In the first case study, an urban area in Montreal's downtown was simulated during the hottest period of summer 2019. Buildings' dynamic energy consumption and cooling load's components were analyzed during this period. The simulation results are validated against measurement data, including electricity consumption and local weather data of a high-rise commercial building in the study area. Both models present good accuracy considering the uncertainties in the modeling parameters and input data. Cooling energy consumption is studied and compared between all buildings in the area. Results show that old low-rise commercial buildings are the least energy-efficient buildings in this region. Different energy efficiency measures, such as retrofitting the building envelope, can improve buildings' energy efficiency. The study on the two-way interaction between buildings and microclimate shows that buildings' surface temperature and configuration affect the local air temperature and wind speed. In this case, the spatial variation of local outdoor air temperature at the hottest time of the period is more than 15 °C, which is significant. On the other hand, local weather data (air temperature and wind speed) affect building energy consumption. Results show that using microclimate data provided by CityFFD instead of the single and uniform weather data for all buildings results in the 5%-23% change in calculated energy consumption of buildings, which shows the importance of using the integrated platform capture the two-way interaction between models.

A second case study of about 1,500 buildings in the Ile-des Soeurs, Montreal, Canada, was investigated to study the effectiveness of the proposed integration model. The results show that the proposed model can provide high-resolution results of local microclimate and airflow data around each building to predict building thermal responses and loads better. The building resilience against the power outage during the 1971 snowstorm of the century in Montreal was studied. A retrofitting analysis was also conducted by adding an external insulation layer to improve the buildings' resilience.

Chapter 6 Integration of CityBEM and Global Environmental Multiscale Models

In this chapter, to develop a multi-scale urban climate and buildings’ energy performance model, CityBEM is integrated with Surface Prediction System (SPS) model with 250-m grid spacing. SPS uses the atmospheric forecasting data of the HRDPS 2.5-km model as the B.C. The SPS 250-m results are extracted for all grid points, and a bi-linear interpolation scheme is used to interpolate data on each building in CityBEM. SPS is a 2D model. The developed multi-scale method by coupling the SPS and CityBEM can be applied for long period simulations such as a couple of months or even years of simulation. The integration of CityBEM and SPS is one-way, and there is no feedback from CityBEM to the near-surface atmospheric fields modeled by the SPS. Therefore, the CityBEM is added as a new module to the TEB scheme at the next step. Buildings’ energy performance, indoor air temperature, surface temperatures are calculated using CityBEM, and anthropogenic heat flux from buildings to the atmosphere and urban canopy air temperature are updated using the new scheme.

The integration of the CityBEM and TEB and using it in the SPS model can capture buildings' impact on the near-surface fields calculated by SPS. Still, there is no feedback from the surface model to the atmosphere (GEM model). Therefore, in future work, a new multi-scale urban climate and buildings’ energy performance model will be developed using the one-way grid nesting of the GEM-LAM model: 10km to 2.5km, 1km, and 250m. The TEB-CityBEM model will be used in all GEM-LAM models.

6.1. Integration of CityBEM and SPS

The surface Prediction system (SPS) is the Canadian external surface modeling system [110,111] that consists of the same ISBA and TEB surface models used in the GEM-LAM model. The SPS has been developed to provide surface and near-surface meteorological variables to improve numerical weather prediction and become a tool for environmental applications. SPS is a 2D model; therefore, it is computationally inexpensive and suitable for high-resolution modeling of surface and near-surface fields. Therefore, developing a multi-scale urban building performance and surface prediction system by coupling CityBEM with the SPS model can be used for high-resolution simulation of surface and near-surface parameters in urban areas. It is suitable for studying urban weather phenomena such as UHI and extreme weather events (heatwave and cold-wave). In this work, an SPS model is developed and used to simulate the Montreal metropolitan area during the 2018 summer heatwave. The horizontal grid spacing of the SPS model is 250-m. The SPS model's output is then interpolated on each building in CityBEM to calculate buildings' energy performance.

6.1.1. Urban and Land Surface Characteristics

The detailed specification of the land surface characteristics at each grid point of the computational domain is essential to forecast meteorological variables at the 250-m scale. For the Montreal metropolitan region, different databases are used to obtain a more realistic urban and land surface characteristics description. Leroux et al. [183] provided an urban classification of the Montreal metropolitan area to specify TEB parameters. They used several pan-Canadian databases for surface characterization. The databases are jointly processed to generate a high- resolution urban LULC classification for Canadian cities automatically. Classes generated by this processing were aggregated into 44 classes with 5 m spatial resolution (Fig. 6-1a). Following the same method, the

CanVec database is used as the main source of information, but using population density, and building footprint for the downtown as well, this classification is converted into the 45 TEB input parameters transposed on the final 250-m grid. Figs. 6-1b and 6-1c show the building fraction and height information for each grid point of the domain obtained from the LULC data.

6.1.2. Atmospheric Forcing

The atmospheric forcing of SPS is the hourly forecasts of the atmospheric fields obtained from the HRDPS 2.5-km model; the precipitation rate is derived at an hourly rate from the Canadian Precipitation Analyses (CaPA) system [184]. In SPS, the atmospheric forcing model's topography is first interpolated to the SPS grid. The forcing fields, such as temperature and specific humidity, are then vertically adjusted according to the difference in elevations between the SPS and the interpolated HRDPS. HRDPS forecasts are performed four times a day, i.e., every 6 hours: 12 am, 6 am, 12 pm, and 6 pm UTC. There are four choices to prepare the 6 hours forcing data for the SPS simulation: 1-6 h, 7-12 h, 13-18 h, 19-24 h. The first six hours are not recommended because the simulation's initialization may result in wrong precipitation and radiation fluxes in the initial hours of simulation [185].

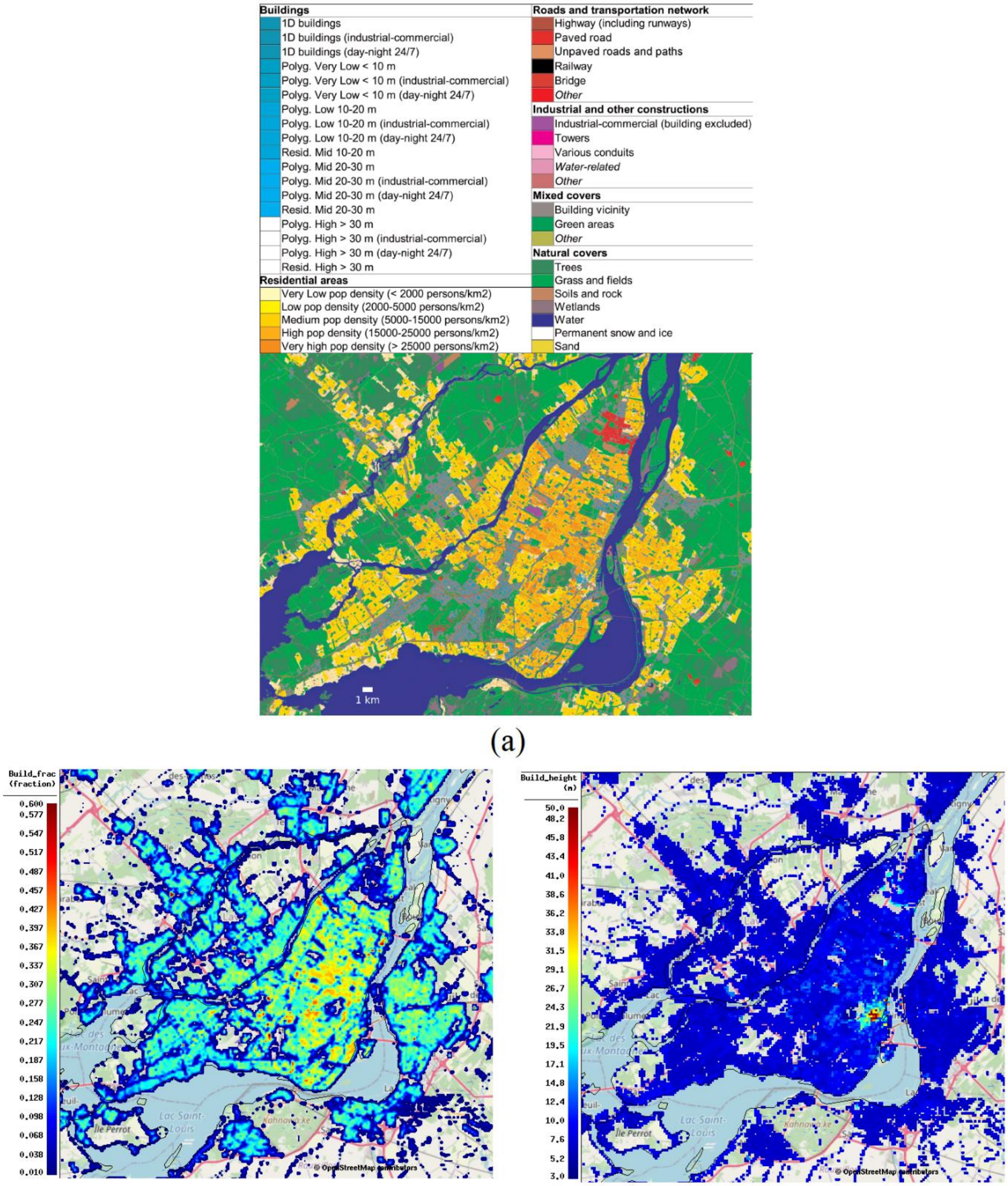

(a)

(b) (c)

Figure 6-1 a) overview of LULC classification over Montreal [183], b) Building fraction of each grid point, c) building height of each grid point.

Previous studies on offline SPS simulation show that the 6 h spin-up to the forecast, in this case, the 7-12 h of HRDPS forecast data, is the best approach for selecting the forcing data and can be considered the standard choice [110,112]. The schematic of the selection of forcing data is shown in Fig 6-2.

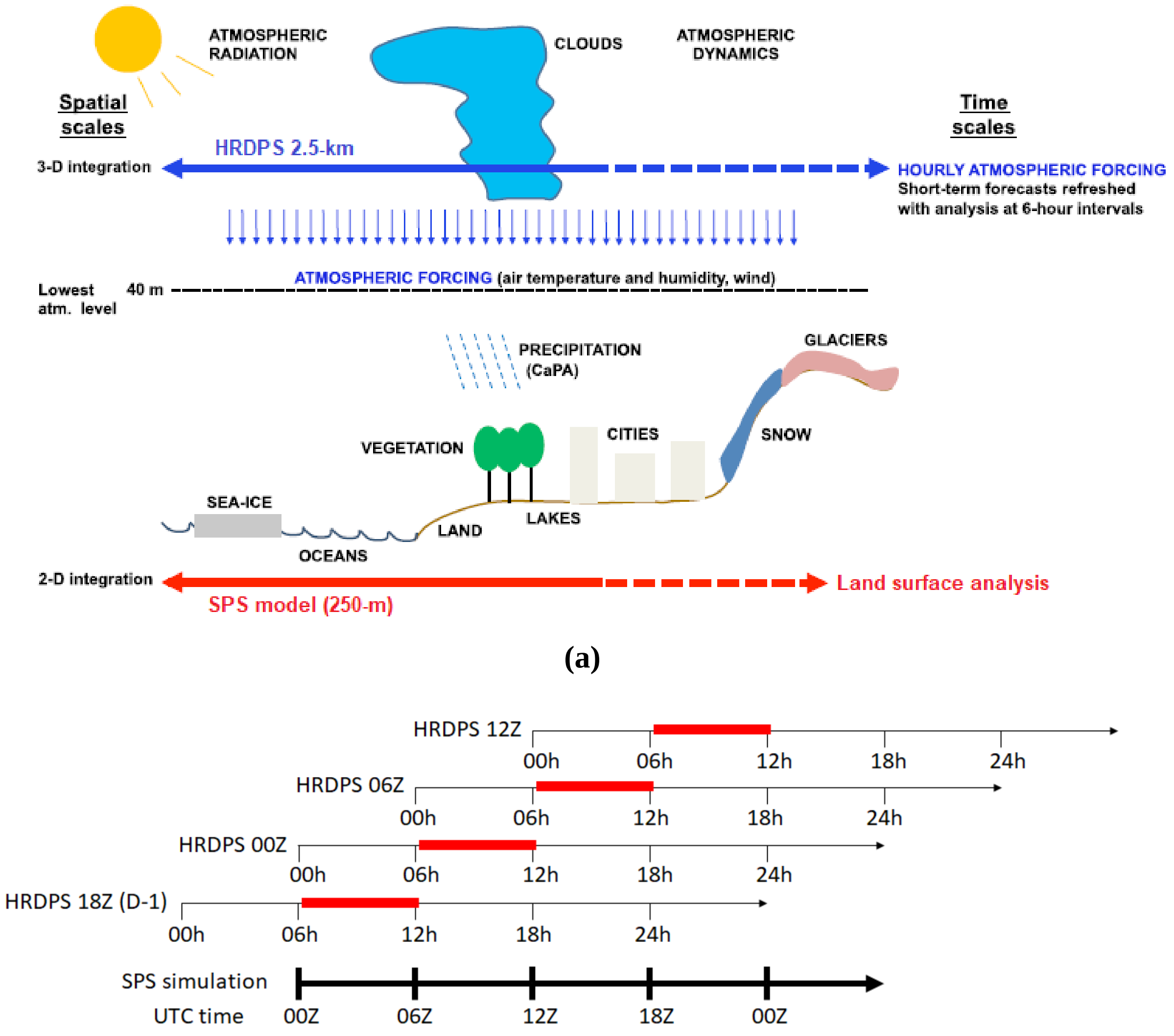

(a)

(b)

Figure 6-2 a) Flowchart of the SPS: SPS is driven by hourly atmospheric fields produced by the HRDPS 2.5-km and downscaled from the lowest atmospheric level to the land surface, b) Schematic of atmospheric forcing configurations in SPS over a diurnal cycle: 6 h spin-up atmospheric forcing in SPS simulations is constrained to HRDPS forecast hours 7–12.

6.1.3. Interpolation of SPS Data on Buildings in CityBEM

After the SPS simulation is finished, the 250-m SPS model's output is interpolated on each building. For this purpose, the coordinate of the building's footprint center point is calculated. Then, four SPS grid points around the building's center point are selected, and weather data are interpolated on the center point using a bi-linear interpolation scheme [186] considering the distance between points and the center of the building (Fig. 6-3).

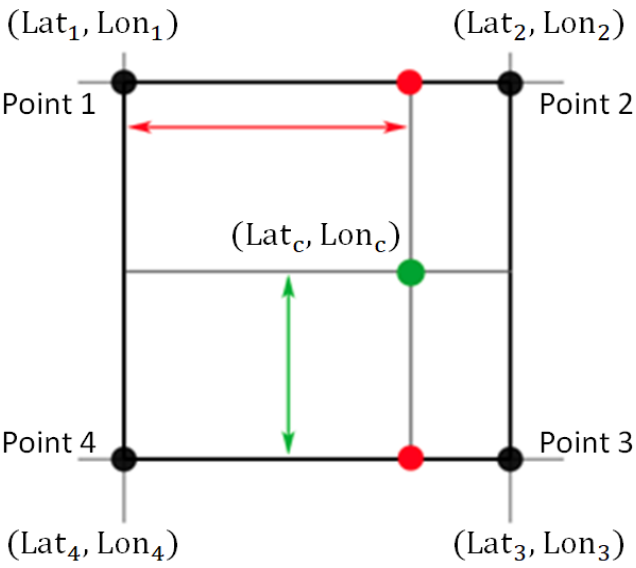

Figure 6-3 Interpolation of SPS output on the center point of the building. Points 1, 2, 3, and 4 are four SPS grid points around the building's center point.

The Montreal 3D building model used for CityBEM simulation is shown in Fig. 6-4. The 3D model of buildings is generated by integrating Microsoft buildings' footprint information and GE API for buildings height, as described in chapter 4. Buildings' type and year of construction for use in the archetype library is obtained from the shapefiles of boundaries of the property assessment units (PAU) in Montreal [146]. The total number of buildings in the area of study is 358295.


(a) **(b)**

Figure 6-4 3D model of buildings in Montreal: a) whole city model, b) downtown area.

6.1.4. Experimental Design

Future climate projections highlight a significant increase in extreme climate events' frequency and intensity, such as heatwaves. Summertime overheating is becoming a concern with significant impacts on energy consumption, greenhouse gas (GHG) emission, and occupants’ health. The overheating of building interior spaces as may arise from such climate change and extreme heat events has been identified as a significant concern to building occupants' comfort and health, particularly vulnerable people such as the elderly, children, and the physically challenged or the sick. The interaction between buildings and microclimate presented in Chapter 5 highlights the importance of using local microclimate for building energy simulation, especially during extreme weather events. Previous studies on GEM-LAM and SPS models also show the impact of high-resolution surface modeling on capturing the near-surface phenomena such as UHI. UHI can cause discomfort, respiratory difficulties, heat cramps and exhaustion, non-fatal heat stroke, and heat-related mortality inside buildings [13]. The 2018 Canadian heatwave was associated with more than 90 deaths in Quebec Province [14], many of which occurred in the dense urban areas due to

UHI. In this section, a continuous forecast is performed by SPS during the four warmest months in the Montreal region, from 0000 UTC 1 May 2018 to 0000 UTC 1 September 2018. This period includes the 2018 heatwave that occurred from June 30 to July 5, 2018. Then, the output of SPS forecasts is used for the buildings' energy simulation using CityBEM only for the heatwave period.

Validation of SPS Result

Measurement data by five weather stations around Montreal provided by the Environment and Climate Change Canada [151] are used to validate the SPS result. The weather stations and their location are shown in Table 6-1 and Fig. 6-5, respectively. All five weather stations are in urban or suburban areas. They are located near the ground, and the average height of sensors is 2 m. Therefore, screen level (1.5 m) air temperature, dew-point temperature, and wind speed calculated by SPS are compared with weather stations' measurement data.

Table 6-1 Name and location of five weather stations for validation of the SPS result.

Weather station	Name	Latitude	Longitude
WS_1	McTavish	45°30'17.070" N	73°34'45.000" W
WS_2	ST-HUBERT	45°31'03.000" N	73°25'01.000" W
WS_3	INTL A	45°28'14.000" N	73°44'27.000" W
WS_4	TRUDEAU INTL	45°28'04.000" N	73°44'30.000" W
WS_5	BELLEVUE	45°25'38.000" N	73°55'45.000" W

Standard metrics to evaluate the accuracy of the forecasting result include mean bias error (MBE, or bias), root mean square error (RMSE), and standard deviation (STDE). These are defined as follows:

$$MBE = \frac{1}{N}\sum_{i=1}^{N}\left(x_{f,i} - x_{o,i}\right) \qquad \text{Eq. 6-1}$$

$$RMSE = \sqrt{\frac{1}{N}\sum_{i=1}^{N}\left(x_{f,i} - x_{o,i}\right)^2} \qquad \text{Eq. 6-2}$$

$$STDE = \sqrt{RMSE^2 - MBE^2} \qquad \text{Eq. 6-3}$$

Where $x_{f,i}$ is the measurement data and $x_{o,i}$ is the simulation result. The MBE is the average forecast error representing the SPS model's systematic error to under or over forecast. MBE gives the average magnitude of forecast errors, while RMSE gives more weight to the largest errors. RMSE without systematic error (STDE) captures the part of the RMSE that is not due to systematic error.

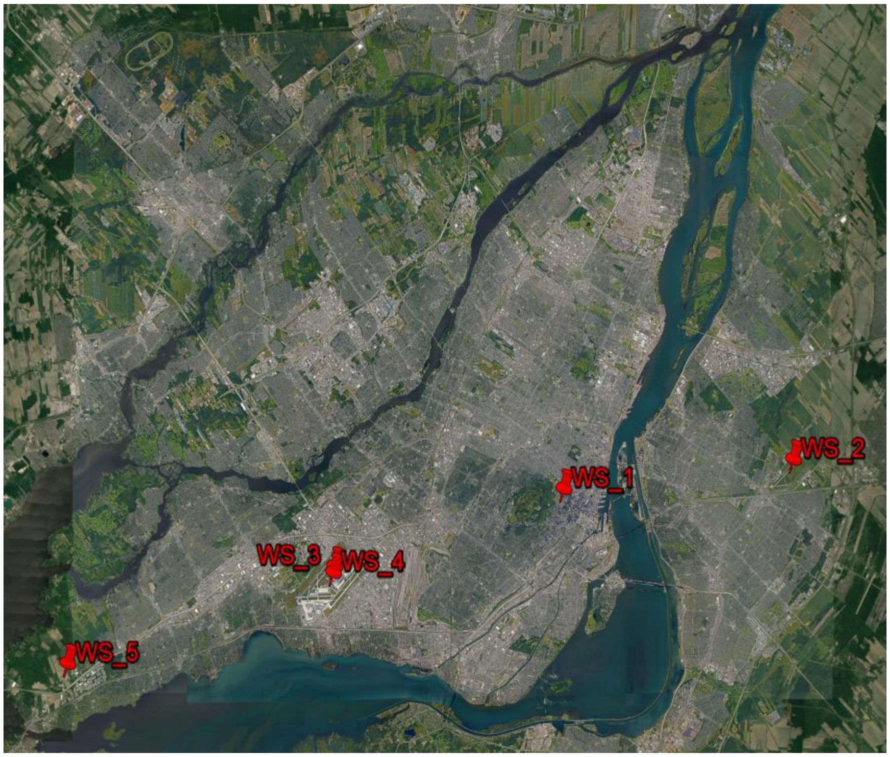

Figure 6-5 Location of the five weather stations in Montreal for validation of the SPS result

Table 6-2 Comparison of SPS result with weather stations' measurement data.

Variable	WS	Station	Bias	RMSE	STDE
Air temperature	WS_1	McTavish	-0.074	2.487	2.486
	WS_2	ST-HUBERT	-0.029	1.859	1.859
	WS_3	INTL A	-0.550	1.867	1.785
	WS_4	TRUDEAU	-0.587	1.995	1.907
	WS_5	BELLEVUE	0.405	1.705	1.656
	-	Average	-0.167	1.982	1.938
Wind speed	WS_1	McTavish	0.396	1.187	1.119
	WS_2	ST-HUBERT	-0.926	1.816	1.563
	WS_3	INTL A	-0.798	1.697	1.498
	WS_4	TRUDEAU	-0.197	1.283	1.268
	WS_5	BELLEVUE	0.596	1.353	1.215
	-	Average	-0.185	1.467	1.332
Dew point temperature	WS_1	McTavish	0.154	2.031	2.026
	WS_2	ST-HUBERT	-0.784	1.940	1.774
	WS_3	INTL A	-0.416	1.852	1.805
	WS_4	TRUDEAU	-0.003	1.975	1.975
	WS_5	BELLEVUE	-0.621	2.031	1.933
	-	Average	-0.334	1.965	1.902

Table 6-2 presents the MBE, RMSE, and STDE of air temperature, wind speed, and dew point temperature compared to the measurement data. Results are presented for all five stations and the average of the stations. The hourly comparison of the simulation and measurement data for the heatwave period is shown in Figs. 6-6 and 6-7. The average MBE, RMSE, and STDE of air temperature are -0.167 ℃, 1.982 ℃, and 1.938 ℃, respectively. The air temperature is a little underestimated during the daytime and overestimated during the nighttime. The average error of simulated air temperature is less than 2 ℃, and the simulation result is in good agreement with measurement data. The average MBE, RMSE, and STDE of simulated wind speed are $-0.185\ m/s$, $1.467\ m/s$, and $1.332\ m/s$, respectively. The RMSE of all stations is less than $1.816\ m/s$. Comparing with the accuracy of previous studies and other NWP systems shows that the simulation results are in good agreement with measurement data. The average MBE, RMSE, and STDE of simulated dew point temperature are -0.334 ℃, 1.965 ℃, and 1.902 ℃, respectively. It shows the good accuracy of the screen level's dew point temperature calculated by SPS compared to the measurement data. In conclusion, comparing the SPS result with observation data from weather stations highlights the simulation result's good accuracy.

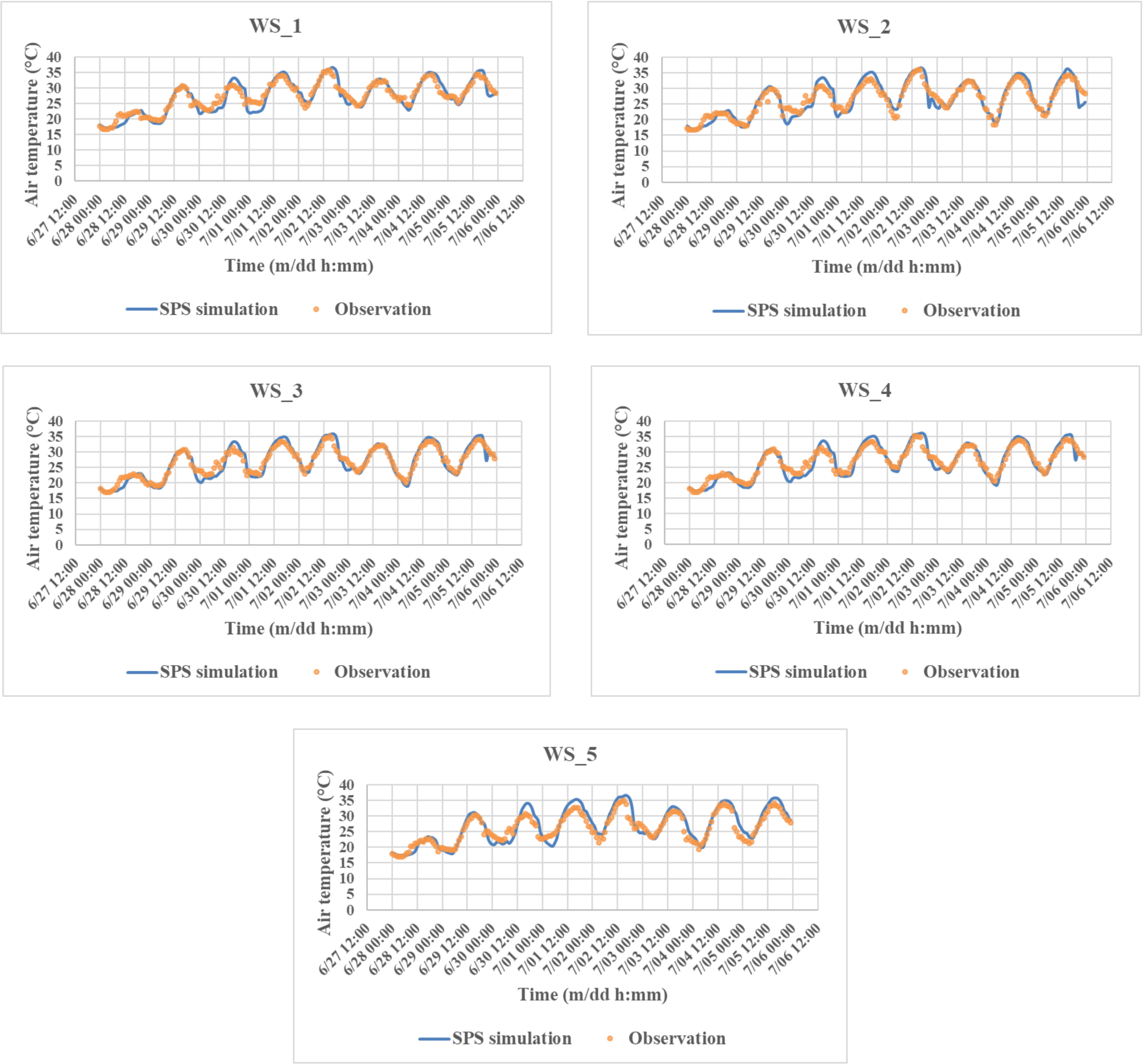

Figure 6-6 Comparison of SPS' near-surface air temperature with measurement data of five weather stations.

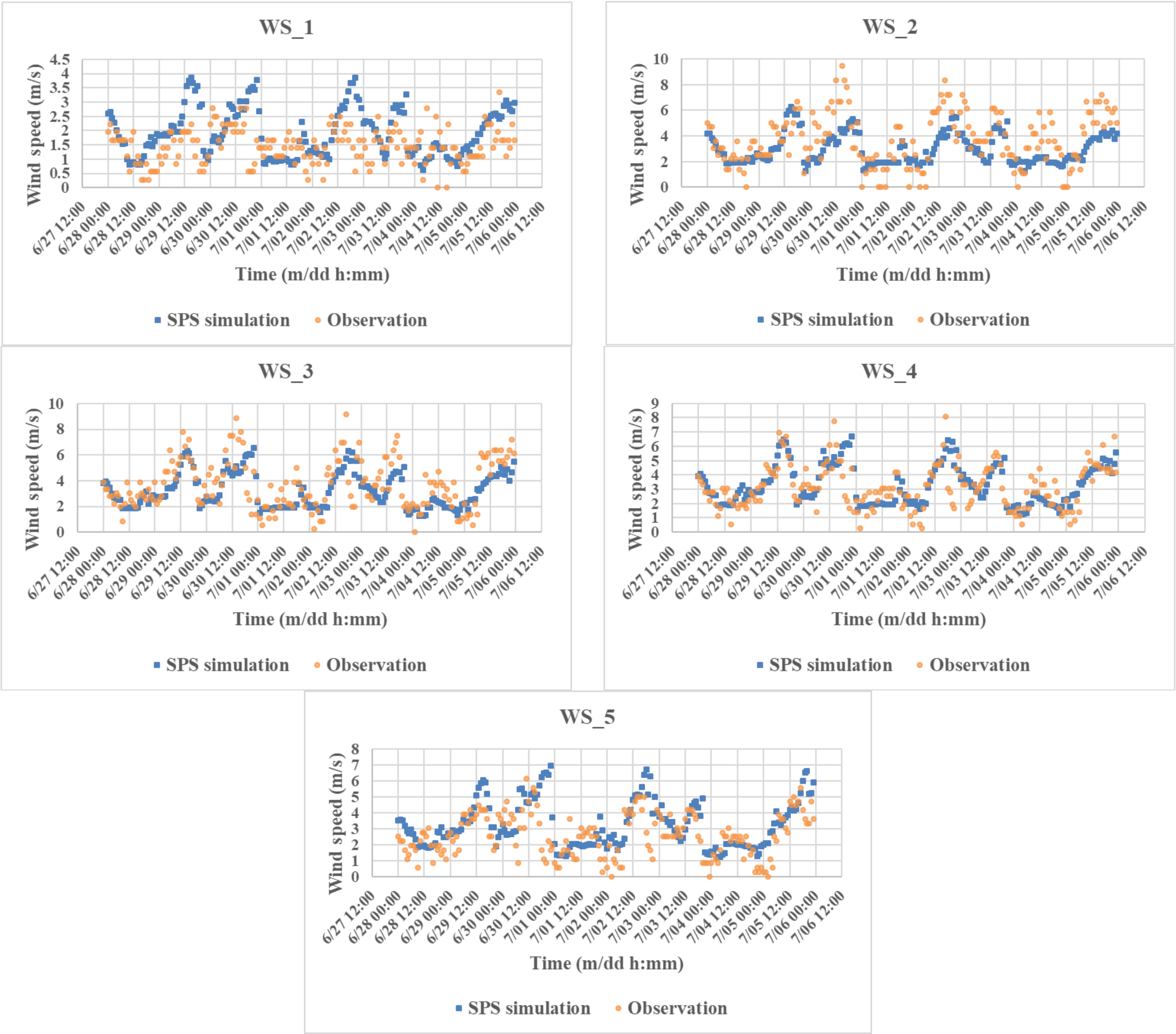

Figure 6-7 Comparison of SPS' near-surface wind speed with measurement data of five weather stations

Vulnerable Buildings and Regions Against Heatwave

In this section, the SPS and CityBEM result on June 29, 4 pm is studied. Fig. 6-8 shows the surface radiative temperature, screen level air temperature, and the Universal Thermal Climate Index (UTCI) calculated by SPS. UTCI is the radiation-based thermal stress index implemented into the SPS and GEM models [104]. The near-surface air temperature of all urban areas is higher than 30 ℃. SPS provides high-resolution results near the surface. Some areas are hotter than other regions and can be considered as local hotspots during the heatwave. Surface radiative temperature and UTCI index highlight the same regions as vulnerable areas against heatwave.

Fig. 6-8d shows the surface temperature gradient obtained from Quebec open dataset [187,188]. This figure is based on the satellite imagery data with 20-m resolution and shows the relative surface temperatures. Comparing the hotspots modeled by SPS with Fig. 6-8d shows that the high-resolution SPS model can accurately predict Montreal's hotspots. Local outdoor air temperature interpolated on the buildings is plotted in Fig. 6-8e. Comparison of the Figs. 6-8e and 6-8b shows that the SPS local weather data are correctly interpolated on each building. Fig. 6-8f presents the buildings' surface temperature calculated by CityBEM. Buildings' year of construction is shows in Fig. 6-8g. in downtown As discussed in chapter 5, the buildings' surface temperature depends on the local microclimate and the building envelope's thermal properties. Usually, the surface temperature of buildings in hotspots is higher than in other areas. It causes more energy consumption and higher indoor air temperature in the lack of air conditioning systems. The results presented by CityBEM can help to find vulnerable buildings against heatwave. Mitigation strategies can be studied to improve buildings' resiliency against heatwave. My future work includes the validation of CityBEM and SPS results using MODIS satellite imagery. Also, a more detailed analysis will be done on the CityBEM result, and different scenarios such as power outage or lack of air conditioning system will be studied to investigate the indoor thermal comfort and building's resiliency against heatwave.

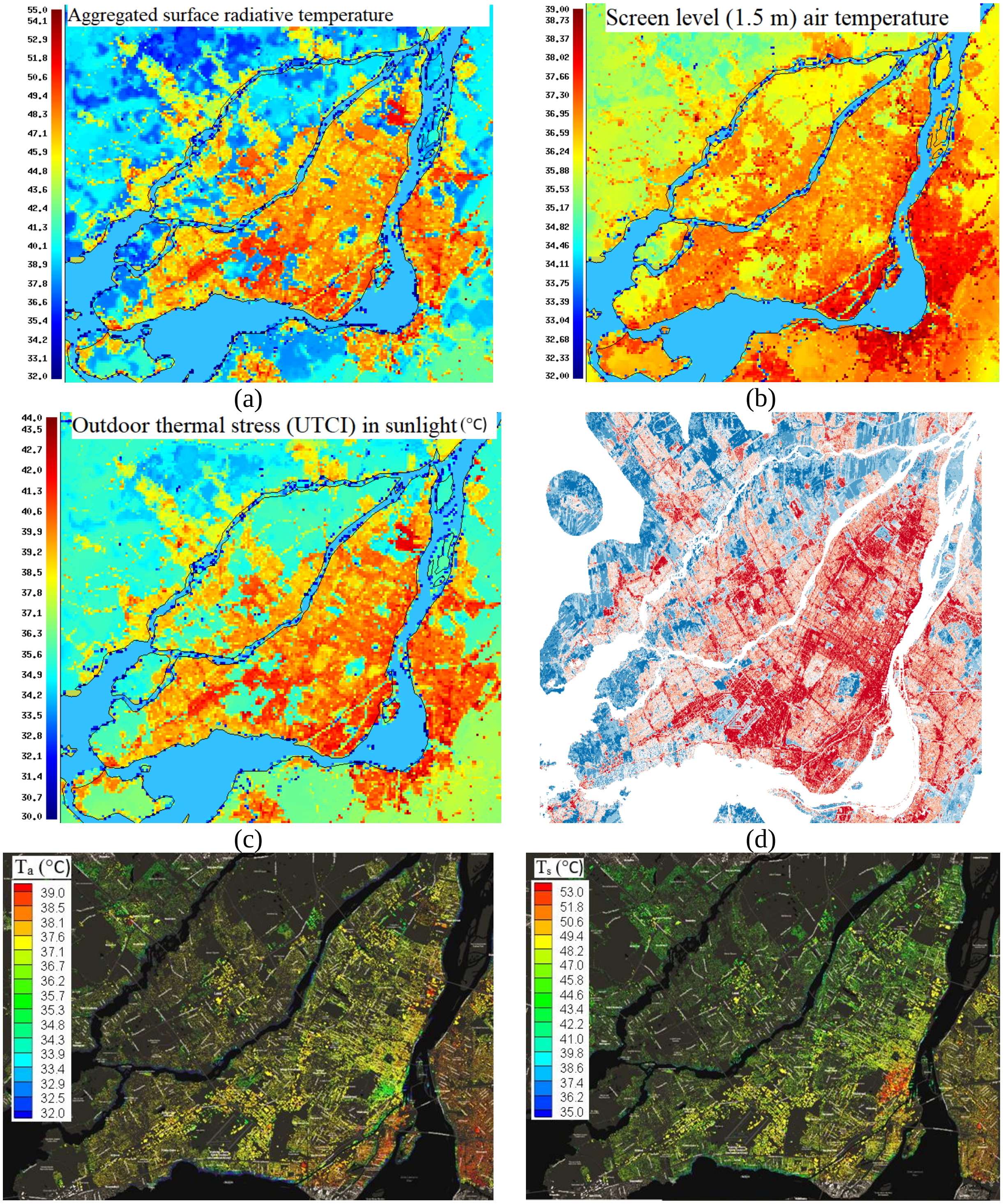
Aggregated surface radiative temperature
55.0
54.1
52.9
51.8
50.6
49.4
48.3
47.1
45.9
44.8
43.6
42.4
41.3
40.1
38.9
37.8
36.6
35.4
34.2
33.1
32.0
Screen level (1.5 m) air temperature
39.00
38.73
38.37
38.02
37.66
37.30
36.95
36.59
36.24
35.88
35.53
35.17
34.82
34.46
34.11
33.75
33.39
33.04
32.68
32.33
32.00
Outdoor thermal stress (UTCI) in sunlight (°C)
44.0
43.5
42.7
42.0
41.3
40.6
39.9
39.2
38.5
37.8
37.1
36.3
35.6
34.9
34.2
33.5
32.8
32.1
31.4
30.7
30.0
T_a (°C)
39.0
38.5
38.1
37.6
37.1
36.7
36.2
35.7
35.3
34.8
34.3
33.9
33.4
32.9
32.5
32.0
T_s (°C)
53.0
51.8
50.6
49.4
48.2
47.0
45.8
44.6
43.4
42.2
41.0
39.8
38.6
37.4
36.2
35.0

(a) (b)

(c) (d)

(e) (f)

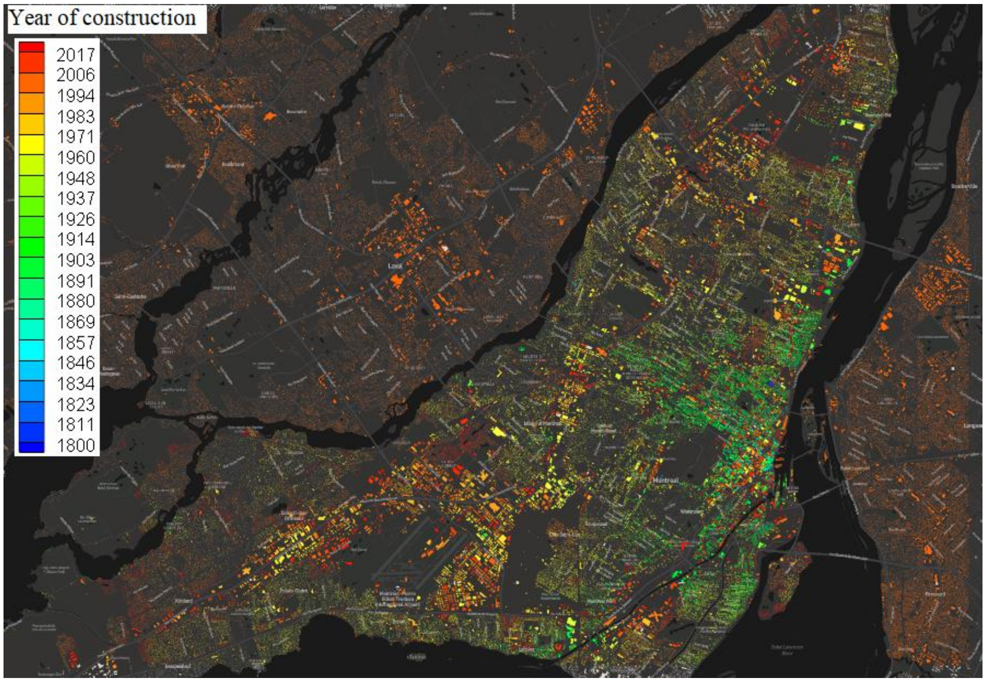

Figure 6-8 a) surface radiative temperature by SPS, b) screen-level air temperature by SPS, c) UTCI calculated by SPS, d) surface temperature obtained from DONNÉES QUÉBEC, e) outdoor air temperature interpolated on buildings, f) buildings' surface temperature calculated by CityBEM, g) buildings' year of construction

6.2. Add CityBEM to the SPS-TEB Model

As already discussed, the TEB model is a simplified urban surface model, especially for modeling the buildings. Therefore, it is crucial to add a detailed building energy model to TEB to improve anthropogenic fluxes' estimation from buildings' surfaces to the atmosphere and provide forecasting results of buildings' energy performance. The multi-scale models studied in previous sections can perform short-term forecasting of buildings' energy analysis. Still, they cannot capture the impact of buildings on near-surface atmospheric fields. Therefore, the CityBEM model is added as a new subroutine to the TEB module of GEM-LAM and SPS models in this section. For this purpose, all the physical equations and components of the CityBEM described in Chapter 4 are entirely added to the TEB model (Fig. 6-9). The archetype library for the estimation of building non-geometrical properties is also defined in the TEB-CityBEM code.

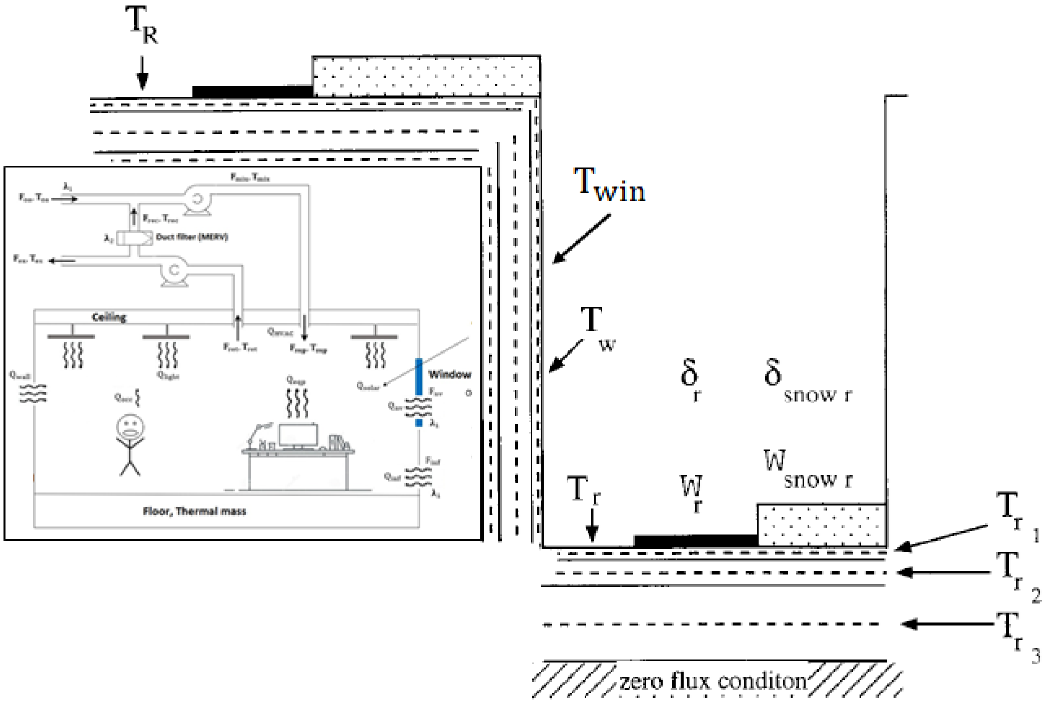

Figure 6-9 Schematic of the TEB-CityBEM model.

6.2.1. Buildings' Geometrical and Non-Geometrical Properties

The urban canopy scheme used in the TEB model is based on 1D analysis, and the real orientation of buildings' façade is not considered for calculation of short-wave radiation. Also, to assign non-geometrical properties to the buildings, buildings' type and year of construction information are required. The current LULC dataset only covers limited buildings and does not include the buildings' year of construction information. To provide this information for each grid point in the SPS model, the coordinates (Latitude and Longitude) of all grid points for the study region are extracted. Then, for each grid point, the building's properties located in that location are extracted from the 3D buildings model and Montreal PAU shapefile. The data is added to the TEB-CityBEM dataset. This method is applied to the SPS 250-m model of Montreal studied in section 6.1.

6.2.2. Experimental Design

The developed TEB-CityBEM model is applied to the SPS model of Montreal with 250-m grid spacing. The model is launched for two days of summer 2018: May 1-2, 2018. Fig. 6-10 shows the near-surface air temperature, window surface temperature, and HVAC energy consumption distribution inside the domain on May 2, 8 pm UTC. Results show that the TEB-CityBEM model is launched successfully on the ECCC server. The near-surface air temperature in urban areas is around 14 °C. Therefore, considering the indoor set-point temperature of 21 °C, buildings are in heating mode. All buildings' window surface temperature is higher than 18 °C, larger than the outdoor air temperature because the indoor air temperature is higher than the ambient air temperature. The glazing also absorbs part of the solar radiation. The HVAC energy consumption results show relatively higher energy consumption in Montreal's downtown due to high-rise buildings and a higher density of buildings in this area.

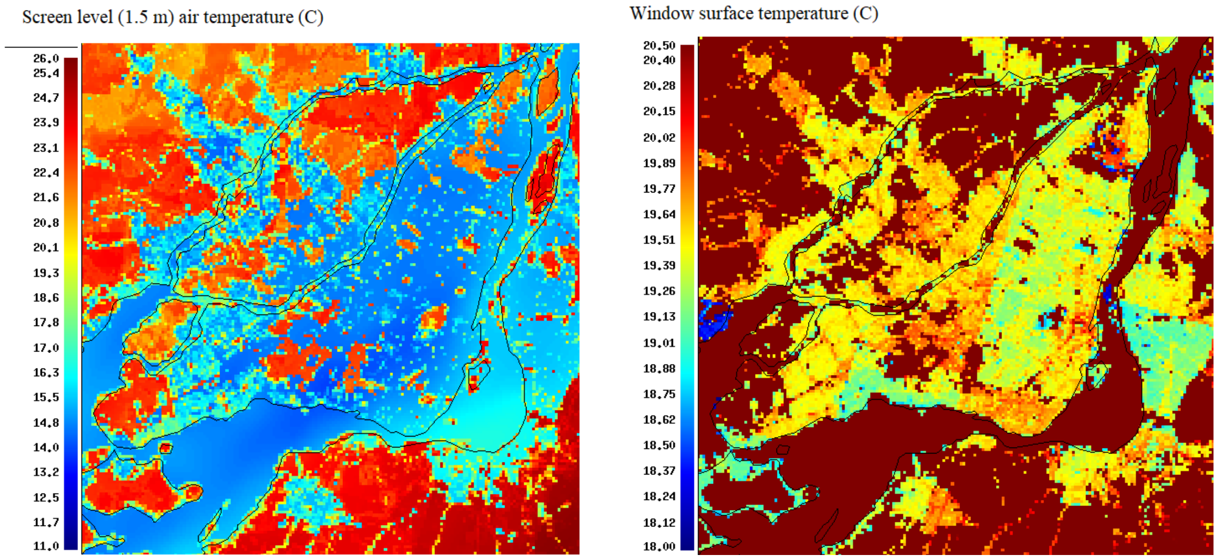

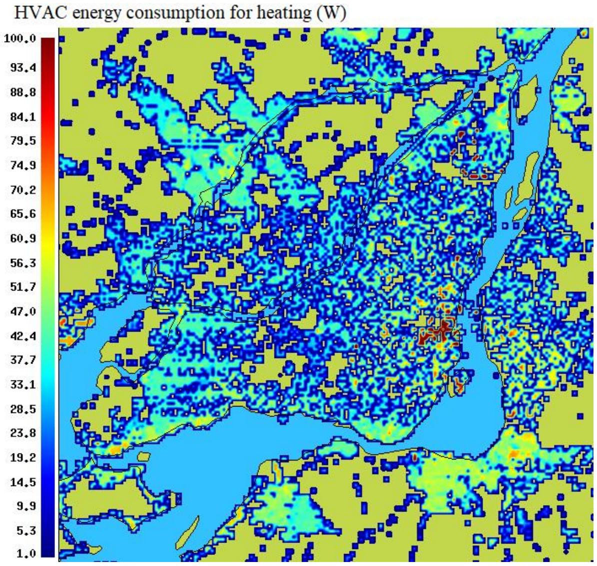

Figure 6-10 TEB-CityBEM result for Montreal simulation on May 2, 2018, 8 pm UTC

The results presented in this section are preliminary analyses showing that the CityBEM model is successfully added to the TEB model. Future work will focus on 1) the validation of the TEB-CityBEM model by verifying that the applied equations are solved correctly, and comparison of energy consumption, surface temperature, and indoor air temperature with measurement data, 2) compare the screen level atmospheric fields with the results obtained only by TEB model and measurement data to study the impact of CityBEM model on the accuracy of surface and near-surface simulation, 3) Use the new TEB-CityBEM model in the GEM-LAM model and the ECCC air quality model (GEM-MACH) to study the impact of CityBEM on the accuracy of urban atmosphere and air quality forecasting result. For this purpose, the TEB-CityBEM model will be implemented to a one-way grid nesting of the GEM-LAM model. The sub-kilometer model of Montreal is shown in Fig. 6-11. Three nested grids with 2.5-km, 1-km, and 250-m grid spacings were set up to focus on the Montreal metropolitan area. The 10-km RDPS model provides the initial and boundary conditions for the HRDPS 2.5-km model.

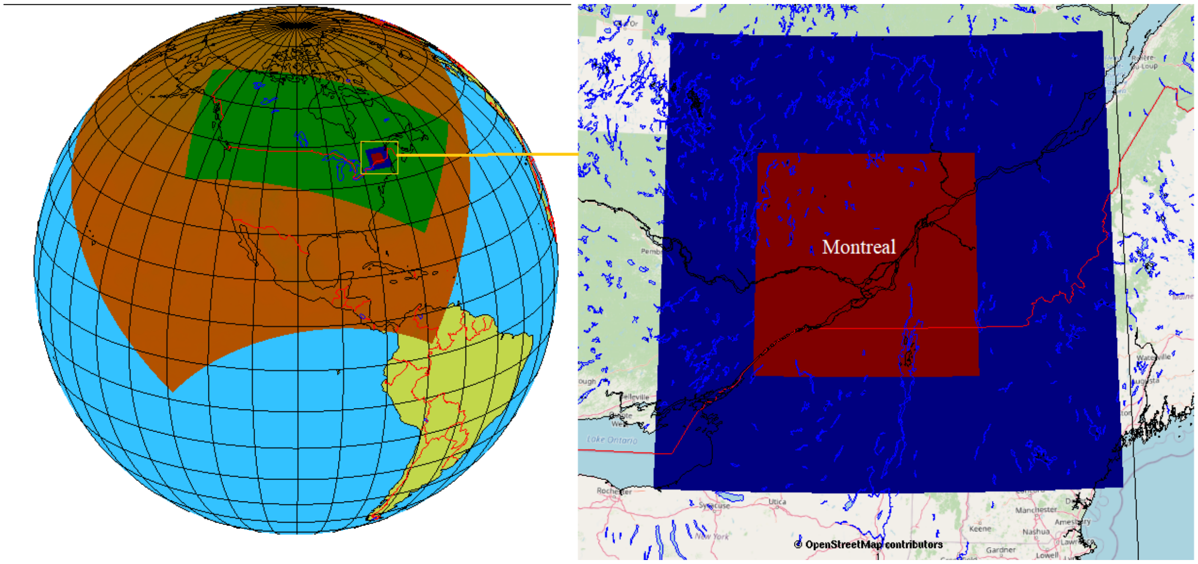

Figure 6-11 Schematic of multi-scale GEM-LAM model.

6.3. Summary

In this chapter, a multi-scale urban building energy and climate simulation tool is developed by coupling SPS and CityBEM models. The developed system can perform kilometer to sub-kilometer and buildings’ scale simulation. The output of the high-resolution SPS models is interpolated on center points of buildings in CityBEM. In this model, there is no feedback from buildings and CityBEM on the atmospheric fields. Therefore, CiyBEM is added to the TEB scheme in the SPS model to capture buildings' impacts on near-surface atmospheric fields. The model is used for simulation of the 2018 summertime in Montreal. Results show that the high-resolution multi-scale model can find the vulnerable areas and buildings against the heatwave.

Chapter 7 Integration of CityBEM and City Reduced Probability of Infection Models

City Reduced Probability of Infection (CityRPI)[1] is a model developed to calculate airborne transmission of COVID-19 in all buildings' indoor spaces in a city. In this chapter, the CityRPI methodology is introduced. Different mitigation strategies for reducing the risk of infection in indoor spaces are studied. To study the impact of different strategies on the infection risk and energy consumption of buildings, CityBEM is integrated with CityRPI. Simultaneous CityBEM and CityRPI simulation is performed. The schematic of the integrated CityBEM-CityRPI model is shown in Fig. 7-1.

7.1. Modeling Aerosol Infection Risk

The aerosol infection risk calculation is based on the modified Wells-Riley Formulation [189,190], which Miller et al. [124] used to calculate airborne transmission of COVID-19 in indoor microenvironments. Miller et al. [127] made five assumptions for applying this approach: i) calculation of aerosol infection risk is based on the presence of one infected person who emits SARS-CoV-2 quanta (a quantum is defined as the dose of airborne droplet nuclei required to cause infection in 63% of susceptible persons) with a constant rate, ii) there are not any earlier SARS-CoV-2 quanta in the space, iii) the latent period of the disease (i.e., the period between exposure and infection) is longer than the time duration of the event. Based on this assumption, the quanta emission rate remains constant during the event, iv) the indoor environment can be modeled as well-mixed, and the infectious respiratory aerosol is evenly distributed throughout the room air, and v) the infectious quanta removing by the ventilation, filtration, deposition on surfaces, and

---

[1] I did the CityRPI project in collaboration with Mr. Maher Albettar and Dr. Leon Wang - https://concordia-cityrpi.web.app/

airborne inactivation is a first-order process considered the in the model. Two types of PI are calculated in this work: conditional PI and absolute PI. The conditional probability of infection (PI_{cond}) is calculated based on the assumed number of infected people inside the room, and the prevalence rate of the disease in the area of study is neglected in the calculation. Absolute probability of infection (PI_{abs}) is calculated based on the PI_{cond} and considering the prevalence rate of the disease in the area of study.

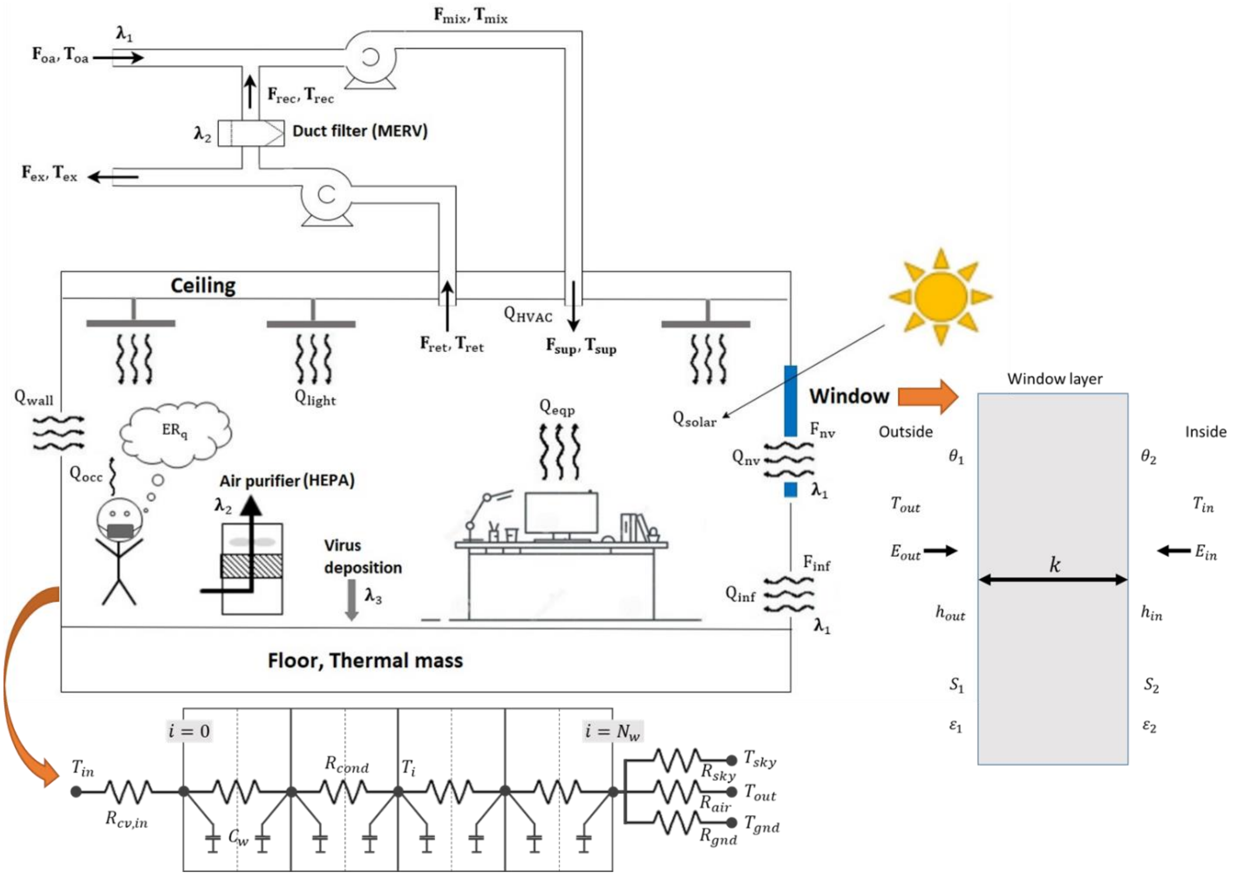

Figure 7-1 Schematic of the CityRPI model combined with CityBEM.

7.1.1. Conditional Probability of Infection

The conditional probability of infection (PI_{cond}) is given by the expression:

$$PI = 1 - e^{-\mu} \qquad \text{Eq. 7-4}$$

where μ is the number of quanta inhaled by a susceptible. Consider a susceptible in the room who inhales at rate B (m^3/h) and is present for T hours. The expected number of quanta inhaled is calculated by Eq. 7-2:

$$\mu = C_{avg} \times B \times T \times (1 - f_m \times M_{in}) \qquad \text{Eq. 7-5}$$

C_{avg} is the time-average quanta concentration (q/m^3); f_m is the fraction of people in the room who wears the mask, and M_{in} is the inhalation mask efficiency. By solving the well-mixed material balance equation for the room, the C_{avg} is calculated using Eq. 7-3.

$$C_{avg} = \frac{G}{\lambda V}\left[1 - \frac{1}{\lambda T}\left(1 - e^{-\lambda T}\right)\right] \qquad \text{Eq. 7-6}$$

V is the volume of the room (m^3); λ is the first-order loss rate coefficient for quanta (h^{-1}); and G is the net quanta emission rate (h^{-1}) which is calculated based on the number of infected people in the room $\left(N_{inf}\right)$, the fraction of people in the room with the mask (f_m), exhalation mask efficiency (M_{ex}), and quanta emission rate by one infected individual ER_q (Eq. 7-4).

$$G = \mathrm{ER}_q(1 - f_m \times M_{ex}) \times N_{inf} \qquad \text{Eq. 7-7}$$

Buonanno et al. [191] calculated the quanta emission rate ER_q of SARS-CoV-2 for different combinations of expiratory activities (oral breathing, speaking, and singing or loudly speaking) and activity levels (resting, light activity, and heavy exercise).

7.1.2. First-order Loss Rate Coefficient (λ)

The infectious quanta can be removed from room air by first-order processes reflecting several mechanisms: outdoor air ventilation (λ_1), filtration (λ_2), deposition on surfaces (λ_3), and airborne inactivation (λ_4).

$$\lambda = \lambda_1 + \lambda_2 + \lambda_3 + \lambda_4 \qquad \text{Eq. 7-8}$$

First, infectious quanta are removed with a first-order rate constant λ_1 equal to the air change of outdoor air per hour (h^{-1}) supplied to the room by the HVAC system or opening the windows. Second, the in-room air filtration using portable air purifiers and/or duct filters in HVAC systems for recirculation of filtered indoor air can remove infectious quanta with a rate constant λ_2. Third, infectious quanta are removed by gravitational settling with a first-order rate constant λ_3. The deposition rate is calculated by Buonanno et al. [133] as the ratio between the settling velocity of super-micrometric particles and the height of the emission source and is equal to 0.24 h^{-1}. Finally, infectious quanta are biologically inactivated with a first-order rate constant λ_4. The quanta inactivation was evaluated based on the SARSCoV-2 half-life (1.1 h) [192] and is equal to 0.63 h^{-1}.

7.1.3. Absolute Probability of Infection

For estimation of infection risk in city-scale where the number of infected individuals in each building is not known, the prevalence of the disease in the community is used to estimate how many infected individuals may be present in the building, and the absolute probability of infection PI_{abs} is calculated based on estimated infected individuals [193].

$$PI_{abs} = 1 - (1 - PI_{cond} \times P_{prev})^{N_{sus}} \qquad \text{Eq. 7-9}$$

$$N_{sus} = N_{tot} \times (1 - F_{immune}) \quad \text{Eq. 7-10}$$

$$P_{prev} = \frac{N_{new}}{P} \times \left(1 - f_{unrep}\right) \times D \quad \text{Eq. 7-11}$$

P_{prev} is the disease prevalence in the community that depends on the state of the pandemic in the region of study and the period. N_{new} and P are the number of daily new cases and the population of the studied region, respectively. f_{unrep} is the fraction of unreported cases. A study on ten diverse geographical sites in the US shows that the estimated number of infections was much greater (6 to 24 times) than the number of reported cases in all sites [194]. D is the duration of the infectious period of SARS-CoV-2 [195]. N_{tot} and N_{sus} are the total number and number of susceptible people in the room, respectively. F_{immune} is the fraction of the population that has had the disease and has some immunity against it. It can be estimated using the total number of infected people in the region of study [194,196].

7.1.4. Outdoor Ventilation Rate and Number of Occupants

The real number of occupants and outdoor ventilation rates are not known for all buildings in a city. These parameters are estimated based on the ASHRAE Standard 62.1-Table 6.2.2.1 [197]. The table provides occupant density D_{occ} $(\#/100m^2)$, and combined outdoor air rate per person R_p $(cfm/person)$ for different occupancy category (building type). Using these two parameters and the floor area of the building A_f (m^2), total number of occupants N_{tot} and air change of outdoor air per hour ACH_{vent} (h^{-1}) can be estimated by

$$N_{tot} = D_{occ} \times \frac{A_f}{100} \quad \text{Eq. 7-12}$$

$$ACH_{vent} = \frac{R_p \times N_{tot} \times 1.699}{A_f \times H} \qquad \text{Eq. 7-13}$$

7.1.5. Development of Archetype Library

For calculation of the indoor probability of infection in all buildings in a city using Eqs. 7-1 to 7-10, several building-related parameters are needed, including floor area, ceiling height, average stay time, the average age of occupants, occupant density, and outdoor air rate per person. The floor area of buildings is obtained from open data sources such as OpenStreetMap (OSM) [198] and Microsoft buildings' footprint [199,200], but other parameters are not available for all buildings in a city. In this work, to estimate all required parameters for PI calculation, an Archetype library is developed. In this library, buildings are classified into 31 different usage types. Then, the required parameters are assigned to each class. The usage type of buildings can be provided by local datasets that are available for most of the cities around the world. For the City of Montreal studied in this work, buildings' usage type information is provided by the shapefiles of boundaries of the property assessment units (PAU) [146]. PAU is the vector geospatial data of the subdivision of the Montreal agglomeration properties containing the general information on the units of property assessments, particularly the codification of use (CUBF), year of construction, and the approximate dimensions.

7.2. Validation of CityRPI and CityBEM Results

In this section, separate validations are done on the CityRPI and CityBEM models.

7.2.1. Validation of Aerosol Infection Risk Calculation

For the validation of the CityRPI model, a real outbreak occurred due to the attendance of a symptomatic index case at a weekly rehearsal of the Skagit Valley Chorale (SVC) [127] is modeled.

Results are compared with those of Miller et al. [127] and COVID-19 Aerosol Transmission Estimator (COVID-19 ATE) [193].

Table 7-1 Parameters used for the simulation of SVC super spreading event

Parameter	Symbol	Unit	Value
Volume	V	(m^3)	810
Duration of event	T	hour	2.5
Volumetric breathing rate	B	(m^3/h)	1.0
Quanta emission rate	ER_q	$quanta/h$	970
Fraction of the population with immunity	F_{immune}	-	0
Fraction of people with mask	f_m	-	0
Total number of people in the room	N_{tot}	-	61
Number of infective people	N_{inf}	-	1
Disease prevalence rate	P_{prev}	%	0.011

Table 7-1 shows the simulation settings of the SVC super spreading event. The mean quanta emission rate of 970 $quanta/h$ was estimated using the Monte Carlo simulation based on the reported infection rate of the event. Conditional and absolute probability of infections are calculated as a function of loss rate λ and results are shown in Fig. 7-2. Infection risks calculated by CityRPI are the same as Miller et al. [127] and COVID-19 ATE, which shows that the calculation of infection risk by the CityRPI model is consistent with other validated works.

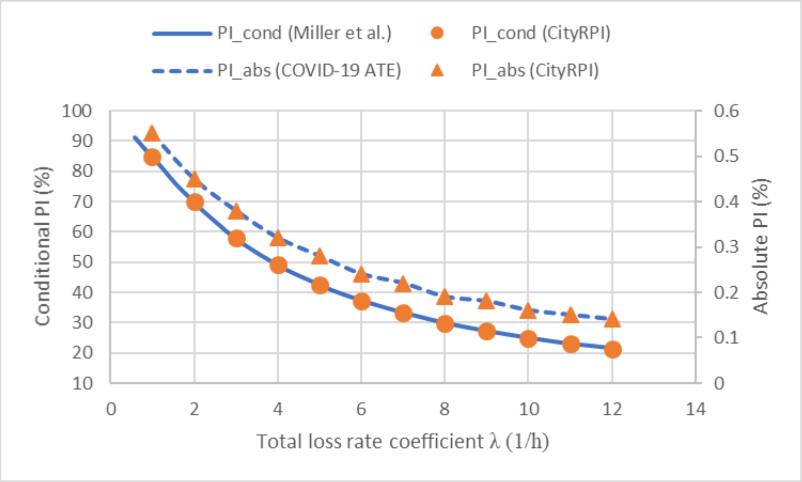

Figure 7-2 Comparison of PI_{cond} and PI_{abs} at different loss rate coefficients for SVC super spreading event calculated by CityRPI, COVID-19 ATE, and Miller et al. [127]

7.2.2. Validation of Indoor Air Temperature Result

Accuracy of the CityBEM for calculation of buildings' energy performance is already investigated by comparing the annual and hourly electricity consumption with corresponding measurement data [85,201]. In this work, for the validation of indoor air temperature results calculated by CityRPI, the City of Montreal is simulated from June 24-29, 2020. The calculated indoor air temperature of two school buildings is compared with measurement data provided by sensors installed in different buildings' rooms. Figs. 7-3a and 7-3b show the schools' aerial view map and weather data (outdoor air temperature and solar radiation) used for the simulation. According to Fig. 7-3b, the studied days are hot and sunny. In the absence of Air conditioning (AC) systems in the buildings, it is expected that indoor air temperature is higher than the cooling-setpoint temperature. School 1 is a two-story building constructed in 1953. There are some Air Conditioning (AC) units in the classrooms, but they did not work during the simulation period because of insufficient power. Two indoor sensors are installed in two classrooms on the first floor. School 2 is a two-story building constructed in 1958 with four indoor sensors to measure indoor air temperature. All sensors are installed in the classrooms, two of them are on the first floor, and two other sensors are on the second floor. There is not any AC system in the classrooms. Due to the lack of AC systems in the buildings, the HVAC model is disabled in CityRPI simulation. Figs. 7-3c and 7-3d compare the indoor air temperature calculated by CityRPI with all sensors data of school one and school 2, respectively. Accuracy of the result is acceptable considering the uncertainties of the input parameters used for CityRPI simulation and the simplified single-zone model used for the whole building. The RMSE between the average temperature of classrooms and simulation results of schools 1 and 2 are 1.78 ℃ and 1.56 ℃, respectively.

(a) (b)

(c) (d)

Figure 7-3 Validation of indoor air temperature calculated by CityRPI: a) aerial view map, b) weather data of simulation period, c) comparison of simulation and measurement data of school 1, d) comparison of simulation and measurement data of school 2.

7.3. Case study and Result

According to equations 7-1 to 7-10, the indoor aerosol infection risk is a function of several parameters. Some of them including the number of occupants, ventilation rate, stay time, and breathing rate depending on the building usage type. Therefore, infection risk and the effectiveness of mitigation measures can change by the type of building. In this section, the City of Montreal is modeled by the CityRPI model. The impact of the following mitigation strategies on the indoor aerosol infection risk is studied for all the buildings: 1) wear a face mask, 2) increase the outdoor air ventilation rate, 3) upgrade to high-efficiency duct filters in HVAC systems, 4) use portable air cleaners in the rooms, 5) spend less time in indoor spaces, 6) reduce the number of occupants in the space. Increasing the outdoor air ventilation rate by opening the windows or more outdoor air from the intakes can improve the room ventilation condition and reduce infection risk. Still, on the other hand, in the winter season, it can significantly increase the energy consumption of the building. Therefore, it is crucial to find the most effective strategy considering both the reduced probability of infection and the building's energy consumption. For this purpose, a simulation is conducted over Montreal from February 12-21, 2020, the coldest days of winter 2019. The effectiveness of three mitigation strategies for improving the indoor ventilation condition (more outdoor air, upgrading duct filter, portable air cleaner) is compared together.

7.3.1. Geometry and Input Data

The simulation area that covers Montreal City is shown in Fig. 7-5. The 3D model of buildings is generated using Microsoft buildings' footprint data and Google Earth buildings' height information [201]. The total number of buildings is 358295. Table 7-2 shows the settings used for the simulation. For all the buildings, the infection risk is calculated for a room with 100 m^2 floor area. The disease prevalence rate in Montreal is calculated using the last updated data by SANTÉ

MONTRÉAL on 10/21/2020 [202]. The number of daily new cases, the total number of confirmed cases, and the total number of deaths on 10/21/2020 are 316, 39712, and 3516, respectively. It was the maximum alert level or red situation in Montreal. Disease prevalence rate and the fraction of people with immunity calculated using this information are presented in Table 7-2. Other parameters that are needed for calculation of infection risk are estimated using the archetype library for each building type.

Table 7-2 Parameters used for the Montreal City simulation

Parameter	Symbol	Unit	Value
Floor area	A_f	m^2	100
Fraction of population with immunity	F_{immune}	-	0.094
Fraction of asymptomatic cases	f_{unrep}	-	0.8
Disease prevalence rate	P_{prev}	%	0.54

7.3.2. Mitigation Strategies by Building Type

In this section, six different mitigation measures that can reduce the indoor aerosol infection risk are applied to all buildings: 1) wear a face mask, 2) increase the outdoor air ventilation rate, 3) upgrade to high-efficiency duct filters in HVAC systems, 4) use portable air cleaners in the rooms, 5) spend less time in indoor spaces, 6) reduce the number of occupants in the space. Fig. 7-4a shows the impact of mitigation measures on the probability of infection in different types of buildings. Mitigation measures are compared with a base scenario, which is: 0% mask usage, no outdoor air ventilation, without any duct filter, without air cleaner, full occupancy, and standard stay time. The CityBEM model covers 31 building types, but in this figure, only the results of 10 essential types of buildings regarding the COVID-19 aerosol infection risk are presented. Wearing masks by all the occupants can reduce the risk of infection by more than 60% in all types of buildings. Staying half time compared to the normal condition in public or crowded rooms can reduce the risk of infection by more than 60% in all buildings except the daycare and can be considered one of the most effective strategies to reduce infection risk. Reduce the number of occupants inside the room can be an effective strategy for reducing the PI by around 50% in all buildings. Using a high-efficiency (MERV-13) duct filter in the buildings with an HVAC system can filter out the recirculated COVID-19 aerosol particles and reduce the infection risk by more than 56% in all buildings. Upgrading the duct filter is the most effective strategy for daycare rooms with 82% RPI. The RPI of the duct filter in Fig. 7-4 is the median of all buildings with the same type. Unlike other strategies that present the same RPI for all buildings with the same usage type, the RPI of duct filter is different for each building because the HVAC system's airflow rate is different for each building depending on the design condition. Fig. 7-4b shows the box plot of duct filter RPI for various building types. In buildings without the HVAC system and air duct filters, using a portable air cleaner can be an alternative strategy to reduce the aerosol infection risk of COVID-19. A portable air cleaner with 480 CFM capacity is modeled in this work. The RPI by using an air cleaner is from 35-72% depending on the buildings' condition. Using an air cleaner with higher capacity can provide a higher RPI. Proper outdoor air ventilation by opening the windows or from air intakes can reduce the concentration of COVID-19 aerosol particles and reduce the risk of infection. In this work, the minimum required ventilation rate suggested by ASHRAE is used for the simulation. The ventilation rate depends on the building type (outdoor airflow rate per person and occupant density). Therefore, the effectiveness of this strategy is considerably different between buildings of various types $(20 \leq RPI \leq 70)$. Enhancing the outdoor air ventilation rate can increase the RPI provided by this strategy. In conclusion, all studied measures can significantly reduce indoor aerosol infection risk of COVID-19. The effectiveness of these measures depends on the building type. Fig. 7-4a provides information regarding the most to least effective measures for each building type. For example, in daycares upgrading the duct filter and half occupancy are the most and least effective strategies to reduce the PI.

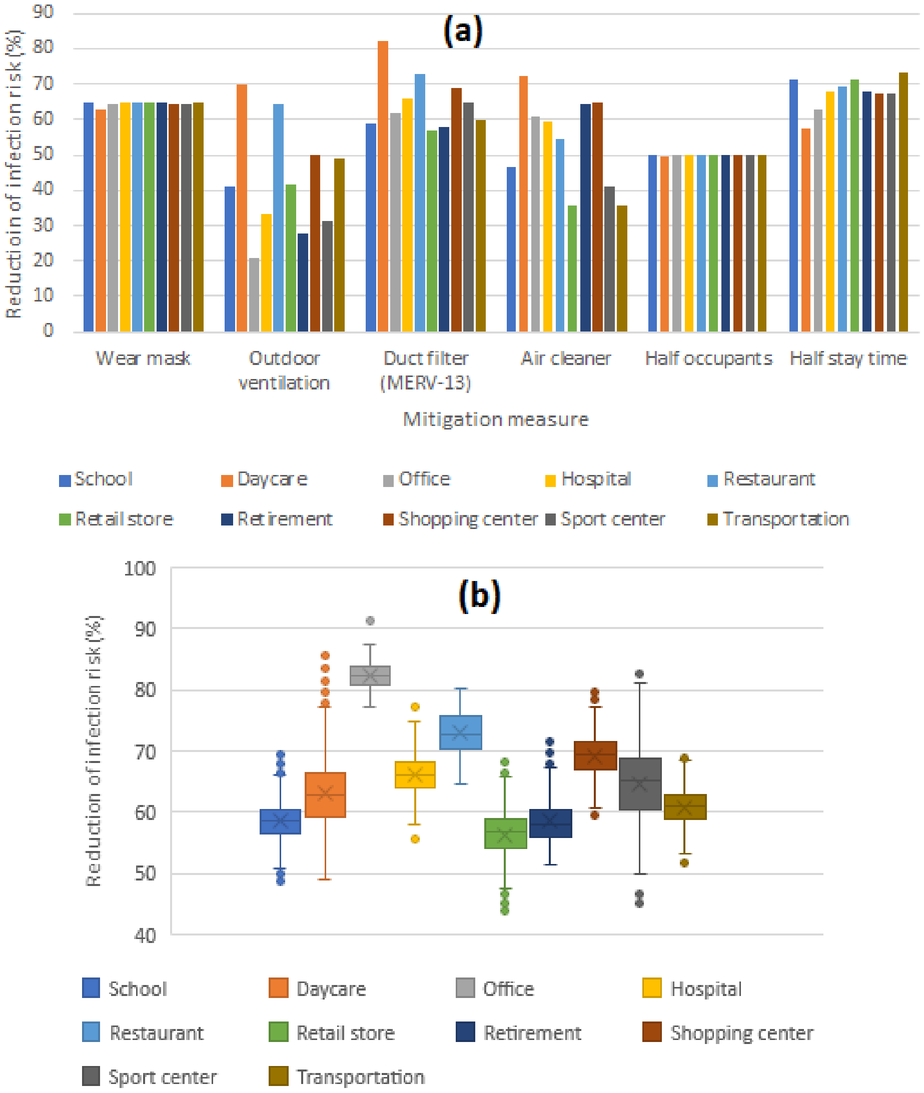

Figure 7-4 a) Impact of 6 mitigation measures on the indoor aerosol infection risk of different types of buildings, b) Range of reduced risk using duct filter for various building types.

According to Fig. 7-4, enhancing indoor air quality using three studied strategies (outdoor air ventilation, duct filter, and portable air cleaner) can reduce the aerosol infection risk of COVID-19 in indoor spaces. Still, they may also affect the energy consumption of the building. During the winter, increasing the outdoor air ventilation rate needs more energy consumption to warm up the cold outdoor air for supplying to the indoor space. On the other hand, portable air cleaners use electricity and increase the energy consumption of the building. Winter is coming, and the number of daily new cases of COVID-19 is rising all around the world. Therefore, it is essential to be prepared for it and make the best decision for reducing the risk of infection and save energy.

7.3.3. HRDPS Weather Data

In this section, mesoscale weather data provided by the High-Resolution Deterministic Prediction System (HRDPS) [145] is used for energy simulation of all buildings in the City of Montreal. HRDPS data are extracted and then interpolated on each building: First, the simulation area's boundaries (Latitude and Longitude) and all HRDPS grid points located inside the domain are specified. In this work, Montreal City is selected for the simulation (Fig. 7-5). Blue circles show the HRDPS grid points. Then, atmospheric elements required for buildings' energy simulation using CityBEM (outdoor air temperature, solar radiation, wind speed, wind direction, and dew point temperature) are extracted for all HRDPS grid points inside the domain. Finally, four HRDPS grid points around each building are selected, and weather data are interpolated on the center of the building based on the distance between the building's center point and grid points [186].

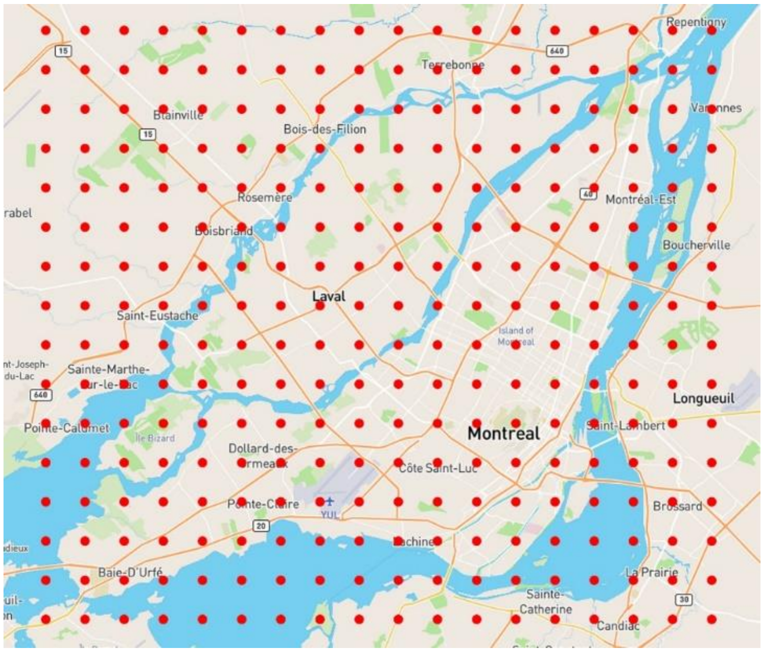

Figure 7-5 HRDPS grid points selected for the Montreal buildings' energy simulation.

In this section, all Montreal buildings are simulated from February 12-21, 2020, the coldest period of winter 2019. Fig. 7-6 shows the peak electricity demand per floor area of all Montreal buildings at 4 AM on February 15, 2020. Results are presented for the base scenario. The figure provides information on the energy performance of the buildings. In buildings with lower energy performance, mitigation measures that do not affect the building's energy consumption, such as wearing a mask, reducing the number of occupants, and reducing the stay time, should be considered the first strategies for reducing the risk infection. Fig. 7-6 also identifies neighborhoods with overall better energy performance. Some regions in the north and south-west of the city identified by red colors include low energy-efficient buildings. On the other hand, Montreal's downtown, highlighted by the white box, presents higher energy performance buildings. The buildings' energy performance depends on several parameters, including age and usage type of the building, and microclimate condition, discussed in detail in the previous chapters [85,201]. I am working on running CityBEM for different scenarios to study each strategy's impact on the peak electricity load. The energy consumption result can help choose the best strategy considering both infection risk and buildings' energy consumption.

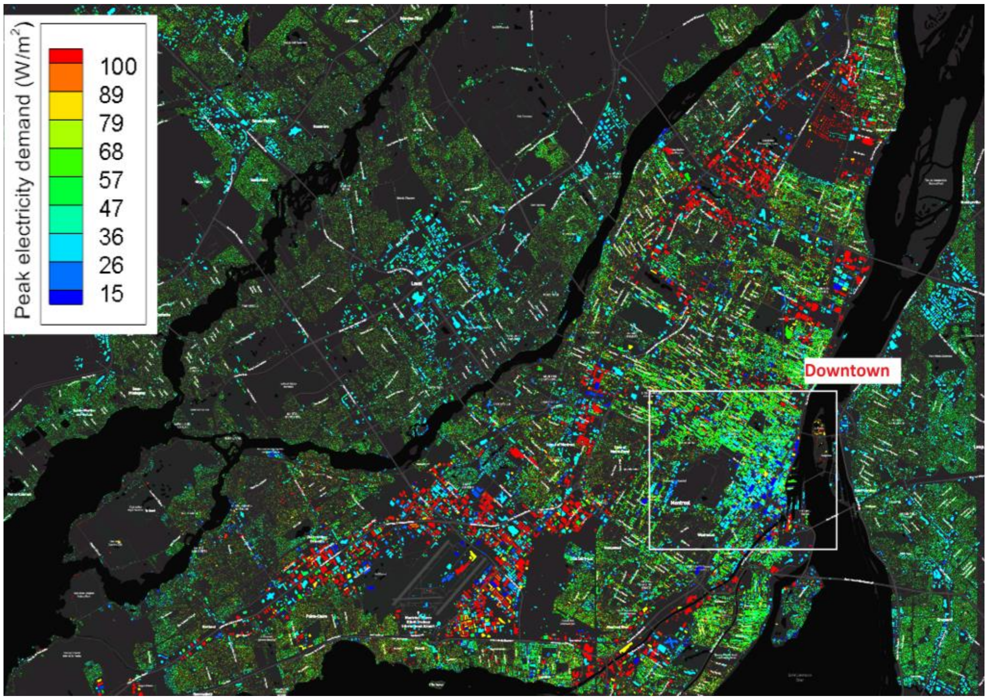

Figure 7-6 Peak electricity demand per floor area of Montreal buildings at 4 AM on February 15, 2020.

7.4. Summary

Recent studies on the COVID-19 virus shows that airborne transmission is a major route of the infection. Airborne transmission is higher in crowded indoor spaces with poor ventilation conditions. Different mitigation strategies can reduce the room's infection risk, including wearing a mask, reducing the occupants' number, reducing the stay time, improving the ventilation condition using duct filters, outdoor air ventilation, and portable air cleaner. These strategies' effectiveness depends on the building type, and other properties and buildings must be studied separately. Also, mitigation strategies may affect the building’s energy consumption. Thus, infection risk and energy consumption must be analyzed simultaneously. In this thesis, a model called CityRPI is developed to calculate the infection risk in all buildings in a city. CityRPI is integrated with CityBEM to study the impact of different strategies on buildings' infection risk and energy consumption. The model is applied to Montreal, and simulation is done for the coldest days of winter 2019. Results show that the effectiveness of strategies depends on the building type and properties. Therefore, it is essential to investigate the impact of scenarios on each building separately. In future work, the effects of strategies on peak load of buildings will be studied to choose the most effective strategy by focusing on both infection risk and energy consumption.

Chapter 8 Conclusions and Future Work

8.1. Conclusions

This research established a new urban building energy model to calculate all buildings' energy performance in a city. The proposed model (CityBEM) includes all essential elements for accurate calculation of the building's energy consumption and is significantly faster than existing UBEM tools. Here, it has concluded that:

- Creating the 3D model of buildings is one major challenge of existing tools. In this work, an automated model is developed for creating the 3D model of buildings. The developed model is accurate and needs minimum manual efforts.
- Estimation of the building's non-geometrical parameters is the second challenge with current tools. In this work, an archetype library is developed to classify the buildings. Then, non-geometrical properties are assigned to each group of buildings. The archetype library is created by gathering data from various datasets.
- Using local microclimate data can significantly impact the accuracy of buildings' energy simulation. Buildings also affect the simulation of local microclimate in urban areas. Therefore, in this work, CityBEM is integrated with two urban microclimate simulation tool to capture the two-way interaction between buildings and microclimate.
- GEM is a numerical weather prediction system developed in ECCC for short-term weather forecasting in Canada and North America. In this work, CityBEM is integrated with the GEM model to perform short-term forecasting of buildings' energy consumption using high-resolution weather forecast data. CityBEM is added as a new module to the GEM. It can

perform accurate buildings’ modeling and improve the calculation of near-surface atmospheric fields in the GEM model.

- The accuracy of the CityBEM is investigated by comparing the results with measurement data of electricity consumption and indoor air temperature of some selected buildings. Results show that CityBEM results' accuracy is acceptable, considering the problem's scale and many uncertainties in the input data.
- Airborne transmission of COVID-19 is a significant route of infection, especially in indoor spaces. The infection risk depends on the ventilation condition and some other properties of indoor environments. The CityRPI model is developed to calculate the airborne infection risk in all buildings' indoor spaces. CityBEM is integrated with CityRPI, and the impact of different mitigation measures are studied on the infection risk and energy consumption of buildings. The effectiveness of strategies depends on the building type, and it is essential to perform separate analyses on each type of buildings.

8.2. Contributions

- This thesis's first contribution is the mathematical and numerical comparison of three coupling strategies for solving the coupled thermal and airflow problem in buildings. The results of this work are used by NIST company for developing the CONTAM-HT model.
- Secondly, I developed the first urban building energy model in Canada to model all buildings' energy performance in large cities or even provinces. Automated generation of 3D buildings’ model and high-resolution 3D model of buildings, trees, terrain, etc., is the next contribution of this thesis.

  - The integrated CityBEM-CityFFD model is developed for solving the two-way impacts between buildings and local urban microclimate. It is the first integration of UBEM and microclimate models.
  - Adding CityBEM to the TEB for modeling buildings and its integration with GEM and SPS models is the next contribution. CityBEM can improve the accuracy of the GEM weather forecasting and GEM-MACH air quality modeling in urban areas. Short-term forecasting simulation of buildings' energy performance will be the new capability of the GEM model.
  - Finally, the CityRPI model is developed for the estimation of airborne transmission of COVID-19 in indoor spaces. The novelty of CityRPI is the capability to model all buildings in a city and study the effectiveness of different strategies in reducing the infection risk.

8.3. Future work

- Complete the integration of CityBEM with the TEB model. Run the multi-scale model equipped with the CityBEM-TEB model and compare the result with measurement data to study the impact of CityBEM on the accuracy of the GEM model.
- The exterior shading by neighbor buildings is not modeled in the CityBEM. A shading model will be added to the CityBEM to improve the accuracy of the model.
- The current version of CityBEM only models the long-wave radiation between buildings, ambient air, and sky. The long-wave radiation between adjacent buildings is not modeled. A new long-wave radiation model will be added to the CityBEM.
- The current geometrical model only includes the 3D model of buildings. It is essential to have the terrain, trees, mountains, and other urban elements in the geometrical model in some cases. A new method will be developed for creating the detailed 3D model of a city using GE API.

- Buildings are modeled as one block in the current version of the CityBEM. An automated multi-zone model will be developed by using one zone for each floor of the building. Different weather data will be used for each floor using CityFFD and/or GEM data to improve the simulation's accuracy.
- CityBEM will model different heatwave mitigation strategies such as natural ventilation, green roof, cool roof, retrofitting of buildings' envelope and glazing, etc. The impact of each scenario on the UHI and energy consumption will be studied.
- The impact of TEB-CityBEM on the urban air quality will be examined by adding the TEB-CityBEM model to the GEM-MACH air quality model of ECCC.
- The impact of mitigation strategies for reducing the indoor infection risk will be studied on the peak heating load of winter 2019. The best strategy for reducing the infection risk and saving energy will be identified for each building class.

References

[1] UN, 2018 Revision of World Urbanization Prospects | Multimedia Library - United Nations Department of Economic and Social Affairs, 2018 Revis. World Urban. Prospect. | Multimed. Libr. - United Nations Dep. Econ. Soc. Aff. (2018). https://doi.org/10.3181/00379727-134-34916.

[2] W. Li, Y. Zhou, K. Cetin, J. Eom, Y. Wang, G. Chen, X. Zhang, Modeling urban building energy use: A review of modeling approaches and procedures, Energy. (2017). https://doi.org/10.1016/j.energy.2017.11.071.

[3] SF Environment, Climate and Sustainability: San Francisco Municipal Progress Report, 2018.

[4] B. Blasio de, One City, TRANSFORMING NEW YORK CITY BUILDINGS FOR A LOW-CARBON FUTURE, Off. Sustain. (2016) 151.

[5] City of Boston, Greenovate Boston: 2014 Climate Action Plan Update, 2014.

[6] Government of Canada, Pan-Canadian Framework on Clean Growth and Climate Change, 2018. https://www.canada.ca/content/dam/themes/environment/documents/weather1/20170113-1-en.pdf%0Ahttps://www.canada.ca/en/services/environment/weather/climatechange/pan-canadian-framework.html%0Ahttp://publications.gc.ca/collections/collection_2017/eccc/En4-29.

[7] Eia, World energy demand and economic outlook EIA’s handling of non-U.S. policies in the International Energy Outlook, U.S. Energy Inf. Adm. (2016).

[8] D.B. Crawley, C.O. Pedersen, L.K. Lawrie, F.C. Winkelmann, Energy plus: Energy simulation program, ASHRAE J. (2000).

[9] C. Cerezo Davila, C.F. Reinhart, J.L. Bemis, Modeling Boston: A workflow for the efficient generation and maintenance of urban building energy models from existing geospatial datasets, Energy. 117 (2016) 237–250. https://doi.org/10.1016/j.energy.2016.10.057.

[10] X. Li, Y. Zhou, S. Yu, G. Jia, H. Li, W. Li, Urban heat island impacts on building energy consumption: A review of approaches and findings, Energy. (2019). https://doi.org/10.1016/j.energy.2019.02.183.

[11] S. Gracik, M. Heidarinejad, J. Liu, J. Srebric, Effect of urban neighborhoods on the performance of building cooling systems, Build. Environ. 90 (2015) 15–29. https://doi.org/10.1016/j.buildenv.2015.02.037.

[12] P. Moonen, T. Defraeye, V. Dorer, B. Blocken, J. Carmeliet, Urban Physics: Effect of the micro-climate on comfort, health and energy demand, Front. Archit. Res. (2012). https://doi.org/10.1016/j.foar.2012.05.002.

[13] M. Baccini, A. Biggeri, G. Accetta, T. Kosatsky, K. Katsouyanni, A. Analitis, H.R. Anderson, L. Bisanti, D. D'Iippoliti, J. Danova, B. Forsberg, S. Medina, A. Paldy, D. Rabczenko, C. Schindler, P. Michelozzi, Heat effects on mortality in 15 European cities, Epidemiology. (2008). https://doi.org/10.1097/EDE.0b013e318176bfcd.

[14] Weather Network, Update: 93 deaths now connected to Quebec heat wave, (2018). https://www.theweathernetwork.com/news/articles/quebec-heat-wave-death-toll-hots-70-montreal-laval-july-2018-heatstroke/106337/.

[15] T. Hong, Y. Chen, X. Luo, N. Luo, S.H. Lee, Ten questions on urban building energy modeling, Build. Environ. (2020). https://doi.org/10.1016/j.buildenv.2019.106508.

[16] S. Leroyer, S. Bélair, S.Z. Husain, J. Mailhot, Subkilometer numerical weather prediction

in an urban coastal area: A case study over the vancouver metropolitan area, J. Appl. Meteorol. Climatol. (2014). https://doi.org/10.1175/JAMC-D-13-0202.1.

[17] A. Lemonsu, S. Belair, J. Mailhot, The new canadian urban modelling system: Evaluation for two cases from the joint urban 2003 Oklahoma City experiment, Boundary-Layer Meteorol. (2009). https://doi.org/10.1007/s10546-009-9414-2.

[18] B. Bueno, L. Norford, G. Pigeon, R. Britter, A resistance-capacitance network model for the analysis of the interactions between the energy performance of buildings and the urban climate, Build. Environ. (2012). https://doi.org/10.1016/j.buildenv.2012.01.023.

[19] U.S. Department of Energy, Buildings energy databook, Energy Effic. Renew. Energy Dep. (2012).

[20] U.S. Department Of Energy, Quadrennial Technology Review: An Assessment of Energy Technologies and Research Opportunities, Quadrenn. Technol. Rev. (2015).

[21] Z. Zhai, M.H. Johnson, M. Krarti, Assessment of natural and hybrid ventilation models in whole-building energy simulations, Energy Build. (2011). https://doi.org/10.1016/j.enbuild.2011.06.026.

[22] C.C. Menassa, N. Taylor, J. Nelson, Optimizing hybrid ventilation in public spaces of complex buildings - A case study of the Wisconsin Institutes for Discovery, Build. Environ. (2013). https://doi.org/10.1016/j.buildenv.2012.12.009.

[23] A. Malkawi, B. Yan, Y. Chen, Z. Tong, Predicting thermal and energy performance of mixed-mode ventilation using an integrated simulation approach, Build. Simul. (2016). https://doi.org/10.1007/s12273-016-0271-x.

[24] G. Brager, S. Borgeson, Y. Lee, Summary report: control strategies for mixed-mode buildings, (2007).

[25] P. Karava, A.K. Athienitis, T. Stathopoulos, E. Mouriki, Experimental study of the thermal performance of a large institutional building with mixed-mode cooling and hybrid ventilation, Build. Environ. (2012). https://doi.org/10.1016/j.buildenv.2012.06.003.

[26] N. Artmann, H. Manz, P. Heiselberg, Climatic potential for passive cooling of buildings by night-time ventilation in Europe, Appl. Energy. (2007). https://doi.org/10.1016/j.apenergy.2006.05.004.

[27] P. Heiselberg, others, Principles of hybrid ventilation, Instituttet for Bygningsteknik, Aalborg Universitet, 2002.

[28] J. Hu, P. Karava, A state-space modeling approach and multi-level optimization algorithm for predictive control of multi-zone buildings with mixed-mode cooling, Build. Environ. (2014). https://doi.org/10.1016/j.buildenv.2014.05.003.

[29] L.L. Wang, W.S. Dols, S.J. Emmerich, Simultaneous solutions of coupled thermal airflow problem for natural ventilation in buildings, in: HVAC R Res., 2012. https://doi.org/10.1080/10789669.2011.591258.

[30] X. Wang, C. Huang, W. Cao, Mathematical modeling and experimental study on vertical temperature distribution of hybrid ventilation in an atrium building, Energy Build. (2009). https://doi.org/10.1016/j.enbuild.2009.03.002.

[31] A. Voeltzel, F.R. Carrié, G. Guarracino, Thermal and ventilation modelling of large highly-glazed spaces, Energy Build. (2001). https://doi.org/10.1016/S0378-7788(00)00074-8.

[32] M.N. Basarir, Numerical study of the airflow and temperature distributions in an atrium, 2009.

[33] Y. Pan, G. Wu, F. Yang, Z. Huang, CFD AND DAYLIGHT SIMULATION

CALIBRATED WITH SITE MEASUREMENT FOR WAITING HALL OF SHANGHAI SOUTH RAILWAY STATION, SimBuild 2008. (84AD).

[34] S. Hussain, P.H. Oosthuizen, Validation of numerical modeling of conditions in an atrium space with a hybrid ventilation system, Build. Environ. (2012). https://doi.org/10.1016/j.buildenv.2011.12.016.

[35] R. Zhang, K.P. Lam, S. chune Yao, Y. Zhang, Coupled EnergyPlus and computational fluid dynamics simulation for natural ventilation, Build. Environ. (2013). https://doi.org/10.1016/j.buildenv.2013.04.002.

[36] G. Walton, W.S. Dols, CONTAM 2.4 user guide and program documentation, 2006.

[37] H.E. Feustel, COMIS-an international multizone air-flow and contaminant transport model, Energy Build. (1999). https://doi.org/10.1016/S0378-7788(98)00043-7.

[38] US DOE, EnergyPlus Engineering Reference, Ref. to EnergyPlus Calc. (2010).

[39] TRNSYS, A Transient System Simulation Program, version 17.1, University of Wisconsin at Madison, Madison, Wisconsin, 2012.

[40] W.S. Dols, S.J. Emmerich, B.J. Polidoro, Coupling the multizone airflow and contaminant transport software CONTAM with EnergyPlus using co-simulation, Build. Simul. (2016). https://doi.org/10.1007/s12273-016-0279-2.

[41] J. Axley, S. Emmerich, S. Dols, G. Walton, An Approach to the Design of Natural and Hybrid Ventilation Systems for Cooling Buildings, Indoor Air. (2002).

[42] S. Yuan, C. Vallianos, A. Athienitis, J. Rao, A study of hybrid ventilation in an institutional building for predictive control, Build. Environ. (2018). https://doi.org/10.1016/j.buildenv.2017.11.008.

[43] D. Qi, J. Cheng, A. Katal, L. Wang, A. Athienitis, Multizone modelling of a hybrid

ventilated high-rise building based on full-scale measurements for predictive control, Indoor Built Environ. (2020). https://doi.org/10.1177/1420326X19856405.

[44] Y. Chen, T. Hong, Impacts of building geometry modeling methods on the simulation results of urban building energy models, Appl. Energy. 215 (2018) 717–735. https://doi.org/10.1016/j.apenergy.2018.02.073.

[45] Y. Chen, T. Hong, M.A. Piette, Automatic generation and simulation of urban building energy models based on city datasets for city-scale building retrofit analysis, Appl. Energy. (2017). https://doi.org/10.1016/j.apenergy.2017.07.128.

[46] C.F. Reinhart, C. Cerezo Davila, Urban building energy modeling - A review of a nascent field, Build. Environ. 97 (2016) 196–202. https://doi.org/10.1016/j.buildenv.2015.12.001.

[47] B. Howard, L. Parshall, J. Thompson, S. Hammer, J. Dickinson, V. Modi, Spatial distribution of urban building energy consumption by end use, Energy Build. 45 (2012) 141–151. https://doi.org/10.1016/j.enbuild.2011.10.061.

[48] L.G. Swan, V.I. Ugursal, Modeling of end-use energy consumption in the residential sector: A review of modeling techniques, Renew. Sustain. Energy Rev. (2009). https://doi.org/10.1016/j.rser.2008.09.033.

[49] K. Fabri, V. Tarabusim, Top-down and bottom-up methodologies for energy building performance evaluation at meso-scale level—A literature review, J. Civ. Eng. Archit. Res. 1 (2014) 283–299.

[50] D. Robinson, F. Haldi, J. Kämpf, P. Leroux, CitySim: Comprehensive micro-simulation of resource flows for sustainable urban planning, in: Proc. Build. Simul. 2009 11th Conf. Int. Build. Perform. Simul. Assoc., 2009. https://doi.org/10.1109/94.765911.

[51] F. Chingcuanco, E.J. Miller, A microsimulation model of urban energy use: Modelling

residential space heating demand in ILUTE, Comput. Environ. Urban Syst. 36 (2012) 186–194. https://doi.org/10.1016/j.compenvurbsys.2011.11.005.

[52] J. Rager, D. Rebeix, G. Cherix, F. Maréchal, M. Capezzali, MEU: An urban energy management tool for communities and multi-energy utilities, in: CISBAT 2013, Lausanne, Switzerland, 2013.

[53] C. Cerezo, T. Dogan, C.F. Reinhart, Towards standardized building properties template files for early design energy model generation, 2014 ASHRAE/IBPSA-USA Build. Simul. Conf. Atlanta, GA, Sep 10-12. (2014). https://doi.org/10.1007/s10533-005-0712-6.

[54] S.J. Quan, Q. Li, G. Augenbroe, J. Brown, P.P.J. Yang, Urban data and building energy modeling: A GIS-based urban building energy modeling system using the urban-EPC engine, in: Lect. Notes Geoinf. Cartogr., 2015. https://doi.org/10.1007/978-3-319-18368-8_24.

[55] G. Happle, J.A. Fonseca, A. Schlueter, Effects of air infiltration modeling approaches in urban building energy demand forecasts, in: Energy Procedia, 2017. https://doi.org/10.1016/j.egypro.2017.07.323.

[56] McNeel R, Rhino 6 for Windows, (2018).

[57] T. Hong, Y. Chen, S.H. Lee, M.A. Piette, CityBES : A Web-based Platform to Support City-Scale Building Energy Efficiency, in: Urban Comput., 2016. https://doi.org/10.1145/12345.67890.

[58] S. Sun, C. Salvaggio, Aerial 3D building detection and modeling from airborne LiDAR point clouds, IEEE J. Sel. Top. Appl. Earth Obs. Remote Sens. (2013). https://doi.org/10.1109/JSTARS.2013.2251457.

[59] S. Kocaman, L. Zhang, A. Gruen, D. Poli, 3D city modeling from high-resolution satellite

images, Proc. ISPRS Work. Topogr. Mapp. from Space, Ankara, Turkey, 14-16 Feb. (2006).

[60] E.P. Baltsavias, A. Gruen, L. Van Gool, Automatic extraction of man-made objects from aerial and space images (III), Volume 3, Taylor & Francis, 2001. http://books.google.com/books?hl=en&lr=&id=kjI4k58eOl4C&pgis=1 (accessed September 17, 2011).

[61] N. Haala, M. Rothermel, S. Cavegn, Extracting 3D urban models from oblique aerial images, in: 2015 Jt. Urban Remote Sens. Event, JURSE 2015, 2015. https://doi.org/10.1109/JURSE.2015.7120479.

[62] S. Malihi, M.J.V. Zoej, M. Hahn, Large-scale accurate reconstruction of buildings employing point clouds generated from UAV imagery, Remote Sens. (2018). https://doi.org/10.3390/rs10071148.

[63] G. Vosselman, Building reconstruction using planar faces in very high density height data, Int. Arch. Photogramm. Remote Sens. (1998). https://doi.org/10.1.1.44.935.

[64] C. Brenner, City Models – Automation in Research and Practice, in: Photogramm. Week 01, 2001: pp. 149–158.

[65] D. Flamanc, G. Maillet, H. Jibrini, 3d city models: an operational approach using aerial images and cadastral maps, Int. Arch. Photogramm. Remote Sens. Spat. Inf. Sci. (2003).

[66] H. Huang, R. Ooka, S. Kato, Urban thermal environment measurements and numerical simulation for an actual complex urban area covering a large district heating and cooling system in summer, Atmos. Environ. (2005). https://doi.org/10.1016/j.atmosenv.2005.07.018.

[67] S.J. Quan, Q. Li, G. Augenbroe, J. Brown, P.P.J. Yang, Urban data and building energy

modeling: A GIS-based urban building energy modeling system using the urban-EPC engine, in: Lect. Notes Geoinf. Cartogr., 2015: pp. 447–469. https://doi.org/10.1007/978-3-319-18368-8_24.

[68] NYC, Building Footprints | NYC Open Data, (2018). https://data.cityofnewyork.us/Housing-Development/Building-Footprints/nqwf-w8eh.

[69] C. Cerezo, J. Sokol, S. AlKhaled, C. Reinhart, A. Al-Mumin, A. Hajiah, Comparison of four building archetype characterization methods in urban building energy modeling (UBEM): A residential case study in Kuwait City, Energy Build. 154 (2017) 321–334. https://doi.org/10.1016/j.enbuild.2017.08.029.

[70] M. Bakillah, J. Lauer, S.H.L. Liang, A. Zipf, J.J. Arsanjani, A. Mobasheri, L. Loos, Exploiting big VGI to improve routing and navigation services, in: Big Data Tech. Technol. Geoinformatics, 2014. https://doi.org/10.1201/b16524.

[71] F.E.A. Horita, L.F.F.G. Assis, L.C. Degrossi, A. Zipf, J.P. de Albuquerque, The use of volunteered geographic information and crowdsourcing in disaster management: A systematic literature review, in: 19th Am. Conf. Inf. Syst. AMCIS 2013 - Hyperconnected World Anything, Anywhere, Anytime, 2013.

[72] H. Senaratne, A. Mobasheri, A.L. Ali, C. Capineri, M. (Muki) Haklay, A review of volunteered geographic information quality assessment methods, Int. J. Geogr. Inf. Sci. (2017). https://doi.org/10.1080/13658816.2016.1189556.

[73] C.C. Fonte, L. Bastin, L. See, G. Foody, F. Lupia, Usability of VGI for validation of land cover maps, Int. J. Geogr. Inf. Sci. (2015). https://doi.org/10.1080/13658816.2015.1018266.

[74] M.F. Goodchild, Citizens as sensors: The world of volunteered geography, GeoJournal.

(2007). https://doi.org/10.1007/s10708-007-9111-y.

[75] P. Neis, D. Zielstra, Recent Developments and Future Trends in Volunteered Geographic Information Research: The Case of OpenStreetMap, Futur. Internet. (2014). https://doi.org/10.3390/fi6010076.

[76] P. Neis, OSMstats - Statistics of the free wiki world map, (2017). http://osmstats.neis-one.org/ (accessed March 15, 2017).

[77] Microsoft, GitHub - microsoft/USBuildingFootprints: Computer generated building footprints for the United States, (2019). https://github.com/microsoft/USBuildingFootprints (accessed August 16, 2020).

[78] Microsoft, GitHub - microsoft/CanadianBuildingFootprints: Computer generated building footprints for Canada, (2019). https://github.com/microsoft/CanadianBuildingFootprints (accessed August 16, 2020).

[79] H. Fan, A. Zipf, Q. Fu, P. Neis, Quality assessment for building footprints data on OpenStreetMap, Int. J. Geogr. Inf. Sci. (2014). https://doi.org/10.1080/13658816.2013.867495.

[80] J.A. Fonseca, A. Schlueter, Integrated model for characterization of spatiotemporal building energy consumption patterns in neighborhoods and city districts, Appl. Energy. (2015). https://doi.org/10.1016/j.apenergy.2014.12.068.

[81] J. Schiefelbein, J. Rudnick, A. Scholl, P. Remmen, M. Fuchs, D. Müller, Automated urban energy system modeling and thermal building simulation based on OpenStreetMap data sets, Build. Environ. (2019). https://doi.org/10.1016/j.buildenv.2018.12.025.

[82] N. Gorelick, M. Hancher, M. Dixon, S. Ilyushchenko, D. Thau, R. Moore, Google Earth Engine: Planetary-scale geospatial analysis for everyone, Remote Sens. Environ. (2017).

https://doi.org/10.1016/j.rse.2017.06.031.

[83] G. Mei, J.C. Tipper, N. Xu, Discrete surface modeling based on Google Earth: A case study, in: Proc. 2nd Int. Conf. Comput. Sci. Netw. Technol. ICCSNT 2012, 2012. https://doi.org/10.1109/ICCSNT.2012.6526125.

[84] J.A. Fonseca, T.A. Nguyen, A. Schlueter, F. Marechal, City Energy Analyst (CEA): Integrated framework for analysis and optimization of building energy systems in neighborhoods and city districts, Energy Build. (2016). https://doi.org/10.1016/j.enbuild.2015.11.055.

[85] A. Katal, M. Mortezazadeh, L. (Leon) Wang, Modeling building resilience against extreme weather by integrated CityFFD and CityBEM simulations, Appl. Energy. (2019). https://doi.org/10.1016/j.apenergy.2019.04.192.

[86] Y. Toparlar, B. Blocken, P. Vos, G.J.F. Van Heijst, W.D. Janssen, T. van Hooff, H. Montazeri, H.J.P. Timmermans, CFD simulation and validation of urban microclimate: A case study for Bergpolder Zuid, Rotterdam, Build. Environ. (2015). https://doi.org/10.1016/j.buildenv.2014.08.004.

[87] F. Salata, I. Golasi, D. Petitti, E. de Lieto Vollaro, M. Coppi, A. de Lieto Vollaro, Relating microclimate, human thermal comfort and health during heat waves: An analysis of heat island mitigation strategies through a case study in an urban outdoor environment, Sustain. Cities Soc. (2017). https://doi.org/10.1016/j.scs.2017.01.006.

[88] Z. Tan, K.K.L. Lau, E. Ng, Urban tree design approaches for mitigating daytime urban heat island effects in a high-density urban environment, Energy Build. (2016). https://doi.org/10.1016/j.enbuild.2015.06.031.

[89] Y. Toparlar, B. Blocken, B. Maiheu, G.J.F. van Heijst, Impact of urban microclimate on

summertime building cooling demand: A parametric analysis for Antwerp, Belgium, Appl. Energy. (2018). https://doi.org/10.1016/j.apenergy.2018.06.110.

[90] P.A. Mirzaei, F. Haghighat, Approaches to study Urban Heat Island - Abilities and limitations, Build. Environ. (2010). https://doi.org/10.1016/j.buildenv.2010.04.001.

[91] B. Blocken, Computational Fluid Dynamics for urban physics: Importance, scales, possibilities, limitations and ten tips and tricks towards accurate and reliable simulations, Build. Environ. (2015). https://doi.org/10.1016/j.buildenv.2015.02.015.

[92] M. Burns, The StL Format | fabbers.com, Ennex Corp. (1989). http://www.fabbers.com/tech/STL_Format.

[93] U. Gandhi, Performing Spatial Joins (QGIS3) — QGIS Tutorials and Tips, (n.d.). https://www.qgistutorials.com/en/docs/3/performing_spatial_joins.html (accessed August 17, 2020).

[94] M. Mortezazadeh, L.L.L.L. Wang, A high-order backward forward sweep interpolating algorithm for semi-Lagrangian method, Int. J. Numer. Methods Fluids. 84 (2017). https://doi.org/10.1002/fld.4362.

[95] J.A. Milbrandt, S. Bélair, M. Faucher, M. Vallée, M.L. Carrera, A. Glazer, The pan-canadian high resolution (2.5 km) deterministic prediction system, Weather Forecast. (2016). https://doi.org/10.1175/WAF-D-16-0035.1.

[96] S. Bélair, A. Méthot, J. Mailhot, B. Bilodeau, A. Patoine, G. Pellerin, J. Côté, Operational implementation of the Fritsch-Chappell convective scheme in the 24-km Canadian regional model, Weather Forecast. (2000). https://doi.org/10.1175/1520-0434(2000)015<0257:OIOTFC>2.0.CO;2.

[97] Z. Mariani, R. Crawford, B. Casati, F. Lemay, A multi-year evaluation of Doppler lidar

wind-profile observations in the Arctic, Remote Sens. (2020). https://doi.org/10.3390/rs12020323.

[98] S. Bélair, R. Brown, J. Mailhot, B. Bilodeau, L.P. Crevier, Operational implementation of the ISBA land surface scheme in the Canadian regional weather forecast model. Part II: Cold season results, J. Hydrometeorol. (2003). https://doi.org/10.1175/1525-7541(2003)4<371:OIOTIL>2.0.CO;2.

[99] S. Ren, C. Stroud, S. Belair, S. Leroyer, M. Moran, J. Zhang, A. Akingunola, P. Makar, Impact of urban land use and anthropogenic heat on air quality in urban environments, in: Int. Tech. Meet. Air Pollut. Model. Its Appl., 2018: pp. 153–158.

[100] V. Masson, A physically-based scheme for the urban energy budget in atmospheric models, Boundary-Layer Meteorol. (2000). https://doi.org/10.1023/A:1002463829265.

[101] A. Lemonsu, A. Leroux, S. Bélair, S. Trudel, J. Mailhot, A general methodology of urban cover classification for atmospheric modelling, in: 86th AMS Annu. Meet., 2006.

[102] V. Masson, C.S.B. Grimmond, T.R. Oke, Evaluation of the Town Energy Balance (TEB) scheme with direct measurements from dry districts in two cities, J. Appl. Meteorol. (2002). https://doi.org/10.1175/1520-0450(2002)041<1011:EOTTEB>2.0.CO;2.

[103] N. Alavi, S. Bélair, S. Leroyer, The Effect of Urban Surface Modification on the Near Surface Air Temperature and Urban Boundary Layer Evolution during Extreme Heat Waves in Montreal, in: 23rd Symp. Bound. Layers Turbul. Conf. Air-Sea Interact., 2018.

[104] S. Leroyer, S. Bélair, L. Spacek, I. Gultepe, Modelling of radiation-based thermal stress indicators for urban numerical weather prediction, Urban Clim. (2018). https://doi.org/10.1016/j.uclim.2018.05.003.

[105] J. Mailhot, S. Bélair, L. Lefaivre, B. Bilodeau, M. Desgagné, C. Girard, A. Glazer, A.M.

Leduc, A. Méthot, A. Patoine, A. Plante, A. Rahill, T. Robinson, D. Talbot, A. Tremblay, P. Vaillancourt, A. Zadra, A. Qaddouri, The 15-km version of the Canadian regional forecast system, Atmos. - Ocean. (2006). https://doi.org/10.3137/ao.440202.

[106] P. Joe, S. Belair, N.B. Bernier, V. Bouchet, J.R. Brook, D. Brunet, W. Burrows, J.P. Charland, A. Dehghan, N. Driedger, C. Duhaime, G. Evans, A.B. Filion, R. Frenette, J. De Grandpré, I. Gultepe, D. Henderson, A. Herdt, N. Hilker, L. Huang, E. Hung, G. Isaac, C.H. Jeong, D. Johnston, J. Klaassen, S. Leroyer, H. Lin, M. MacDonald, J. MacPhee, Z. Mariani, T. Munoz, J. Reid, A. Robichaud, Y. Rochon, K. Shairsingh, D. Sills, L. Spacek, C. Stroud, Y. Su, N. Taylor, J. Vanos, J. Voogt, J.M. Wang, T. Wiechers, S. Wren, H. Yang, T. Yip, The environment Canada pan and parapan American science showcase project, Bull. Am. Meteorol. Soc. (2018). https://doi.org/10.1175/BAMS-D-16-0162.1.

[107] M. Kanda, M. Kanega, T. Kawai, R. Moriwaki, H. Sugawara, Roughness lengths for momentum and heat derived from outdoor urban scale models, J. Appl. Meteorol. Climatol. (2007). https://doi.org/10.1175/JAM2500.1.

[108] R. Schoetter, V. Masson, A. Bourgeois, M. Pellegrino, J.P. Lévy, Parametrisation of the variety of human behaviour related to building energy consumption in the Town Energy Balance (SURFEX-TEB v. 8.2), Geosci. Model Dev. (2017). https://doi.org/10.5194/gmd-10-2801-2017.

[109] B. Bueno, G. Pigeon, L.K. Norford, K. Zibouche, C. Marchadier, Development and evaluation of a building energy model integrated in the TEB scheme, Geosci. Model Dev. (2012). https://doi.org/10.5194/gmd-5-433-2012.

[110] M.L. Carrera, S. Bélair, V. Fortin, B. Bilodeau, D. Charpentier, I. Doré, Evaluation of snowpack simulations over the canadian rockies with an experimental

hydrometeorological modeling system, J. Hydrometeorol. (2010). https://doi.org/10.1175/2010JHM1274.1.

[111] N.B. Bernier, S. Bélair, B. Bilodeau, L. Tong, Near-surface and land surface forecast system of the Vancouver 2010 Winter Olympic and Paralympic Games, J. Hydrometeorol. (2011). https://doi.org/10.1175/2011JHM1250.1.

[112] L. Separovic, S.Z. Husain, W. Yu, D. Fernig, High-resolution surface analysis for extended-range downscaling with limited-area atmospheric models, J. Geophys. Res. (2014). https://doi.org/10.1002/2014JD022387.

[113] S. Leroyer, S. Bélair, J. Mailhot, I.B. Strachan, Microscale numerical prediction over Montreal with the Canadian external urban modeling system, J. Appl. Meteorol. Climatol. (2011). https://doi.org/10.1175/JAMC-D-11-013.1.

[114] M.C. Rochoux, S. Bélair, M. Abrahamowicz, P. Pellerin, Subgrid-scale variability for thermodynamic variables in an offline land surface prediction system, J. Hydrometeorol. (2016). https://doi.org/10.1175/JHM-D-15-0016.1.

[115] H. Lu, C.W. Stratton, Y.W. Tang, Outbreak of pneumonia of unknown etiology in Wuhan, China: The mystery and the miracle, J. Med. Virol. (2020). https://doi.org/10.1002/jmv.25678.

[116] Z. Xu, L. Shi, Y. Wang, J. Zhang, L. Huang, C. Zhang, S. Liu, P. Zhao, H. Liu, L. Zhu, Y. Tai, C. Bai, T. Gao, J. Song, P. Xia, J. Dong, J. Zhao, F.S. Wang, Pathological findings of COVID-19 associated with acute respiratory distress syndrome, Lancet Respir. Med. (2020). https://doi.org/10.1016/S2213-2600(20)30076-X.

[117] WHO, Coronavirus (COVID-19) events as they happen, (2020). https://www.who.int/emergencies/diseases/novel-coronavirus-2019/events-as-they-

happen.

[118] WHO, Coronavirus disease (COVID-19), (2020). https://www.who.int/emergencies/diseases/novel-coronavirus-2019 (accessed July 28, 2020).

[119] WHO, Q&A on coronaviruses (COVID-19), Who. (2020) 1–2. https://www.who.int/news-room/q-a-detail/q-a-coronaviruses.

[120] CDC, Infection Control: Severe acute respiratory syndrome coronavirus 2 (SARS-CoV-2) | CDC, Centers Dis. Control Prev. (2020). https://www.cdc.gov/coronavirus/2019-ncov/hcp/infection-control-recommendations.html?CDC_AA_refVal=https%3A%2F%2Fwww.cdc.gov%2Fcoronavirus%2F2019-ncov%2Finfection-control%2Fcontrol-recommendations.html.

[121] UCDC, Q & A on COVID-19: Basic facts, (2020). https://www.ecdc.europa.eu/en/covid-19/facts/questions-answers-basic-facts.

[122] A. Carducci, I. Federigi, M. Verani, Covid-19 airborne transmission and its prevention: Waiting for evidence or applying the precautionary principle?, Atmosphere (Basel). (2020). https://doi.org/10.3390/atmos11070710.

[123] E.L. Anderson, P. Turnham, J.R. Griffin, C.C. Clarke, Consideration of the Aerosol Transmission for COVID-19 and Public Health, Risk Anal. (2020). https://doi.org/10.1111/risa.13500.

[124] L. Morawska, J. Cao, Airborne transmission of SARS-CoV-2: The world should face the reality, Environ. Int. (2020). https://doi.org/10.1016/j.envint.2020.105730.

[125] S. Asadi, N. Bouvier, A.S. Wexler, W.D. Ristenpart, The coronavirus pandemic and aerosols: Does COVID-19 transmit via expiratory particles?, Aerosol Sci. Technol.

(2020). https://doi.org/10.1080/02786826.2020.1749229.

[126] S. Tang, Y. Mao, R.M. Jones, Q. Tan, J.S. Ji, N. Li, J. Shen, Y. Lv, L. Pan, P. Ding, X. Wang, Y. Wang, C.R. MacIntyre, X. Shi, Aerosol transmission of SARS-CoV-2? Evidence, prevention and control, Environ. Int. (2020). https://doi.org/10.1016/j.envint.2020.106039.

[127] S.L. Miller, W.W. Nazaroff, J.L. Jimenez, A. Boerstra, G. Buonanno, S.J. Dancer, J. Kurnitski, L.C. Marr, L. Morawska, C. Noakes, Transmission of SARS-CoV-2 by inhalation of respiratory aerosol in the Skagit Valley Chorale superspreading event, Indoor Air. (2020). https://doi.org/10.1111/ina.12751.

[128] H. Qian, T. Miao, L. LIU, X. Zheng, D. Luo, Y. Li, Indoor transmission of SARS-CoV-2, MedRxiv. (2020). https://doi.org/10.1101/2020.04.04.20053058.

[129] H. Nishiura, H. Oshitani, T. Kobayashi, T. Saito, T. Sunagawa, T. Matsui, T. Wakita, M. Suzuki, Closed environments facilitate secondary transmission of coronavirus disease 2019 (COVID-19), MedRxiv. (2020). https://doi.org/10.1101/2020.02.28.20029272.

[130] R. Zhang, Y. Li, A.L. Zhang, Y. Wang, M.J. Molina, Identifying airborne transmission as the dominant route for the spread of COVID-19, Proc. Natl. Acad. Sci. U. S. A. (2020). https://doi.org/10.1073/pnas.2009637117.

[131] L. Morawska, J.W. Tang, W. Bahnfleth, P.M. Bluyssen, A. Boerstra, G. Buonanno, J. Cao, S. Dancer, A. Floto, F. Franchimon, C. Haworth, J. Hogeling, C. Isaxon, J.L. Jimenez, J. Kurnitski, Y. Li, M. Loomans, G. Marks, L.C. Marr, L. Mazzarella, A.K. Melikov, S. Miller, D.K. Milton, W. Nazaroff, P. V. Nielsen, C. Noakes, J. Peccia, X. Querol, C. Sekhar, O. Seppänen, S. ichi Tanabe, R. Tellier, K.W. Tham, P. Wargocki, A. Wierzbicka, M. Yao, How can airborne transmission of COVID-19 indoors be

minimised?, Environ. Int. (2020). https://doi.org/10.1016/j.envint.2020.105832.

[132] M.A. Kohanski, L.J. Lo, M.S. Waring, Review of indoor aerosol generation, transport, and control in the context of COVID-19, Int. Forum Allergy Rhinol. (2020). https://doi.org/10.1002/alr.22661.

[133] G. Buonanno, L. Stabile, L. Morawska, Estimation of airborne viral emission: Quanta emission rate of SARS-CoV-2 for infection risk assessment, Environ. Int. (2020). https://doi.org/10.1016/j.envint.2020.105794.

[134] J. Curtius, M. Granzin, J. Schrod, Testing mobile air purifiers in a school classroom: Reducing the airborne transmission risk for SARS-CoV-2, MedRxiv. (2020). https://doi.org/10.1101/2020.10.02.20205633.

[135] H. Dai, B. Zhao, Association of the infection probability of COVID-19 with ventilation rates in confined spaces, Build. Simul. (2020). https://doi.org/10.1007/s12273-020-0703-5.

[136] J. Lelieveld, F. Helleis, S. Borrmann, Y. Cheng, F. Drewnick, G. Haug, T. Klimach, J. Sciare, H. Su, U. Poeschl, Model Calculations of Aerosol Transmission and Infection Risk of COVID-19 in Indoor Environments, MedRxiv. (2020). https://doi.org/10.1101/2020.09.22.20199489.

[137] W. Ford, Numerical Linear Algebra with Applications: Using MATLAB, 2014. https://doi.org/10.1016/C2011-0-07533-6.

[138] W.S. Dols, B.J. Polidoro, NIST Technical Note 1887 CONTAM User Guide and Program Documentation Version 3.2, 2015. https://doi.org/10.6028/NIST.TN.1887.

[139] ASHRAE, ASHRAE Handbook Fundamentals 2017, SI Edition, in: ASHRAE Handb., 2017.

[140] J.F. Kreider, P.S. Curtiss, A. Rabl, Heating and cooling of buildings: design for efficiency, CRC Press, 2009.

[141] H. Kotani, R. Satoh, T. Yamanaka, Natural ventilation of light well in high-rise apartment building, Energy Build. (2003). https://doi.org/10.1016/S0378-7788(02)00166-4.

[142] J.E. Dennis, R.B. Schnabel, Numerical Methods for Unconstrained Optimization and Nonlinear Equations, 1996. https://doi.org/10.1137/1.9781611971200.

[143] J. Hensen, Modelling Coupled Heat and Air Flow: Ping-Pong vs Onions, in: IEA Air Infiltration Vent., 1995. https://doi.org/10.1.1.10.5228.

[144] T. Cebeci, P. Bradshaw, Physical and Computational Aspects of Convective Heat Transfer, 1984. https://doi.org/10.1007/978-3-662-02411-9.

[145] Environment Canada, HRDPS data in GRIB2 format, Gov. Canada. (2020). https://weather.gc.ca/grib/grib2_HRDPS_HR_e.html.

[146] City of Montreal, Unités d'évaluation foncière - Jeu de données, (2020). https://donnees.montreal.ca/ville-de-montreal/unites-evaluation-fonciere (accessed August 19, 2020).

[147] G.N. Walton, Thermal Analysis Research Program Reference Manual, Natl. Bur. Stand. (1993).

[148] D. Arasteh, C. Kohler, B. Griffith, Modeling windows in energy plus with simple performance indices, 2009.

[149] A. Schwarzenberg-Czerny, On matrix factorization and efficient least squares solution., Astron. Astrophys. Suppl. Ser. 110 (1995) 405.

[150] R. Legg, Chapter 5 - Room Heat Gains, Air Diffusion, and Air Flow Rates, in: R. Legg (Ed.), Air Cond. Syst. Des., Butterworth-Heinemann, 2017: pp. 81–102.

https://doi.org/https://doi.org/10.1016/B978-0-08-101123-2.00005-4.

[151] ECCC, Historical Data - Climate - Environment and Climate Change Canada, (2020). https://climate.weather.gc.ca/historical_data/search_historic_data_e.html (accessed October 5, 2020).

[152] L. Lecamwasam, J. Wilson, D. Chokolich, Guide to best practice maintenance & operation of HVAC systems for energy efficiency, Department of Climate Change and Energy Efficiency, 2012.

[153] O. Agent, Recommendations on Specific Fan Power and Fan System Efficiency Air Infiltration and Ventilation Centre, 2009.

[154] H. Butler, M. Daly, A. Doyle, S. Gillies, S. Hagen, T. Schaub, The GeoJSON Format, Internet Eng. Task Force. (2016). https://doi.org/10.17487/RFC7946.

[155] J. Marsch, Level of detail • OSM Buildings, (2018). https://osmbuildings.org/blog/2018-02-28_level_of_detail/ (accessed August 17, 2020).

[156] K. Hormann, A. Agathos, The point in polygon problem for arbitrary polygons, Comput. Geom. Theory Appl. (2001). https://doi.org/10.1016/S0925-7721(01)00012-8.

[157] L. Sullivan, InterQuartile Range (IQR), (2016). https://sphweb.bumc.bu.edu/otlt/mph-modules/bs/bs704_summarizingdata/bs704_summarizingdata7.html (accessed August 18, 2020).

[158] City of Montreal, Digital Surface Model (DSM) - Dataset, (2020). https://donnees.montreal.ca/ville-de-montreal/modele-numerique-de-surface-mns (accessed August 18, 2020).

[159] D. Anguelov, C. Dulong, D. Filip, C. Frueh, S. Lafon, R. Lyon, A. Ogale, L. Vincent, J. Weaver, Google street view: Capturing the world at street level, Computer (Long. Beach.

Calif). (2010). https://doi.org/10.1109/MC.2010.170.

[160] G. Gröger, L. Plümer, CityGML - Interoperable semantic 3D city models, ISPRS J. Photogramm. Remote Sens. (2012). https://doi.org/10.1016/j.isprsjprs.2012.04.004.

[161] D.W. Winiarski, M.A. Halverson, W. Jiang, Analysis of Building Envelope Construction in 2003 CBECS, Richland, WA (United States), 2007. https://doi.org/10.2172/1013953.

[162] U.S. Department of Energy, Commercial Prototype Building Models, U.S. Dep. Energy. (2017).

[163] Légis Quebec, B-1.1, r. 2 - Construction Code, (2020). http://legisquebec.gouv.qc.ca/en/ShowDoc/cr/B-1.1, r. 2 (accessed August 19, 2020).

[164] Government of Ontario, O. Reg. 332/12: BUILDING CODE, (n.d.). https://www.ontario.ca/laws/regulation/r12332 (accessed August 19, 2020).

[165] K. Ahmed, A. Akhondzada, J. Kurnitski, B. Olesen, Occupancy schedules for energy simulation in new prEN16798-1 and ISO/FDIS 17772-1 standards, Sustain. Cities Soc. (2017). https://doi.org/10.1016/j.scs.2017.07.010.

[166] M. Mortezazadeh, L. (Leon) Wang, Modelling urban airflows by a new parallel high-order semi-Lagrangian 3D fluid flow solver, in: COBEE 2018 4th Int. Conf. Build. Energy Environ., Melbourne, Australia, 2018.

[167] NVIDIA, NVIDIA CUDA C Programming Guide Version 4.1, NVIDIA Corporation, Santa Clara, 2011.

[168] Environment and Climate Change Canada, Historical Data - Climate - Environment and Climate Change Canada, Past Weather Clim. (2017). http://climate.weather.gc.ca/historical_data/search_historic_data_e.html.

[169] Y. Tominaga, A. Mochida, R. Yoshie, H. Kataoka, T. Nozu, M. Yoshikawa, T. Shirasawa,

AIJ guidelines for practical applications of CFD to pedestrian wind environment around buildings, J. Wind Eng. Ind. Aerodyn. (2008). https://doi.org/10.1016/j.jweia.2008.02.058.

[170] N. Antoniou, H. Montazeri, M. Neophytou, B. Blocken, CFD simulation of urban microclimate: Validation using high-resolution field measurements, Sci. Total Environ. (2019). https://doi.org/10.1016/j.scitotenv.2019.133743.

[171] M. Mortezazadeh, L. (Leon) Wang, Solving city and building microclimates by fast fluid dynamics with large timesteps and coarse meshes, Build. Environ. (2020). https://doi.org/10.1016/j.buildenv.2020.106955.

[172] SC, 2011 Census of Population Program – Data products, (2011).

[173] R. Rocha, Montreal is 375 years old, but how old are her buildings?, (2018).

[174] Google, Google Maps, (2018).

[175] M. Mosteiro-Romero, J.A. Fonseca, A. Schlueter, Seasonal effects of input parameters in urban-scale building energy simulation, in: Energy Procedia, 2017. https://doi.org/10.1016/j.egypro.2017.07.459.

[176] K. Sun, T. Hong, A framework for quantifying the impact of occupant behavior on energy savings of energy conservation measures, Energy Build. (2017). https://doi.org/10.1016/j.enbuild.2017.04.065.

[177] C. Cerezo, J. Sokol, S. AlKhaled, C. Reinhart, A. Al-Mumin, A. Hajiah, Comparison of four building archetype characterization methods in urban building energy modeling (UBEM): A residential case study in Kuwait City, Energy Build. (2017). https://doi.org/10.1016/j.enbuild.2017.08.029.

[178] HQ, Getting an estimate | Hydro-Québec, (2018).

[179] Natural Resources Canada, Energy Efficiency Trends in Canada 1990 to 2010, 2013.

https://doi.org/http://oee.nrcan.gc.ca/publications/statistics/trends11/pdf/trends.pdf.

[180] ECCC, Historical Data - Climate - Environment and Climate Change Canada, (2018).

[181] R.D. Bornstein, D.S. Johnson, Urban-rural wind velocity differences, Atmos. Environ. (1977). https://doi.org/10.1016/0004-6981(77)90112-3.

[182] W. O'Brien, I. Bennet, Simulation-based evaluation of high-rise residential building thermal resilience, in: ASHRAE Trans., 2016.

[183] A. Leroux, J.R. Gauthier, A. Lemonsu, S. Bélair, J. Mailhot, Automated urban land use and land cover classification for mesoscale atmospheric modeling over Canadian cities, Geomatica. (2009).

[184] J.F. Mahfouf, B. Brasnett, S. Gagnon, A Canadian precipitation analysis (CaPA) project: Description and preliminary results, Atmos. - Ocean. (2007). https://doi.org/10.3137/ao.v450101.

[185] G. Balsamo, J.F. Mahfouf, S. Bélair, G. Deblonde, A land data assimilation system for soil moisture and temperature: An information content study, J. Hydrometeorol. (2007). https://doi.org/10.1175/2007JHM819.1.

[186] H. Wendland, Scattered Data Approximation, Cambridge University Press, 2004. https://doi.org/10.1017/CBO9780511617539.

[187] DONNÉES QUÉBEC, Urban heat / cool islands and surface temperature 2012 - Surface temperatures - Quebec data, (2016). https://www.donneesquebec.ca/recherche/fr/dataset/ilots-de-chaleur-fraicheur-urbains-et-temperature-de-surface/resource/7e5fa576-070a-48a5-846e-aa0ec6905faa (accessed November 12, 2020).

[188] CERFO, Identification et localisation des îlots de chaleur et de fraîcheur pour tout le

Québec urbain Cadre méthodologique général et principales étapes du projet, 2013. www.cerfo.qc.ca.

[189] M. Nicas, W.W. Nazaroff, A. Hubbard, Toward understanding the risk of secondary airborne infection: Emission of respirable pathogens, J. Occup. Environ. Hyg. (2005). https://doi.org/10.1080/15459620590918466.

[190] L. Gammaitoni, M.C. Nucci, Using a Mathematical Model to Evaluate the Efficacy of TB Control Measures, Emerg. Infect. Dis. (1997). https://doi.org/10.3201/eid0303.970310.

[191] G. Buonanno, L. Morawska, L. Stabile, Quantitative assessment of the risk of airborne transmission of SARS-CoV-2 infection: Prospective and retrospective applications, Environ. Int. (2020). https://doi.org/10.1016/j.envint.2020.106112.

[192] N. Van Doremalen, T. Bushmaker, D.H. Morris, M.G. Holbrook, A. Gamble, B.N. Williamson, A. Tamin, J.L. Harcourt, N.J. Thornburg, S.I. Gerber, J.O. Lloyd-Smith, E. De Wit, V.J. Munster, Aerosol and surface stability of SARS-CoV-2 as compared with SARS-CoV-1, N. Engl. J. Med. (2020). https://doi.org/10.1056/NEJMc2004973.

[193] J.L. Jimenez, 2020_COVID-19_Aerosol_Transmission_Estimator - Google Sheets, (2020). https://docs.google.com/spreadsheets/d/16K1OQkLD4BjgBdO8ePj6ytf-RpPMlJ6aXFg3PrIQBbQ/edit#gid=519189277 (accessed October 19, 2020).

[194] F.P. Havers, C. Reed, T. Lim, J.M. Montgomery, J.D. Klena, A.J. Hall, A.M. Fry, D.L. Cannon, C.F. Chiang, A. Gibbons, I. Krapiunaya, M. Morales-Betoulle, K. Roguski, M.A.U. Rasheed, B. Freeman, S. Lester, L. Mills, D.S. Carroll, S.M. Owen, J.A. Johnson, V. Semenova, C. Blackmore, D. Blog, S.J. Chai, A. Dunn, J. Hand, S. Jain, S. Lindquist, R. Lynfield, S. Pritchard, T. Sokol, L. Sosa, G. Turabelidze, S.M. Watkins, J. Wiesman, R.W. Williams, S. Yendell, J. Schiffer, N.J. Thornburg, Seroprevalence of Antibodies to

SARS-CoV-2 in 10 Sites in the United States, March 23-May 12, 2020, JAMA Intern. Med. (2020). https://doi.org/10.1001/jamainternmed.2020.4130.

[195] A.W. Byrne, D. McEvoy, A.B. Collins, K. Hunt, M. Casey, A. Barber, F. Butler, J. Griffin, E.A. Lane, C. McAloon, K. O’Brien, P. Wall, K.A. Walsh, S.J. More, Inferred duration of infectious period of SARS-CoV-2: rapid scoping review and analysis of available evidence for asymptomatic and symptomatic COVID-19 cases, BMJ Open. (2020). https://doi.org/10.1136/bmjopen-2020-039856.

[196] Y. Gu, Estimating True Infections | COVID-19 Projections Using Machine Learning, (2020). https://covid19-projections.com/estimating-true-infections/ (accessed October 12, 2020).

[197] ASHRAE, Ventilation for acceptable indoor air quality, ASHRAE Stand. (2010).

[198] P. Weber, M. (Muki) Haklay, OpenStreetMap: User-Generated Street Maps, IEEE Pervasive Comput. (2008). https://doi.org/10.1109/MPRV.2008.80.

[199] Microsoft, GitHub - microsoft/CanadianBuildingFootprints: Computer generated building footprints for Canada, (2019). https://github.com/Microsoft/CanadianBuildingFootprints.

[200] Microsoft, Computer generated building footprints for the United States: microsoft/USBuildingFootprints, (2019). https://github.com/microsoft/USBuildingFootprints.

[201] A. Katal, M. Mortezazadeh, L. (Leon) Wang, Urban Microclimate and Building Thermal/Energy Modelling – from 3D City Generation to Dynamic Urban Simulations. Manuscript submitted for publication., (2020).

[202] SANTÉ MONTRÉAL, Public, (2020). https://santemontreal.qc.ca/en/public/coronavirus-covid-19/situation-of-the-coronavirus-covid-19-in-montreal/#c43669 (accessed October

21, 2020).

Appendix A

Airflow path models

Airflow paths represent openings between zones or to ambient. The power-law equation is often used to model the airflow from zone i to zone j through path ij $\left(F_{ij}\right)$, which is

$$F_{ij} = C_{ij}\left(\Delta P_{ij}\right)^{n_{ij}} \tag{A.1}$$

Where

C_{ij} is the flow coefficient of the flow path ij

n_{ij} is the flow exponent of path $ij \cong \begin{cases} 0.5 & \text{large openings} \\ 1 & \text{narrow openings} \\ 0.6-0.7 & \text{crack} - \text{like openings} \end{cases}$

ΔP_{ij} is the pressure difference across the path ij.

Orifice airflow equation is another version of the power-law equation:

$$F_{ij} = C_{d,ij}A_{ij}\sqrt{2\rho\Delta P_{ij}} \tag{A.2}$$

Where

$C_{d,ij}$ is the discharge coefficient if path ij

A_{ij} is the area of path ij (m^2)

The power-law model can be integrated with leakage area formulation to calculate air leakage through the building envelope

$$F_{ij} = C_{ij}\left(\Delta P_{ij}\right)^{n_{ij}} \tag{A.3}$$

$$C_{ij} = L_{ij}C_{d,ij}\sqrt{2\rho}\left(\Delta P_{r,ij}\right)^{0.5-n} \tag{A.4}$$

Where

L_{ij} is the effective leakage area (m^2)

$\Delta P_{r,ij}$ is the reference pressure difference (Pa)

$C_{d,ij}$ is the discharge coefficient. There are two reference conditions$\cong \begin{cases} 1.0 & \text{if } \Delta P_{r,ij} = 4\, pa \\ 0.6 & \text{if } \Delta P_{r,ij} = 10\, pa \end{cases}$

Shaft airflow model is used to model low resistance airflow between buildings level through the atria, elevator shafts, and stairwells.

$$F_{ij} = f_{turb}\sqrt{\rho}\left(\Delta P_{ij}\right)^{n_{ij}} \tag{A.5}$$

Appendix B

Tridiagonal matrix algorithm

The tridiagonal matrix algorithm (TDMA), also known as the Thomas algorithm, is a simplified form of Gaussian elimination that can be used to solve the tridiagonal system of equations

$$a_i x_{i-1} + b_i x_i + c_i x_{i+1} = d_i, \quad i = 1, \dots n, \tag{B.1}$$

Where a_1 and c_n are zero. Equation (A.1) can be written in the matrix form

$$\begin{pmatrix} b_1 & c_1 & 0 & \cdots & \cdots & 0 \\ a_2 & b_2 & c_2 & \cdots & \cdots & 0 \\ 0 & a_3 & b_3 & c_3 & \cdots & 0 \\ \cdots & \cdots & \cdots & \cdots & \cdots & c_{n-1} \\ 0 & \cdots & \cdots & 0 & a_n & b_n \end{pmatrix} \begin{pmatrix} x_1 \\ x_2 \\ \vdots \\ x_{n-1} \\ x_n \end{pmatrix} = \begin{pmatrix} d_1 \\ d_2 \\ \vdots \\ d_{n-1} \\ d_n \end{pmatrix} \tag{B.2}$$

The TDMA consists of two parts: a forward elimination phase and a backward substitution phase. At the forward elimination phase, the coefficients a_i, b_i and c_i are modified as follows

$$c_i^* = \begin{cases} \dfrac{c_1}{b_1} & ; i = 1 \\ \dfrac{c_i}{b_i - c_{i-1}^* a_i} & ; i = 2,3, \dots, n-1 \end{cases} \tag{B.3}$$

$$d_i^* = \begin{cases} \dfrac{d_1}{b_1} & ; i = 1 \\ \dfrac{d_i - d_{i-1}^* a_i}{b_i - c_{i-1}^* a_i} & ; i = 2,3, \dots, n-1 \end{cases} \tag{B.4}$$

The solution is then obtained by back substitution

$$x_n = d_n^* \tag{B.5}$$

$$x_i = d_i^* - c_i^* x_{i+1} \quad ; i = n-1, n-2, \dots, 1 \tag{B.6}$$

The solution is obtained in $O(n)$ operations, instead of $O(n^3/3)$ required by Gaussian elimination. The TDMA is only applicable to diagonally dominant matrices, i.e.,

$$|b_i| > |a_i| + |c_i| \quad , i = 1,2, \dots, n. \tag{B.7}$$

Appendix C

The winding number $\omega(R, C)$ of a point R for a closed curve $C(t) = \left(x(t), y(t)\right)^t, t \in [a, b], C(a) = C(b)$, is the number of revolutions made around R while traveling once along C, provided that R is not visited in doing so. $\omega(R, C)$ can be calculated by integrating the differential of the angle $\varphi(t)$ between the edge $\overline{RC(t)}$ and the positive horizontal axis through R (Fig. 3(a)). As $C(t)$ is a closed curve, this always yields $\omega. 2\pi$ with $\omega \in \mathbb{Z}$ denoting the winding number.

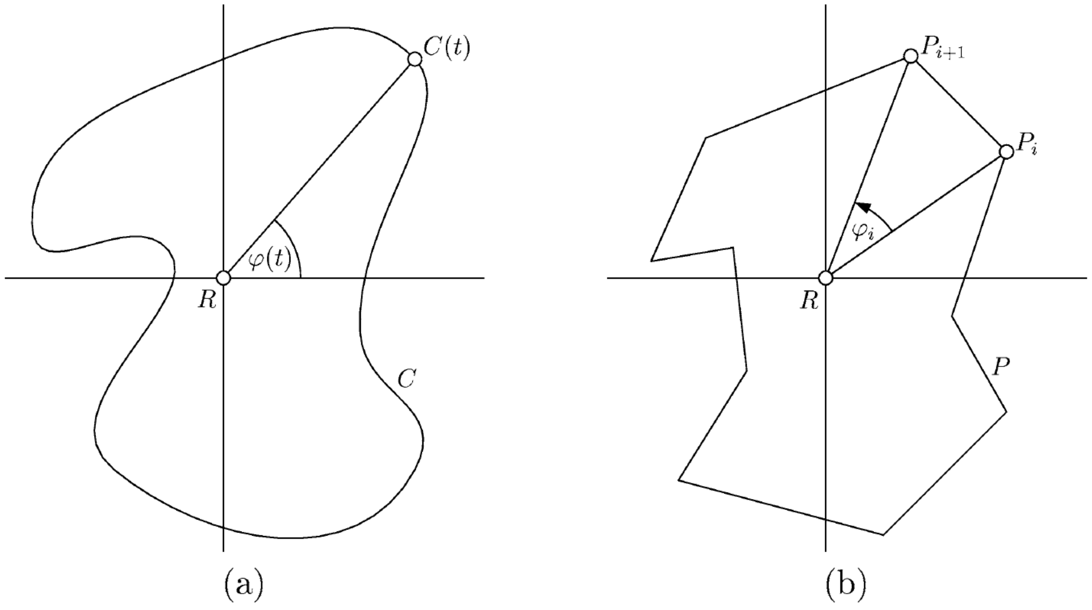

Fig. 1 (a) The continuous angle $\varphi(t)$ for curves. (b) The discretely signed angle φ_i for polygons.

Without loss of generality, we assume $R = (0, 0)$ so that $\varphi(t) = arctan(y(t)/x(t))$ and

$$\omega(R,C) = \frac{1}{2\pi}\int_a^b d\varphi(t) = \frac{1}{2\pi}\int_a^b \frac{d\varphi}{dt}(t)dt = \frac{1}{2\pi}\int_a^b \frac{\dot{y}(t)x(t) - y(t)\dot{x}(t)}{x(t)^2 + y(t)^2}dt \qquad \text{(C1)}$$

A closed polygon P represented as an array of n points $P_0, P_1, \dots, P_{n-1},\ P_n = P_0$ can be seen as a piecewise linear curve $t \rightarrow \left(x_i(t-i), y_i(t-i)\right)^T, t \in [i, i+1]$, with $\left(x_i(t), y_i(t)\right)^T = tP_{\mathrm{i+1}} + (1-t)P_{\mathrm{i}}$. Using Eq. (A1) we obtain

$$\begin{aligned}\omega(R,P) &= \frac{1}{2\pi}\sum_{i=0}^{n-1}\int_0^1 \frac{\dot{y}_i(t)x_i(t) - y_i(t)\dot{x}_i(t)}{x_i(t)^2 + y_i(t)^2}dt \\ &= \frac{1}{2\pi}\sum_{i=0}^{n-1} \arccos\left[\frac{\langle P_i | P_{i+1}\rangle}{\|P_i\|\|P_{i+1}\|}\right].\mathrm{sign}\begin{vmatrix} P_i^x & P_{i+1}^x \\ P_i^y & P_{i+1}^y \end{vmatrix} = \frac{1}{2\pi}\sum_{i=0}^{n-1}\varphi_i\end{aligned} \qquad \text{(C2)}$$

where φ_i is the signed angle between the edges $\overline{RP_\imath}$ and $\overline{RP_{\imath+1}}$ (Fig. 3(b)).

Eq. (A2) can be used for creating an algorithm for computing the winding number, but it involves expensive calls to the *arccos* and *sqrt* routines. A simple observation lets us replace this formula with a more efficient one.

Define the unit vector $\mathbf{w}(R,u) = \overline{RC(t)}/\left|\overline{RC(t)}\right|$ which gives a continuous function $W(R)\colon C \to S^1$ mapping the point $C(t)$ on **C** to the point $\mathbf{w}(R,u)$ on the unit circle $S^1 = \{(x,y)|\, x^2 + y^2 = 1\}$. This map can be represented in polar coordinates as $W(R)(t) = (\cos\theta(t), \sin\theta(t))$ where $\theta(t)$ is a positive counterclockwise angle in radians. Pick any point Q on S^1. Then, as the curve $W(R)$ wraps around S^1, it passes Q a certain number of times. If we count (+1) when it passes Q counterclockwise, and (–1) when it passes clockwise, then the accumulated sum is precisely the total number of times that $W(R)$ wraps around S^1, and is equal to the winding number $wn(R,C)$. Further, if we take an infinite ray P starting at R and extending in the direction of the vector Q, then intersections where P crosses the curve C correspond to the points where $W(R)$ passes Q. To do the math, we have to distinguish between positive and negative crossings where C crosses P from right-to-left or left-to-right. This can be determined by the sign of the dot product between a normal vector to C and the direction vector $q = Q$ [52], and when the curve C is a polygon, one just needs to make this determination once for each edge. For a horizontal ray P from R, testing whether an edge's endpoints are above and below the ray suffices. If the edge crosses the positive ray from below to above, the crossing is positive (+1); but if it crosses from above to below, the crossing is negative (–1). One then simply adds all crossing values to get $wn(R,C)$.